

Contrôle optique du transport de la lumière dans un nuage d'atomes d'ytterbium froids

Apoorva Apoorva

Institut de Physique de Nice

Présentée en vue de l'obtention du grade de docteur en Physique d'Université Côte d'Azur

Dirigée par : **Robin Kaiser**

Soutenue le : **16 décembre 2025**

Devant le jury composé de :

Giovanni Modugno, Professeur, LENS, Université de Florence
Jérôme Beugnon, Professeur, Laboratoire Kastler Brossel, Sorbonne Université
Romain Dubessy, Professeur, Laboratoire de Physique des interactions ioniques et moléculaires, Aix-Marseille Université
Virginia D'Auria, Professeure, Institut de Physique de Nice, Université Côte d'Azur
Robin Kaiser, Directeur de Recherche, CNRS, Institut de Physique de Nice

cnrs
INPHYNI INSTITUT DE PHYSIQUE DE NICE
erc European Research Council Established by the European Commission
anr agence nationale de la recherche
MARIE CURIE ACTIONS

Contrôle optique du transport de la lumière dans un nuage d'atomes d'ytterbium froids

Apoorva Apoorva

Jury :

Rapporteurs :

Giovanni Modugno, Professeur,
LENS, Université de Florence

Jérôme Beugnon, Professeur,
Laboratoire Kastler Brossel, Sorbonne Université

Examinateurs :

Romain Dubessy, Professeur,
Laboratoire de Physique des interactions ioniques et moléculaires, Aix-Marseille Université

Virginia D'Auria, Professeure,
Institut de Physique de Nice, Université Côte d'Azur

Directeur de Thèse :

Robin Kaiser, Directeur de Recherche,
CNRS, Institut de Physique de Nice

Résumé

Contrôle optique du transport de la lumière dans un nuage d'atomes d'ytterbium froids

L'objectif de l'expérience est de démontrer le phénomène tant attendu de la localisation d'Anderson, qui implique la suppression complète du coefficient de diffusion dans un système fortement désordonné en raison de l'interférence destructive entre plusieurs ondes partielles diffusées par le désordre. La démonstration de la localisation nécessite, comme condition préalable, une connaissance précise des propriétés de transport de la lumière. Par conséquent, la mesure de la diffusion de la lumière dans un ensemble atomique contrôlé et bien caractérisé constitue un pont essentiel vers les études de localisation.

Cette thèse explore l'interaction de la lumière au sein d'avec un ensemble atomique froid et optiquement dense d'atomes d'ytterbium (Yb). Elle se concentre sur deux aspects principaux : le contrôle des états atomiques à l'aide de champs optiques spécialement conçus, et le transport de la lumière dans des milieux fortement diffusants.

La première partie décrit l'optimisation et la caractérisation d'un piège magnéto-optique (MOT) à largeur de raie étroite, fonctionnant sur la raie d'intercombinaison $^1S_0 \rightarrow {}^3P_1$ à 556 nm. Nous commençons par motiver le choix de l'Yb et tirons parti de sa raie d'intercombinaison étroite, qui offre une voie alternative et très efficace, par rapport aux atomes alcalins, pour atteindre des températures ultra-froides en chargeant un piège magnéto-optique (MOT) en deux étages. La caractérisation du MOT démontre des températures de nuages atomiques aussi basses que 14 μK, avec un nombre d'atomes de l'ordre de $5 * 10^8$. La densité optique maximale sur la transition $^3P_1$ atteint des valeurs allant jusqu'à 100, suffisantes pour entrer dans le régime de diffusion multiple.

Nous présentons ensuite le contexte théorique et l'observation expérimentale des décalages lumineux dans les atomes froids de ^{174}Yb. La mise en œuvre de décalages lumineux accordables comme outil pour manipuler la structure de l'état interne et démontrer avec succès le contrôle indépendant des sous-niveaux magnétiques $m = \pm 1, 0$ de l'état $^3P_1$ sans avoir besoin d'un champ magnétique externe. En nous appuyant sur ce mécanisme, nous démontrons un analogue entièrement optique de l'effet Faraday. Nos observations confirment l'émergence de la biréfringence et de la rotation de polarisation à la suite d'un habillage optique différentiel, ouvrant ainsi de nouvelles perspectives.

Enfin, nous avons introduit une nouvelle méthode expérimentale permettant de préparer directement l'excitation optique *in situ* au cœur de notre échantillon atomique optiquement dense d'Yb, ce qui a permis d'observer directement l'évolution spatiale cette excitation et sa dynamique temporelle en mesurant la population des différents états internes. Nous avons extrait les paramètres de diffusion en nous affranchissant des effets de bord du nuage, ce qui nous a permis d'obtenir une image plus complète du transport de la lumière dans des ensembles denses et optiquement épais. Les résultats valident non seulement les modèles théoriques, mais ouvrent également la voie à un contrôle précis des interactions lumière-matière dans des systèmes quantiques complexes.

Dans l'ensemble, ces travaux établissent de nouvelles méthodes pour contrôler, sonder et comprendre les interactions lumière-matière dans des ensembles atomiques ultra-froids optiquement denses. L'effet Faraday induit optiquement offre un accès réglable et sans champ magnétique à la biréfringence atomique, tandis que l'étude in situ de la propagation de la lumière permet de contrôler la fréquence des photons qui

se propagent dans l'ensemble dense.
Mots clés : Localisation d'Anderson, ensemble atomique froid, diffusion multiple, coefficient de diffusion, effet Faraday.

Abstract

Optical control of light transport in a cold ytterbium atomic cloud

The aim of the experiment is to demonstrate the long-awaited phenomenon of Anderson localization, which involves the complete suppression of the diffusion coefficient in a strongly disordered system due to destructive interference between multiple partial waves scattered by the disorder. Demonstrating localization requires, as a prerequisite, precise knowledge of light transport properties. Therefore, measuring light diffusion in a controlled and well-characterized atomic ensemble provides an essential bridge toward localization studies.

This thesis explores the interaction of light within an optically dense, cold atomic ensemble of ytterbium atoms. It focuses on two main aspects: the control of atomic states by engineered optical fields and the transport of light in strongly scattering media.

The first part describes the optimization and characterization of a narrow-linewidth magneto-optical trap (MOT), operating on the $^1S_0 \rightarrow {}^3P_1$ intercombination line at 556 nm. We begin by motivating the choice of Yb and benefit from its narrow intercombination line, which provides an alternative and highly efficient route to achieve ultracold temperatures by loading a two-stage magneto-optical trap (MOT), compared to alkali atoms. The characterization of MOT reveals atomic cloud temperatures as low as 14 μK, with atom numbers on the order of $5 * 10^8$. The peak optical density on the $^3P_1$ transition reaches values up to 100, sufficient to enter the multiple-scattering regime.

Next, we present both the theoretical background and the experimental observation of light shifts in cold ^{174}Yb atoms. The implementation of tunable optical shifts as a tool to engineer internal state structure and successfully demonstrate the independent control of the magnetic sublevels $m = \pm 1, 0$ of the $^3P_1$ state without the need for an external magnetic shift. Building on this mechanism, we demonstrate an all-optical analogue of the Faraday effect. Our observations confirm the emergence of birefringence and polarization rotation as a result of differential optical dressing, opening new possibilities.

Finally, we introduced a new experimental method to directly prepare *in situ* optical excitation in the deep core of our optically thick atomic sample of Yb, enabling direct observation of the spatial evolution of the excitation and its temporal dynamics through monitoring of the internal state populations. We extracted the diffusion parameters without relying on boundary effects, providing a more complete picture of light transport in dense, optically thick ensembles. The results not only validate theoretical models but also pave the way for precise control of light-matter interactions in complex quantum systems.

Overall, this work establishes new methods to control, probe, and understand light–matter interactions in optically dense ultracold atomic ensembles. The optically induced Faraday effect offers tunable, magnetic-field-free access to atomic birefringence, while the in-situ study of light propagation enables control of photon frequency launched into the dense ensemble.

Keywords: Anderson localization, Cold Atomic ensemble, Multiple Scattering, Diffusion coefficient, Faraday Effect.

To my parents,

for their endless love, support, and encouragement.

Acknowledgements

I would like to express my sincere gratitude to the people with whom I have shared the most exciting and meaningful moments during my PhD journey.

I am deeply grateful to my supervisor, Robin Kaiser, for giving me the opportunity to work on such a scientifically rich project. His constant support, insightful discussions, and generous sharing of knowledge have greatly contributed to my scientific growth. His passion for physics is undeniable. I am especially thankful for the balance of freedom and thoughtful guidance he provided in the laboratory, both in good times and in challenging ones. His expertise has been invaluable in helping me develop the skills necessary to become an experimental physicist.

My heartfelt thanks go to Raphaël Saint-Jalm for nurturing my scientific skills. He has been an exceptional source of support and advice throughout my PhD. After joining our lab as a permanent researcher in the middle of my doctoral journey, he was always ready to step into the experimental work, offer help, and share his expertise. I am deeply grateful for the many fruitful discussions we had, which greatly enriched my research experience.

I would like to express my sincere thanks to the two exceptionally talented postdoctoral researchers I had the privilege of working with during my PhD: Antoine Glicenstein and Daniel Benedicto Orenes. Their genuine passion for physics and sincere attitude created a truly special and stimulating atmosphere in the laboratory. I will be forever grateful for their constant encouragement, deep insight, and the generous help and support they offered throughout my research.

Warm thanks are also due to Hector Letellier and Álvaro Mitchell Galvão de Melo, who initiated our project and welcomed me with great kindness when I joined the lab. Their guidance helped me settle into the laboratory environment quickly and confidently, and they generously shared their valuable knowledge. I am especially thankful for their support beyond research, helping me with communication in French, assisting me in finding accommodation, and comforting me during some of the most difficult moments of my life.

My sincere thanks go to the other members of the Yb team, the two PhD students Naudson Lucas Lopes Matias and Bérengère Pinoche. It has been a great pleasure to work alongside them.

I also thank to Robin Kaiser, Raphaël Saint-Jalm, Antoine Glicenstein, and Álvaro Mitchell Galvão de Melo for taking the time to review my thesis and provide valuable feedback. I also wish to acknowledge the members of my thesis jury: Giovanni Modugno, Jérôme Beugnon, Romain Dubessy, and Virginia d'Auria, for generously dedicating their time to evaluate my work.

Further gratitude is extended to the administrative, electronics, mechanical, and IT teams at INPHYNI. I am especially thankful to Nathalie Hamel, Elvire Di Concetto, Christine, Cindy, Nathalie, Magali, Sandra, and Arnaud Dusaucy, whose work and support ensured the smooth functioning of the laboratory.

I am also thankful to Côte d'Azur University for its support, in particular the Welcome Center team, Konstanze Beck, Estelle Noye, and Léa Delorme, for guiding international researchers through visa procedures. I would also like to thank the Doctoral School EDSFA, especially its administrative coordinator Catherine Briet, for providing essential information that ensured the successful submission of my thesis. My gratitude is also extended to my annual committee members, Geoffroy Aubry and

Antoine Reserbat-Plantey, for their valuable guidance and thoughtful evaluation of my progress each year.

I would also like to mention my office colleagues: Serigne, Klint, Juliette, Shiyi, Hazel, Apoorav, and Jean Philips, for creating such a friendly and pleasant environment in the office. I also cherish the good memories of the time spent with friends from Sophia Antipolis: Martial, Stéphane, Sardon, Pierre, Nolan, and Alexei.

Finally, I would like to express my heartfelt gratitude to my family in India for their constant moral support, motivation, and love. My dearest parents have always been the greatest inspiration in my life. I am equally thankful to my sister and brother for their unwavering care throughout my PhD. I fondly remember my beloved little niece, whose smiles always brightened my days.

Table des matières

Introduction 1

1 Introduction 1

1.1 Introduction and Motivation . . . 1

1.1.1 Early Experimental Efforts and Controversies . . . 2

1.2 Motivation for Cold-Atomic Ensemble . . . 3

1.2.1 Toward Localization in Cold Atoms: Three Complementary Routes 3

Magnetic field-assisted Anderson localization . . . 3

Optically Induced Zeeman Splitting via Light Shifts . . . 4

Diagonal Disorder via Random Light Shifts . . . 4

1.3 Scope and structure of this thesis . . . 5

2 Magneto-optical Trap - 1S0 to 3P1 transition 6

2.1 Fundamental properties of Ytterbium atoms . . . 7

2.2 Fundamentals of Laser-Atom Interaction . . . 9

2.2.1 Radiation pressure force . . . 9

2.2.2 Doppler cooling . . . 10

2.2.3 Magneto-optical Trap . . . 11

Doppler Temperature . . . 14

2.3 Experimental Setup . . . 15

Capture velocity and the necessity of two-stage cooling . 15

2.3.1 Laser Diode Systems . . . 16

Second harmonic generation (SHG) Cavity Alignment Protocol . 16

2.3.2 Atomic Oven and Vacuum System . . . 19

2.3.3 Optical Setup . . . 20

2.4 Optimization and characterization of a magneto-optical trap (MOT) . . 22

2.4.1 Magnetic Field Compensation Using Spectroscopy 24
Qualitative Check via Molasses Drift 24
Method 1: Spectroscopy-based magnetic field compensation 24
Method 2: Minimizing the spectral linewidth of the $^3P_1$ transition 25
2.4.2 Laser Control and Timing 27
Magnetic Field Gradient Ramp 28
2.4.3 MOT Characterization 29
Estimating $^3P_1$ Optical density via Broad-Line Imaging . 29
Doppler Broadening and Effective b_0 on the Narrow $^3P_1$ Transition 31
2.4.4 Atom Number Calculation from 2D Absorption Imaging 33
Optical Density Calculation 33
2D Gaussian Fit with Offset 34
Temperature: 34
Limitations of Logarithmic OD at High Optical Densities and Alternative Fitting Method 36
2.4.5 Spectroscopy on the Green MOT 37
Linewidth of $^3P_1$ state with optical density 40
Problem encounted 41

3 From Light Shifts to the All-optical Faraday effect 42
3.1 Introduction and Motivation 42
3.2 The AC Stark Effect: Background Theory 43
3.2.1 Theoretical Model 44
3.2.2 Interaction Hamiltonian 45
3.2.3 Time-Dependent Schrödinger Equation 46
3.2.4 Rotating Frame and RWA 46
3.2.5 Adiabatic Elimination and Effective light Shifts 47
Polarization cases (explicit forms): 49
3.2.6 Eigenstates and Physical Picture 49
Sign and validity. 50
3.3 Experimental Setup and Methods 50

3.3.1 Light shifter (1539 nm) laser system: stabilization, detuning control, and power delivery . . . 50
Frequency tuning and stability. . . . 50
3.3.2 LS power calibration and beam alignment inside the rectangular glass cell . . . 51
Total transmission and per-surface model. . . . 51
Alignment using fluorescence “Holes”. . . . 52
3.3.3 Beam waist estimation of the LS beam . . . 53
3.3.4 Detection Methods and Resonance Shift Extraction . . . 54
3.3.5 Imaging Geometry and Setup . . . 55
3.3.6 Error Estimation in the light shift measurement using the Bootstrapping method . . . 61
3.3.7 Inhomogeneous Broadening Due to Imaging Geometry . . . 62
3.3.8 Polarization-Dependent Light Shift Measurements . . . 63
Choice of quantization axis. . . . 64
3.4 Experimental Verification of Light-Shift Scaling . . . 65
3.4.1 Universal scaling: Δ' vs P/Δ_{LS} . . . 67
Spectral linewidth of the light shifted spectrum: . . . 68
3.5 Two dressing beam test of polarization selectivity and additivity . . . 69
3.5.1 Effective Hamiltonian . . . 71
3.5.2 Full control of the $^3P_1$ Zeeman manifold . . . 72
3.6 Optically Induced Faraday Rotation . . . 73
3.6.1 Physical Mechanism . . . 73
3.7 Faraday Rotation in Atomic Media . . . 74
3.7.1 Zeeman Splitting and Magnetically Induced Faraday Effect . . . 75
3.7.2 Optically induced Faraday rotation with a linearly polarized probe 76
3.8 Experimental Methodology: Stokes Parameter Measurement . . . 77
3.8.1 Probe–Dressing Beam Geometry . . . 77
3.8.2 Waveplate Compensation and Polarimetry . . . 78
Three waveplates are needed. . . . 78
3.8.3 Why Stokes Polarimetry is Essential . . . 79
3.8.4 Data Acquisition . . . 79

3.8.5 Data Treatment . . . 80
Summary. . . . 81
3.9 Results and Discussion . . . 81
Rotation θ vs. probe intensity: . . . 81
Rotation θ vs. optical depth: . . . 82
Dependence on light shift: . . . 82
3.9.1 Discussion of deviations . . . 82
3.9.2 Summary . . . 84

4 Transport of Light in Optically Dense Atomic Ensemble 86
4.1 Introduction and Motivation . . . 86
4.1.1 Why Ultracold atomic ensembles are an ideal candidate for studying light propagation in disordered media . . . 87
4.1.2 Challenges in In Situ Probing . . . 88
4.2 Theoretical Background . . . 88
4.2.1 Random walk model . . . 89
Beyond independent scattering: . . . 91
4.3 From Initial Idea to Method Development . . . 92
4.4 Light-Shift Calibration and Spatial Excitation Profiles . . . 94
4.4.1 Light shift calibration . . . 98
Spatial profile of the excited atoms in the light shifted $^3P_1$ state . . . 99
Mapping of the light-shifted potential landscape inside the dense atomic ensemble: . . . 100
4.5 Excitation detection spatially and temporally . . . 102
4.5.1 Experimental setup and Timing sequence . . . 103
Choice of blue probe parameters . . . 105
4.5.2 Principle of the time-resolved absorption imaging . . . 105
4.6 Experimental Data . . . 107
4.6.1 Method of data acquisition and processing . . . 107
4.6.2 Control of Photon Frequency Launched into the Dense Ensemble 113
Doppler-Induced Frequency Redistribution in Our System 115
4.7 Conclusion . . . 115

5 Conclusion **116**

5.1 Outlook 117

A Laboratory relocation and issues encountered **118**

B Derivation of the Excitation Radius **120**

C Preliminary measurement of excited-state population during driven dynamics (Rabi oscillations) **121**

Bibliography **123**

Chapter 1

Introduction

1.1 Introduction and Motivation

Light is an outstanding tool for exploring the physics of wave transport and localization in disordered systems. Photons do not interact with one another and propagate with minimal dissipation. At the same time, optical experiments, especially those based on cold atoms, allow excellent control over the basic parameters of light–matter interaction, such as wavelength, geometry, and polarization. This combination makes optics uniquely well-suited for testing theoretical ideas in mesoscopic physics.

In dilute atomic gases, light undergoes a single-pass absorption and reemission process, a regime often referred to as ballistic transport. However, once the optical depth rises above unity, photons have a high probability of being rescattered before escaping the medium. Each scattering event changes the direction and phase of the scattered light, and the resulting transport is governed by multiple scattering, best described in terms of random walks of photons through the disordered atomic ensemble. The cumulative effect of these random paths leads to diffusive propagation of light. The ballistic to diffusive transition is an intriguing phenomenon, though experimentally challenging to study. However, another phenomenon, Anderson localization, may emerge when disorder and interference become sufficiently strong, with important implications for both fundamental physics and potential technological applications.

The first theoretical prediction of localization for electronic states in the context of the metal-to-insulator transition was made by P. W. Anderson in 1958 [1]. He used a perturbative expansion to analyze how disorder affects the electron's wavefunction and derived a criterion for when electrons would become localized. In other words, wave transport can be completely suppressed in a strongly disordered system due to destructive interference between the multiple partial waves scattered by the disorder. While originally developed for electronic systems, the concept is universal and has been extended to many types of waves, including acoustic waves, matter waves, surface plasmon polaritons, and light [2, 3]. It does not depend on the charge of the particle but only on the interplay between wavelength and disorder strength.

An important aspect of localization is its dependence on dimensionality. Scaling theory [4] predicts that in one and two dimensions, even weak disorder is sufficient to localize all states. In three dimensions, however, a finite threshold of disorder is required to cross the mobility edge that separates extended from localized states. The transition is characterized by critical exponents and universality classes [5]. This makes three-dimensional (3D) localization of light especially interesting but also experimentally

challenging. The critical point of the transition is reached when the dimensionless conductance g takes on a certain threshold value. This is closely connected to the Ioffe–Regel criterion [6, 7], which can be written as $k\ell \sim 1$. Here $k = 2\pi/\lambda$ is the wavenumber and ℓ the transport mean free path. In simple terms, it means the wave is scattered so frequently that the electric field doesn't even get through one full oscillation between scattering events. Achieving the regime where the transport mean free path ℓ becomes comparable to the optical wavelength λ is notoriously difficult in optical systems.

1.1.1 Early Experimental Efforts and Controversies

The most intriguing and challenging phenomena of Anderson localization of light in 3D have attracted researchers in optics for more than four decades. Several experimental works have reported signatures of the localization of light in 3D.

The first experimental claim came from Wiersma [8], who investigated light transport in strongly scattering semiconductor (GaAs) powders. Gallium arsenide was chosen because of its very high refractive index ($n \sim 3.5$), which dramatically enhances scattering. By carefully preparing submicron GaAs particles, they reported evidence consistent with the scaling theory of localization at the transition point, observing a dramatic suppression of transmission attributed to a mobility edge in three dimensions. Their approach was based on transmission measurements through varying thickness, where the observed decay followed a quadratic dependence ($T \propto L^{-2}$), in contrast to classical diffusion, which predicts a linear decrease of transmission with sample thickness. The major critique of the approach was that it could merely be absorption or nonlinear effects.

Shortly afterward, Chabanov and Genack [9] introduced a different approach by analyzing statistical fluctuations of transmission in strongly scattering waveguides in the microwave regime. Their study showed that the variance of normalized transmission can serve as a reliable criterion of localization, since it is less affected by absorption than the average transmission. One of the main outcomes of this work was recognizing a fluctuation threshold, $\mathrm{var}(s_a) > \frac{2}{3}$ is a universal signature distinguishing diffusive propagation from Anderson localization. Their observation that three-dimensional localization cannot be achieved in aluminum samples shifted the focus away from average intensity and toward statistical measures, which have proven to be more reliable indicators of localization.

Soon after, Aegerter et al [10] reported the first experimental attempt to extract critical exponents associated with Anderson localization of light. By performing time-resolved transmission measurements of short optical pulses in strongly scattering samples of TiO_2 powders, they extracted the critical exponents governing the transition. In particular, they observed a slowdown of the diffusion coefficient consistent with a power-law decay at the mobility edge and determined a critical disorder parameter of $(k\ell)_c \approx 4.2$ in reasonable agreement with the Ioffe–Regel criterion. A critical exponent is also determined for the divergence of the localization length of $\nu \approx 0.45$, providing one of the first experimental benchmarks for scaling theory in 3D optical systems.

Till now, the question of whether Anderson localization of light really occurs in three dimensions has remained unsettled. Later investigations cast doubt on the original claims, pointing out that the supposed signatures of localization could just as easily be explained by other effects — including absorption, fluorescence, or even nonlinear

Raman scattering in TiO_2 powders [11, 12].

In particular, Skipetrov and Page [13] argued that in strongly scattering media, absorption and fluorescence can mimic exponential decay and alter transport statistics in ways that resemble localization. One limitation comes from the refractive index of transparent materials at optical frequencies, which rarely exceeds $n \approx 4$. As a result, optical scattering cannot be made arbitrarily strong, making it difficult to reach the Anderson localization threshold.

1.2 Motivation for Cold-Atomic Ensemble

These barriers have pushed researchers to find an alternative platform where the disorder and its associated effects can be well controlled. The cold atom experiments offer an ideal solution because atoms act as nearly identical point scatterers, with a well-defined resonance and tunable optical response. This makes them an appealing setting for studying localization under well-defined conditions. Unlike condensed matter scatterers such as powders, the scattering cross section of the cold atoms is large and tunable with detuning. Absorption can be suppressed by working off-resonance, with precisely known internal level structure and densities that can be tuned in real time. The geometry and disorder can be engineered at will, ranging from dilute thermal clouds to optically dense ensembles. Furthermore, alkaline-earth(-like) atoms such as ytterbium and strontium provide additional advantages; their narrow intercombination transitions naturally enhance multiple scattering, while the absence of hyperfine structure in the ground state of the bosonic isotopes eliminates unwanted inelastic channels. These features make cold atoms an ideal medium to explore mesoscopic transport and Anderson localization of light, with a level of experimental control that is unattainable in traditional condensed matter samples.

1.2.1 Toward Localization in Cold Atoms: Three Complementary Routes

While diffusion is the natural first step in characterizing light transport in cold-atom ensembles, the ultimate goal of our experimental work is to study Anderson localization of light (3D) in a ytterbium atomic ensemble. Achieving localization requires pushing beyond simple multiple scattering to regimes where interference between scattering paths fully suppresses transport. Three promising and largely non-conventional approaches have been identified for cold atoms.

A common way to describe the onset of Anderson localization is through the Ioffe–Regel criterion $k\ell \sim 1$. In practice, though, getting to this regime with cold atomic gases is tricky. Vectorial scattering of light and the cooperative dipole–dipole interactions between atoms usually work against localization, pushing the photons toward delocalization instead.

Magnetic field-assisted Anderson localization One approach that seems particularly promising is to use magnetic fields to promote localization [14]. In cold-atom gases, especially those like ytterbium (Yb) and strontium (Sr) that have a non-degenerate ground state and a degenerate excited state, the light–matter interaction is simplified. In the absence of an external magnetic field, the three Zeeman sublevels of the excited

state ($m = -1, 0, +1$) are degenerate. Light couples all these transitions simultaneously, and the multiple scattering process involves polarization-dependent interference among them. The near-field part of the dipole-dipole Green's tensor couples strongly between atoms, especially via the $m = 0$ channel, which tends to destroy localization by opening radiative escape paths.

When a magnetic field is applied to lift the degeneracy of m states via the Zeeman effect, this can select the transition channels and suppress mixing. If the driving light is tuned into resonance with a specific Zeeman transition (say ($m = +1$), one can effectively isolate that channel. This reduces mixing between m-states and thereby modifies the nature of multiple scattering.

As a result, the near-field dipole–dipole interactions, which normally tend to suppress interference, become much weaker. This makes light propagation behave more like a scalar-wave process, where polarization effects play a smaller role. Under these conditions, it becomes possible to explore magnetic-field-driven localization.

Optically Induced Zeeman Splitting via Light Shifts A second route, which is experimentally appealing, is to replace static magnetic fields with optical control of the Zeeman sublevels. As discussed in Chapter 3 (Light shift), Off-resonant dressing beams that couple the $^3P_1$ manifold to the $^3D_1$ state can induce vector light shifts, effectively mimicking the role of a magnetic field. By adjusting the intensity and polarization of these beams, the degeneracy of the $m = \pm 1$ states can be lifted, which is necessary for selective transport. Compared to conventional magnetic-field control, this optical scheme offers several practical advantages that are discussed in detail in Chapter 3. From the standpoint of localization, the induced splitting functions in much the same way as a real field, reducing resonant dipole-dipole interactions that favor delocalization and allowing long-lived, narrow optical modes to emerge.

Diagonal Disorder via Random Light Shifts A third approach to Anderson localization of light is to apply a three-dimensional speckle field. Instead of relying solely on the positional randomness of atomic scatterers, one can introduce disordered light shifts of the atomic levels by shining a speckle pattern onto the sample. This spatially random light shift acts as diagonal disorder in the Anderson model, closely analogous to on-site energy fluctuations in disordered crystals. In practice, imposing on-site disorder via a speckle field means that each atom's resonance frequency is spatially shifted (i.e., local detuning), which suppresses resonant dipole–dipole exchange (i.e., reduces coherent hopping) and can thereby favor localization. This idea is consistent with approaches using non-Hermitian Hamiltonians to model light localization in cold atomic systems, where both positional and diagonal disorder play a role (see, e.g., [15] for a mobility edge along the imaginary axis in such systems).

All three different approaches toward Anderson localization of light in 3D are promising. Unlike condensed-matter samples, where the disorder landscape is fixed, these strategies—using magnetic fields, optically induced Zeeman splitting, and engineered diagonal disorder—demonstrate the versatility of a cold atomic ensemble. Therefore, the cold atoms are the best suited to investigate the crossover from diffusion to localization, and to test theoretical predictions of mobility edges in open, disordered systems.

1.3 Scope and structure of this thesis

The main focus of this thesis work is to develop a comprehensive understanding of light diffusion in a disordered, optically thick ensemble of ^{174}Yb, which is a prerequisite for addressing Anderson localization of light. Three main approaches towards strong localization were discussed in the last section. In particular, we focused on enabling the observation of Anderson localization under diagonal disorder [16, 14] introduced via an optical speckle field. Therefore, the main objective of this work is to develop and characterize a tunable and optically controllable platform based on a cold atomic cloud of ^{174}Yb for a detailed study of light transport and light-induced energy shifts in three dimensions. Consequently, this work establishes the experimental groundwork, which is a crucial step toward the controlled implementation of diagonal disorder and the eventual observation of Anderson localization of light.

The second **chapter** 2 describes the reconstruction, optimization, and characterization of a narrow-linewidth magneto-optical trap (MOT) operating on the $^1S_0 \rightarrow ^3P_1$ intercombination line at 556 nm [17]. Considerable effort was devoted to overcoming practical challenges such as stabilizing the laser power and frequency, maintaining proper polarization for six well-balanced MOT beams, and compensating residual magnetic fields. After addressing these issues, the characterization of the MOT was discussed. Absorption imaging on the broader 399 nm transition is performed, achieving ultracold temperatures of 14 μK with atom numbers on the order of $5 * 10^8$. The peak optical density on the $^3P_1$ transition reaches values up to 100 on a narrow-linewidth transition $^1S_0 \rightarrow {}^3P_1$, optically dense enough to be in the multiple-scattering regime.

In the third **chapter** 3, the theoretical framework and the experimental demonstration of light shifts of the $^3P_1$ state are discussed. We present the tunable optical shifts of the magnetic sublevels $m = \pm 1, 0$ of the $^3P_1$ state, demonstrating independent control of the magnetic sublevels without the need for an external magnetic field. A clean and optical method to control and break the degeneracy of the $^3P_1$ state. Building on this mechanism, we also demonstrate a novel method to induce and measure Faraday rotation purely through optical means. Our observations confirm the emergence of birefringence and polarization rotation as a result of differential optical dressing.

The fourth **chapter** 4 addresses the central goal of the project: in-situ measurements of light diffusion in an optically dense cloud [18, 19], a prerequisite to observe localization. By launching controlled optical excitations in the deep core of the atomic cloud, we track photon transport via multiple scattering in real time. Under conditions where the cloud size exceeds the transport mean free path, we observe a crossover from ballistic to diffusive transport regime. The measured diffusion coefficient, transport velocity, and transport time are in good agreement with theoretical diffusion models.
The comprehensive study of light-induced energy shifts and photon transport in dense atomic clouds sets the foundation for the next experimental milestone.

Chapter 2

Magneto-optical Trap - 1S0 to 3P1 transition

Since the mid-1980s, the laser cooling and trapping of atoms have been extensively developed, ultimately leading to the observation of Bose-Einstein condensation (BEC) [20]. Early cold atom experiments have been conducted with alkali atoms for many physical and practical reasons. The presence of a single electron in their outer shell resembles the hydrogen-like energy level, making alkali atoms well understood, easier to manipulate, and facilitating the isolation of the required transitions. Commercial lasers and technologies were readily available, as their wavelengths fall within the visible and near-infrared ranges.

Despite being favorable candidates for cooling and trapping, and even achieving a BEC, their internal structure presents significant obstacles to observing Anderson localization of light. Experiments on light scattering in three-dimensional ensembles of cold Rubidium atoms have so far failed to demonstrate any clear evidence of Anderson localization [21, 22], primarily due to Zeeman degeneracy in both the ground and excited states, which leads to polarization-dependent scattering and optical pumping into different internal states. This breaks the symmetry between time-reversed scattering paths and reduces the contrast of coherent backscattering (CBS), a precursor to strong localization. Additionally, their hyperfine splitting gives rise to off-resonant hyperfine Raman scattering, which manifests as residual absorption and acts as a dissipative mechanism, fundamentally incompatible with the interference-based nature of Anderson localization. Factors such as residual absorption, internal state dynamics, and polarization effects [16] explain the absence of localization signatures in cold alkali systems. In the context of challenges posed by Zeeman and hyperfine degeneracy, isotopes such as ^{174}Yb offer a promising alternative. Unlike alkali atoms, ^{174}Yb has zero nuclear spin, resulting in no hyperfine structure or Zeeman degeneracy in the ground state. This makes the atomic structure easier to model and enables more quantitative comparisons between theory and experiment. These advantages make Ytterbium an excellent candidate for observing phenomena such as multiple scattering, diffusive transport, and light localization [23].

At the end of the 1990s, several groups were involved in exploring the alkaline earth metal-like atoms with no nuclear spin and successfully managed to have BEC of Ytterbium atoms by 2003 [24, 25]. Since then, many successive approaches have been demonstrated to improve the cold atomic sources, aiming to increase the atomic flux, fast loading rates [26], and efficient cooling [27], and maximize the steady-state atom

number using the implementation of a core-shell magneto-optical trap [28].

Although alkali atoms such as rubidium or cesium rely on a single broad transition, they can still achieve sub-Doppler temperatures through polarization-gradient cooling. In contrast, Ytterbium and other alkaline-earth-like atoms benefit from the presence of a narrow intercombination line, which provides an alternative and highly efficient route to achieve ultracold temperatures. These characteristics are particularly beneficial for our experimental studies of light transport in optically dense media, where multiple scattering plays a central role.

In this chapter, we describe the implementation and characterization of a narrow-linewidth magneto-optical trap (MOT) on the intercombination line of Ytterbium (Yb). We begin by motivating the choice of Yb and detailing its relevant atomic properties. We then present the theoretical basis of the optical molasses and the principles of operation of MOT, followed by a description of our laser systems and experimental arrangement. Finally, we discuss the performance of the MOT via imaging techniques, magnetic-field compensation, spectroscopy on the trapped ensemble, and other practical considerations and problems encountered.

2.1 Fundamental properties of Ytterbium atoms

Ytterbium is an alkaline-earth-like metal with two electrons in its outer shell and a ground-state electronic configuration of $[\mathrm{Xe}], 4f^{14}, 6s^2$. In its neutral metallic form, it is strongly diamagnetic and relatively stable due to a filled 4f subshell. Ytterbium has seven naturally occurring stable isotopes, with an atomic number of 70 and an average atomic mass of 173.04. Among these, ^{174}Yb is the most abundant, comprising approximately $\approx 31.8\%$ of the natural isotope distribution, which is advantageous for achieving high atomic flux in cold atom experiments.

We work with ^{174}Yb, a bosonic isotope with nuclear spin zero. In contrast to alkali atoms, Ytterbium has two valence electrons and exhibits both spin-allowed and spin-forbidden transitions. Under the electric dipole selection rules ($\Delta S = 0$), the transition between electronic states of different multiplicities is normally forbidden. However, in heavy atoms such as Ytterbium (Z=70), relativistic spin-orbit coupling introduces mixing between singlet and triplet manifolds. As a result, transitions that are spin-forbidden in lighter atoms become weakly allowed in Ytterbium. This results in the presence of narrow intercombination lines, such as the $^1S_0$ to $^3P_1$ transition at 555.8 nm. Thus, Ytterbium has two primary cooling transitions from its ground state ($^1S_0$), each with significantly different linewidths and timescales. Figure 2.1 illustrates the relevant energy levels and transition parameters used in our laser cooling scheme.

The $^1S_0 \rightarrow {}^1P_1$ transition in Ytterbium, often referred to as the blue line, occurs at 398.9 nm and is dipole-allowed. It has a short excited-state lifetime of approximately 5.46 ns, corresponding to a natural linewidth of $\Gamma_b/2\pi = 29.1$ MHz. Because of this broad linewidth, atoms can scatter photons at a high rate, resulting in strong radiation pressure. This makes the transition particularly effective for initial slowing and cooling of the atoms. In our setup, atoms moving at typical thermal velocities of around 300 m/s can be decelerated to about 30 m/s, which is well below the capture velocity of the MOT (approximately 40 m/s) [29]. However, the trade-off is that this transition has a relatively high Doppler cooling limit of approximately 699 µK, which limits how cold the atoms can get during this stage.

It is important to note that the blue transition is not perfectly closed. While the dominant decay pathway from the $^1P_1$ excited state is the electric dipole transition back to the ground state $^1S_0$, there exists a weak intercombination decay channel that leads to long-lived triplet states. Specifically, atoms can decay from $^1P_1$ to the $^3P_{0,1}$ states via intermediate triplet states such as $^3D_1$ and $^3D_2$, as shown in Figure 2.1 [30, 31]. The transition rate for this leakage is on the order of 10^{-8}, meaning that the overall probability of shelving into the ^1P manifold is extremely small. Thus, although not strictly closed, the transition is sufficiently cycling for practical purposes in laser cooling.

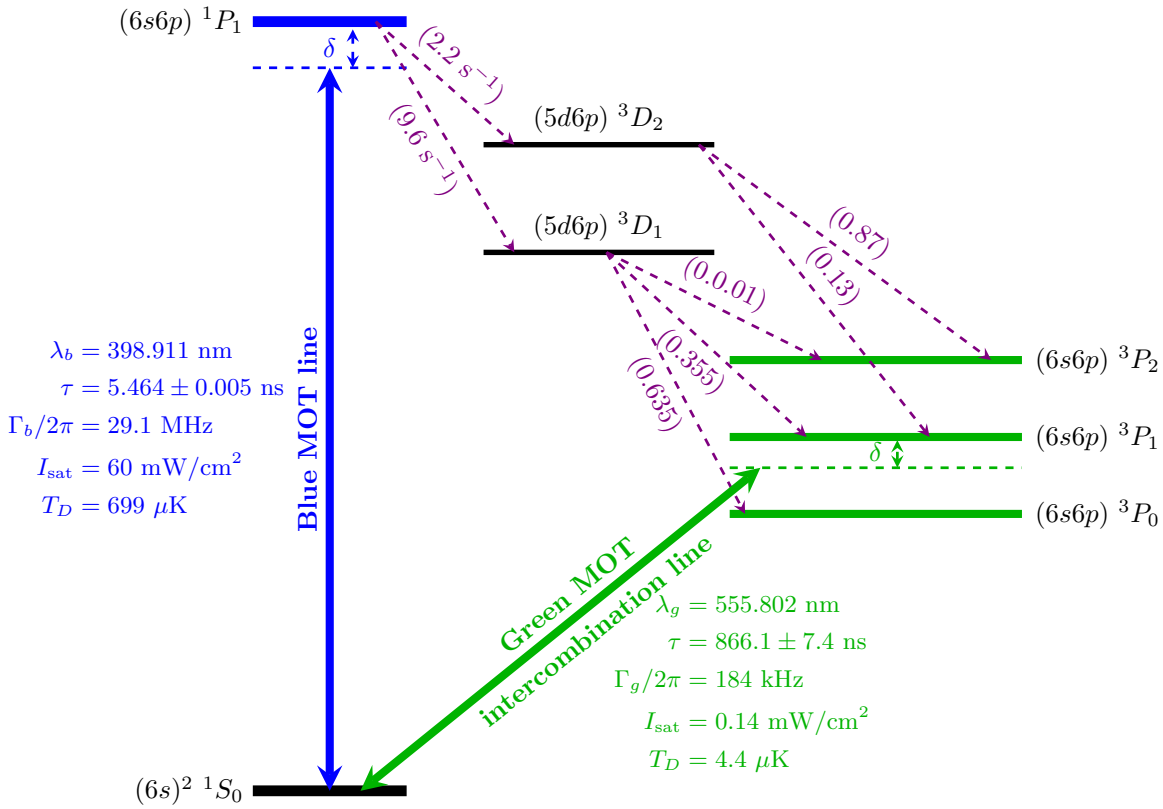

Figure 2.1: Energy-level diagram of the Ytterbium atom showing relevant electronic states and optical transitions used for laser cooling and state manipulation [32]. For each transition, the corresponding wavelength (λ), excited-state lifetime (τ)[33, 34, 35], natural linewidth (Γ), saturation intensity (I_{sat}), and Doppler temperature (T_D) are indicated. The strong dipole-allowed transition at 398.911 nm (blue MOT line) and the narrow intercombination line at 555.802 nm (green MOT line) are used for cooling. The $(5d6s)\,^3D_1$ state serves as a quenching state for the $(6s6p)\,^3P_1$ level[30].

The 3D MOT can be operated without the need to repump atoms from the long-lived triplet states, as their population remains negligible and does not significantly impact performance. In our current setup, our MOT operates without any repumper lasers. However, we have two repumper lasers available for future implementation: one addressing the $^3P_2 \rightarrow {}^3D_1$ transition and the other targeting the $^3P_0 \rightarrow {}^3S_1$ transition (this transition is not depicted in Figure 2.1). Previous studies have shown that using

repumpers can increase the trapped atom number in the $^1P_1$ MOT stage by up to 30% [31].

The second cooling transition, commonly referred to as the “green” line, is the $^1S_0 \rightarrow {}^3P_1$ intercombination transition at 555.8 nm. This transition is nominally electric-dipole forbidden by spin-selection rules but becomes weakly allowed due to spin–orbit coupling, resulting in a very narrow linewidth of $2\pi \times 184$ kHz. The corresponding Doppler temperature is 4.4 µK, making it well-suited for Doppler cooling and compression stages. As a consequence, the reduced temperature leads to an increase in phase-space density. Moreover, magneto-optical traps operating on such narrow lines can provide tighter spatial confinement, which under appropriate conditions yields higher atomic densities.

2.2 Fundamentals of Laser-Atom Interaction

2.2.1 Radiation pressure force

Doppler cooling is a key technique in atomic physics that reduces the motion of atoms, and thus their temperature, by exploiting the interaction of an atom with red-detuned (i.e., the laser frequency is slightly below the atomic resonance frequency) laser light. This interaction results in a reduction of kinetic energy due to the Doppler effect and a radiation pressure force. Consider an atom moving with an initial velocity v_i opposite to the direction of an incoming photon of momentum $\hbar\vec{k}$, as illustrated in Fig. 2.2. When the laser light is tuned to be resonant with the atomic transition in the atom’s rest frame (the light is Doppler-shifted into resonance due to the motion of the atom), the atom can absorb the photon. This absorption imparts momentum $\hbar\vec{k}$ to the atom in the direction of the photon, causing a change in the atom’s velocity.

As a result, the final velocity of the atom of mass M after absorption is: $v_f = v_i - \frac{\hbar k}{M}$. This momentum kick slows the atom slightly. When the light is counter-propagating with respect to the direction of atom velocity. Through repeated absorption-emission cycles, the atom loses kinetic energy over time. Since spontaneous emission is random in direction, its average momentum effect cancels out, leaving a net deceleration. This cumulative effect results in the cooling of the atomic ensemble.

For ^{174}Yb, the recoil velocity associated with the broad "blue" transition ($^1P_1$ at $\lambda_b = 398.9$ nm, $M = 174$ amu) is approximately 5.75 mm/s, corresponding to a Doppler shift of $\Delta\omega = kv_r \approx 2\pi \times 90$ kHz. For the narrower "green" intercombination line ($^3P_1$ at 555.8 nm), the recoil velocity is about 4.13 mm/s, yielding a Doppler shift near $2\pi \times 46.6$ kHz. The key difference lies in how these shifts compare to each line’s natural linewidth. For the broad transition, the recoil-induced Doppler shift is small relative to its linewidth of 29.1 MHz, making it well-suited for applications such as Doppler cooling, Zeeman slowing, and initial trapping stages. In contrast, the Doppler shift for the $^3P_1$ transition is around 26 % of its 184 kHz linewidth, making it more sensitive to recoil and motion. This sensitivity makes $^3P_1$ valuable for precision measurements, as it allows the detection of very small frequency shifts. However, it also demands more careful experimental control, as small vibrations, residual thermal motion, or laser frequency instability can shift the transition out of resonance.

The average radiation pressure force acting on a two-level atom, moving with velocity $\vec{v}$, arises from momentum exchange during cycles of photon absorption and spontaneous

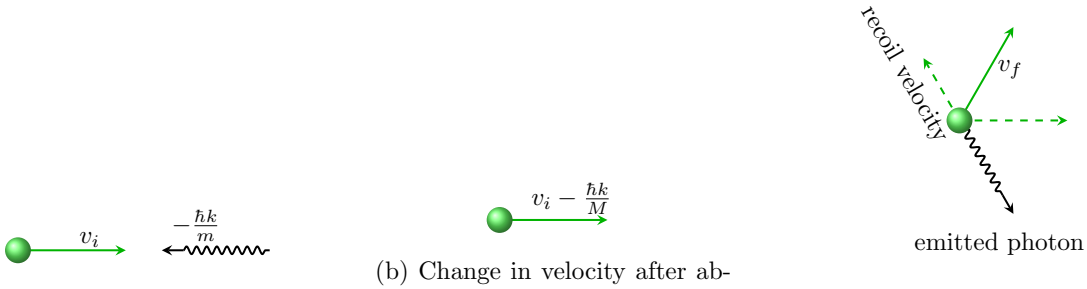

(a) Preferential Absorption

(b) Change in velocity after absorption

(c) Single spontaneous emission

Figure 2.2: Sequential depiction of atom-photon interaction processes. (a) An atom moving with initial velocity v_i absorbs a photon, experiencing a momentum change of $-\hbar k$. (b) As a result of this absorption, the atom's velocity decreases to $v_i - \frac{\hbar k}{M}$. (c) Subsequently, the excited atom emits a photon in a random direction, resulting in a recoil and altering its overall velocity to v_f.

emission. When the atom interacts with near-resonant light, each absorption event transfers a momentum $\hbar\vec{k}$ to the atom in the direction of the photon's wavevector $\vec{k}$. While the subsequent spontaneous emission occurs in a random direction, the average over many cycles results in a net force in the direction of the incident light. This force is proportional to the photon scattering rate Γ_{sc} and can be expressed as:

$$\vec{F} = \hbar\vec{k}\,\Gamma_{\text{sc}}. \tag{2.1}$$

$$\Gamma_{\text{sc}} = \frac{\Gamma}{2} \cdot \frac{s_0}{1 + s_0 + \left(\frac{2\Delta}{\Gamma}\right)^2} \tag{2.2}$$

where the terms are defined as follows:

- Γ is the natural linewidth of the excited state,
- $s_0 = \frac{I}{I_{\text{sat}}}$ is the on-resonance saturation parameter, where I is the intensity of the light and I_{sat} is the saturation intensity,
- $\Delta = \delta - \vec{k} \cdot \vec{v}$ is the Doppler-shifted detuning, where $\delta = \omega - \omega_0$ is the laser detuning from atomic resonance.

For a two-level atom illuminated by near-resonant light, the total radiation pressure force experienced by the atom can be expressed as [36]: The scattering force from a single laser beam propagating in the $\pm x$ direction is given by:

$$F_{\pm} = \pm\hbar k \cdot \frac{\Gamma}{2} \cdot \frac{s_0}{1 + s_0 + \left(\frac{2\Delta}{\Gamma}\right)^2} \tag{2.3}$$

2.2.2 Doppler cooling

Doppler cooling and trapping are key techniques that have been used widely in atomic physics and quantum optics for various applications since their first realization by Hänsch and Schawlow in 1975 [37]. When an atom moves toward a laser beam that is

slightly red-detuned, it sees the light Doppler-shifted closer to resonance. This increases the scattering rate from the two counter-propagating beams of equal intensity and frequency, exerting a net force opposing the motion, this is the friction force [38].

The total force due to two counter-propagating beams is:

$$F_{\text{net}}(v) = F_+ + F_- = \hbar k \cdot \frac{\Gamma}{2}\left[\frac{s_0}{1 + s_0 + \left(\frac{2(\delta - kv)}{\Gamma}\right)^2} - \frac{s_0}{1 + s_0 + \left(\frac{2(\delta + kv)}{\Gamma}\right)^2}\right] \tag{2.4}$$

- v_x is the component of the atom's velocity along the axis of the laser beams in the 1D case.

In the low-velocity limit ($kv \ll \Gamma$), the net force can be approximated linearly as:

$$F_{\text{net}}(v_x) \approx -\alpha v \tag{2.5}$$

where α is a damping coefficient, leading to a viscous-like friction force.

$$\alpha = 8\hbar k^2 \delta \frac{s_0}{\Gamma\left(1 + s_0 + \left(\frac{2\delta}{\Gamma}\right)^2\right)^2} \tag{2.6}$$

This analysis can be extended to three-dimensional (3D) systems by considering three orthogonal pairs of counter-propagating laser beams, each aligned along a Cartesian axis (x, y, and z). The total force is then the vector sum of the forces in each dimension, resulting in a 3D optical molasses configuration. The steady-state temperature is reached when cooling balances heating.

2.2.3 Magneto-optical Trap

The optical molasses technique is useful to cool atoms by reducing their kinetic energy. However, it does not provide spatial confinement. To achieve both cooling and trapping, a distinguished location in space must be defined where the cold atoms can accumulate. This can be achieved by using the technique of Magneto-Optical Trap (MOT) as proposed by Dalibard and first observed in 1987 [39].

As illustrated in Figure 2.3, in one dimension (1D), a quadrupole magnetic field along the z-axis introduces a spatially varying Zeeman shift in the $J = 1$ excited state, splitting it into magnetic sublevels $m = -1, 0, +1$. The ground state ($J = 0$) remains unsplit due to the absence of magnetic sublevels. For Ytterbium (Yb), a magnetic field gradient of 1 G/cm results in a Zeeman splitting of approximately 2 MHz/cm between adjacent magnetic sublevels, which ensures sufficient frequency discrimination between transitions at different positions in the trap. Two counter-propagating, red-detuned laser beams with opposite circular polarizations σ^+ (propagating in the $-z$ direction) and σ^- (in the $+z$ direction), drive position-dependent optical transitions. Due to the selection rules $\Delta m = \pm 1$, the σ^+ beam couples $m = 0 \to m = +1$, while the σ^- beam couples $m = 0 \to m = -1$. For atoms displaced to $z < 0$, the magnetic field $B(z) < 0$ lowers the energy of the $m = +1$ level, bringing it closer to resonance with the red-detuned σ^+ light. This results in higher scattering from the σ^+ beam, exerting a force toward the trap center. Similarly, at $z > 0$, $B(z) > 0$ shifts the $m = -1$ level closer to resonance, enhancing absorption of the σ^- beam and again producing a

restoring force toward $z = 0$. Thus, atoms experience a net position-dependent optical force that cools and confines them near the trap center, leveraging both the Zeeman effect and optical selection rules.

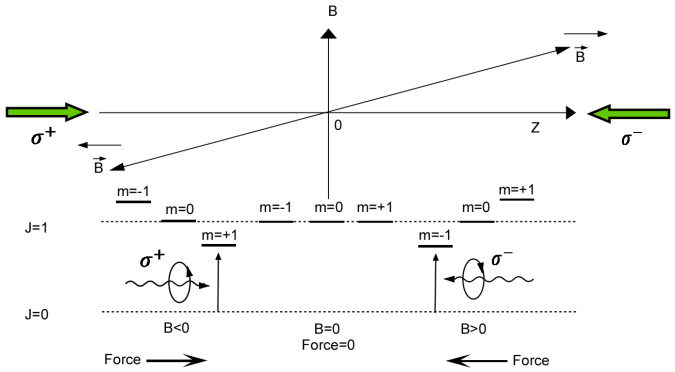

Figure 2.3: Optical transitions from $J = 0$ to $J' = 1$ in a 1D Magneto-Optical Trap. A position-dependent magnetic field split the excited state due to Zeeman effect. Two counter-propagating circularly polarized beams drive transitions that create a restoring force toward the center of the trap.

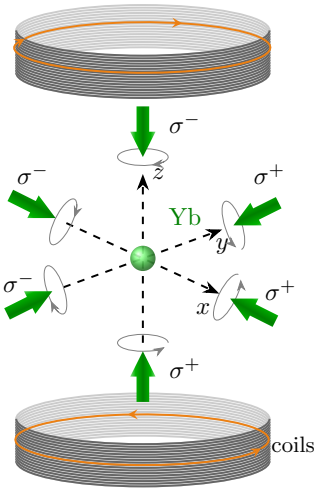

Figure 2.4: Schematic of a 3D Magneto-Optical Trap. Three pairs of counter-propagating, circularly polarized laser beams and a quadrupole magnetic field confine and cool atoms at the center of the trap.

The total force acting on an atom in a magneto-optical trap arises from the combined effect of two counter-propagating laser beams and the spatially varying magnetic field. The position dependence of this force originates from the Zeeman effect, which shifts the atomic energy levels in the presence of a magnetic field. Specifically, the Zeeman detuning of the excited state is given by

$$\Delta E = m_j g_J \mu_B B(z), \tag{2.7}$$

where m_j is the magnetic quantum number, g_J is the Landé g-factor for the excited state, μ_B is the Bohr magneton, and $B(z)$ is the spatially dependent magnetic field. Near the trap center, the magnetic field increases approximately linearly with position z, such that the position-dependent detuning in angular frequency units is

$$\omega_z = \beta z, \tag{2.8}$$

with the detuning gradient

$$\beta = \frac{g_J \mu_B}{\hbar} \frac{dB}{dz}, \tag{2.9}$$

which quantifies how rapidly the Zeeman shift changes with position.

In the low-intensity limit, where the scattering force is approximately linear in laser intensity, the net radiation pressure force acting on an atom due to two counter-propagating laser beams of equal frequency is

$$F(v) = F_+ + F_-, \tag{2.10}$$

where F_+ and F_- are the forces exerted by the beams propagating in the $+z$ and $-z$ directions, respectively. This force depends on both the atom's velocity v (via the Doppler shift) and its position z (via the Zeeman shift). The full expression for the force along the z-axis is given by [38]

$$F(z,v) = \hbar k \frac{\Gamma}{2} \left[\frac{I_{\sigma_+}/I_{\text{sat}}}{1 + s_0 + \left(\frac{2(\delta - kv - \beta z)}{\Gamma}\right)^2} - \frac{I_{\sigma_-}/I_{\text{sat}}}{1 + s_0 + \left(\frac{2(\delta + kv + \beta z)}{\Gamma}\right)^2} \right], \tag{2.11}$$

where $I_{\sigma_\pm}$ are the intensities of the circularly polarized beams and $s_\pm \equiv \frac{I_{\sigma_\pm}}{I_{\text{sat}}}$ and (for equal beam intensities), defining $s_+ = s_- = s_0$.

In the limit of small velocities and small displacements near the trap center, this force can be approximated by a linear expansion,

$$F(z,v) \approx -\alpha v - \kappa z, \tag{2.12}$$

Here, α characterizes the velocity-dependent damping, while κ represents the position-dependent restoring force coefficient. These coefficients are given by:

$$\alpha = \frac{8\hbar k^2 |\delta|}{\Gamma} \frac{s_0}{\left(1 + s_0 + \left(\frac{2\delta}{\Gamma}\right)^2\right)^2} \tag{2.13}$$

and

$$\kappa = \frac{8k|\delta|}{\Gamma} \frac{s_0}{\left[1 + s_0 + \left(\frac{2\delta}{\Gamma}\right)^2\right]^2} \cdot g_J \mu_B \frac{dB}{dz} \tag{2.14}$$

With $F = -\kappa z$, the effective potential is harmonic:

$$U(z) = \frac{\kappa z^2}{2} \tag{2.15}$$

Since the restoring potential is harmonic, atoms at finite temperature explore this potential according to thermal equilibrium. By the equipartition theorem, the mean potential energy in the z-direction is

$$\frac{1}{2}\kappa \langle z^2 \rangle = \frac{1}{2} k_B T. \tag{2.16}$$

This directly relates the cloud's spatial variance to the trap spring constant, yielding the characteristic width.

$$\Delta z = \sqrt{\frac{k_B T}{\kappa}} \tag{2.17}$$

At the Doppler limit $k_B T_D = \hbar\Gamma/2$ and using the $\delta = -\Gamma/2$ and low saturation $s_0 \ll 1$, the spring constant is taken from eq. (2.14),

$$\Delta z = \sqrt{\frac{\Gamma I_{\text{sat}}}{2k \left(\frac{g_J \mu_B}{\hbar} \frac{dB}{dz}\right) I}} \tag{2.18}$$

For a total atom number N, the peak density can be estimated as $n_{\text{peak}} \sim \frac{N}{\Delta z^3}$.

At low densities, Δz depends only on cooling and trapping parameters and remains independent of N.

In the same analogy as in 1D MOT, to achieve both cooling and trapping in 3D. The distinguished location in space must be defined to concentrate the atoms in a small region. This spatial confinement is achieved using a pair of anti-Helmholtz coils, which define a spatial region with a zero magnetic field at the center of the trap by generating a quadrupole magnetic field. Together with three orthogonal pairs of red-detuned counter-propagating laser beams with appropriate circular polarization and a quadrupole magnetic field, it helps to achieve the necessary restoring force and defines the trap center, also known as a Magneto-Optical Trap (MOT), as illustrated in Figure 2.4.

This magnetic field introduces a position-dependent Zeeman shift, so whenever atoms try to escape the zero magnetic field region, the polarized light causes those atoms to experience a restoring force toward the center of the trap. Therefore, the atoms start to accumulate in a small region and form a magneto-optical trap. However, each spontaneous emission event occurs in a random direction, imparting momentum kicks to the atoms that act as a heating mechanism.

The overall dynamics, therefore, result from two competing effects: a cooling (friction) force that removes kinetic energy from the atoms, and heating due to momentum diffusion, which arises from the stochastic recoils during spontaneous emission. This competition imposes a fundamental limit on the minimum achievable temperature in Doppler cooling.

Doppler Temperature To determine the Doppler cooling limit [36], we balance the cooling effect of the friction force with the heating caused by random photon recoils. In the low-velocity limit, the radiation pressure force can be written as

$$F(v) \approx -\alpha v,$$

where α is the friction coefficient taken from eq. (2.6).

The cooling rate is therefore given by the loss of kinetic energy per unit time,

$$\left(\frac{dE}{dt}\right)_{\text{cool}} = \langle Fv \rangle = -\alpha \langle v^2 \rangle.$$

At the same time, heating arises from momentum diffusion due to spontaneous emission and absorption events. Each scattering event imparts a momentum $\hbar k$, leading to a momentum diffusion constant

$$D_p \simeq (\hbar k)^2 \Gamma_{\text{sc}},$$

where Γ_{sc} is the scattering rate. The corresponding heating rate in one dimension is

$$\left(\frac{dE}{dt}\right)_{\text{heat}} = \frac{d}{dt}\left(\frac{p^2}{2M}\right) = \frac{D_p}{M}.$$

At equilibrium, heating balances cooling,

$$\left(\frac{dE}{dt}\right)_{\text{heat}} = -\left(\frac{dE}{dt}\right)_{\text{cool}}.$$

Introducing the effective temperature via the equipartition relation,

$$\frac{1}{2}M\langle v^2\rangle = \frac{1}{2}k_B T,$$

we obtain the Doppler cooling temperature

$$T_D = \frac{\hbar\Gamma}{2k_B}\cdot\frac{1+\left(\frac{2\delta}{\Gamma}\right)^2}{2|2\delta/\Gamma|} \tag{2.19}$$

This expression shows that the minimum temperature occurs for a detuning of $\delta = -\Gamma/2$, giving

$$k_B T_{\min} = \frac{\hbar\Gamma}{2}. \tag{2.20}$$

The important Doppler cooling parameters of Yb are shown in the following table (2.1).

Table 2.1: Characteristics for the ${}^1S_0 \to {}^1P_1$ ("blue") and ${}^1S_0 \to {}^3P_1$ ("green") transitions.

Category	Parameter	Blue	Green	Unit
Doppler Cooling Parameters				
Saturation intensity	$I_{\text{sat}} = \frac{\pi}{3}\frac{hc\Gamma}{\lambda^3}$	60	0.14	mW/cm^2
Doppler temperature	$T_D = \frac{\hbar\Gamma}{2k_B}$	699	4.41	µK
Velocity at T_D	$v_D = \sqrt{\hbar\Gamma/2M}$	183	14.5	mm/s
Recoil Parameters				
Recoil velocity	$v_{\text{rec}} = \hbar k/M$	5.75	4.13	mm/s
Recoil frequency	$\omega_{\text{rec}}/2\pi$	7.21	3.71	kHz
Resonance width	$\Gamma/v_{\text{rec}}k$	2020	24.7	–
Recoil temperature	$T_{\text{rec}} = \frac{\hbar^2k^2}{Mk_B}$	0.692	0.356	µK

2.3 Experimental Setup

Capture velocity and the necessity of two-stage cooling In a magneto-optical trap (MOT), the capture velocity v_c defines the maximum atomic velocity at which atoms can be effectively slowed and trapped by the scattering force of the cooling lasers within the spatial extent of the laser beams. This velocity depends critically

on the natural linewidth Γ of the atomic transition used for cooling. For narrow-line transitions, such as the green MOT operating on a transition with a linewidth of $\Gamma_g = 184\,\text{kHz}$, the scattering force is significantly weaker, leading to a substantially reduced capture velocity of approximately 10 cm/s. In contrast, broad-line MOTs (e.g., the blue MOT) with linewidths in the MHz range can capture atoms moving at velocities up to $\sim 40\,\text{m/s}$.

For this reason, we employ a two-stage cooling strategy: atoms are first pre-cooled in the broad-line blue MOT before being transferred into the green MOT for further cooling to ultracold temperatures. This two-stage cooling strategy is crucial for achieving efficient loading and trapping of atoms in the narrow-line green MOT.

2.3.1 Laser Diode Systems

Our magneto-optical trap (MOT) setup employs two primary laser sources: a frequency-doubled TOPTICA TA-SHG Pro system, which provides 556 nm light for the green MOT, and an M Squared SolsTiS laser operating at 399 nm for the blue MOT and for generating the counter-propagating slowing beam (discussed in a later section). As part of my doctoral work, I was responsible for maintaining and optimizing both laser systems. Although both systems were pre-installed, I was responsible for their routine realignment, SHG cavity optimization, and diagnosing the degradation that occurs over time.

The laser system used to generate 399 nm light for the Yb Blue MOT was previously described in detail in the previous doctoral work by A. de Melo [17]. It consists of a Verdi V18 pump laser and a Ti:Sa laser (Solstis), followed by a second harmonic generation (SHG) cavity stabilized via the Hänsch-Couillaud method, yielding up to 2.5 W of blue light of wavelength 399 nm.
In the following, the focus will be on the TOPTICA DL pro/TA-SHG pro system, which generates green light at 556 nm via second harmonic generation (SHG) of a 1112 nm fundamental wavelength (see Figures 2.5-2.7).

Second harmonic generation (SHG) Cavity Alignment Protocol

1. Tapered Amplifier (TA) Optimization: The optimization procedure begins by maximizing the output power of the tapered amplifier (TA) by carefully adjusting the input coupling mirrors (TA-1 and TA-2) while monitoring output power on the TOPTICA DLC pro interface (see Figures 2.8b). At a drive current of 5.6 A, the target output was approximately 1.8 W.

2. SHG Incoupling and Safety: Once the TA was optimized, I routinely aligned the incoupling mirror to the SHG cavity, monitoring the green output power (556 nm) and/or beam transmission. All work was performed in accordance with proper laser safety protocols, including the use of a mask, goggles, and gloves.

3. Cavity Mirror Alignment: The SHG cavity contains four mirrors (RM1 → RM2 →RM3 → RM4) as indicated in Figure 2.5 , with RM2 being fixed and piezo-actuated for resonance scanning. Using an IR viewer and pinhole paper, I ensured that the incoming and reflected beams were well superimposed and avoided any physical contact with the nonlinear doubling crystal.

4. Beam Walk and Mode Optimization: Beam walk was performed using mirrors RM1 and RM4 (or M3 and M4 if needed), adjusting in both X and Y axes to overlap the mode with the cavity axis. Mode quality was assessed via the cavity

interface and by observing the green output beam. The goal was to enhance the fundamental transverse mode while suppressing higher-order modes, following the manual's recommendation that the fundamental mode should dominate by at least a factor of 10 (see Figure 2.8a).

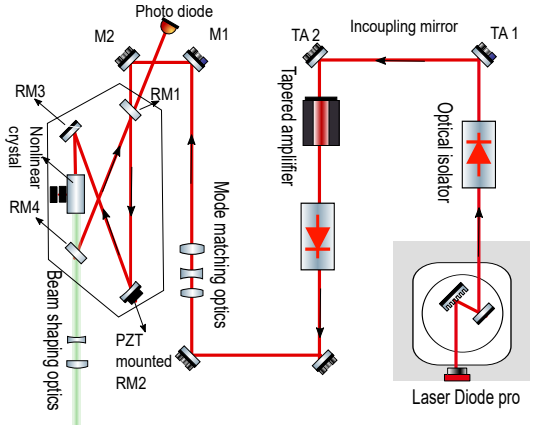

Figure 2.5: Diagram of SHG cavity and tapered amplifier alignment

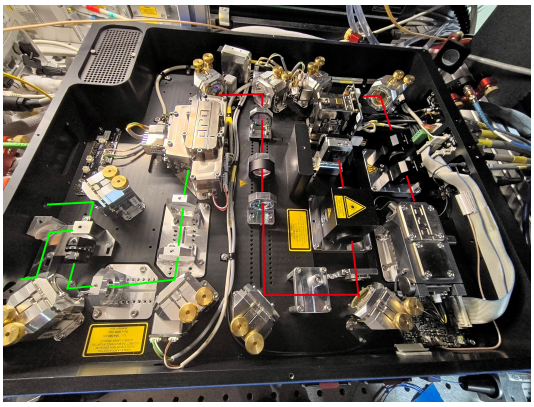

Figure 2.6: Inside view of the Toptica TA-SHG pro laser system

This procedure required iterative alignment, visual diagnostics, and fine mechanical adjustments to maintain stable SHG output, optimize mode matching, and ensure long-term reliability of the laser system.

Initial Observations Before Diode Optimization

After approximately one year of operation, the system's performance had noticeably degraded, necessitating realignment and troubleshooting. The service and diagnostic reports from the TOPTICA manufacturer support provided valuable insights. The following observations were recorded:

- **Diode laser threshold power:** 70 mW (expected ∼48 mW)
- **Fundamental wavelength:** 1111.3 nm at 190 mA (target: 1112.0 nm)
- **Diode output power:** 45 mW (expected 60 mW)
- **TA output power:** ∼400 mW (expected 2 W)
- **SHG output power:** unstable, with visible higher-order modes (expected 1.3 W)

DL pro Diode Optimization Procedure

The diode threshold was measured to be 70 mA, higher than expected from the datasheet, potentially indicating alignment drift or feedback issues. Following TOPTICA's recommended protocol, the DL pro diode feedback was re-optimized using the procedure outlined below (see Figure 2.7 for hardware reference).

Feedback Optimization Procedure: We performed a diode feedback optimization to assess and improve alignment at the DL pro output:

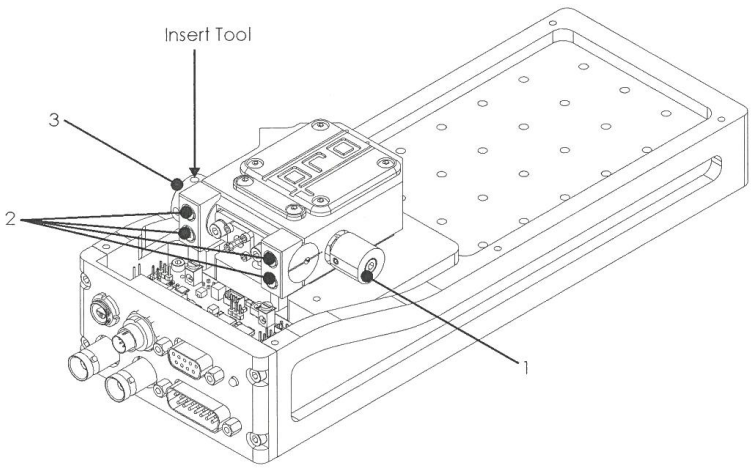

Figure 2.7: DL pro feedback adjustment mechanism [40].

Setup: According to the TOPTICA alignment procedure, a fast photodetector is placed at the DL pro isolator output at a small angle to suppress back reflections. This configuration allows monitoring of relative power changes, rather than absolute power levels.

Feedback Sensitivity Test: After locating the DL pro's diode and collimation system, which is the silver stainless steel cylinder (marked "3", see Figure 2.7), it was gently perturbed (apply torque to the cylinder in either direction) by inserting a small screwdriver in the indicated location. This allowed us to observe how the output power responded to mechanical perturbations. Asymmetrical power change was observed, where power increased in one direction and decreased in the other. This behavior confirmed that the diode feedback was misaligned.

Screw Adjustment: The mounting screws (marked "2") were slightly adjusted using an Allen key to maximize output power and reduce the threshold current. Criss-cross movements were used to avoid asymmetric tightening. Small adjustments were sufficient to correct the diode-collimator coupling without disturbing laser alignment.

After optimization, we recorded changes in output power and threshold. Though there was partial improvement, the system remained sensitive, and achieving clean single-mode operation required further tuning of current, piezo voltage, and temperature.

Results After Optimization:

Table 2.2: Pre- and post-optimization performance metrics.

Parameter	**Before**	**After**
Threshold power	70 mW	40 mW
Wavelength @ 190 mA	1111.3 nm	1112.0 nm
Diode output power	45 mW	54 mW

Following diode optimization, further improvements were observed in both the amplifier and SHG stages. The amplifier input coupling was re-optimized using the pre-TA mirrors, resulting in a TA output power of 1.77 W at 5600 mA, approaching the nominal 2 W specification at 6000 mA.

The SHG output initially stabilized around 800 mW, with noticeably improved mode quality. After additional fine-tuning of the cavity alignment, we achieved a 13:1 ratio of

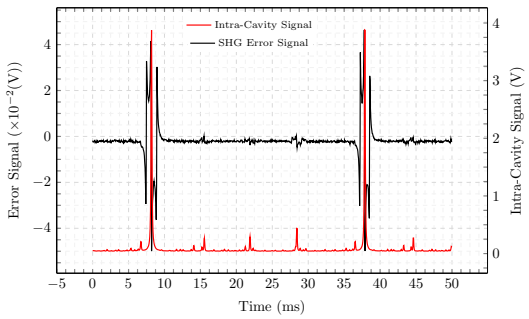

(a) SHG cavity signals during a piezo scan of the cavity second (RM2) mirror. The SHG error signal (black, left axis) and intra-cavity transmission signal (red, right axis) are shown as a function of time. The voltage applied to the piezo actuator modulates the cavity length, causing periodic resonance peaks when the cavity becomes resonant with the incoming light. The sharp peaks in the intra-cavity signal correspond to constructive interference within the cavity, while the zero-crossings in the error signal indicate the lock points used in Pound-Drever-Hall (PDH) stabilization.

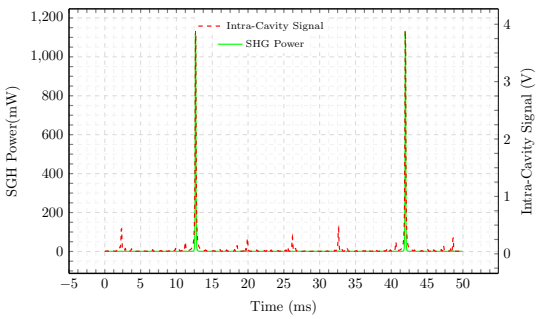

(b) SHG output power (green, left axis) and intra-cavity signal (red, right axis) during a piezo scan of the second (RM2) mirror of the cavity, is plotted as a function of time. The voltage applied to the piezo actuator modulates the cavity length, producing periodic resonance peaks when the cavity becomes resonant with the incoming 1112 nm light. These resonances enhance the intra-cavity field via constructive interference. The output power increases at these resonances due to more efficient frequency doubling, resulting in higher SHG (556 nm) generation.

fundamental to higher-order transverse modes (see Figure 2.8a), and the output power increased to 1.1 W.

This experience gave me in-depth exposure to diode feedback optimization, external cavity diode laser tuning, SHG cavity alignment, and hands-on laser diagnostics.

2.3.2 Atomic Oven and Vacuum System

At room temperature, the saturated vapor pressure of Yb is $\approx 10^{-18}$ Torr [41], resulting in an extremely low number of atoms in the vapor, effectively negligible for experimental purposes. The atomic beam apparatus used here is based on a design previously developed in our lab and described in detail in earlier doctoral work. Details of the vacuum chamber and oven setup can be found in [41, 17]. The Ytterbium atomic source consists of a commercial resistively heated oven (OEM S40 DZ35 K, Riber), illustrated as element 1 in Figure 2.9b, capable of reaching temperatures up to 1000°C. In our experimental operation, for typical operation, the oven is maintained at 460°C to provide a stable and sufficient Yb atomic flux. The melting point of Yb is 824°C.

The vacuum and oven systems comprise an independently heated crucible and nozzle, a collimating microtube array, and a differential pumping section, all designed for stable Yb flux and long-term operation. A mechanical shutter is positioned in front of the nozzle and can be actuated externally, enabling precise control over the atomic beam flux. The oven is integrated into the system via an ultra-high vacuum (UHV) cross, equipped with an ion-getter pump (NEXTorr Z200, SAES; 75 L/s for N2) illustrated as element 2 and a manual UHV gate valve (CF40, VAT) illustrated as element 4 in Figure 2.9b, and four viewports (3) for oven spectroscopy. This section, following the gate valve, features two window ports (5), which enable transverse absorption

spectroscopy of the atomic beam (not yet fully implemented). A pneumatic UHV valve (CF40, VAT) (4) isolates the oven from the science chamber. This allows the science chamber to remain under vacuum when the oven is being heated or refilled. To maintain a pressure gradient between the oven and the science cell, two differential pumping tubes (40 mm in length, 12 mm in inner diameter) are installed on either side of the pneumatic valve.

Before the science cell, a second UHV cross houses an additional ion-getter pump (NEXTorr Z200, 75L/s-N2). The science chamber consists of a rectangular quartz cell (Japan Cell) (6), with dimensions 50 mm × 50 mm × 100 mm. It is broadband AR-coated from 399 nm to 700 nm, accommodating both the 399 nm and 556 nm transitions used for laser cooling of Yb. Two anti-Helmholtz coils (7) are mounted above and below the cell to generate the magnetic field gradient required for the magneto-optical trap (MOT). The pressure in the science chamber was maintained at approximately 10^{-9} mbar, while the oven side operated at around 10^{-8} mbar. Although the ion pump controller indicated a pressure of 10^{-7} mbar, this was attributed to a false current; the actual pressure in the science cell was estimated to be $\sim 10^{-9}$ mbar, confirmed via MOT lifetime measurements[41].

2.3.3 Optical Setup

The laser source for the ^{174}Yb green MOT operates at 556 nm, addressing the $^1S_0$ to $^3P_1$ intercombination transition. The frequency stabilization system was initially based on a FALC (Fast Analog Linewidth Controller) module, as described in the thesis [17]. However, during attempts to optimize the servo parameters — specifically when adjusting the gain on the error signal — the FALC unit became unreliable. Changes in gain settings caused unintended shifts in the offset of the error signal, compromising the lock stability.

To overcome this limitation, we implemented a locking system based on a Red Pitaya FPGA platform. It has a user friendly interface. The Red Pitaya lock enabled reliable operation over extended periods, with the added benefit of easier tuning of servo parameters and diagnostic access to the error signals.

Initially, the setup employed a 2×6 polarization-maintaining fiber splitter (2×6 Evanescent Optics Inc.) to produce the six MOT beams. This configuration simplified alignment and ensured good polarization control at the output fibers. Stable polarization is critical for the operation of the green MOT.

During the operation of the green MOT, stability issues were observed, with the trapped atom cloud drifting by approximately half its size. This behavior was attributed to beam imbalance caused by power fluctuations originating from time-dependent polarization distortions. The source of the problem was identified as a 2×6 PM fiber splitter that failed to maintain linear polarization at 556 nm. The output polarization was analyzed by tracing the polarization state on the Poincaré sphere using Polarization Analyzer(Schäfter & Kirchhoff SK010PA). Ideally, well-aligned input light would produce minimal deviation during fiber-induced birefringence variations. However, alignment to the equatorial plane could not be achieved, and the output was elliptical despite stable input alignment. The original 2×6 splitter was conclusively shown to degrade polarization, with poor Polarization Extinction Ratio (PER) (mean PER 5 dB at worst).

To address this, we implemented the following measure: we transitioned to a hybrid

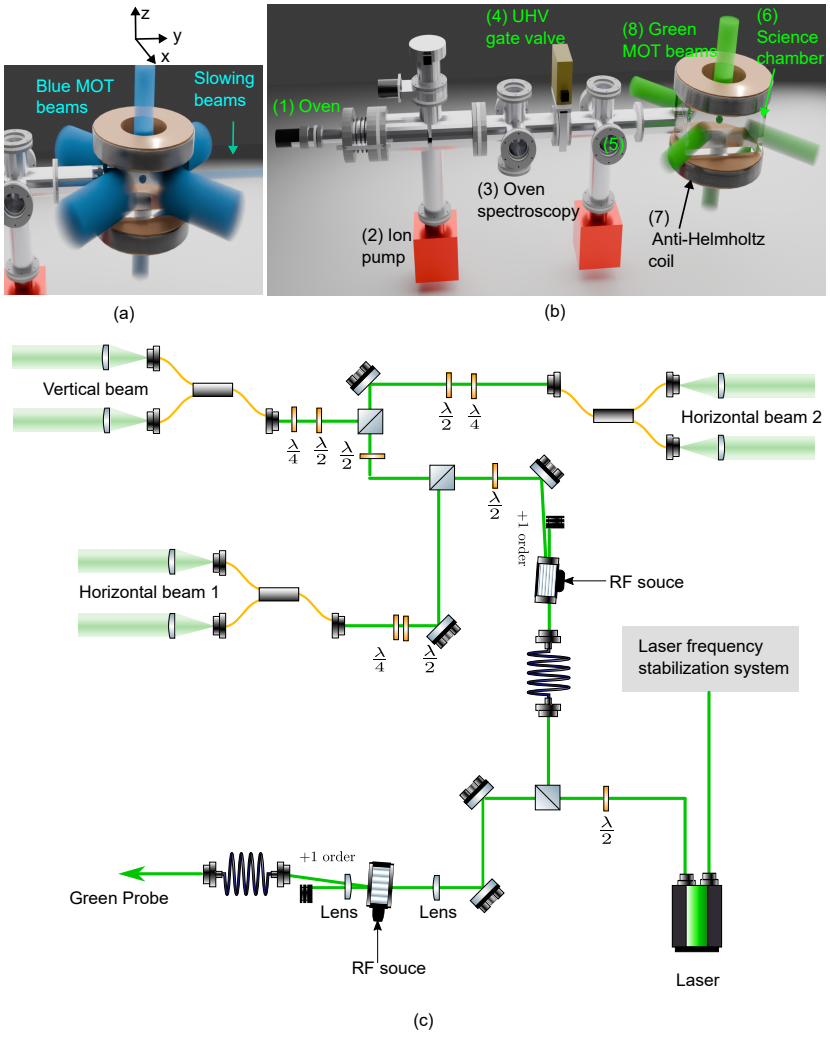

Figure 2.9: **Experimental setup for laser cooling and trapping of ^{174}Yb atoms.**(a) Schematic illustration of the 3D six-beam blue MOT configuration used for initial cooling of Yb atoms on the strong $^1S_0 \rightarrow {}^1P_1$ transition at 399 nm. Slowing beams (from the right) counter-propagate against the atomic flux emerging from the oven to decelerate atoms before capture in the blue MOT. (b) Diagram of the ultra-high vacuum (UHV) experimental chamber. Key components include: The oven (1) produces a thermal beam of Yb atoms, which passes through the oven spectroscopy region (2) and is pumped by an ion pump (3). A UHV gate valve (4) isolates the oven from the main trapping region. Atoms enter the science chamber (6), where they are cooled and trapped first in the blue MOT, followed by a narrow-line green MOT using 556 nm light ($^1S_0 \rightarrow {}^3P_1$). The magnetic field gradient for the MOT is provided by a pair of anti-Helmholtz coils (7). Green MOT beams (8) are used for further cooling and compression. (c) Optical layout for beam preparation and delivery for both Green MOT stages and probing. The output is split via free-space optics and coupled into fiber splitters to produce the vertical and horizontal MOT beams. Each path includes appropriate polarization optics ($\lambda/2$, $\lambda/4$ waveplates) for power balancing and to control polarization before fiber coupling.

free-space and fiber-based beam delivery system (Figure 2.9c). The stabilized laser output is first divided in free space using a series of beam splitters and wave plates,

allowing for precise control of power distribution and polarization. The beams are then coupled into Thorlabs (PN560R3A1) 1×2 fiber splitters for delivery to the MOT chamber. Although this approach required more careful alignment and coupling, it provided greater flexibility and improved control over beam parameters compared to the damaged 2×6 splitter. The polarization state was monitored on a Poincaré sphere to evaluate stability. A small trace on the sphere indicated good alignment and indicated minimal drift of the polarization state despite fiber bending, thermal variation, or mechanical perturbations. The measured PER values exceeded manufacturer specifications (Thorlabs (PN560R3A1) 1×2 fiber splitters) in all cases, that is, greater than the mean PER by 25 dB.

A schematic of the final setup is shown in Figure 2.9c. The laser output is frequency stabilized and, as described in the thesis [17], is split into three primary paths corresponding to the vertical and two horizontal beam pairs. Waveplates are used to control polarization before fiber coupling. The green cooling beams are delivered through polarization-maintaining fibers and expanded to ≈20 mm diameters at $1/e^2$.

We utilize a Direct Digital Synthesizer (DDS) to drive the Acousto-Optic Modulator (AOM), providing precise and rapid control over the laser frequency. This setup enables rapid switching between different frequency states and ensures stable long-term operation. The laser is locked to the A10 hyperfine component of the R(158) 25-0 transition in molecular iodine. To reach the relevant transition in ^{174}Yb, we apply a frequency shift of approximately 150 MHz using the AOM. The AOM frequency is chosen such that, after the shift, the laser light is resonant with the atomic transition of interest in ^{174}Yb. The flexibility of DDS-based control allows us to fine-tune this offset and switch it on or off as needed, depending on the experimental sequence. The laser frequencies and intensities are controlled via direct digital synthesis (DDS) boards, which are synchronized with a master timing sequence.

2.4 Optimization and characterization of a magneto-optical trap (MOT)

I began my PhD in May 2022 with a focus on the development and optimization of a magneto-optical trap (MOT) for the ^{174}Yb isotope, with particular attention to refining the green MOT stage, particularly through the implementation of optical molasses and compensation coils to minimize the effects of residual magnetic fields that affect the narrow-line cooling transition. Due to the narrow linewidth of 184 kHz on the 556 nm transition, even small stray fields (on the order of 100 mG) can significantly perturb the MOT. Stray (unwanted) magnetic fields superimpose on the intended field gradient. They shift the zero point of the magnetic field or distort the field profile, which degrades the cooling/trapping efficiency. During the initial phase of the project in Sophia Antipolis, we employed optical molasses to reduce the effects of residual magnetic fields.

In the MOT setup, three orthogonal pairs of compensation coils arranged in a Helmholtz configuration are used to produce uniform magnetic fields along the x, y, and z directions. These coils serve to cancel residual magnetic fields from environmental sources such as the Earth's field or nearby magnetic materials. Each coil pair is composed of a large rectangular winding, approximately 47 cm × 33 cm in size, designed to produce a sufficiently uniform magnetic field over the volume of the MOT. The coil dimensions were chosen to ensure uniformity across the trapping region The procedure to determine

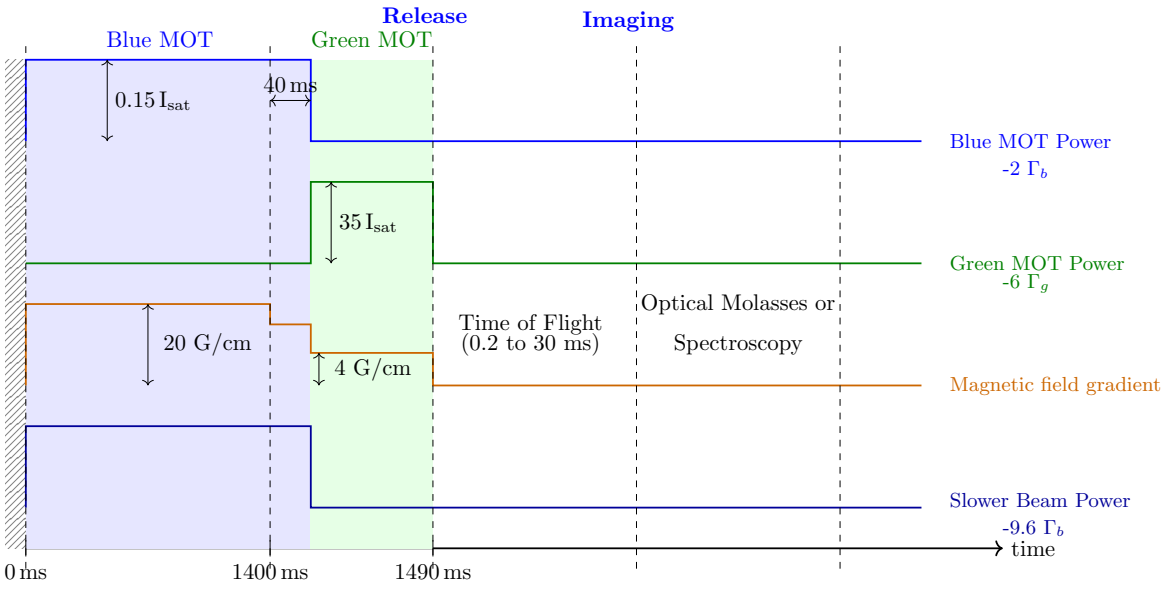

Figure 2.10: Chronogram illustrating the time sequence steps involved in the optical molasses and green spectroscopy.

Table 2.3: Zeeman and Doppler shift for the ${}^1S_0 \rightarrow {}^1P_1$ ("blue") and ${}^1S_0 \rightarrow {}^3P_1$ ("green") transitions.

Category	Parameter	Blue	Green	Unit
Zeeman and Doppler Shifts				
Doppler detuning	$v_\Gamma = \Gamma/k$	1.16e4	1.02e2	mm/s
Landé factor	g_J	1.035	1.49282	–
Zeeman shift	$g_J\mu_B/h$	1.4	2.09	kHz/mG
Zeeman detuning	$B_\Gamma = \hbar\Gamma/g_J\mu_B$	2.01e4	87.9	mG

the optimal currents for these coils involves the following steps:

1) MOT loading: The MOT is loaded under standard operating conditions, with the anti-Helmholtz gradient field turned on.

2) Switch to molasses mode: Turn off the gradient field while keeping the compensation coils active at initial trial current values. The optical molasses beams remain on to provide velocity damping, but no spatial restoring force exists in the absence of the gradient.

3) Observe cloud dynamics: The atomic cloud is observed immediately after the magnetic gradient field is switched off. In the ideal case, the cloud should begin to expand symmetrically. Any horizontal drift indicates the presence of an uncompensated magnetic field.

4) Iterative adjustment: The compensation coil currents are adjusted iteratively to minimize the horizontal drift.

The fluorescence position is monitored during molasses for several tens of milliseconds to ensure no drift in the horizontal direction. To compensate for the magnetic field in the vertical direction, we performed the spectroscopy. Under optimal compensation

conditions, the atomic ensemble achieves a temperature of approximately 60 µK with a population of 2×10^8 atoms at detuning $-6\Gamma_g$. The method to measure the temperature and atom number is explained in the later section. Each of the steps described above is visual in Chronogram 2.10.

In March 2023, our laboratory was relocated to Nice. Following the move, we re-optimized the MOT setup. To calibrate the compensation values, we applied several techniques to fine-tune the magnetic field compensation.

2.4.1 Magnetic Field Compensation Using Spectroscopy

Qualitative Check via Molasses Drift After switching off the quadrupole gradient, we left the red-detuned molasses on and observed the cloud's center-of-mass motion. In the presence of a residual offset field B, the $^3P_1$ Zeeman shift

$$\Delta\nu_Z = \left(\frac{g_J \mu_B}{h}\right) B \approx 2.09 \text{ kHz/mG} \cdot B$$

produces a scattering-rate imbalance between counter-propagating beams, yielding a small constant horizontal force. The cloud then exhibits a measurable horizontal drift during a few-millisecond molasses interval. Under our conditions, a displacement of approximately 0.7 mm corresponds to $\sim \Gamma/2\pi = 184$ kHz, and thus to ~ 90 mG. This confirms that the method is sensitive but only qualitative, since converting the observed drift into B depends on $\alpha(\delta, s_0)$ and residual beam imbalances. Consequently, precise magnetic-field compensation was performed by spectroscopy on the narrow $^1S_0 \rightarrow {}^3P_1$ line (via merging Zeeman components or linewidth minimization), while the molasses drift method was used only as a quick diagnostic.

Method 1: Spectroscopy-based magnetic field compensation To accurately null the residual magnetic fields, we performed spectroscopy on the narrow intercombination transition $^1S_0 \rightarrow {}^3P_1$. In the presence of uncompensated fields, the Zeeman sublevels with $m = \pm 1$ are split, and the absorption spectrum exhibits three distinct peaks. By adjusting the compensation coil currents, we reduced this splitting until the three components merged into a single, narrow resonance. The procedure was carried out as follows: after the MOT loading and time-of-flight expansion (see Chronogram 2.10), the atomic cloud was illuminated by a narrow-linewidth 556 nm probe laser. The probe frequency was scanned across the transition, and the resulting absorption (or fluorescence) spectrum was recorded. For cross-compensation, we first fixed the current along one axis at a relatively high value, then systematically scanned the currents in the two orthogonal directions. This allowed us to identify the set of compensation values that minimized the linewidth and yielded a symmetric single resonance. This method provides sub-0.1 G accuracy, far beyond what can be achieved from qualitative molasses drift alone.

The spectroscopy was performed using a circularly polarized green probe on the narrow $^1S_0 \rightarrow {}^3P_1$ transition at 556 nm. As shown in Table 2.3, a magnetic field as small as 0.1 G is sufficient to resolve the natural linewidth of approximately 184 kHz via Zeeman splitting. The compensation coil changes by 0.1 G per 40 mA. First, we fixed the coil currents in the x and y directions at previously determined values ($I_X = 249$ mA and $I_Y = 142$ mA) and varied the z-axis coil current, I_Z.

We increase the value of I_Z from I_Z=0 mA (Figure 2.11a) to I_Z=1294 mA (Figure 2.11e) and observe the Zeeman splitting of the $^3P_1$ state by recording the absorption

images on a broad transition. All three peaks are clearly visible at very low or high values of I_z in figures (2.11a, 2.11e). At I_z=499 mA, all the three peaks are converges to a single peak and become narrower, indicating optimal magnetic field compensation. Increasing I_Z further results in renewed peak splitting due to overcompensation. The estimated intersection current is 540 ±38 mA from Figure 2.11f.

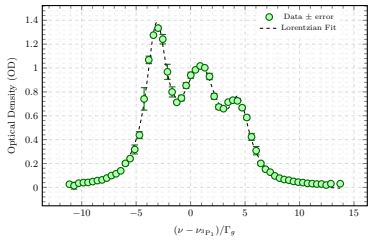

(a) $I_Z = 0$ mA. The stray magnetic field is not yet compensated. Multiple peaks indicate transitions from $J_g = 0$ to different $J_i = 1, m_J = \pm 1$ levels.

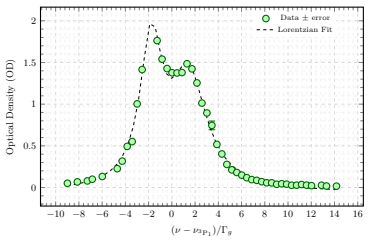

(b) $I_Z = 195$ mA. The Zeeman components are beginning to merge. The line is narrowing, but still slightly asymmetric or not fully merged.

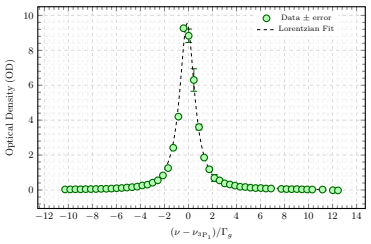

(c) $I_Z = 499$ mA. The absorption peak is narrow and symmetric.

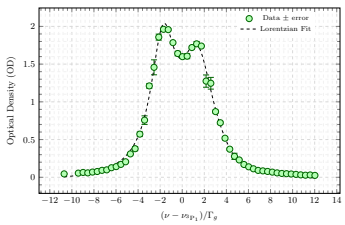

(d) $I_Z = 894$ mA. Overcompensation: the line starts to broaden. The applied magnetic field is too strong in the opposite direction.

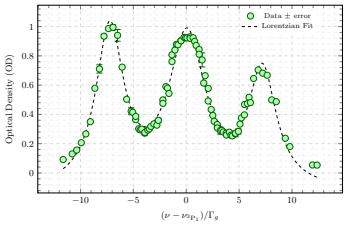

(e) $I_Z = 1294$ mA. The applied compensation field exceeds the stray field, and Zeeman splitting reappears.

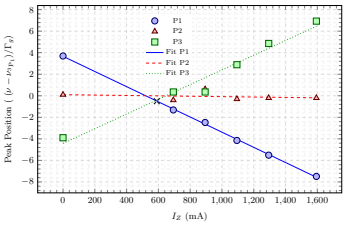

(f) The minimum separation (convergence of peaks) occurs around $I_Z = 540$ mA.

Figure 2.11: Absorption spectra for varying coil currents I_Z, showing the effect of magnetic field compensation.

We began by scanning the I_Y current while keeping $I_X = 249$ mA and $I_Z = 540$ mA fixed as shown in Figures 2.12a–2.12c.

Next, we optimized the X-axis compensation current. With $I_Y = 150$ mA and $I_Z = 540$ mA as illustrated in Figures 2.13a–2.13c.

We fit the peak positions versus coil current using linear fit and determined the intersection points of these lines, which correspond to zero magnetic field along that axis. The uncertainties in the intersection points were calculated using error propagation from the fit parameters, taking into account correlations between the slope and intercept. This yielded optimized compensation currents of: $I_X = 249 \pm 25$ mA, $I_Y = 223 \pm 69$ mA, $I_Z = 540 \pm 38$ mA.

Method 2: Minimizing the spectral linewidth of the $^3P_1$ transition In **Method 2**, we scanned the compensation current around the previously determined values and recorded the spectral linewidth of the $^3P_1$ transition. As shown in Figure 2.14, the linewidth reaches a minimum when the residual magnetic field is compensated. The

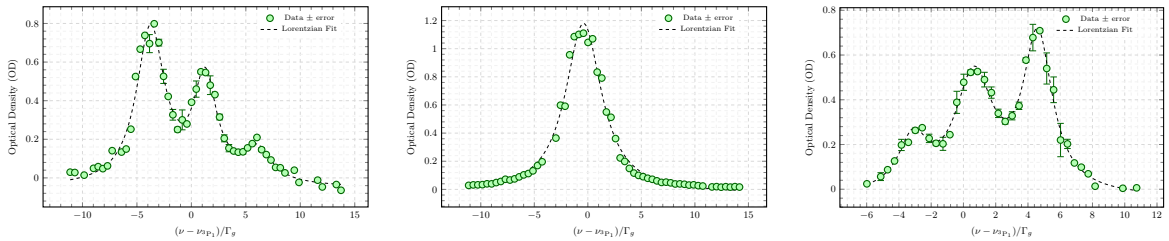

(a) $I_Y = -1000$ mA. The spectrum shows clear Zeeman splitting due to a strong uncompensated field along the Y-axis.

(b) $I_Y = 150$ mA. A single, narrow resonance is observed, indicating that this value effectively cancels the field in the Y-direction.

(c) $I_Y = 1300$ mA. Splitting reappears due to overcompensation.

Figure 2.12: Spectra for different I_Y currents showing the compensation and overcompensation of the magnetic field along the Y-axis.

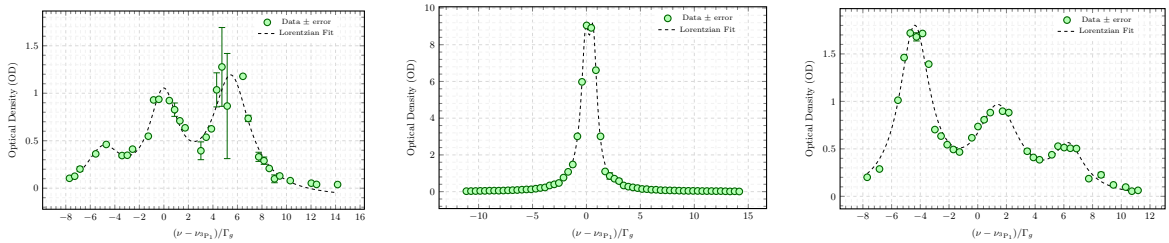

(a) $I_X = 0$ mA. Zeeman splitting indicates incomplete compensation.

(b) $I_X = 249$ mA. The resonance is narrow and symmetric, confirming this as the optimal current for X-axis compensation.

(c) $I_X = 448$ mA. Overcompensation.

Figure 2.13: Spectra for different I_X currents showing incomplete, optimal, and overcompensated magnetic fields along the X-axis.

linewidth exhibits a quadratic dependence on residual magnetic field, and thus on the compensation current. We fit the data to a parabola $w(I) = a(I - I_0)^2 + w_0$, where I_0 corresponds to the current that minimizes the magnetic field, and w_0 is the minimum linewidth. The fit also provides statistical uncertainties in both I_0 and w_0. This method yielded:

$$I_X = 245 \pm 14.9 \text{ mA}, \quad I_Y = 194 \pm 29 \text{ mA}, \quad I_Z = 570 \pm 7 \text{ mA},$$

with corresponding minimum linewidths of 244.8 ± 6.5 kHz, 341.3 ± 7.0 kHz, and 278.0 ± 6.4 kHz, respectively.

The results from both methods are summarized below:

Both methods yield results that are consistent within their respective uncertainties. In particular, the X and Y directions show good agreement. For the Z direction, Method 2 provides a slightly higher optimal current with significantly reduced uncertainty, suggesting higher precision due to the sharper dependence of linewidth on field in that direction. These optimized compensation values were used for subsequent cold atom experiments.

At these settings, the magnetic field is well-compensated in all directions.

Axis	Method 1 (mA)	$\pm\sigma$	Method 2 (mA)	$\pm\sigma$
X	249	25	245	15
Y	223	69	194	29
Z	540	38	570	7

Table 2.4: Comparison of optimized compensation coil currents from Zeeman splitting (Method 1) and linewidth minimization (Method 2).

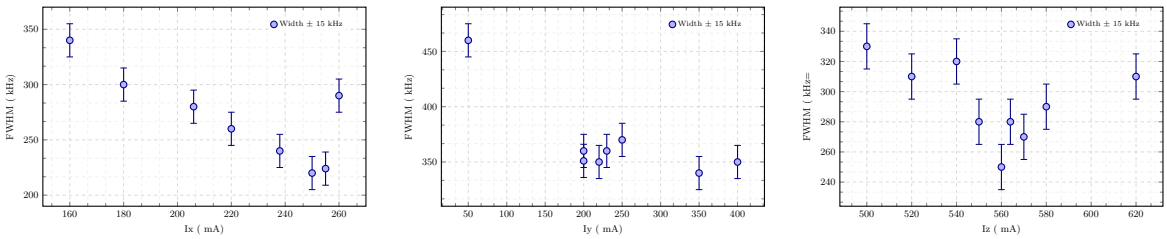

Figure 2.14: Width of the 556 nm green spectroscopy resonance as a function of the scanned compensation coil current along each principal axis. The resonance linewidths were extracted by resolving the Zeeman-split intercombination peaks and adjusting the compensation currents to minimize magnetic field-induced broadening. One axis was scanned while the other two compensation currents were held fixed at optimized values. This method helps identify the cross-compensation values necessary to achieve magnetic field nulling, as sharp resonance corresponds to minimal field-induced broadening. Measurements were performed using a time-of-flight technique and probing with a narrow-linewidth 556 nm laser. Error bars represent a standard deviation from Lorentzian fits to the spectral data.

As a final confirmation of effective compensation, we released the atoms and tracked their center-of-mass motion during the time-of-flight (TOF) process. In the absence of residual magnetic field gradients, the atomic cloud should move ballistically under gravity alone, without horizontal drift as shown in Figure 2.19.

We have discussed in detail why understanding the MOT motion is essential for investigating the physical phenomena explored in Chapter 3.

2.4.2 Laser Control and Timing

Figure 2.15 illustrates the timing sequence used for loading atoms into the Magneto-Optical Trap (MOT), releasing them, and subsequently performing imaging. The temporal coordination of laser and magnetic fields is essential for achieving optimal atom cooling, trapping, and precise measurement. This timing sequence has been implemented in the laboratory setup in Nice, following the relocation of the experiment from Sophia Antipolis to Nice.

MOT Loading Phase (0 ms – 1000 ms) The experimental sequence begins with a 1000 ms Blue MOT loading phase. During this period, atoms are collected and cooled in the MOT using six retro-reflected 399 nm beams with a diameter of approximately $2''$ $(1/e^2)$, corresponding to intensities of $0.023\, I_{\text{sat}}$ for each horizontal beam and $0.01\, I_{\text{sat}}$ for each vertical beam, detuned by $-2\,\Gamma_b$. A magnetic field gradient of 13.0 G/cm is applied to enable spatial trapping via the Zeeman effect. A counter-propagating

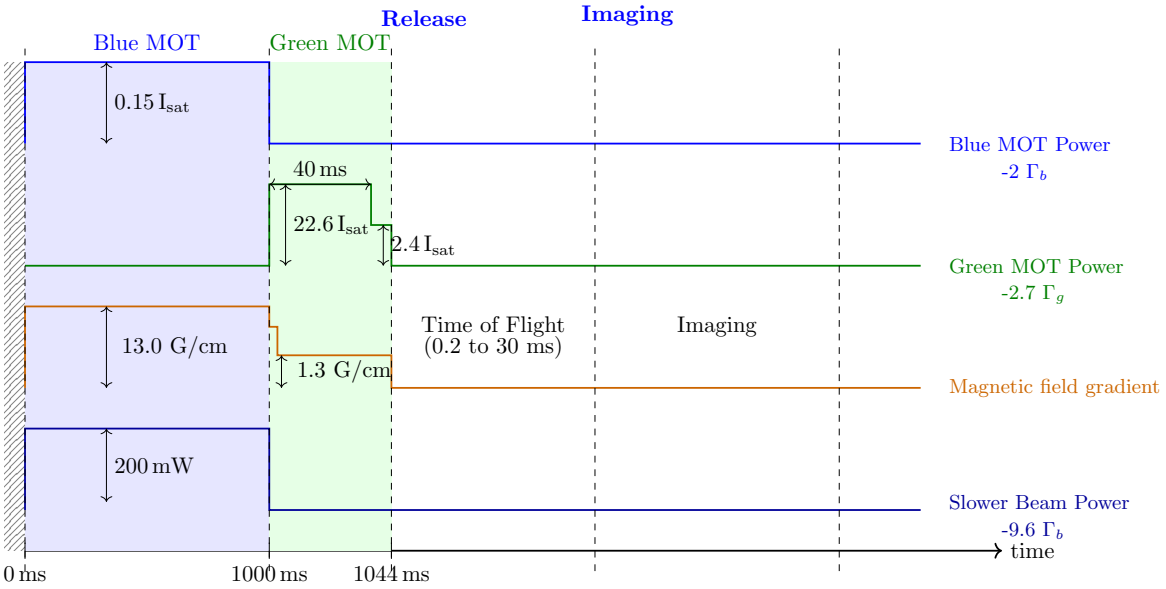

Figure 2.15: Timing sequence for MOT loading, transfer, and imaging.

slowing beam, detuned by $-9.6\,\Gamma_b$ with total power 300 mW, remains on during the entire loading stage to decelerate atoms emerging from the oven and enhance capture efficiency. Under these conditions, the loading time and lifetime of the Blue MOT are approximately 250 ms and 400 ms, respectively.

Transition to Green MOT (1000 ms – 1044 ms) After a loading time of 1 sec, the blue MOT beams operating on the ${}^1S_0 \rightarrow {}^1P_1$ transition at 399 nm, along with the slowing beam, are switched off. At the same time, the green MOT beams, addressing the narrow ${}^1S_0 \rightarrow {}^3P_1$ intercombination transition at 556 nm, are turned on with a detuning of $-2.7\,\Gamma_g$.

Magnetic Field Gradient Ramp Because the ${}^1S_0 \rightarrow {}^3P_1$ line is narrow ($\Gamma/2\pi =$ 184 kHz), a large magnetic-field gradient produces strong spatial Zeeman detuning and drastically reduces the fraction of atoms that are near resonance at the moment of transfer. The resonance varies as

$$\frac{d\nu}{dz} = \frac{g_J \mu_B}{h} \frac{dB}{dz},$$

so that one natural linewidth corresponds to only $L_\Gamma \approx 0.068$ mm at 13 G/cm, 0.135 mm at 6.5 G/cm, and 0.677 mm at 1.3 G/cm.

To maximize transfer while maintaining stability, we employ a two-step reduction of the gradient: a fast pre-ramp from 13.0 to 6.5 G/cm (20 μs) to enlarge the resonant volume at the instant the green beams are applied, followed by a further reduction to 1.3 G/cm for green-MOT loading and compression. This sequence increases capture on the narrow line and mitigates heating or losses associated with abrupt large changes in the magnetic field.

The green MOT beams remains on for 40 ms at intensities of approximately 4.6 I_{sat} per horizontal beam and 2 I_{sat} per vertical beam. This is followed by a 4 ms intensity ramp-down phase with reduced powers (0.5 I_{sat} for horizontal beams and 0.22 I_{sat} for vertical beams), promoting further cooling.

Time-of-Flight and Imaging After the green MOT stage, all trapping light and magnetic fields are turned off, initiating a Time-of-Flight (TOF) period. The atomic cloud expands freely during TOF, allowing it to perform the required measurements. Absorption imaging is performed after TOF to obtain spatial and temporal information about the atom cloud. This step is essential for characterizing the cloud's temperature, size, and spatial density.

The slower beam remains off after the initial MOT loading, as its purpose is confined to enhancing atom capture during the initial loading stage

2.4.3 MOT Characterization

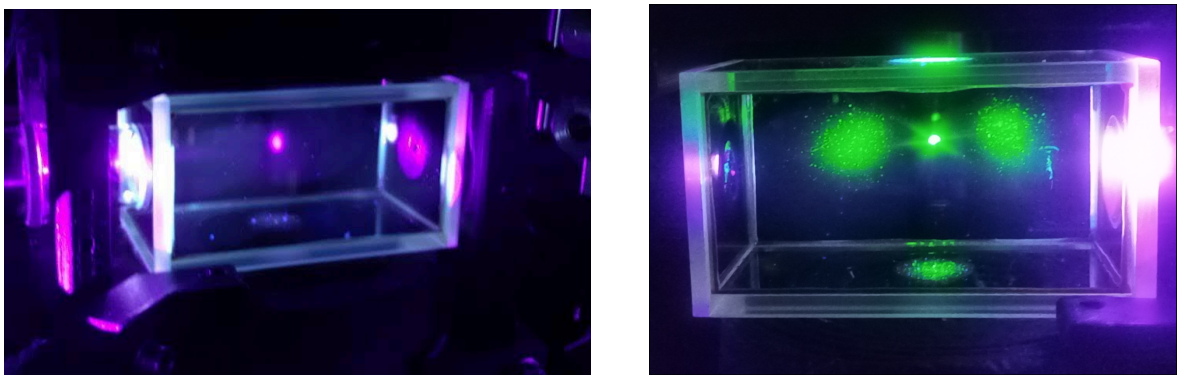

(a) Blue MOT (b) Green MOT

Figure 2.16: The Blue and Green Magneto-Optical Traps (MOTs)

Time-of-Flight (TOF) Absorption Imaging and Temperature Extraction

In our experiment with ^{174}Yb, we measured the peak optical density ($b_{0,b}$) on the 399 nm blue transition, where the transition linewidth is broad ($\Gamma_b = 29$ MHz). Although, in principle, it is possible to perform OD measurements using a detuned probe, in practice, this approach was not feasible due to the large frequency shifts required. Detuning sufficiently far from resonance to avoid high absorption in the center of the cloud (typically tens of MHz) would require large AOM frequency shifts. As a result, we performed imaging on resonance and fit the transmission profile using the exponential-of-Gaussian model (described in a later section), which enabled reliable extraction of the peak OD by leveraging the well-resolved wings of the profile.

Estimating $^3P_1$ Optical density via Broad-Line Imaging We carry out most of our experimental investigations—such as light shift characterization, study of light propagation, and MOT dynamics—on the narrow $^1S_0 \rightarrow {}^3P_1$ intercombination line at 556 nm. However, we do not directly measure the peak optical density ($b_{0,g}$) on this transition. Instead, we image the atomic cloud on the broader $^1S_0 \rightarrow {}^1P_1$ transition at 399 nm and extract the peak OD from the on-resonance absorption profile. This OD is then used to infer the OD on the $^3P_1$ line at 556 nm.

This approach is motivated by the practical limitations of narrow-line imaging. The $^3P_1$ transition has a linewidth of only ~ 184 kHz, making it highly sensitive to

laser frequency noise, detuning instabilities, and Doppler shifts. Additionally, due to the low scattering rate, absorption imaging on this transition yields weak signals, which are particularly susceptible to technical noise and saturation artifacts. These limitations make it difficult to obtain reliable and repeatable OD measurements directly on the $^3P_1$ line. By contrast, the broad $^1P_1$ transition (linewidth ~ 29 MHz) allows for high signal-to-noise imaging on resonance. We use an exponential-of-Gaussian fitting method to robustly extract the peak OD from the transmission profile, even in the high-absorption regime where central pixels saturate. To extrapolate from the blue OD ($b_{0,b}$) to the green OD ($b_{0,g}$), we use the fact that, for low-intensity imaging in the linear absorption regime, the resonant OD is proportional to the scattering cross section σ_0, which scales as:

$$\sigma_{sc,0} = \frac{3\lambda^2}{2\pi}. \tag{2.21}$$

For a cloud with a Gaussian density profile, the absorption optical depth along the probe direction is, from the Beer–Lambert law,

$$\mathrm{OD} = \rho \sigma_{sc,0} L \tag{2.22}$$

where:

- ρ is the density along the imaging direction,
- L is the effective path length (typically the width of the cloud).

For a three-dimensional Gaussian density distribution with rms radii σ_x, σ_y, and σ_z, the on-axis optical depth is obtained by integrating the Beer–Lambert law along the probe direction. Following Ref. [17], the on-resonance optical depth at the center of the atomic cloud (denoted b_0) can be written as:

$$b_0 = \frac{3\lambda^2}{(2\pi)^2} \frac{N}{\sigma_x \sigma_y}. \tag{2.23}$$

where:

- N is the total number of atoms,

Thus, assuming the same atom number and Gaussian spatial distribution, the ratio of peak optical densities is:

$$\frac{\mathrm{b_{0,g}}}{\mathrm{b_{0,b}}} = \left(\frac{\lambda_{\mathrm{green}}}{\lambda_{\mathrm{blue}}}\right)^2 = \left(\frac{556\,\mathrm{nm}}{399\,\mathrm{nm}}\right)^2 \approx 1.94.$$

Therefore,

$$\mathrm{b_{0,g}} \approx 1.94 \times \mathrm{b_{0,b}}.$$

This relation allows us to estimate the b_0 relevant for the $^3P_1$ transition measurements based on absorption imaging data from the $^1P_1$ transition. It offers a practical and accurate alternative to narrow-line imaging, while maintaining a consistent and quantitative understanding of the sample properties. The optical density we measure using the Beer–Lambert law assumes that all atoms are on resonance with the probe light, i.e., the absorption cross-section is maximal. But in reality, Doppler broadening spreads the atomic absorption over a range of frequencies. If the probe is on resonance with only a fraction of the atoms (those with near-zero velocity), the effective OD is reduced compared to the ideal (Doppler-free) case.

Doppler Broadening and Effective b_0 on the Narrow $^3P_1$ Transition While this transition has a narrow natural linewidth of

$$\Gamma_g = 2\pi \times 184 \text{ kHz}, \tag{2.24}$$

The finite temperature of the atomic ensemble leads to Doppler broadening, which spreads the atomic absorption over a range of frequencies. As a result, the peak absorption cross-section is reduced, and the effective optical density observed in absorption imaging is lower than the ideal (Doppler-free) value.

1. **Doppler-Broadened Effective Linewidth**

   At finite temperature T, the atoms have a velocity distribution along the probe axis. This causes a frequency spread due to the Doppler effect. The Doppler broadening of an atomic transition at finite temperature follows a Gaussian profile [**metcalf1999**, 42]. The full width at half maximum (FWHM) of the Doppler broadening is:

$$\Delta\nu_D = \frac{1}{\lambda_g}\sqrt{\frac{8k_B T \ln 2}{M}}. \tag{2.25}$$

   Here:

   - M is the atomic mass of ^{174}Yb ($m = 2.89 \times 10^{-25}$ kg),
   - T is the temperature in Kelvin,

   At a MOT temperature of $T = 15\,\mu$K, the Doppler width is approximately

$$\Delta\nu_D \approx 113 \text{ kHz}. \tag{2.26}$$

2. **Reduction of Effective OD**

   When Doppler broadening is present, the effective optical depth at resonance is reduced because the absorption profile is no longer a pure Lorentzian of natural width Γ, but instead a Voigt profile arising from the convolution of the natural Lorentzian and the Gaussian Doppler distribution. The reduction factor is determined by the ratio of the Voigt profile at zero detuning to the Lorentzian peak cross-section. The correction factor $C(\Gamma_g, \Delta\nu_D)$, describing the reduction of the effective optical depth due to Doppler broadening, has been introduced and applied in recent studies on ytterbium [18] and strontium [43].

$$b_{0,g}(T) = b_{0,g}(0 \text{ K}) \times C(\Gamma_g, \Delta\nu_D), \tag{2.27}$$

   with

$$C(\Gamma_g, \Delta\nu_D) = \sqrt{\pi}\,\theta\, e^{\theta^2}\,\mathrm{Erfc}(\theta), \qquad \theta = \frac{\sqrt{\ln 2}\,\Gamma_g}{2\pi\Delta\nu_D}. \tag{2.28}$$

   The natural linewidth is smaller than the Doppler width, as quantified by

$$\frac{2\pi\Delta\nu_D}{\Gamma_g} \simeq 0.62 < 1, \tag{2.29}$$

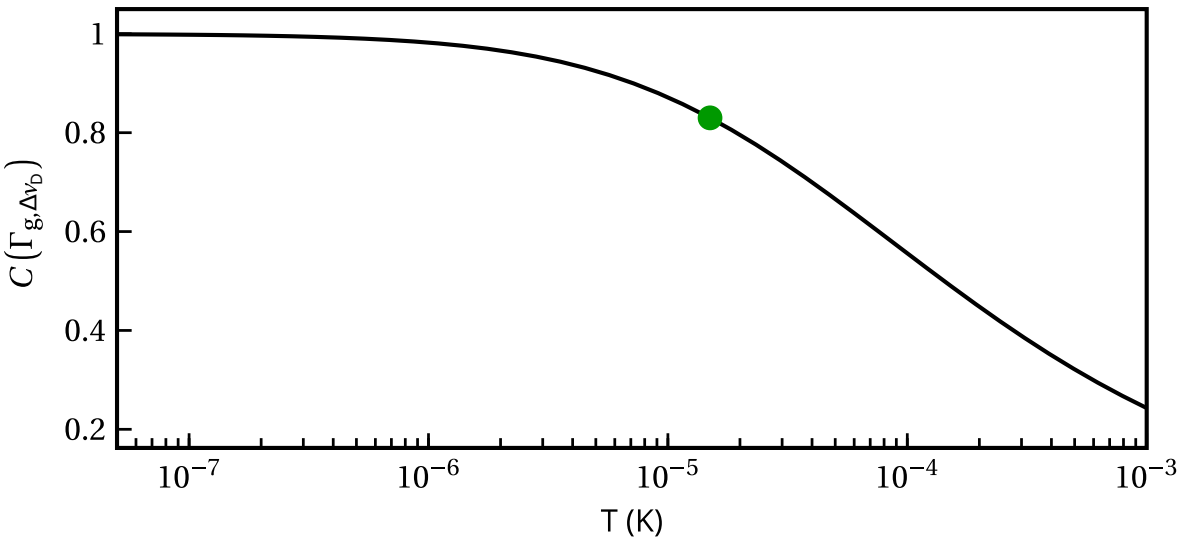

Figure 2.17: The correction factor $C(\Gamma_g, \Delta\nu_D)$ for the effective optical depth as a function of temperature. The curve shows the suppression of resonant absorption due to Doppler broadening of the $^1S_0 \rightarrow {}^3P_1$ inter-combination line. The green point indicates the experimental condition at $T = 15$ μK,corresponding to a reduction of the effective optical depth to $C \simeq 0.83$.

and Erfc(a) is the complementary error function.

The dependence of the correction factor $C(\Gamma_g, \Delta\nu_D)$ on temperature is shown in Fig. 2.17. As expected, the reduction becomes more pronounced with increasing temperature. The green point marks the experimental condition at $T = 15$ μK corresponding to $C \simeq 0.83$.

This expression explicitly quantifies the suppression of resonant absorption due to the thermal velocity distribution: in the limit $2\pi\Delta\nu_D \ll \Gamma_g$, the reduction factor approaches unity, while for $2\pi\Delta\nu_D \gg \Gamma_g$ it decreases approximately as $\sqrt{\pi ln(2)\Gamma_g/2\pi\Delta\nu_D}$.

For the $^1S_0 \rightarrow {}^3P_1$ intercombination line of ^{174}Yb, with $\Gamma_g = 184$ kHz and a Doppler width of about $\Delta\nu_D \sim 110$ kHz, this analysis yields

$$\frac{b_{0,\mathrm{g}}(T)}{b_{0,g}(T = 0K)} \approx 0.83, \tag{2.30}$$

showing that Doppler broadening reduces the effective optical depth by roughly 15–20%.

3. **Final Result**

To correct for this in the analysis, one can apply a correction factor:

$$\mathrm{b}_{0,\mathrm{g}} \approx 1.66 \times \mathrm{b}_{0,\mathrm{b}}. \tag{2.31}$$

This relation provides a practical and accurate estimate of the green OD from blue imaging under typical experimental conditions.

2.4.4 Atom Number Calculation from 2D Absorption Imaging

Absorption imaging has been performed on the broad transition $^1P_1$ to characterize the trapped atoms and measure the atomic cloud at different time-of-flight (TOF) expansions. Figure 2.18 shows a set of Time-of-Flight (TOF) absorption images and the corresponding data analysis for temperature extraction illustrated in Figure 2.21.

These images were captured at increasing time intervals after the release of atoms from the Magneto-Optical Trap (MOT), illustrating the ballistic expansion of the atomic cloud. The TOF absorption images show the spatial distribution of the atomic cloud at different free expansion times: 5.0 ms, 10.0 ms, 20.0 ms, 25.0 ms, and 30.0 ms. As the time increases, the cloud expands due to its thermal velocity distribution. The density profile is darker at earlier times due to higher optical density and becomes more dilute as the cloud expands. The total number of atoms in the cloud was determined using a 2D Gaussian fit to the absorption image obtained during time-of-flight (TOF) imaging. The optical density (OD) of the atomic cloud is followed as:

$$\mathrm{OD}(x,y) = \mathrm{b}_{0,b} \exp\left(-\frac{(x-x_0)^2}{2\sigma_x^2} - \frac{(y-y_0)^2}{2\sigma_y^2}\right) + \mathrm{Offset}, \tag{2.32}$$

where $\mathrm{b}_{0,b}$ is the peak optical density, (x_0, y_0) is the center of the cloud, and σ_x, σ_y are the standard deviations of the Gaussian distribution along the respective axes. Offset is the background offset.

The total atom number N is calculated from the integrated optical density using:

$$N = \frac{1}{\sigma_{sc,0}} \int \mathrm{OD}(x,y)\, dx\, dy = \frac{2\pi\sigma_x\sigma_y\, \mathrm{b}_{0,b}}{\sigma_{sc,0}}, \tag{2.33}$$

where $\sigma_{sc,0}$ is the resonant absorption cross-section[44], given by:

$$\sigma_{sc} = \frac{\sigma_{sc,0}}{1 + I/I_{\mathrm{sat}} + (2\delta/\Gamma)^2}, \tag{2.34}$$

The total atom number was extracted from absorption images using the $^1S_0 \rightarrow {}^1P_1$ transition of ^{174}Yb at 399 nm. Since the imaging was performed well below the saturation intensity ($I \ll I_{\mathrm{sat}}$), the absorption cross-section simplifies to its on-resonance value:

$$\sigma_{sc,0} = \frac{3\lambda^2}{2\pi}, \tag{2.35}$$

where $\lambda = 399\,\mathrm{nm}$ is the imaging wavelength.

Optical Density Calculation To account for background and probe beam intensity variation, three images were recorded:

- I_{atoms}: with atoms present,
- I_{probe}: probe beam without atoms,
- I_{bg}: background (no probe, no atoms).

The optical density (OD) at each pixel was calculated using:

$$\mathrm{OD}(x,y) = -\ln\left(\frac{I_{\mathrm{atoms}}(x,y) - I_{\mathrm{bg}}(x,y)}{I_{\mathrm{probe}}(x,y) - I_{\mathrm{bg}}(x,y)}\right) \tag{2.36}$$

2D Gaussian Fit with Offset The OD image was fitted to a two-dimensional Gaussian function with a constant offset to account for residual background using the equation (2.32).

Since the background was subtracted using the three-image method before fitting, the resulting OD image contains only the atomic signal. Any constant offset in the fit is numerical and does not contribute to the atom number calculation. In our case of absorption image, the fitted offset is typically small, with Offset $\sim 10^{-2}$ or less.

The total number of atoms is calculated using equation (2.33): With $\sigma_x \approx \sigma_y \approx 900\,\mu$m, extracted from a Gaussian fit to the atomic cloud in the x and y directions, as shown in Figures 2.20a and 2.20b, and the fitted $b_{0,b}$ from the image 2.18,

We obtain a total atom number:

$$N \approx 2 \times 10^8. \tag{2.37}$$

This method provides a robust, quantitative estimate of the atom number in the MOT, assuming accurate calibration of the imaging system and low probe intensity.

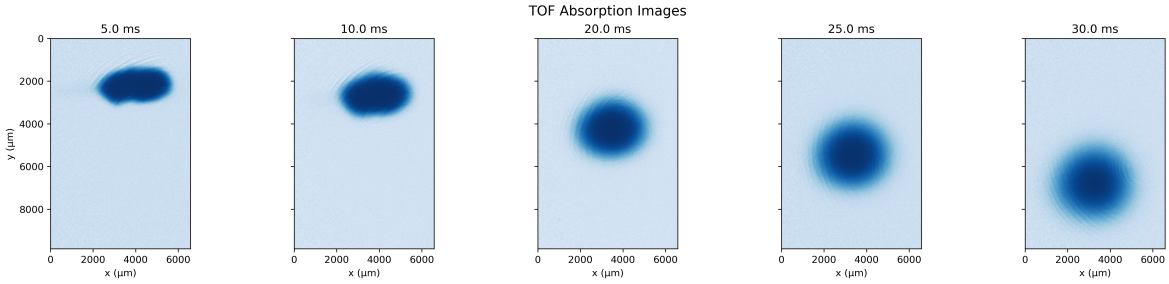

Figure 2.18: Absorption images of the atomic cloud at different time-of-flight (TOF) durations, indicated above each image. These images, taken using blue transition imaging at 399 nm, illustrate the ballistic expansion of the cloud.

For a time-of-flight (TOF) of 30 ms, we fit the atomic cloud profiles with a 1D Gaussian function in both the Y and X directions. The fitted width is approximately 900 µm.

Temperature: To determine the temperature of the atomic ensemble, we analyze the ballistic expansion of the cloud during the time-of-flight (TOF) period. When the trapping potential is turned off, the atoms expand freely due to their thermal velocity distribution. Assuming a non-interacting gas and negligible external forces, the time evolution of the cloud size in the radial direction is given by:

$$\sigma(t)^2 = \sigma_0^2 + \frac{k_B T}{M} t^2, \tag{2.38}$$

where:

- $\sigma(t)$ is the root mean square (rms) width of the cloud at time t,
- σ_0 is the initial rms width of the cloud,
- T is the temperature of the atomic ensemble,
- t is the time-of-flight (TOF) duration.

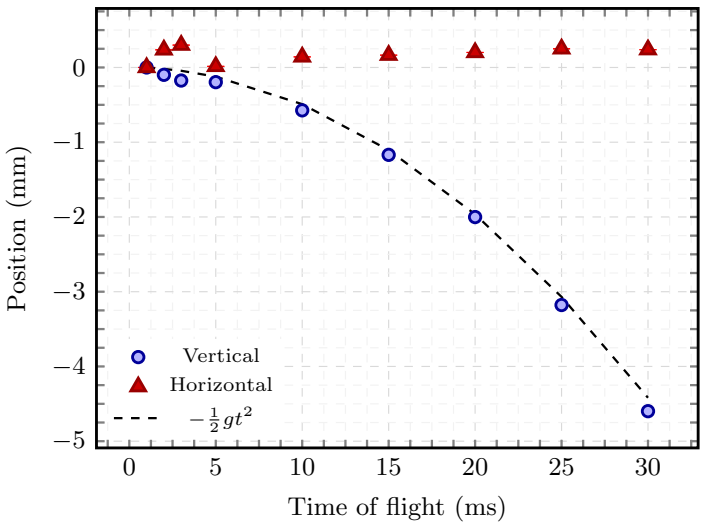

Figure 2.19: Measured vertical (blue circles) and horizontal (red triangles) positions of the atomic cloud as a function of time-of-flight (TOF). The vertical displacement follows a ballistic trajectory due to gravity and is compared to the theoretical trajectory $-\frac{1}{2}gt^2$ (dashed line), plotted using $g = 9.81\text{m/s}^2$ without any free parameters. The horizontal position remains effectively constant, confirming that there is no drift due to the stray magnetic field.

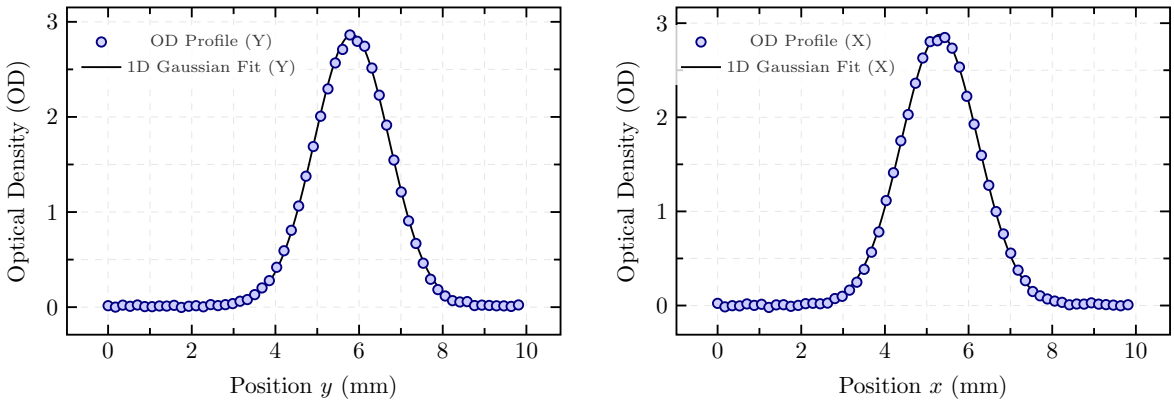

(a) Absorption profile along the vertical (Y) axis with 1D Gaussian fit.

(b) Absorption profile along the horizontal (X) axis with 1D Gaussian fit.

Figure 2.20: Comparison of one-dimensional cuts of the absorption image along the two orthogonal axes. The atomic density distribution is well described by Gaussian fits in both the X and Y directions.

This expression results from assuming a Gaussian density distribution and a one-dimensional rms velocity spread given by $v_{rms} = \sqrt{k_B T/M}$. By imaging the cloud at different TOF durations and extracting $\sigma(t)$ via Gaussian fits, the temperature T can be determined from the slope of a linear fit to $\sigma^2(t)$ versus t^2.

The graph (Figure 2.21) shows the square of the cloud width, σ^2, plotted against the square of the TOF duration, t^2. Each data point (blue circles with error bars) corresponds to a fitted width from the respective absorption image. The data are fit with a linear function (black dashed line).

From the slope of the linear fit, the temperature T of the atomic cloud was extracted

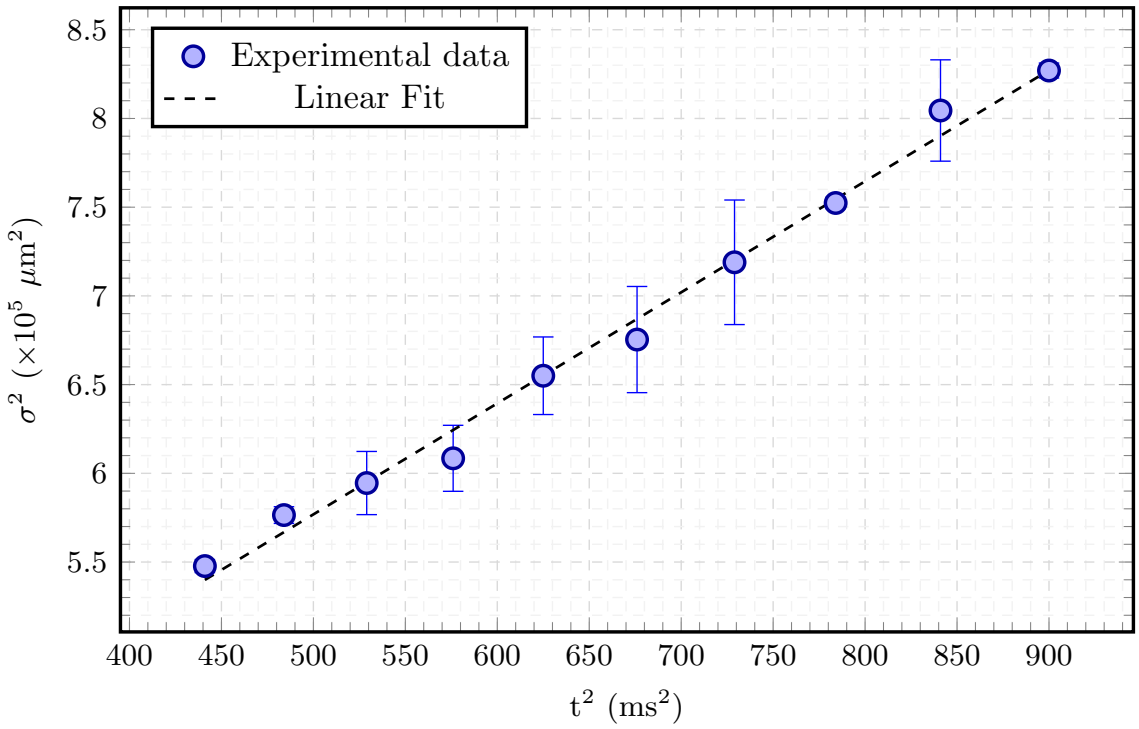

Figure 2.21: Plot of σ^2 vs. t^2 with a linear fit to extract atomic temperature and size of the MOT

to be 13 µK. This method offers a reliable and non-invasive approach to thermometry in ultracold atom experiments. In this experiment, the 2D Gaussian fit yielded a symmetric cloud with a standard deviation $\sigma_0 = 514$ μm. From the Equation 2.19, the Doppler temperature at a detuning of -2.77 Γ is 13.16 µK. The close agreement between the experimentally measured temperature and the theoretical Doppler temperature confirms the validity of the fitting method and indicates that the cloud is effectively cooled near the Doppler limit under these experimental conditions.

By contrast, Eq. (2.17) gives a much smaller MOT size of $\Delta z = 111$ μm, since it relies on a simplified single-particle, low-velocity model, neglecting the collective effects and multiple scattering which become significant at high optical density. All the consequences arises from these effects expands the cloud well beyond the single-particle prediction. As a result, the observed initial rms width $\sigma_0 = 514$ μm is nearly five times larger than Δz.

Limitations of Logarithmic OD at High Optical Densities and Alternative Fitting Method The Beer-Lambert law gives:

$$\mathrm{OD}(x) = -\ln\left(\frac{I_{\mathrm{atoms}}(x) - I_{\mathrm{bg}}(x)}{I_{\mathrm{probe}}(x) - I_{\mathrm{bg}}(x)}\right) \tag{1.14}$$

While the Beer-Lambert law provides a straightforward means of calculating the optical density via the logarithmic formula in Eq. (1.14), this method becomes unreliable in the regime of high absorption. Specifically, when the atomic cloud is optically thick, the transmitted probe intensity at the center can approach the camera's noise floor, resulting in artificially capped OD values (typically OD ≈ 6–7), regardless of the true absorption. This occurs because:

- When atoms $I_{\text{atoms}} - I_{\text{bg}} \to 0$, even small fluctuations due to camera readout noise or photon shot noise lead to large variations in the logarithm, leading to significant numerical uncertainties in the extracted OD.
- When the transmitted intensity is very low due to strong absorption, the recorded signal on a 16-bit sensor may be only a few counts above the background. In this regime, a difference of just one analog–digital unit (ADU) in the camera readout corresponds to a large fractional change in intensity. Because the OD is obtained from a logarithm, such small discrete steps in intensity translate into disproportionately large variations in the extracted OD.

To mitigate these limitations, we instead model the transmitted intensity profile using a phenomenological exponential-of-Gaussian form:

$$T(x) = \frac{I_{atoms}}{I_{probe}} = \exp\left(-\mathrm{b}_0 \cdot \exp\left(-\frac{(x-x_0)^2}{2\sigma^2}\right)\right), \tag{2.39}$$

which corresponds to a Gaussian absorption profile. This approach offers two key advantages:

1. It avoids direct use of the central pixels, where $I \approx 0$, and instead relies on the wings of the profile, where the transmitted signal is still measurable and the noise is minimal.
2. It provides a robust estimate of the peak b_0, even when the absorption saturates the camera or introduces artifacts in the central region.

2.4.5 Spectroscopy on the Green MOT

Our primary goal is to optimize the performance of the Magneto-Optical Trap (MOT) by identifying the optimum detuning of the green MOT to achieve the maximum peak optical density (b_0) and to determine the resonance frequency of the ${}^1S_0 \to {}^3P_1$ green transition. Due to the narrow natural linewidth of the green ${}^3P_1$ transition (approximately 184 kHz), the MOT is particularly sensitive to frequency drifts and lock instabilities. Even small drifts in the green laser lock can lead to a significant change in the MOT detuning, degrading MOT performance. For this reason, we perform spectroscopic checks not only at the start of each day but sometimes multiple times per day, especially during long experimental runs. These routine calibrations are essential for maintaining MOT stability and ensuring consistent experimental conditions. Consequently, we perform spectroscopic scans on the trapped ensemble using fluorescence or absorption methods.

We begin by performing absorption imaging on the blue transition of ${}^{174}\mathrm{Yb}$ at a time-of-flight (TOF) of 20 ms after green MOT loading to obtain the resonance frequency of the ${}^1P_1$ transition by scanning the blue probe frequency as shown in Figure 2.22a. Now, we optimize the frequency of the green MOT beams to efficiently trap atoms on the ${}^3P_1$ transition. This method involves scanning the frequency of the green MOT beam and measuring the resulting absorption signal with the blue probe on resonance, as illustrated in Figures 2.22b.

The frequency of the green MOT beam, corresponding to the maximum peak optical density (OD), indicates the optimal detuning for maximum atom capture and efficient

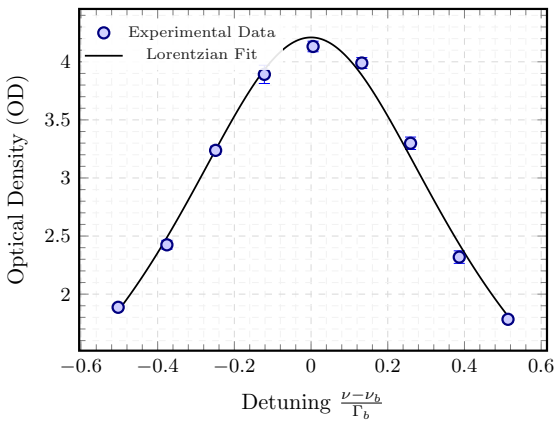

(a) Absorption imaging on the $^1P_1$ transition, performed by scanning the frequency of the blue probe beam to determine the resonance frequency of the transition. The x-axis shows the detuning $(\nu - \nu_b)/\Gamma_b$, where ν_b is the resonance frequency and Γ_b is the natural linewidth of the $^1P_1$ transition.

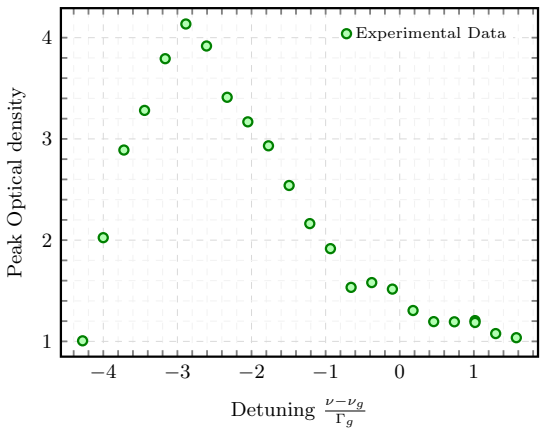

(b) Absorption imaging on the blue transition at a time-of-flight (TOF) of 20 ms, performed by scanning the green MOT beam frequency to determine the optimal detuning -2.7 Γ_g for maximum peak optical density (b_0), providing an indicator of the trapping efficiency.

Figure 2.22: (a) Determination of the resonance frequency of the blue $^1P_1$ transition using absorption imaging. (b) Optimization of the green MOT beam detuning by scanning its frequency and measuring the absorption signal with the blue probe held on resonance. Together, these measurements enable accurate frequency calibration and efficient operation of MOT

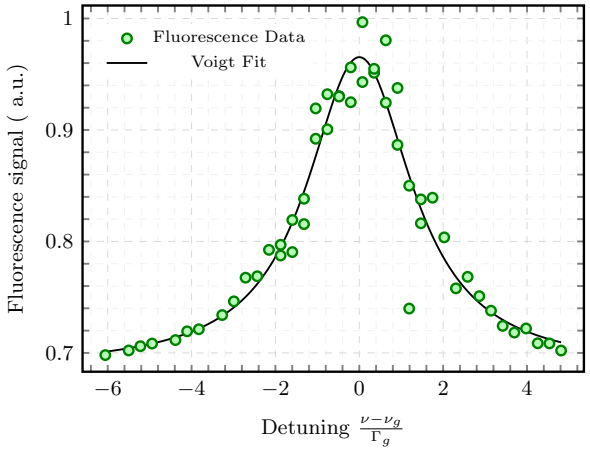

(a) Fluorescence spectrum of the $^1S_0 \rightarrow {}^3P_1$ transition by scanning the frequency of the green MOT beam, fitted with a Voigt profile.

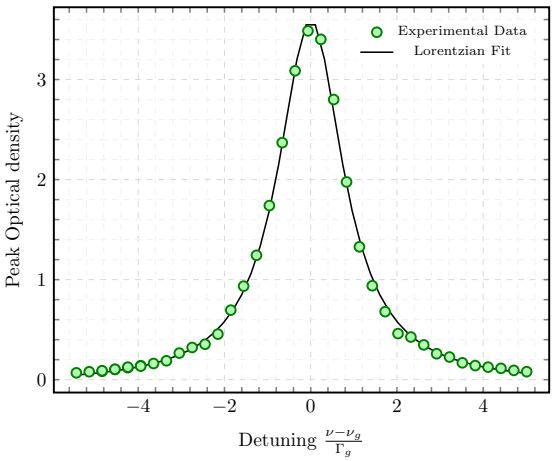

(b) Optical density as a function of green probe frequency.

Figure 2.23: Comparison of fluorescence and absorption spectra related to the green MOT. (a) shows the Voigt-fitted fluorescence spectrum of the $^1S_0 \rightarrow {}^3P_1$ transition, and (b) shows the optical density versus green probe detuning.

MOT operation. The data is fitted with a Voigt profile which accounts for both the Lorentzian natural linewidth and Gaussian contributions from residual Doppler broadening. To determine the resonance frequency of the $^3P_1$ transition, we perform

fluorescence spectroscopy by scanning the green MOT beam frequency, as shown in Figure 2.23a. Additionally, we perform absorption spectroscopy by scanning the green probe frequency on the ${}^1S_0 \rightarrow {}^3P_1$ transition, as shown in Figure 2.23b.

Finally, we perform absorption imaging to measure the on-resonance peak optical density. This method allows us to measure the peak optical density $b_{0,b}$ on resonance of the ${}^1P_1$ transition. The value of $b_{0,b}$ obtained from the blue transition serves as a reference point for determining the $b_{0,g}$ for the green transition, as discussed earlier.

These measurements provide direct access to the optical density and are especially relevant for calibrating imaging parameters. In practice, either method—fluorescence or absorption—is sufficient for locating the resonance of the green MOT, but both are used here to verify consistency and ensure reproducibility in daily operation. Performing these checks regularly helps us monitor the stability of the MOT and ensures that experimental conditions remain reproducible across successive runs.

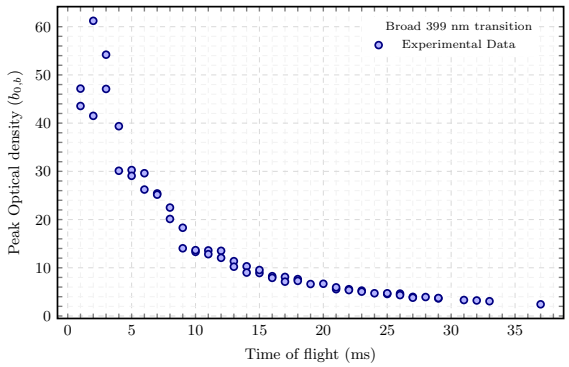

(a) Peak optical depth as a function of time of flight for the broad transition. The data points represent experimental measurements of the peak optical density $b_{0,b}$. The decay in optical depth reflects the cloud expansion. Typical initial optical depths reach $b_{0,b} \sim 60$

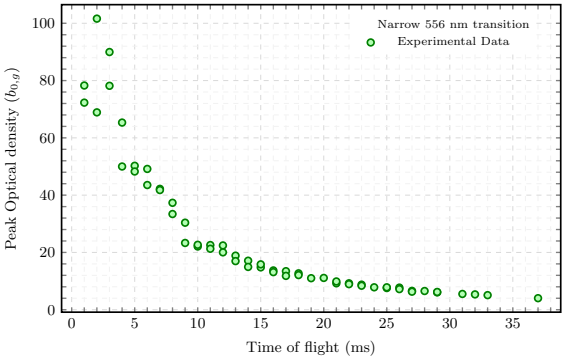

(b) Peak optical depth as a function of time of flight for the narrow transitions. The data points represent experimental measurements of the peak optical density $b_{0,g}$ calculated using the scaling relation obtained in Eq. (2.31). Typical initial optical depths reach $b_{0,g} \sim 100$, corresponding to total atom numbers up to 1.5×10^8.

In practice, the fit to Eq. (2.39) yields two main parameters: the peak optical depth $b_{0,b}$ on the blue transition and the rms cloud width $\sigma(t)$. Representative fits give peak optical depths up to $b_{0,b} \sim 60$ Fig. 2.24a, depending expansion time. Using the scaling relation obtained in Eq. (2.31), we obtain the corresponding peak optical depth for the green intercombination line, with typical values reaching $b_{0,g} \sim 100$. These fitted parameters are then used, together with Eq. (2.33), to extract the total atom number. Figure 2.25 shows the measured atom number as a function of the time of flight (ToF) after release from the MOT, with typical values up to 1.5×10^8 atoms.

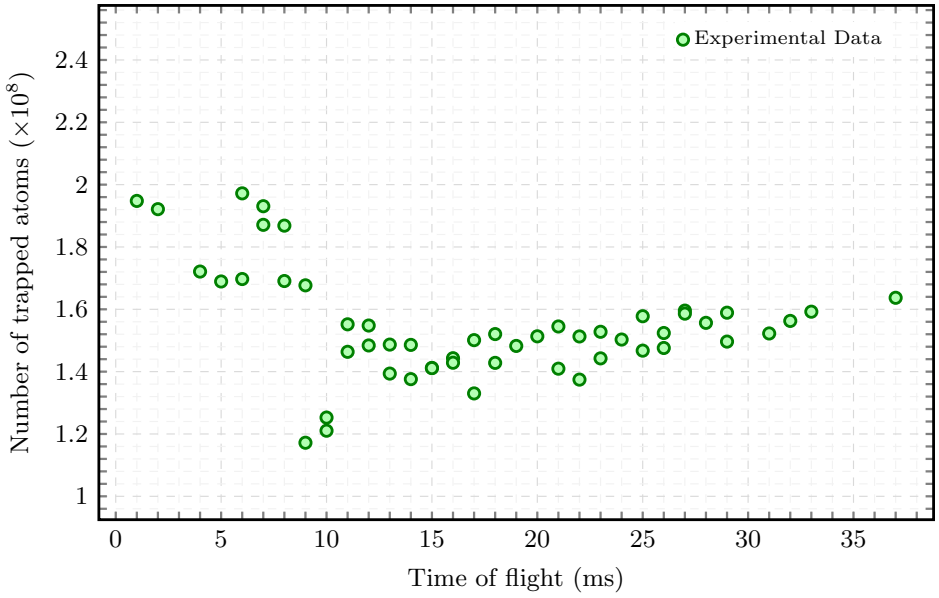

Figure 2.25: Total number of trapped ^{174}Yb atoms as a function of time of flight, obtained from the fitted peak optical depth on the blue transition $b_{0,b}$, and using an initial rms cloud size of $\sigma \simeq 365\ \mu$m. Typical atom numbers are in the range of $1\text{–}3\times10^8$.

Linewidth of $^3P_1$ state with optical density The linewidth of $^3P_1$ state is measured at $\frac{I}{I_{sat}} = 0.027$ at different optical density $b_{0,g}$ and the dependence of Γ/Γ_g on the on-resonance optical depth ($b_{0,g}$) was analyzed using a fit[45] given by:

$$\frac{\Gamma}{\Gamma_g} = \sqrt{1 + \alpha\, \mathrm{b_{0,g}}}. \tag{2.40}$$

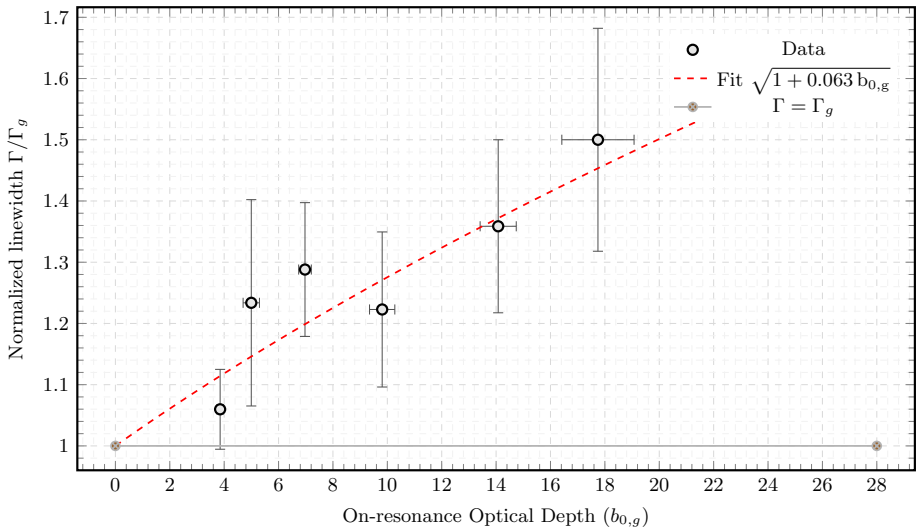

Figure 2.26: Normalized linewidth Γ/Γ_g of the $^1S_0 \rightarrow {}^3P_1$ transition in ^{174}Yb as a function of on-resonance optical depth $b_{0,g}$. The black circles show the experimentally measured linewidth. The dashed red line represents a fit.

Problem encounted After moving to Nice in March 2023, we encountered environmental challenges, notably increased humidity and temperature instability in the lab. These factors affected system stability and laser alignment. A particularly critical incident occurred in June 2023, when water from the air conditioning system leaked onto the optical table, resulting in condensation on key components, including the Verdi pump. These events, documented with photographs (see A), underscored the importance of environmental control for precision atomic physics experiments.

Chapter 3

From Light Shifts to the All-optical Faraday effect

3.1 Introduction and Motivation

The interaction between light and atomic systems gives rise to several fundamental effects, among which the AC Stark shift, commonly referred to as the light shift, is particularly significant. A coherent light field near-resonant with an atomic transition modifies the energy levels of the atom. This occurs through the electric dipole interaction with the oscillating field. They were initially studied in alkali atoms, whose single-valence-electron structure makes them comparatively straightforward systems for precision measurements and applications in laser cooling and trapping [46, 47].

Over time, light shifts have evolved from being regarded as systematic perturbations to becoming a powerful resource. The light shift depends on the intensity, frequency, and polarization of the applied light. It can be harnessed to modify atomic transition frequencies for high-precision spectroscopic control, to engineer state-dependent optical potentials [48], to enable controlled optical pumping, and to serve metrological applications [49, 50, 51]. In many atomic physics experiments, however, light shifts are an intrinsic effect that must be either suppressed or carefully controlled [52].

Ytterbium is of central importance in optical lattice clocks and quantum simulation platforms, where precise control of light shifts underpins both accuracy and coherence [51]. In optical lattice clock experiments with bosonic isotopes such as ^{174}Yb, the differential light shift between the clock states can be canceled at a so-called magic wavelength [53]. At this specific wavelength, the polarizabilities of the ground and excited states are equal, allowing for state-insensitive trapping [54] and high-precision spectroscopy even in the presence of a strong trapping potential. This state-insensitive trapping at the magic wavelength is critical for suppressing light-induced frequency shifts in optical lattice clocks and for achieving long coherence times.

In our research on Anderson localization in a disordered potential (e.g., one generated by a speckle field), understanding and controlling light shifts is particularly important. Uncontrolled light shifts can distort the effective potential landscape and induce dephasing, or decoherence, that masks localization signatures.

In isotopes with nonzero nuclear spin, nearby hyperfine states can mix and contribute to the overall polarizability, thereby making it difficult to isolate the purely electronic contribution to the light shifts. In this work, we focus on ^{174}Yb, which has a nuclear spin $I = 0$ and therefore exhibits no hyperfine structure, so the $^3P_1 \rightarrow {}^3D_1$ transition

involves only electronic angular momentum sublevels. The absence of hyperfine mixing provides a uniquely clean environment for investigating light shifts; the differential shifts among the m_J substates arise solely from tensorial light–atom coupling, without additional complications from nuclear spin.

Later, we present spatially resolved imaging of the light shift, providing a comprehensive picture of how it manifests under realistic experimental conditions and how it depends on laser parameters, resulting in observable inhomogeneous broadening. Finally, we explore optically induced Faraday rotation as a sensitive probe of the resulting differential light shift.

The central aim of this chapter is to investigate not only the light shift in the ${}^3P_1 \rightarrow {}^3D_1$ transition of a cold atomic cloud, but also its role in enabling a novel manifestation of the Faraday effect. Traditionally, the Faraday effect is the rotation of the polarization axis of linearly polarized light traversing a medium that arises from magnetically induced circular birefringence. In contrast, our approach seeks to realize and characterize a purely optically induced Faraday effect, achieved in the absence of an external magnetic field. Here, differential light shifts among magnetic sublevels, resulting from a circularly polarized dressing laser, give rise to birefringence and a measurable rotation of the probe polarization.

In particular, we demonstrate independent control of the $m = \pm 1$ substates of the ${}^3P_1$ manifold via optical dressing, without applying any magnetic field. This control establishes a new pathway for generating birefringence entirely through optical means. Beyond its fundamental interest, such an approach opens opportunities for precision control of atomic systems in quantum optics and metrology, where magnetic-field-free birefringence could be advantageous. Beyond Anderson localization, this study contributes to a broader effort in atomic physics: to achieve fine control over light–matter interactions in multi-level systems, advancing both fundamental understanding and practical applications ranging from optical lattice clocks to quantum simulators. The structure of this chapter is as follows. First, we derive the interaction Hamiltonian for the ${}^3P_1 \rightarrow {}^3D_1$ system under varying polarization and detuning. The subsequent section describes the experimental setup employed to induce and observe the light shift.

3.2 The AC Stark Effect: Background Theory

The AC Stark effect describes the modification of atomic energy levels under the influence of an oscillating electric field. One of the earliest clear demonstrations was reported by Autler and Townes in 1955, who observed near-resonant splitting of atomic states in a strong microwave field [55]. Their work, now known as the Autler-Townes effect, established the principle that coherent driving fields reshape atomic eigenstates. In the optical domain, the same mechanism manifests as frequency shifts of atomic resonances in the presence of off-resonant light, widely referred to as the light shift. In the dressed-state picture, these shifts and splittings emerge naturally as the eigenvalues of atom field hybrid states [56].

In the present work, we investigate the AC Stark shift of the ${}^3P_1$ manifold in bosonic ^{174}Yb, induced by near-resonant coupling to the ${}^3D_1$ manifold. Our objective is twofold: (i) to calculate the expected Stark shifts of the ${}^3P_1$ sublevels as a function of laser detuning and polarization, and (ii) to compare these predictions with spectroscopic measurements performed on the ${}^1S_0 \rightarrow {}^3P_1$ transition. A detailed understanding of these shifts is essential not only for precision spectroscopy but also for engineering

controlled optical potentials and for realizing anisotropic effects such as optically induced birefringence.

3.2.1 Theoretical Model

The light-shift (dressing) beam couples $^3P_1$ off-resonantly to $^3D_1$ near $\lambda_{\mathrm{LS}} = 1539$ nm, while a weak probe interrogates the $^1S_0 \to {}^3P_1$ line at $\lambda_g = 555.802$ nm to read out the induced shift. We define the detunings

$$\Delta_{\mathrm{LS}} \equiv \omega_{\mathrm{LS}} - \left(\omega_{^3D_1} - \omega_{^3P_1}\right), \qquad \delta \equiv \omega_{\mathrm{probe}} - \left(\omega_{^3P_1} - \omega_{^1S_0}\right), \tag{3.1}$$

with the usual convention that $\Delta_{\mathrm{LS}} < 0$ (> 0) denotes red (blue) detuning from $^3P_1 \to {}^3D_1$. The natural linewidths we use are

$$\frac{\Gamma_g}{2\pi} = 184 \text{ kHz} \quad \text{for} \quad {}^3P_1, \qquad \frac{\Gamma_{LS}}{2\pi} = 483 \text{ kHz} \quad \text{for} \quad {}^3D_1, \tag{3.2}$$

and the $^3D_1 \to {}^3P_1$ branching ratio is $\eta \approx 0.355$ [30]. When needed, we include the branching in an effective scattering rate for a given Zeeman channel $m \to m'$ as

$$\tilde{\Gamma}(m_j, m_{j'}) \;=\; \eta\Gamma_{LS}. \tag{3.3}$$

Figure 3.1 summarizes the $^3P_1$–$^3D_1$ level scheme.

In our work, we consider a seven-level system consisting of the ground state $^1S_0$, the three Zeeman sublevels of the $^3P_1$ manifold, and the three sublevels of the $^3D_1$ manifold:

$$|1\rangle = {}^1S_0 \quad \text{(reference ground state)}, \tag{3.4}$$
$$|2{-}4\rangle = {}^3P_1,\ m_j = -1, 0, +1, \tag{3.5}$$
$$|5{-}7\rangle = {}^3D_1,\ m_{j'} = -1, 0, +1. \tag{3.6}$$

Here, m_j denotes the projection of the total electronic angular momentum along the quantization axis. Although the $^1S_0$ state is not directly coupled by the light-shift (dressing) laser, we include it to define an absolute zero of energy and to facilitate later comparison with spectroscopic measurements.

The total Hamiltonian can be written as a sum of the bare atomic energies and the interaction with the laser field:

$$H = H_0 + H_{\mathrm{int}}(t), \tag{3.7}$$

where the free-atom Hamiltonian is

$$H_0 = \sum_{j=1}^{7} E_j \left|j\right\rangle \left\langle j\right|. \tag{3.8}$$

with the ground state taken as the zero of energy ($E_1 = 0$), the $^3P_1$ manifold centered at $E_{2,3,4} = \hbar\omega_{eg}$, and the $^3D_1$ manifold at $E_{5,6,7} = \hbar\omega_{fg}$.

where ω_{eg} and ω_{fg} correspond to the $^3P_1$ and $^3D_1$ energies relative to the $^1S_0$ ground state.

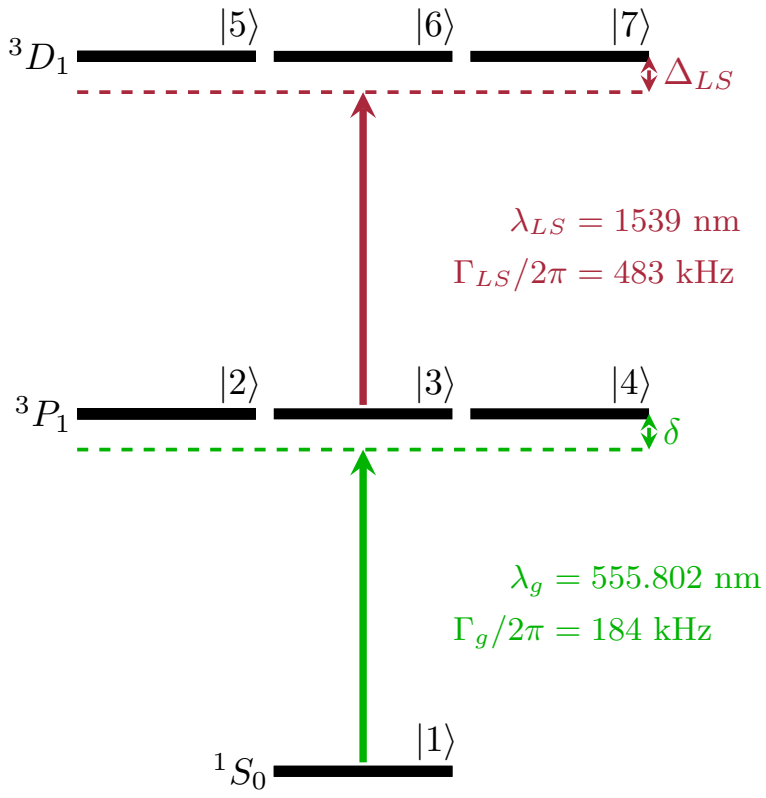

Figure 3.1: Level scheme and detuning conventions. The probe at $\lambda_g = 555.802$ nm addresses $^1S_0 \to {}^3P_1$ with linewidth $\Gamma_g/2\pi = 184$ kHz (green), while the dressing beam at $\lambda_{\mathrm{LS}} = 1539$ nm couples $^3P_1 \to {}^3D_1$ with linewidth $\Gamma_{LS}/2\pi = 483$ kHz (red) [33]. We define δ as the probe detuning and Δ_{LS} as the LS detuning. Horizontal black bars indicate the three Zeeman sublevels $m_j = \{-1, 0, +1\}$ in each J=1 manifold.

3.2.2 Interaction Hamiltonian

The dressing laser couples the $^3P_1 \to {}^3D_1$ transition. In the dipole approximation, the interaction Hamiltonian is given by

$$H_{\mathrm{int}}(t) = \sum_{i=2}^{4} \sum_{j=5}^{7} \hbar\, \Omega_{ij}(t)\, |i\rangle \langle j| + \mathrm{h.c.}, \tag{3.9}$$

where

$$\Omega_{ij}(t) = \frac{\vec{d}_{ij} \cdot \vec{E}(t)}{\hbar} \tag{3.10}$$

is the Rabi frequency for the dipole coupling between states i and j.

The dipole selection rules ($\Delta m_j = 0, \pm 1$) restrict the set of nonzero couplings. For a monochromatic field we write $\Omega_{ij}(t) = \Omega_{ij} e^{-i\omega_L t}$ and work with the constant complex amplitudes Ω_{ij}.

Physically, the structure of these couplings is determined by the laser polarization: linear polarization can be decomposed into spherical components ϵ_q with $q = -1, 0, +1$, which directly control the relative strength of allowed transitions.

3.2.3 Time-Dependent Schrödinger Equation

The atomic state can be expressed as a superposition of the seven levels:

$$|\psi(t)\rangle = \sum_{j=1}^{7} c_j(t)\,|j\rangle\,. \tag{3.11}$$

The Schrödinger equation then reads:

$$i\hbar\frac{d}{dt}\,|\psi(t)\rangle = H\,|\psi(t)\rangle\,. \tag{3.12}$$

Expanding in the $|j\rangle$ basis leads to a set of coupled differential equations for the amplitudes $c_j(t)$:

$$i\hbar\frac{d}{dt}c_i(t) = \sum_{j=1}^{7} H_{ij}(t)c_j(t). \tag{3.13}$$

Explicitly, the system is:

$$\begin{aligned}
i\hbar\dot{c}_1 &= 0\\
i\hbar\dot{c}_2 &= \hbar\omega_{eg}c_2 + \hbar\Omega_{25}(t)c_5 + \hbar\Omega_{26}(t)c_6\\
i\hbar\dot{c}_3 &= \hbar\omega_{eg}c_3 + \hbar\Omega_{35}(t)c_5 + \hbar\Omega_{36}(t)c_6 + \hbar\Omega_{37}(t)c_7\\
i\hbar\dot{c}_4 &= \hbar\omega_{eg}c_4 + \hbar\Omega_{46}(t)c_6 + \hbar\Omega_{47}(t)c_7\\
i\hbar\dot{c}_5 &= \hbar\omega_{fg}c_5 + \hbar\Omega^*_{25}(t)c_2 + \hbar\Omega^*_{35}(t)c_3\\
i\hbar\dot{c}_6 &= \hbar\omega_{fg}c_6 + \hbar\Omega^*_{26}(t)c_2 + \hbar\Omega^*_{36}(t)c_3 + \hbar\Omega^*_{46}(t)c_4\\
i\hbar\dot{c}_7 &= \hbar\omega_{fg}c_7 + \hbar\Omega^*_{37}(t)c_3 + \hbar\Omega^*_{47}(t)c_4
\end{aligned} \tag{3.14}$$

This 7×7 system describes the full coherent dynamics of the ${}^3P_1 \to {}^3D_1$ manifold under the action of the 1536 nm light shift laser with arbitrary laser polarization and detuning. In the far-detuned regime, the excited ${}^3D_1$ states can be adiabatically eliminated, resulting in an effective light shift on the ${}^3P_1$ manifold. This shift depends on the laser intensity, polarization, detuning, and the angular momentum structure of the states, producing both scalar and tensorial contributions that can be measured spectroscopically.

3.2.4 Rotating Frame and RWA

In this section, we model the dynamics induced solely by the light-shift (LS) laser at 1539 nm. The 556 nm laser is not included in this calculation; only the interaction between the ${}^3P_1 \to {}^3D_1$ manifold is considered. We restrict to the ${}^3P_1$–${}^3D_1$ subspace (six states). To remove the fast oscillatory terms, we transform into a rotating frame at the laser frequency ω_L. The detuning is defined as

$$\Delta_{\mathrm{LS}} = \omega_L - (\omega_{fg} - \omega_{eg}), \tag{3.15}$$

which is the difference between the laser frequency and the atomic two-photon resonance.

After applying the rotating wave approximation (RWA), the Hamiltonian takes a block-diagonal form:

$$H_{\mathrm{RWA}} = \hbar \begin{pmatrix} 0 & 0 & 0 & \frac{\Omega_{25}}{2} & \frac{\Omega_{26}}{2} & 0 \\ 0 & 0 & 0 & \frac{\Omega_{35}}{2} & \frac{\Omega_{36}}{2} & \frac{\Omega_{37}}{2} \\ 0 & 0 & 0 & 0 & \frac{\Omega_{46}}{2} & \frac{\Omega_{47}}{2} \\ \frac{\Omega_{25}^*}{2} & \frac{\Omega_{35}^*}{2} & 0 & -\Delta_{LS} & 0 & 0 \\ \frac{\Omega_{26}^*}{2} & \frac{\Omega_{36}^*}{2} & \frac{\Omega_{46}^*}{2} & 0 & -\Delta_{LS} & 0 \\ 0 & \frac{\Omega_{37}^*}{2} & \frac{\Omega_{47}^*}{2} & 0 & 0 & -\Delta_{LS} \end{pmatrix} \tag{3.16}$$

$$H_{\mathrm{RWA}} = \hbar \begin{pmatrix} 0_{3\times3} & V/2 \\ V^\dagger/2 & -\Delta_{LS} I_3 \end{pmatrix}, \qquad V \;=\; \Omega_0^2\, M \tag{3.17}$$

where $0_{3\times3}$ is the ${}^3P_1$ subspace, $-\Delta_{LS} I_3$ is the energy of the ${}^3D_1$ manifold in the rotating frame, and V is the 3×3 matrix of couplings between ${}^3P_1$ and ${}^3D_1$. In this rotating frame, the ${}^3P_1$ states lie at zero energy, while the ${}^3D_1$ states are offset by Δ_{LS}.

3.2.5 Adiabatic Elimination and Effective light Shifts

We write the state as a block vector

$$|\psi\rangle = \begin{pmatrix} \mathbf{c}_P \\ \mathbf{c}_D \end{pmatrix},$$

where $\mathbf{c}_P$ and $\mathbf{c}_D$ are 3-component amplitude vectors. The Schrödinger equation gives

$$i\dot{\mathbf{c}}_P = \frac{1}{2} V\, \mathbf{c}_D, \tag{3.18}$$

$$i\dot{\mathbf{c}}_D = \frac{1}{2} V^\dagger \mathbf{c}_P - \Delta_{LS} \mathbf{c}_D. \tag{3.19}$$

If the detuning is large compared with the couplings, $|\Delta_{LS}| \gg |\Omega_{ij}|$, then population in the ${}^3D_1$ manifold is negligible and its dynamics can be adiabatically eliminated. Setting $\dot{\mathbf{c}}_D \approx 0$ in (3.19) gives

$$\mathbf{c}_D \approx \frac{1}{2\Delta_{LS}} V^\dagger \mathbf{c}_P. \tag{3.20}$$

Substituting (3.20) into (3.18),

$$i\dot{\mathbf{c}}_P = \frac{1}{2} V \left(\frac{1}{2\Delta_{LS}} V^\dagger \mathbf{c}_P \right) = \frac{1}{4\Delta_{LS}} V V^\dagger \mathbf{c}_P.$$

Thus the effective Hamiltonian acting on the ${}^3P_1$ manifold is

$$H_{\mathrm{eff}}({}^3P_1) = \frac{\hbar}{4\Delta_{LS}} V V^\dagger, \tag{3.21}$$

For arbitrary polarization, each matrix element can be decomposed via Wigner–Eckart as,

$$\Omega_{mm'} = \Omega_0 \sum_{q=-1}^{+1} C^{1\, m_{j'}}_{1\, m_j;\, 1\, q}\, \epsilon_q\, \delta_{m_{j'},\, m_j+q}. \tag{3.22}$$

Where,

$$\Omega_0 = \frac{E_0}{\hbar} \left\langle {}^3D_1 \right\| \mathbf{d} \left\| {}^3P_1 \right\rangle, \qquad \sum_q |\epsilon_q|^2 = 1. \tag{3.23}$$

with E_0 is the electric-field amplitude of the dressing beam and $\langle {}^3D_1 \| \mathbf{d} \| {}^3P_1 \rangle$ is the reduced dipole matrix element, C_{ij} encodes the Clebsch–Gordan factor for the $J{=}1 \leftrightarrow J'{=}1$ link, and ϵ_q are the spherical polarization components of the dressing beam ($q = 0, \pm 1$).

$$M = \begin{pmatrix} C_{25}\epsilon_0 & C_{26}\epsilon_{+1} & 0 \\ C_{35}\epsilon_{-1} & C_{36}\epsilon_0 & C_{37}\epsilon_{+1} \\ 0 & C_{46}\epsilon_{-1} & C_{47}\epsilon_0 \end{pmatrix}, \qquad H_{\text{eff}} = \hbar \frac{\Omega_0^2}{4\Delta_{LS}} \Big(M\, M^\dagger \Big), \tag{3.24}$$

with M the dimensionless matrix in parentheses. For $J{=}1 \leftrightarrow J'{=}1$, all allowed Zeeman couplings share the same magnitude of the Clebsch–Gordan coefficient,

$$\left| C^{1 m_{j'}}_{1 m_j ; 1 q} \right| = \frac{1}{\sqrt{2}} \quad \text{for nonzero channels,} \tag{3.25}$$

and vanish otherwise, enforcing the selection rules shown in Fig. 3.2.

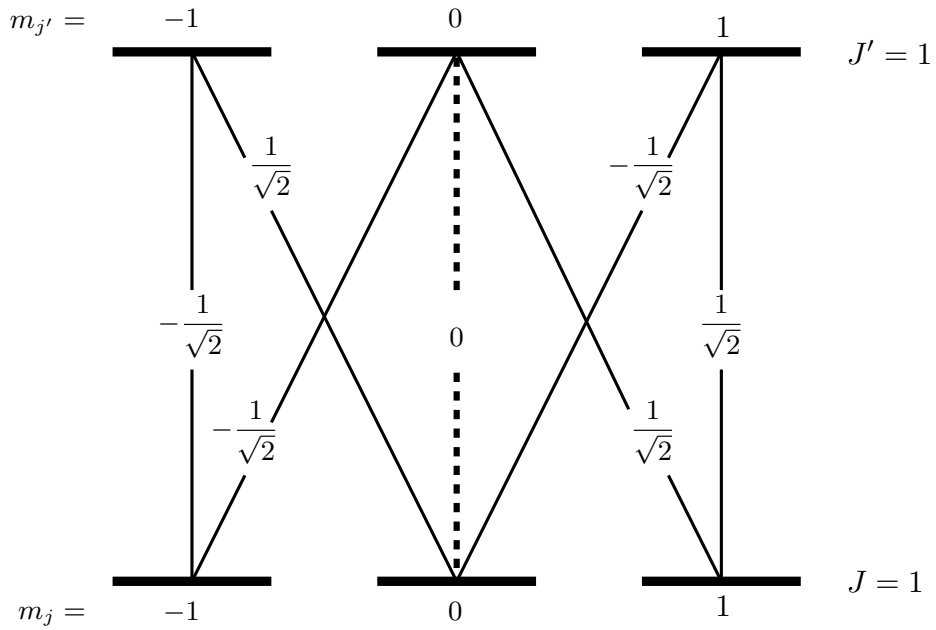

Figure 3.2: Zeeman-resolved coupling map for $J{=}1 \leftrightarrow J'{=}1$. Solid lines indicate allowed dipole couplings with Clebsch–Gordan magnitude $1/\sqrt{2}$, the π link $m_j{=}0 \to m_{j'}{=}0$ is forbidden.

Role of Polarization

The light-induced shift Hamiltonian for the ${}^3P_1$ manifold becomes:

$$H_{\text{eff}} = \frac{\hbar \Omega_0^2}{8\Delta_{LS}} \begin{pmatrix} |\epsilon_0|^2 + |\epsilon_{+1}|^2 & -\epsilon_0 \epsilon_{-1}^* & -\epsilon_{+1}\epsilon_{-1}^* \\ -\epsilon_{-1}\epsilon_0^* & |\epsilon_{-1}|^2 + |\epsilon_{+1}|^2 & -\epsilon_{+1}\epsilon_0^* \\ -\epsilon_{-1}\epsilon_{+1}^* & -\epsilon_{+1}^*\epsilon_0 & |\epsilon_{-1}|^2 + |\epsilon_0|^2 \end{pmatrix}. \tag{3.26}$$

The diagonal elements of H_{eff} correspond to the light shift of the individual Zeeman sublevels, while the off-diagonal elements describe polarization-induced mixing between the sublevels.

Polarization cases (explicit forms): In the experiment, the quantization axis is taken along the beam propagation direction ($\hat{z}$). A linearly polarized dressing field along the horizontal ($\hat{x}$) direction can be expressed in the spherical basis as

$$\hat{x} = \frac{1}{\sqrt{2}}(\hat{\epsilon}_{-1} - \hat{\epsilon}_{+1}) \quad \Rightarrow \quad \epsilon_{+1} = -\frac{1}{\sqrt{2}},\ \epsilon_{-1} = +\frac{1}{\sqrt{2}},\ \epsilon_0 = 0. \tag{3.27}$$

Substituting these components into Eq. (3.26)

$$H_{\text{eff}} = \frac{\hbar\Omega_0^2}{16\Delta_{LS}} \begin{pmatrix} 1 & 0 & 1 \\ 0 & 2 & 0 \\ 1 & 0 & 1 \end{pmatrix} \tag{3.28}$$

in the basis $\{|m_j = -1\rangle, |m_j = 0\rangle, |m_j = +1\rangle\}$. Only $\Delta m_j = \pm 1$ couplings are allowed; the $\Delta m_j = 0$ (π) transition vanishes for polarization perpendicular to the quantization axis. The nonzero off-diagonal elements $H_{13} = H_{31}$ represent coherent coupling between $|m_j = -1\rangle$ and $|m_j = +1\rangle$.

3.2.6 Eigenstates and Physical Picture

Diagonalizing H_{eff}

$$\begin{aligned} v_1 &= \tfrac{1}{\sqrt{2}}\left(|m_j = -1\rangle - |m_j = +1\rangle\right), & \lambda_1 &= 0, \\ v_2 &= |m_j = 0\rangle, & \lambda_2 &= \frac{\hbar\Omega_0^2}{8\Delta_{LS}}, \\ v_3 &= \tfrac{1}{\sqrt{2}}\left(|m_j = -1\rangle + |m_j = +1\rangle\right), & \lambda_3 &= \frac{\hbar\Omega_0^2}{8\Delta_{LS}}. \end{aligned}$$

This shows that within the $^3P_1$ manifold, the antisymmetric combination (v_1) remains unshifted, while the orthogonal symmetric combination of $|m = \pm 1\rangle$ together with $|m = 0\rangle$ experiences an identical energy shift proportional to Ω_0^2/Δ_{LS}. Physically, the light couples only to specific superpositions of Zeeman sublevels set by the polarization, leaving the dark state unaffected.

The corresponding frequency shift is

$$\Delta' = \frac{\Omega_0^2}{8\Delta_{LS}}, \tag{3.29}$$

With the standard two-level definition of saturation,

$$s \equiv \frac{I}{I_{\text{sat}}} = \frac{2\Omega_0^2}{\Gamma^2}, \tag{3.30}$$

Considering our multilevel system, the saturation intensity $\tilde{I}_{sat} = \frac{\pi hc}{3\lambda^3}\tilde{\Gamma}$, where $\tilde{\Gamma}(m_j, m_{j'}) = \eta\Gamma_{LS}$ with branching ratio $\eta = 0.355$. where Γ_{LS} is the natural linewidth of the $^3D_1$ state.

$$\Omega_0^2 = \frac{\tilde{\Gamma}^2}{2}\frac{I}{\tilde{I}_{\text{sat}}}, \tag{3.31}$$

Substituting into Eq. (3.29) gives

$$\Delta' = \frac{\tilde{\Gamma}^2}{16\,\Delta_{LS}}\frac{I}{\tilde{I}_{\text{sat}}}. \tag{3.32}$$

Sign and validity. The light shift is inversely proportional to the Δ_{LS}:

$$\Delta' \propto \frac{1}{\Delta_{LS}}\,. \tag{3.33}$$

Thus red detuning ($\Delta_{LS} < 0$) shifts the addressed eigenstates down in frequency (negative (Δ')), while blue detuning ($\Delta_{LS} > 0$) shifts them up. The derivation assumes the far-detuned, low-saturation regime

$$|\Delta| \gg \Gamma,\, \Omega_0\,, \qquad s \ll 1, \tag{3.34}$$

so that the population of $^3D_1$ is negligible and the power broadening/scattering is small.

3.3 Experimental Setup and Methods

Before presenting the measurements of the light shift versus power and detuning, we summarize the key elements of the apparatus and analysis workflow that connect the theoretical model to the data.

3.3.1 Light shifter (1539 nm) laser system: stabilization, detuning control, and power delivery

The dressing light is generated by a Koheras/NKT single-frequency single frequency distributed feedback (DFB) fiber seed laser at 1539 nm (nominal output ~ 40 mW), amplified by a BoostiK fiber amplifier to deliver up to 2 W at the experiment. After amplification, the light is delivered via polarization-maintaining (PM) fiber to the experiment. Typical available powers at the atoms range from 10 mW to 1 W. The specified free-running linewidth is < 0.1 kHz, ensuring phase coherence over all interrogation times used here.

Frequency tuning and stability. The fiber section of the Adjustik seed laser with the DFB grating and doped region is mounted under tension on a substrate. Coarse detuning Δ_{LS} is set by thermal tuning in response to both thermo-optic and physical changes in the optical path length, which means by changing the temperature of the substrate, resulting change in the temperature of the laser cavity and its length due to thermal contraction or expansion. whereas fine detuning and fast scans are performed via the internal piezo strain actuator [1]. For Koheras modules, temperature control of the laser substrate provides smooth tuning with mK-level stability (setpoint resolution $10^{-3}\,^\circ$C, typical stability $\sim 5 \times 10^{-3}\,^\circ$C over $\sim 10^3$ h), while piezo tuning gives fast, linear wavelength control with a responsivity of order 0.45 ppm/V and a mechanical resonance well above the bandwidths used here. Slow thermal drifts from the module case temperature are $\lesssim 0.1$–0.2 pm/°C.

Combined thermal and piezo actuation of the seed laser enables a 130 GHz detuning range centered at 1539.2020 nm. The total thermal tuning span is 1000 pm, corresponding to a frequency shift from -60 GHz to $+70$ GHz, or a wavelength shift from -490 pm to $+580$ pm relative to the center.

[1] See the NKT Photonics application note on Koheras fiber-laser wavelength tuning for details on thermal and piezo tuning coefficients, stability

In addition to front-panel control, the laser provides a differential input/output via the Wavelength ± pins on the rear interface, which couple directly to the internal piezo strain actuator. Applying a differential control voltage produces a linear frequency shift; a negative voltage results in a lower output wavelength, while a positive voltage results in a higher output wavelength. On the laser user interface, the Modulation Gain setting allows choosing between Narrow and Wide piezo gain. The Narrow gain setting reduces the actuator sensitivity, meaning that a larger voltage change is required to achieve the same frequency shift as in Wide gain. We work with Wide modulation gain, the responsivity is such that a voltage change of 7 mV corresponds to a frequency shift of about 12 MHz, setting the minimum resolvable piezo-based frequency scans accessible through the user interface.

Since no external wavelength meter was available at 1539 nm in our laboratory, the detuning was referenced directly to the Koheras internal display. The 12 MHz step size associated with Wide modulation gain, therefore defines the effective frequency resolution of all scans reported here. To identify the absolute resonance frequency, we relied on the trapped atoms themselves: when the light shift laser is tuned into resonance with the $^3P_1 \rightarrow {}^3D_1$ transition, the population of the $^3P_1$ state is rapidly depleted, and the green MOT fluorescence vanishes. This loss of fluorescence provided an unambiguous experimental signature of resonance, from which detunings Δ_{LS} were defined.

The output power at the atoms is set by controlling the BoostiK fiber amplifier that follows the Koheras seed. The amplifier is network-enabled, and we interfaced with it directly via Ethernet using a Python (`pip`) control library provided by NKT Photonics. This allows automated setting of the amplifier gain and, consequently, precise control of the light shift beam power from the sub-10 mW regime up to nearly 1 W delivered at the experiment. For experimental operation, the amplifier defines the overall available power envelope, while acousto-optic modulators (AOMs) in each beamline provide rapid power modulation and on/off switching. The AOMs are synchronized with the experimental sequence and offer an extinction ratio better than 10^{-4}, ensuring that the dressing beams can be effectively suppressed during preparation and detection stages. In this way, power adjustments can be synchronized with the timing sequence, guaranteeing reproducibility and stability across measurement runs.

3.3.2 LS power calibration and beam alignment inside the rectangular glass cell

Because the 1539 nm (LS) beam is invisible to the eyes and the rectangular vacuum cell is not AR-coated at this wavelength, we must account for multiple window losses and internal reflections. We therefore calibrate the power at the atoms from external measurements and the measured cell transmission.

Total transmission and per-surface model. Let T_{cell} be the measured *end-to-end* transmission of the cell (entrance window → exit window), obtained as

$$T_{\mathrm{cell}} \equiv \frac{P_{\mathrm{after}}}{P_{\mathrm{before}}}. \tag{3.35}$$

For our cell at 1539 nm we measure $T_{\mathrm{cell}} \simeq 0.60$. The beam traverses *four* uncoated glass–vacuum interfaces in total (two on entry, two on exit). Approximating the

interfaces as identical and neglecting bulk absorption over the short path, the per-surface transmission is

$$t \;=\; T_{\text{cell}}^{1/4}. \tag{3.36}$$

The atomic cloud is located approximately midway inside the cell, so the power that actually reaches the atoms (after two surfaces) is

$$P_{\text{atoms}} \;=\; P_{\text{before cell}}\, t^2 \;=\; P_{\text{before}}\, \sqrt{T_{\text{cell}}}. \tag{3.37}$$

With $T_{\text{cell}} \simeq 0.60$ we obtain

$$P_{\text{atoms}} \;\approx\; 0.77 \times P_{\text{before cell}}, \tag{3.38}$$

which is the factor we use throughout this work. This procedure avoids the need to measure power within the vacuum region, yet accurately accounts for the dominant loss mechanism at 1539 nm (uncoated windows). The corresponding on-axis peak intensity for a Gaussian beam is

$$I = \frac{2P_{\text{atoms}}}{\pi w^2}, \tag{3.39}$$

with w the $1/e^2$ waist. Equation (3.39) is used to convert the power to intensity for comparison with the theoretical scaling $\Delta' \propto I/\Delta_{LS}$.

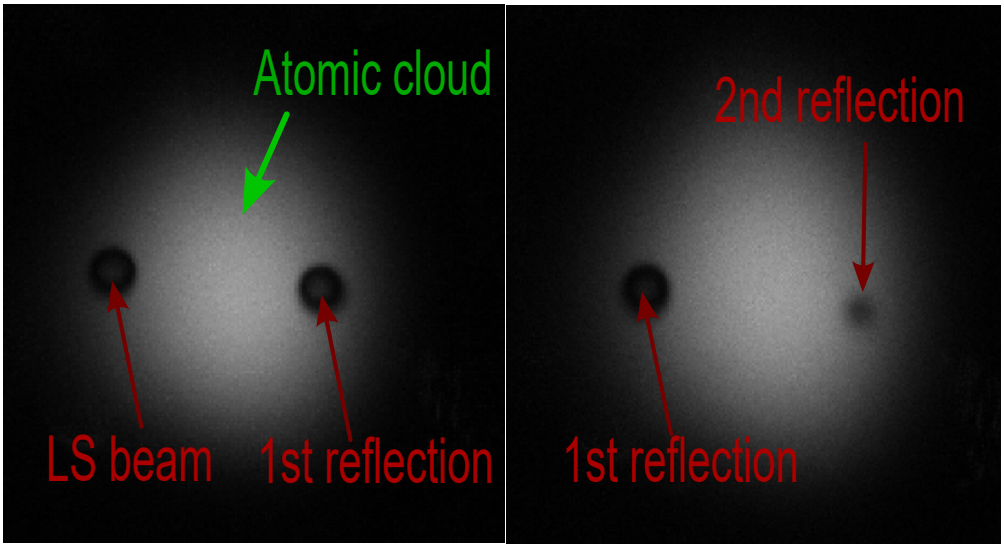

Figure 3.3: Fluorescence image of the atomic cloud taken along the propagation axis of the 1539 nm light-shift (LS) beam. The green probe beam excites the entire cloud, while the resonant LS beam simultaneously drives population into the $^3D_1$ state. This optical pumping results in a distinct dark hole at the LS beam position, clearly visible on the atomic cloud. Multiple faint reflections of the LS beam from the uncoated borofloat cell surfaces are also observed. This configuration provides a convenient way to align the LS beam onto the atomic sample and to quantify its effective transmission (approximately 66%) through the uncoated 1.5 cm thick borofloat cell.

Alignment using fluorescence "Holes". To align the light shift (LS) beam onto the atomic cloud (despite its invisibility to the eyes), we image the MOT fluorescence at 555.8 nm along the LS propagation axis while the LS light is on or near resonance.

In this condition, the LS beam optically pumps local atoms to $^3D_1$, suppressing green fluorescence and producing a well-defined dark hole at the beam location. Because the cell is uncoated, weak specular reflections from the internal faces generate secondary (displaced) dark spots as well. We use the primary dark spots to center the LS beam on the cloud and note the positions of the first reflections for later analysis of inhomogeneous light shifts (see Fig. 3.3). This method simultaneously verifies overlap and provides a qualitative check that ghost beams are not clipping the atom cloud.

3.3.3 Beam waist estimation of the LS beam

The waist of the 1539 nm light-shift (LS) beam cannot be directly measured at the position of the atoms inside the vacuum cell. Instead, the beam waist was estimated using a free-space mirror substitution method. The distance L from the fiber collimator output to the atom plane (cell center) was measured.

A mirror was then inserted to reflect the LS beam, and its transverse profile was recorded on a camera[2] placed at the same effective distance L.

The recorded beam profile was fitted with a two-dimensional Gaussian distribution. From the fit, we extracted the $1/e^2$ beam radius at the atom plane,

$$w(z = 0.36 \text{ m}) = 1.05 \pm 0.04 \text{ mm}. \tag{3.40}$$

The uncertainty was calculated from the covariance matrix of the fitted function. We measured the transverse $1/e^2$ beam radii at three axial positions and fitted them to the Gaussian-beam propagation law,

$$w(z) = w_0\sqrt{1 + \left(\frac{z - z_0}{z_R}\right)^2}, \qquad z_R = \frac{\pi w_0^2}{\lambda}, \tag{3.41}$$

with $\lambda = 1539$ nm. The measured radii were $(z_1, w_1) = (0.35 \text{ m}, 1.0 \text{ mm})$, $(z_2, w_2) = (0.40 \text{ m}, 1.2 \text{ mm})$, and $(z_3, w_3) = (0.48 \text{ m}, 1.66 \text{ mm})$. A least-squares fit yields

$$w_0 = 0.095 \pm 0.009 \text{ mm}, \qquad z_0 = 0.161 \pm 0.023 \text{ m}, \tag{3.42}$$

and a Rayleigh length $z_R = \pi w_0^2/\lambda \approx 18.44$ mm.

The LS beam was collimated using a fiber collimator [3] at the output of the fiber. We define the coordinate $z = 0$ at the center of the collimator lens, and measure distances along the beam propagation axis from this point.

At the atom plane (taken to be $z = 0.36$ m) the fitted beam radius is

$$w(0.36 \text{ m}) = 1.03 \pm 0.034 \text{ mm}. \tag{3.43}$$

The fitted radius at the atom plane with the mirror-substitution measurement, $w(z = 0.36 \text{ m}) = 1.03 \pm 0.034$ mm, is consistent with the Gaussian-beam propagation law 1.05 ± 0.04 mm, validating the Gaussian-beam model and fit parameters.

[2] Allied Vision Alvium 1800 U-030 SWIR camera, 5 μm pixel size.

[3] Schäfter & Kirchhoff collimator (focal length 8 mm, doublet optics, AR-coated 980–1550 nm, Ø12 mm housing)

3.3.4 Detection Methods and Resonance Shift Extraction

For all light-shift measurements, an ensemble of approximately 10^8 ^{174}Yb atoms was prepared in a standard MOT configuration, as described in Chapter 2. The dressing beam was overlapped with the atomic cloud, and a weak probe beam resonant with the intercombination line $^1S_0 \rightarrow {}^3P_1$ ($\lambda_g = 555.8$ nm, $\Gamma_g/2\pi = 184$ kHz) coonter-propagating to the light shift (dressing) beam. The light shift of the $^3P_1$ manifold is probed using a weak green probe beam while a light shift beam interacts with the atoms. The transmitted probe is imaged by a CCD camera to extract the spectroscopic signal. The setup is shown in Figure 3.4.

The probe beam was expanded to a diameter ~ 2 mm larger than the MOT size (a typical cloud size full width half maximum of 0.9 mm) to ensure nearly uniform illumination of the ensemble. This ensured that the measured fluorescence reflected the intrinsic resonance properties rather than local intensity variations. The probe power was chosen such that the scattering rate was sufficient for high signal-to-noise fluorescence detection, while remaining below the saturation regime to avoid power broadening beyond the natural width. All the light shift measurements are taken at relatively low optical thickness $b_{0,g} \approx 2 - 5$, and the reason is explained in the next subsection.

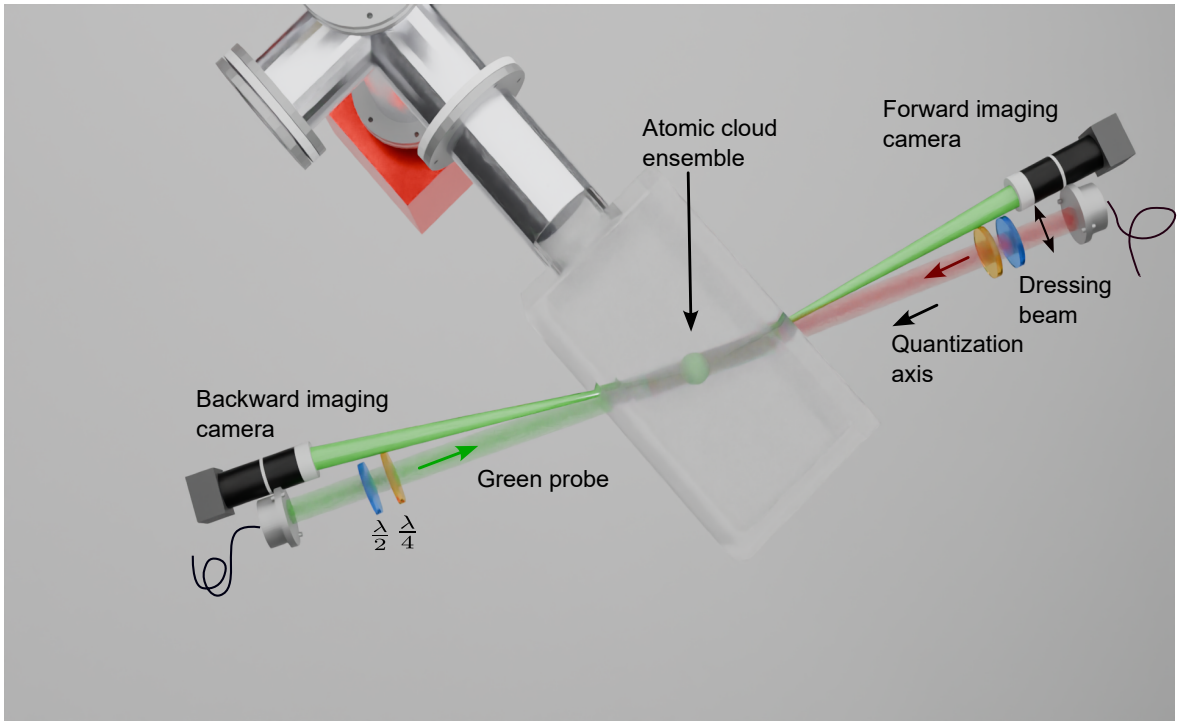

Figure 3.4: Experimental setup for measuring the light shift. The green probe beam passes through the atomic sample, and fluorescence is imaged by a camera in the forward and backward directions, respectively, to the probe beam. A dressing beam induces the light shift on the $^3P_1$ manifold.

Experimental Timing Sequence

The measurement sequence, illustrated in Fig. (3.5), consisted of the following stages:

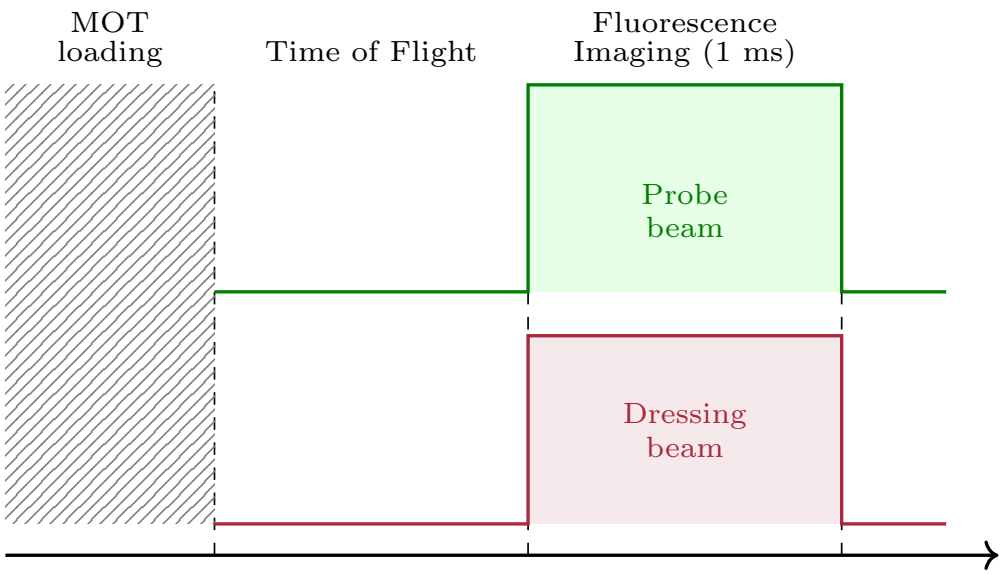

Figure 3.5: Chronogram of the experimental sequence used for the light shift and Faraday rotation measurements. The timing of the main control signals is shown: preparation of the atomic sample, application of the 1539 nm light-shift (LS) pulse with controlled detuning and power, and the subsequent probing of the $^3P_1$ state with the green laser. The shaded regions indicate detection windows during which fluorescence images are acquired.

- **MOT Loading:** An ensemble of approximately 10^8 ^{174}Yb atoms was prepared in a standard MOT configuration, as described in Chapter 2.
- **Time-of-Flight Expansion:** The atoms were released and allowed to expand for 0.2–30 ms. Longer expansion times reduced optical density.
- **Light shift Beam and Probe Beam:** Both beams are turned on together for 1 ms during the detection phase. A linearly polarized light shift (dressing) beam at 1539 nm was applied with fixed detuning Δ_{LS} and power P. The probe beam is used for scanning across resonance to record the fluorescence signal polarized at 45° to probe all the states.
- **Probe Scan and Detection:** To measure the resonance profile, a weak 555.8 nm probe beam was scanned across the $^1S_0 \rightarrow {}^3P_1$ transition. At each probe frequency, a new MOT was prepared, and the resulting fluorescence was recorded. In Figures 3.6 and 3.8, each panel shows the recorded fluorescence from a fresh MOT loading. Each scan produced a spectrum of integrated counts versus probe detuning.

3.3.5 Imaging Geometry and Setup

The experimental geometry is shown in Fig. 3.4. Fluorescence was collected simultaneously in two near-collinear directions at ±10° relative to the probe propagation axis using CCD cameras. The solid angle of collection of the fluorescence is 0.004 sr for both measurements.

For each probe frequency step, the CCD image was integrated over the whole region shown in Fig. 3.6 and 3.8. Since the light shift beam had a finite Gaussian waist

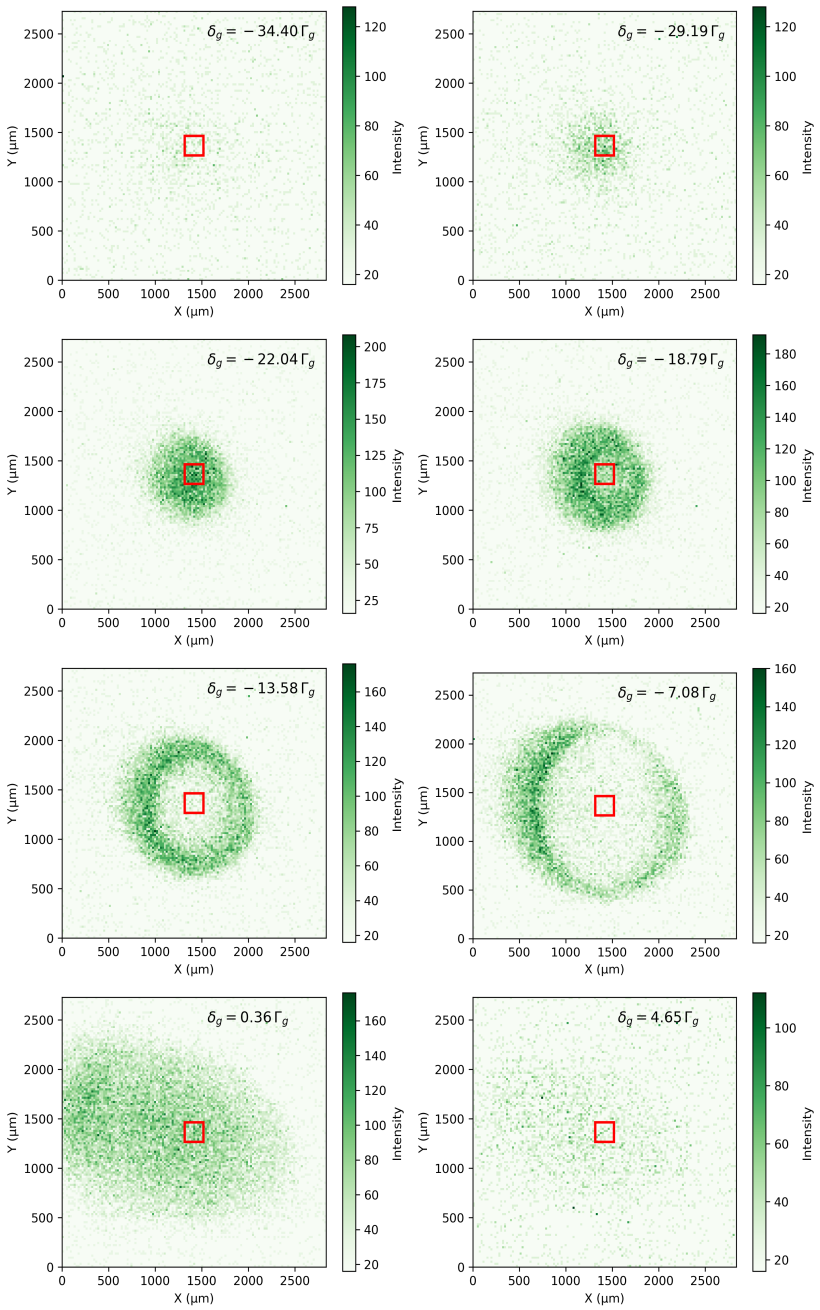

Figure 3.6: **Backward fluorescence images used for light-shift spectroscopy.** The probe frequency was scanned across the dressed $^3P_1$ resonance and bare resonance while recording fluorescence with a CCD camera. Each panel corresponds to a different probe detuning. The red square marks the 210×210 μm^2 region of interest (ROI) used in the analysis, chosen to minimize inhomogeneities from the Gaussian profile of the light shift beam. Integrated counts within the ROI were used to construct spectra, which were subsequently fitted with Voigt profiles to extract the local light shift and linewidth.

($w \sim 1$ mm), the intensity was not perfectly homogeneous across the cloud with FWHM (~ 1 mm). To mitigate spatial inhomogeneities of the dressing beam, we restricted the analysis to a central region of interest (ROI) indicated by the red square 10×10 pixels (typically corresponding to the 210×210 μm^2) region of the atomic ensemble,

corresponding to the most uniform intensity portion of the probe volume. This choice balances signal-to-noise while minimizing systematic shifts from intensity gradients across the MOT.

The summed counts within the ROI as a function of probe frequency provide the effective fluorescence spectrum Fig. 3.7. The data were averaged over multiple experimental runs to reduce statistical noise, and the error bars correspond to the standard deviation of repeated measurements. The lineshape was fitted using a Voigt profile. The fitted line center directly yields the local light shift Δ_{LS}, while the ROI restriction minimizes systematic broadening due to the Gaussian inhomogeneity of the dressing beam across the atomic cloud.

From both the forward- and backward-detection cameras, we extracted the integrated fluorescence as a function of probe detuning. For each probe frequency step, a CCD exposure was taken with the same integration time for 1 ms, and the fluorescence counts were summed over a fixed central region of interest (ROI) corresponding to the atomic cloud. This yields a direct measure of the total scattered light.

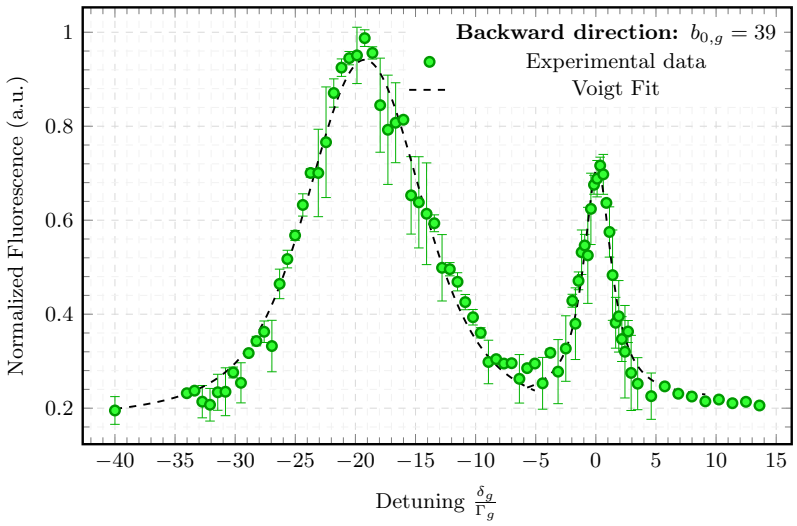

Figure 3.7: Normalized diffuse fluorescence is collected in the backward direction from the atomic cloud with a light shift beam applied at $b_{0,g} \approx 39$. The circles show experimental data, and the dashed line is a Voigt-profile fit. Error bars represent the standard deviation obtained from repeated measurements under identical conditions. The camera is positioned at $\sim 10^\circ$ relative to the probe propagation axis. Peaks appear at both the bare $^3P_1$ resonance and the light-shifted resonance, reflecting enhanced scattering when the probe frequency is resonant with either transition. The analysis is restricted to the central 210×210 μm^2 region of the cloud to minimize the effect of dressing-beam inhomogeneity. The relative amplitudes of the two peaks differ because the probe couples with different strengths to the bare and LS-dressed transitions.

At high optical depth ($b_0 \approx 39$), the recorded fluorescence in both the forward and backward directions originates mainly from multiple scattering of the probe light within the atomic cloud. Figures 3.7 and 3.9 show typical spectra recorded in the presence of a light shift beam in forward and backward direction, respectively. Two peaks are observed: one at the bare $^3P_1$ resonance and another at the light-shifted resonance induced by the light shift beam. In practice, the forward and backward fluorescence images of the atomic cloud were acquired simultaneously.

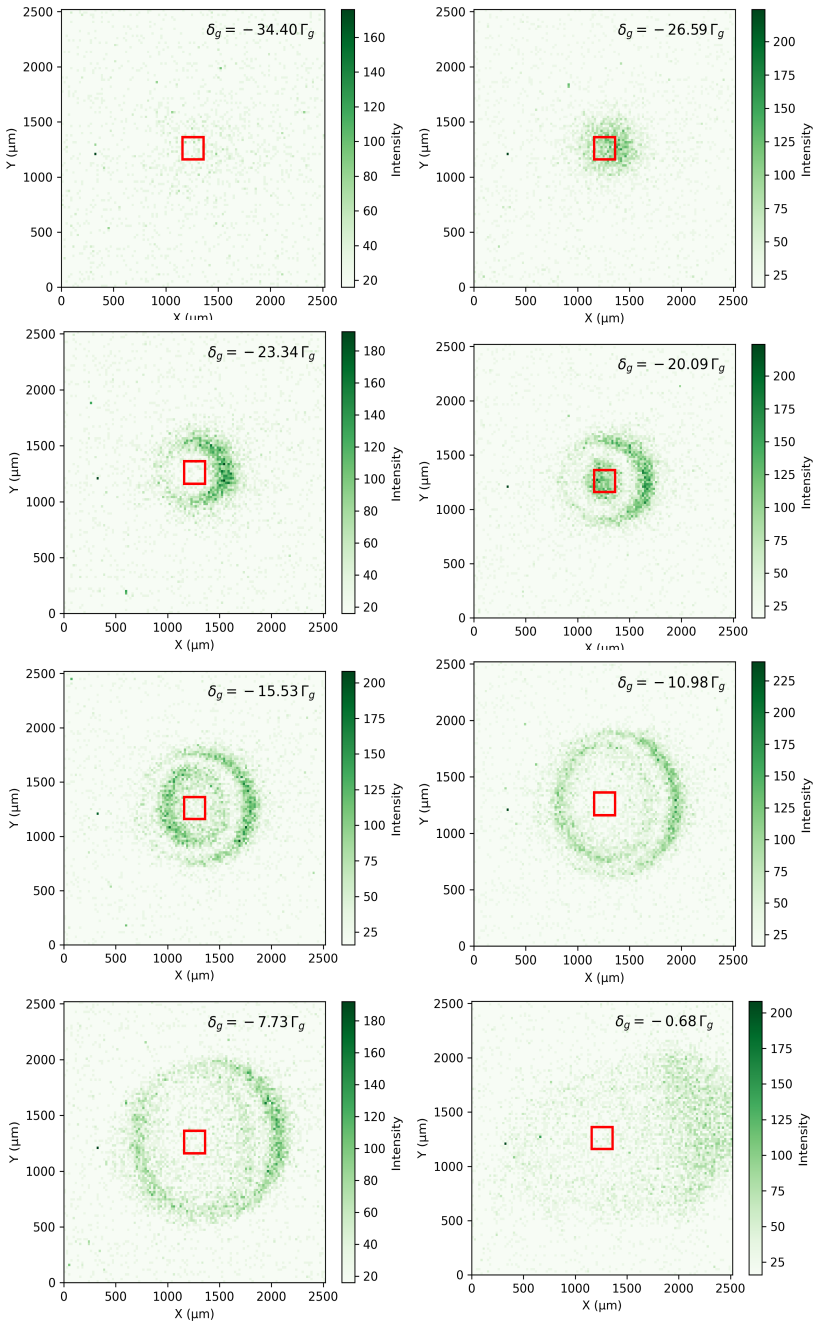

Figure 3.8: **Forward fluorescence images.** In the forward collection geometry, the probe beam is transmitted through the atomic cloud, and the resulting fluorescence is detected with a CCD camera. Each panel corresponds to a different probe detuning. Here, the recorded signal includes interference between the transmitted probe and the coherent forward-scattered light. This produces characteristic dips at both the bare resonance and the LS-dressed resonance, due to multiple scattering in dense media [45]. The red square again marks the 210×210 μm^2 region of interest used to extract spectra.

The overall spectral shape, including the reduction of signal near resonance and the broad double-peaked structure in the forward direction (3.9), reflects the behavior of diffuse transmission in optically thick atomic media [45]. As discussed in that work, these features arise from the variation of optical thickness with detuning and the

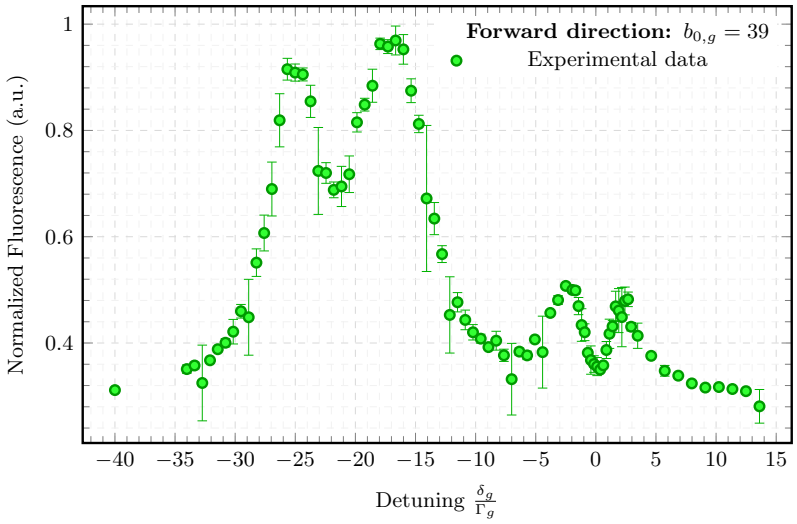

Figure 3.9: Forward-collected fluorescence from the atomic cloud at high optical depth ($b_{0,g} \approx 39$). The circles show experimental data. Error bars represent the standard deviation obtained from repeated measurements under identical conditions. Unlike the backward direction, where fluorescence peaks on resonance, the forward signal shows dips at both the free-space $^3P_1$ resonance and at the LS-dressed resonance, reflecting the behavior of diffuse transmission in optically thick atomic media that suffer from multiple scattering [see text for details] [45]. Restricting the analysis to the central 210×210 μm region ensures a nearly uniform dressing intensity across the probed volume. The relative amplitudes of the two peaks differ because the probe couples with different strengths to the bare and LS-dressed transitions.

redistribution of multiply scattered light between forward and backward directions. Because the light mean free path $\ell(\delta)$ and hence the optical thickness $b(\delta)$ vary strongly with detuning $b(\delta_g) = \frac{b_0}{1+(\frac{2\delta_g}{\Gamma_g})^2}$ [45], each direction (forward and backward) weights the detuning dependence differently.

At high optical depth, $b_0 \approx 39$, the probe beam in the forward direction (diffuse transmission) undergoes many scattering events, typically originating from deeper inside the medium. Thus, near resonance the medium is opaque (large b), and far off resonance it becomes transparent (small b). The diffuse transmission $T_d(\delta)$ shows a double-peaked structure, minimal at resonance and maximal at detunings where the optical thickness drops to about $b \simeq 1.1$. While in the backward direction (diffuse reflection), photons are recorded that scatter once or a few times near the front surface. The diffuse reflection $R_d(\delta)$ is fitted with a Voigt profile, peaking at resonance (more reflection when the medium is opaque). Therefore, the "double-bump" in transmission (forward direction) and the single Voigt profile in reflection (backward direction) arise purely from how photons propagate through a resonant medium of varying optical thickness.

In the presence of the LS beam, the original Zeeman sublevels of $^3P_1$ are mixed and split into new dressed states whose composition depends on the polarization and intensity of the dressing field. Because the probe is linearly polarized, it does not couple equally to these dressed states: its effective Rabi frequency is proportional to the overlap between the probe polarization vector and the dressed-state eigenvectors. As a result, the probe drives the bare transition (in the absence of the LS beam) with a

different transition strength than it drives the LS-dressed transition (in the presence of the dressing field), leading to the different peak heights and relative amplitudes observed in the figures 3.7 and 3.9.

Measurement of the Light Shift

Having established in the previous section that both forward and backward fluorescence provide reliable in-situ probes of the dressed-state resonance. To avoid the multiple-scattering effects that become significant at high optical density, we now focus exclusively on fluorescence detected in the backward direction. All measurements presented in this section were performed at a temperature of 14 μK. To measure the light shift, we perform fluorescence spectroscopy on the $^1S_0 \rightarrow {}^3P_1$ transition. For each setting of detuning and light-shift power, the probe laser frequency is scanned across the resonance. By choosing the appropriate probe polarization, we selectively address either the unshifted (bare) transition or the light-shifted dressed state created by the LS beam.

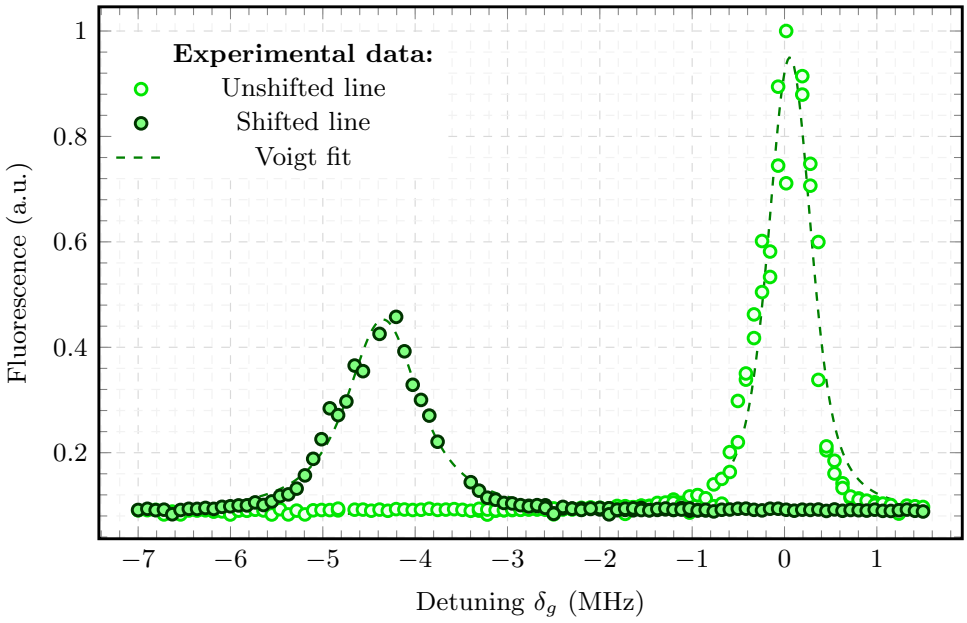

Figure 3.10: Fluorescence spectra of the $^1S_0 \rightarrow {}^3P_1$ transition recorded using two different probe polarizations. The dressing beam remains on during both measurements. Each dataset is fitted with a Voigt profile (dashed lines), from which the resonance frequency is extracted. The light shift Δ' is defined as the difference between the two fitted line centers. The relative amplitudes of the two peaks differ because the probe couples with different strengths to the bare and LS-dressed transitions. The dark green curve shows no peak at $\delta_g = 0$ because the probe polarization was chosen to address only the light-shifted transition.

A typical dataset consists of normalized fluorescence counts as a function of probe detuning δ_g (see Fig. 3.10). The bright-green points correspond to the reference spectrum obtained using a probe polarization that addresses the bare (unshifted) transition, providing the unperturbed resonance at frequency $\delta_g = 0$. The darker-green points show the spectrum recorded with an orthogonal probe polarization that couples

predominantly to the LS-dressed state. The resonance is visibly displaced, as expected from the AC Stark effect. The spectral profile is well described by a Voigt function, which accounts for both the Lorentzian natural linewidth and Gaussian contributions from residual Doppler broadening:

$$F(\delta) = a \cdot \text{Voigt}(\delta - \delta_0; \sigma, \gamma) + \text{offset}, \tag{3.44}$$

where δ_0 is the resonance frequency shift, σ is the Gaussian width, γ is the Lorentzian width, a is the amplitude, and offset is a background offset.

The Lorentzian component γ is dominated by the natural linewidth ($\Gamma_g/2\pi$ = 184 kHz), while the Gaussian part σ captures Doppler broadening due to finite temperature, inhomogeneous probe intensity, and technical laser linewidth.

Both datasets in Figure. 3.10 are fitted with Voigt profiles (dashed lines), and the frequency difference between the two fitted centers defines the light shift:

$$\Delta'(\Delta_{\text{LS}}, P) = \nu(\Delta_{\text{LS}}, P) - \nu_{g,0}. \tag{3.45}$$

where $\nu(\Delta_{\text{LS}}, P)$ is the resonance obtained under dressing conditions. By repeating this procedure for multiple LS powers and detunings, a complete dataset $\{\Delta'(P, \Delta_{\text{LS}})\}$ was assembled and discussed in the next section.

3.3.6 Error Estimation in the light shift measurement using the Bootstrapping method

The statistical uncertainties from nonlinear least-squares fits, using a Voigt$(\delta - \delta_0; \sigma, \gamma)$ function, which provides estimates for δ_0, σ, and Γ, were found to be underestimated because they assume uncorrelated, purely Gaussian noise in each data point. To obtain robust error bars, we used a random sampling method called Bootstrap [57].

- From the original fluorescence spectrum (δ_i, F_i) corresponding to each experimental data point as shown in Figure 3.10. We have drawn about fifty bootstrap samples by randomly resampling the original points with replacement.
- Each bootstrap sample was fitted with the Voigt function, yielding a set of fitted resonance centers $\{\delta_0^{(j)}\}$.
- The average of this set of values was taken as the best estimate of the resonance position, and the spread of the distribution (its standard deviation) defined the statistical uncertainty σ_{δ_0} [58].

$$\bar{\delta}_0 = \frac{1}{N}\sum_{j=1}^{N} \delta_0^{(j)}, \quad \sigma_{\delta_0} = \sqrt{\frac{1}{N-1}\sum_{j=1}^{N}\left(\delta_0^{(j)} - \bar{\delta}_0\right)^2}.$$

For the Figure 3.10, the extracted resonance center is given by $\Delta' = -4.41 \pm 0.03$ MHz representing the measured light shift. With 50 bootstraps, the error bars are about 2–3 times larger than those from the least-squares Voigt fit. The line-width of the shifted spectrum is found to be 0.389 ± 0.02 MHz.

3.3.7 Inhomogeneous Broadening Due to Imaging Geometry

Inhomogeneous broadening occurs when atoms in the cloud experience different local light intensities, leading to a spatially varying light shift.

In our experiment, the atomic cloud has a Gaussian spatial density distribution with an rms radius $\sigma = 500$ μm, while the dressing beam has a Gaussian intensity profile with a $1/e^2$ waist of $w_0 = 1$ mm.

$$I(r) = I_0\, e^{-2r^2/w_0^2}, \tag{3.46}$$

where I_0 is the peak intensity and w_0 is the $1/e^2$ waist of the beam.

Because the beam is tilted by an angle θ relative to the imaging axis, the intensity experienced by atoms along the line-of-sight (LOS) direction varies as

$$I(z) = I_0\, e^{-2(z\sin\theta)^2/w_0^2}, \tag{3.47}$$

where z is the coordinate along the imaging direction.

The atomic density distribution is also Gaussian,

$$n(z) \propto e^{-z^2/(2\sigma^2)}, \tag{3.48}$$

with σ the rms width of the atomic cloud. The local light shift is proportional to the local intensity,

$$\Delta(z) = \Delta_0\, \frac{I(z)}{I_0}, \tag{3.49}$$

where Δ_0 is the maximum light shift at the beam center.

To quantify how much the dressing-beam intensity varies along the line of sight (LOS) due to the combined effects of the Gaussian beam profile and the finite extent of the atomic cloud. Since the detected fluorescence originates from atoms distributed along the imaging axis, the relevant quantity is not the local intensity $I(z)$ but its density-weighted average. We therefore define the mean intensity along the LOS as

$$\langle I\rangle_{\mathrm{LOS}} = \frac{\displaystyle\int_{-\infty}^{+\infty} n(z)\, I(z)\, dz}{\displaystyle\int_{-\infty}^{+\infty} n(z)\, dz}, \tag{3.50}$$

The mean intensity experienced by atoms contributing to a pixel signal is the density-weighted average

$$\frac{\langle I\rangle_{\mathrm{LOS}}}{I_0} = \frac{1}{\sqrt{1 + \frac{4\sigma^2}{w_0^2}\sin^2\theta}}, \tag{3.51}$$

To estimate the inhomogeneous broadening associated with the intensity variation along the LOS, we compute the RMS intensity fluctuation

$$\sigma^2_{I,\mathrm{LOS}} = \langle I^2\rangle_{\mathrm{LOS}} - \langle I\rangle^2_{\mathrm{LOS}}, \tag{3.52}$$

where

$$\langle I^2\rangle_{\mathrm{LOS}} = \frac{\displaystyle\int n(z)\, I(z)^2\, dz}{\displaystyle\int n(z)\, dz} = I_0^2\, \frac{1}{\sqrt{1 + 8\sigma^2\sin^2\theta/w_0^2}}. \tag{3.53}$$

Combining these two expressions yields the RMS fractional intensity variation

$$\frac{\sigma_{I,\mathrm{LOS}}}{I_0} = \sqrt{\frac{1}{\sqrt{1+\frac{8\sigma^2}{w_0^2}\sin^2\theta}} - \frac{1}{1+\frac{4\sigma^2}{w_0^2}\sin^2\theta}}. \tag{3.54}$$

Substituting the parameters above with $\theta = 10^\circ$ gives

$$\frac{\sigma_{I,\mathrm{LOS}}}{I_0} \approx 0.0204.$$

Because the light shift scales linearly with intensity, $\Delta' = \alpha I$, this corresponds to a Gaussian distribution of light shifts with a full width at half maximum (w_G) of

$$w_G = 2.355\,\Delta_0\,\frac{\sigma_{I,\mathrm{LOS}}}{I_0}. \tag{3.55}$$

For an on-axis light shift of $\Delta_0 = 4$ MHz, this yields

$$w_G \approx 2.355 \times 4\ \mathrm{MHz} \times 0.0204 \approx 0.19\ \mathrm{MHz}. \tag{3.56}$$

The total observed spectral line is therefore a convolution of this Gaussian broadening with the natural Lorentzian linewidth of the ^{174}Yb $^3P_1$ state, $\Gamma_g = 0.184$ MHz. The resulting Voigt linewidth can be well approximated by the empirical expression given by [59]:

$$w_V \approx 0.5325\,\Gamma_L + \sqrt{0.2543\,\Gamma_L^2 + w_G^2}\,, \tag{3.57}$$

where Γ_L is the Lorentzian FWHM. Substituting $\Gamma_L = 0.184$ MHz and $w_G = 0.19$ MHz gives

$$w_V \approx 0.31\ \mathrm{MHz}, \tag{3.58}$$

corresponding to an apparent linewidth about 1.7× the natural width Γ_g.

This show that the inhomogeneous broadening is much larger than Γ_g. The linewidth increases with increasing light shift.

3.3.8 Polarization-Dependent Light Shift Measurements

A striking feature of the $^3P_1 \to {}^3D_1$ dressing scheme is its polarization sensitivity.

Figure 3.11 shows the measured light shift as a function of the dressing laser detuning Δ_{LS} around the $^3P_1 \to {}^3D_1$ transition for two different probe polarizations. The quantization axis is chosen along the vertical direction, along the dressing beam polarization.

Two distinct cases are compared:

- **Horizontal probe polarization (red triangles)**: The probe couples predominantly to the $|m = \pm 1\rangle$ sublevels of the $^3P_1$ manifold, which are symmetrically coupled by the light shift beam. In this configuration, the observed shift corresponds to the average light shift of the dressed symmetric state, leading to a strong dependence $\propto 1/\Delta_{\mathrm{LS}}$.
- **Vertical probe polarization (green circles)**: Here, the probe addresses primarily the $|m = 0\rangle$ sublevel. Since the light shift laser with vertical polarization does not couple $|m = 0\rangle$ to $^3D_1$ (Clebsch–Gordan coefficient vanishes), the $|m = 0\rangle$ state forms a *dark state* with respect to the LS field. Consequently, the measured shift is strongly suppressed, and the data show near-zero light shift across the detuning range.

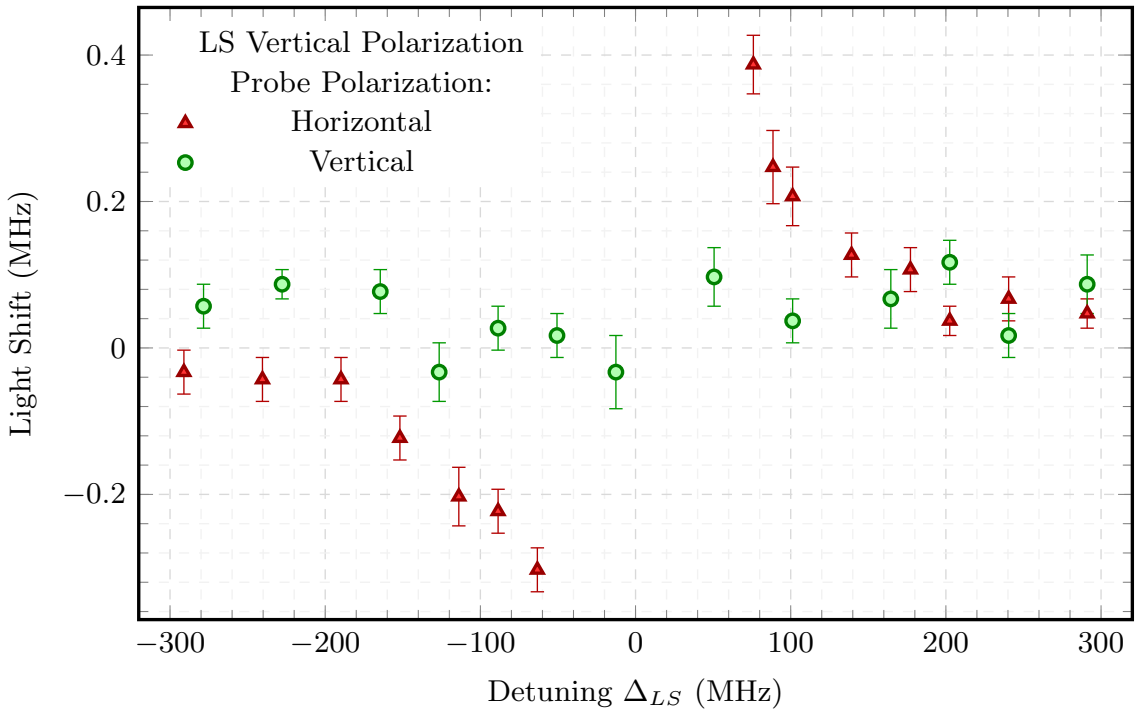

Figure 3.11: Polarization dependence of the light shift of the $^3P_1$ state. The measured light shift is shown for horizontal (red triangles) and vertical (green circles) probe polarizations. The polarization of the light shift beam is vertical. For horizontal polarization, the probe overlaps with the shifted states of the effective Hamiltonian, resulting in the expected dispersive dependence on detuning. In contrast, for vertical polarization, the probe couples predominantly to the dark state ($\lambda_1 = 0$), which remains unshifted, leading to near-vanishing shifts. The clear dichotomy between the two polarizations directly demonstrates the role of Clebsch–Gordan couplings in the $J = 1 \to J' = 1$ manifold and confirms the multi-level structure underlying the Stark effect.

Error bars represent the bootstrapped uncertainties of the resonance center fits. The clear contrast between horizontal and vertical probe polarizations directly demonstrates the state-selective nature of the light shift Hamiltonian [Eq. (3.28)] and provides an experimental verification of the dark-state eigenvalue $\lambda_1 = 0$ identified in our theoretical model. This polarization dependence highlights how atomic sublevels can be selectively shifted or protected from light shifts by appropriate choices of geometry and polarization, and it **highlights the critical role of polarization in tailoring light shifts in multi-level atomic systems**.

Choice of quantization axis. Throughout this chapter, unless stated otherwise, we assume the quantization axis is defined along the propagation direction of the LS beam. This choice was used in the derivation of the effective Hamiltonian [Eq. (3.28)] and in the discussion of the light-shift eigenstates.

For the polarization-dependent measurements shown in Figure 3.11, however, it is more natural to choose the quantization axis along the LS polarization (vertical). In this basis, the $|m = 0\rangle$ sublevel of the $^3P_1$ manifold is dark to the vertical LS polarization, and therefore the vertical probe predominantly interrogates this unshifted state. Conversely,

the horizontal probe couples to the light-shifted symmetric superposition of $|m = \pm 1\rangle$.

This alternative quantization-axis choice does not alter the underlying physics: in both descriptions, one eigenstate remains unshifted (dark), while the other two are shifted by $-\hbar\Omega_0^2/(8\Delta_{LS})$. It simply provides a clearer physical interpretation of the polarization-resolved measurements.

In summary, these polarization-resolved measurements confirm the theoretical picture of bright and dark states within the $^3P_1$ manifold, and demonstrate how specific sublevels can be rendered immune or highly sensitive to the AC Stark effect depending on geometry. This not only highlights the critical role of polarization in tailoring light shifts in multi-level atomic systems, but also establishes a solid foundation for the next step: exploring how the magnitude of the light shift scales with the dressing-beam intensity at fixed polarization.

3.4 Experimental Verification of Light-Shift Scaling

To test the perturbative prediction of Eq. (3.32), we measured the light shift Δ' of the $^3P_1$ manifold as a function of the dressing-beam power P at several detunings Δ_{LS} from the $^3P_1 \rightarrow {}^3D_1$ transition.

As shown in Fig. 3.12, the measured light shift varies linearly with the light shift beam power P at each detuning. This behavior follows the expected relation $\Delta' \propto I/\Delta_{\mathrm{LS}}$. The slope changes sign with Δ_{LS}, in agreement with the symmetry predicted for the light-shift effect. The small offsets observed in the linear fits may result from residual probe-induced shifts and gradual drifts in the frequency reference. Their magnitudes are small compared to the linear slopes and do not affect the extracted scaling.

For a fixed beam waist, the theoretical scaling law derived in Eq. (3.32) predicts

$$\Delta' = \frac{\tilde{\Gamma}^2}{16\,\Delta_{\mathrm{LS}}}\,\frac{I}{\tilde{I}_{\mathrm{sat}}}. \tag{3.59}$$

At fixed detuning, this predicts a linear relation:

$$\Delta'(P) = \left(\frac{\tilde{\Gamma}^2}{16\,\Delta_{\mathrm{LS}}\tilde{I}_{\mathrm{sat}}}\cdot\frac{2}{\pi w^2}\right)P, \tag{3.60}$$

so that the slope is:

$$S(\Delta_{\mathrm{LS}}) = \frac{d(\Delta')}{dP} = \left(\frac{\tilde{\Gamma}^2}{8\pi\, w^2\tilde{I}_{\mathrm{sat}}}\,\frac{1}{\Delta_{\mathrm{LS}}}\right). \tag{3.61}$$

By rearranging Eq. (3.61), we can express the effective beam waist as

$$w_{\mathrm{eff}} = \sqrt{\frac{\tilde{\Gamma}^2}{8\pi\,\tilde{I}_{\mathrm{sat}}S(\Delta_{\mathrm{LS}})}\,\frac{1}{\Delta_{LS}}}. \tag{3.62}$$

To interpret the measured slopes (table (3.1)), it is useful to introduce an "effective waist" w_{eff}, defined as the value of the beam waist that would reproduce the experimentally observed slope when inserted into the theoretical scaling law of Eq. (3.61). This quantity is not intended to represent the true Gaussian beam waist, but rather the intensity scale that the atoms effectively experience. It is not necessarily the same as the waist we measured (3.43), because in the real experiment, the atoms may not be

located exactly at the beam center, or the mode shape might not be perfectly Gaussian. There can also be calibration errors in the measured power (about 5%) and in the detuning (about 4%).

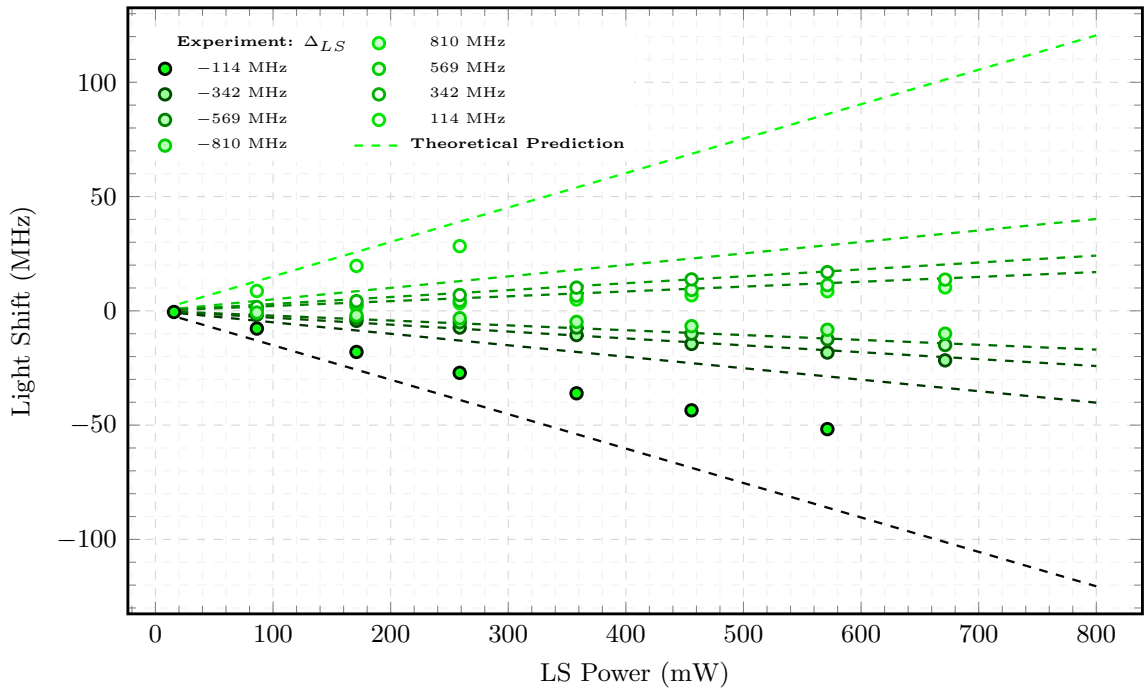

Figure 3.12: Measured light shift Δ' of the $^3P_1$ manifold versus light shift beam power P, shown for several detunings Δ_{LS} from the $^3P_1 \rightarrow {}^3D_1$ transition. A clear linear dependence of the light shift on P is observed, consistent with the perturbative expression $\Delta' = \frac{\Omega_0^2}{8\Delta_{\mathrm{LS}}}$,. The sign of the slope changes with the detuning changes from red ($\Delta_{\mathrm{LS}} < 0$) to blue ($\Delta_{\mathrm{LS}} > 0$).

Given the experimentally measured slope $S(\Delta_{\mathrm{LS}})$ at detuning Δ_{LS}, one can solve for the effective waist w_{eff} of the light beam. Table (3.1) summarizes the results of linear fits $\Delta' = S(\Delta_{\mathrm{LS}})P + b$ to the experimental data at various detunings, and compares the extracted slopes to the theoretical prediction. An effective waist w_{eff} is also deduced from the slope magnitude, providing a self-consistency check of the beam characterization.

The extracted slopes $S(\Delta_{\mathrm{LS}})$ quantify the efficiency with which a given dressing power produces a light shift at detuning Δ_{LS}. According to Eq. (3.32), one expects

$$S(\Delta_{\mathrm{LS}}) \propto \frac{1}{\Delta_{\mathrm{LS}}}. \tag{3.63}$$

This means that the slope is larger in magnitude when the dressing laser is closer to resonance, and the sign reverses as the detuning changes from red ($\Delta_{\mathrm{LS}} < 0$) to blue ($\Delta_{\mathrm{LS}} > 0$). Our measurements are fully consistent with this behavior; red-detuned data yield positive slopes (i.e., a downward shift of the resonance with increasing power), whereas blue-detuned data produce negative slopes, as shown clearly in Fig. (3.12). Typical detunings explored range from $|\Delta_{\mathrm{LS}}| = -800$ to 800 MHz.

These measured slopes in Table 3.1, extracted from linear fits to the experimental data shown in Fig. 3.12, are compared with the theoretical predictions of Eq. (3.32),

showing good overall agreement within the experimental uncertainties. The measured slopes are consistently 20–38% smaller in magnitude than the corresponding theoretical values.

The average effective waist obtained from the measurements is 1.24 mm, which is in close agreement with the actual beam waist of 1.052 mm, indicating good consistency between experiment and theory.

Table 3.1: Comparison of experimental and theoretical slopes of the light shift versus power at different detunings of the dressing laser. The extracted effective waist is obtained by inverting the theoretical slope expression for each detuning. The weighted average gives $w_{\text{eff}} = 1.24\,\text{mm}$, consistent with the independent optical estimate.

Detuning (MHz)	Measured Slope (MHz/mW)	Theory Slope (MHz/mW)	Intercept (MHz)	Effective Waist (mm)	Slope Error (MHz/mW)
−341.681	−0.034400	−0.050459	+1.4660	1.274	+0.01606
−113.894	−0.097200	−0.151376	+0.6183	1.313	+0.05418
−569.467	−0.023600	−0.030275	+0.9792	1.192	+0.00668
−809.908	−0.015800	−0.021287	+0.7403	1.221	+0.00549
+113.894	+0.117500	+0.151376	−1.3632	1.194	−0.03388
+341.682	+0.031700	+0.050459	−1.1297	1.327	−0.01876
+569.471	+0.021700	+0.030275	−0.9718	1.243	−0.00858
+809.915	+0.016400	+0.021287	−0.7611	1.199	−0.00489
		Average Effective Waist:		1.24 mm	

3.4.1 Universal scaling: Δ' vs P/Δ_{LS}

An alternative representation of the data is obtained by plotting the measured light shift Δ' against the normalized detuning Δ_{LS}/P. In this form, the dependence on light shift beam power is absorbed into the horizontal axis, so that all datasets taken at different powers and detunings are expected to fall on the same universal curve,

$$\Delta' \propto \frac{1}{\Delta_{\text{LS}}/P}. \tag{3.64}$$

Indeed, the data collapse onto a curve consistent with this $1/x$ scaling. The sign reversal across resonance is clearly visible, and the magnitude agrees with the theoretical prediction. Residual deviations likely stem from power broadening, imperfect beam waist determination, and non-ideal polarization purity. This representation highlights that the experiment probes the fundamental $\propto I/\Delta_{LS}$ light-shift scaling, independent of the specific beam power used.

The theoretical model predicts that the light shift should scale as

$$\Delta' = K\frac{P}{\Delta_{\text{LS}}}, \tag{3.65}$$

The light shift can be expressed compactly with a single proportionality constant K that depends only on the atomic parameters, beam waist, and polarization configuration. This implies that if one plots the measured shift Δ' against the ratio $\frac{P}{\Delta_{\text{LS}}}$, all datasets, regardless of detuning or dressing power, should collapse onto a straight line through

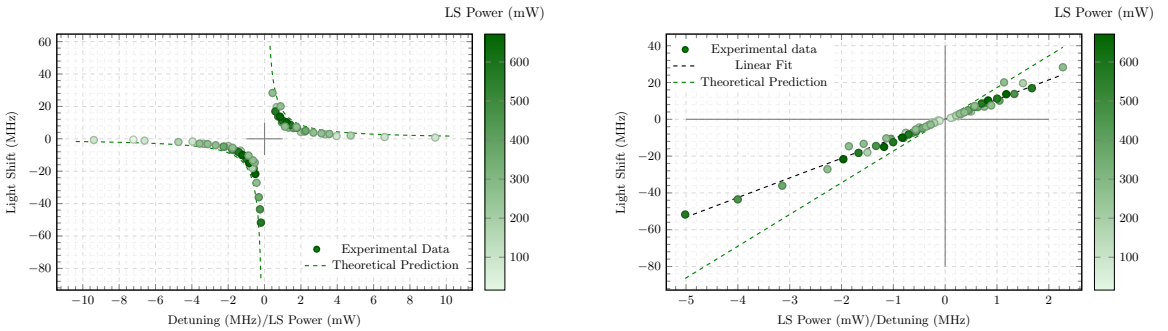

(a) Collapse versus Δ/P.

(b) Collapse versus P/Δ_{LS}.

Figure 3.13: Two equivalent representations of the light-shift scaling. (a) Plotting the data against Δ_{LS}/P removes the direct power dependence, causing all datasets to merge into a curve with a $1/x$-type behavior. (b) The light shift is plotted versus P/Δ_{LS}, the data collapse onto a straight line through the origin, highlighting the linear proportionality $\Delta' \propto P/\Delta_{\mathrm{LS}}$. Both representations confirm the universality of the scaling law.

the origin. Figure (3.13b) demonstrates this collapse explicitly. Each color corresponds to a different LS power, but when scaled by P/Δ, all points fall on a single line. The theoretically predicted slope is $K = 17.2$ MHz^2/mW while the linear fit to the experimental data yields $K = 10.7$ MHz^2/mW.

The systematic difference between the two values is consistent with the deviations discussed above, primarily the uncertainty in the effective beam waist and calibration of the optical power and detuning.

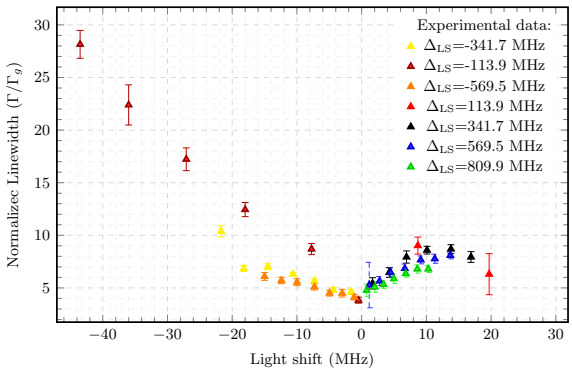

Figure 3.14: Normalized spectral linewidth as a function of light shift for various detunings Δ_{LS}. Each color corresponds to a different detuning value. The linewidth increases with increasing light shift, showing significant broadening for larger shifts compared to the unshifted resonance.

Spectral linewidth of the light shifted spectrum: As shown in Figure 3.14, the linewidth increases with increasing light shift and becomes significantly broader than the natural linewidth of $^3P_1$ transition as discussed in section 3.3.7.

3.5 Two dressing beam test of polarization selectivity and additivity

To further validate the polarization-resolved Stark-shift model, we performed an experiment with two independent dressing beams derived from a common source. Each beam was frequency-shifted by a separate acousto-optic modulator (AOM), such that their detunings differed by $\Delta_{\mathrm{LS}} = 160\,\mathrm{MHz}$. The two beams, LS1 and LS2, were linearly polarized along orthogonal axes (horizontal and vertical, respectively) and co-propagated along the quantization axis $\hat{z}$ (Fig. 3.15). A weak green probe at 555.8 nm counter-propagated through the atoms, with its polarization toggled between horizontal and vertical. The experiment proceeded in two stages,

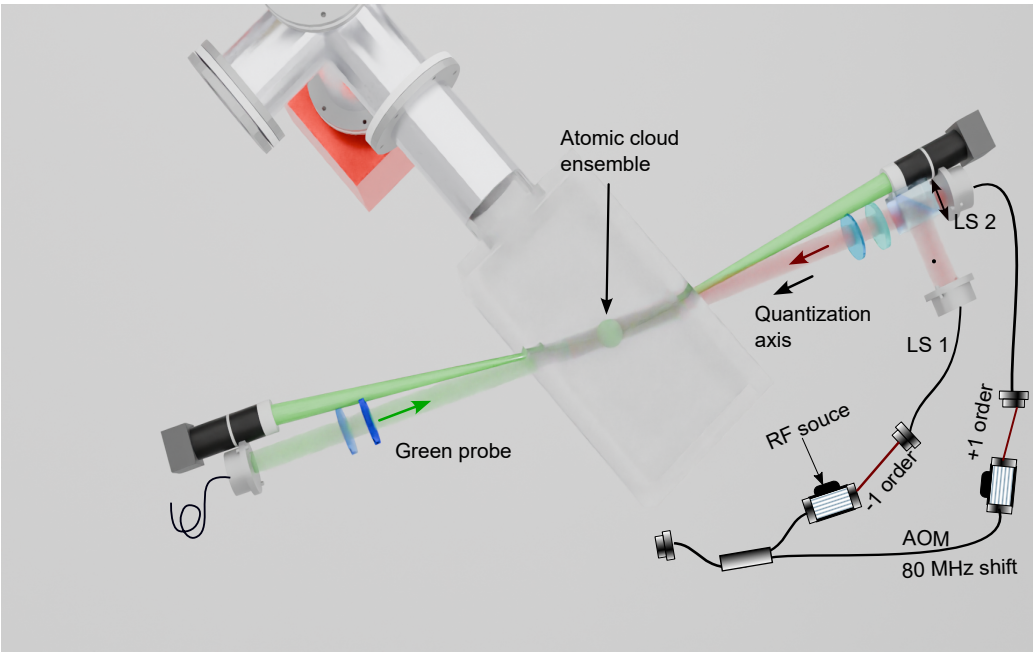

Figure 3.15: **Two-dressing-beam experimental setup.** The atomic ensemble is simultaneously illuminated by two far-detuned light-shift (LS) beams derived from a common source and frequency-shifted using an acousto-optic modulator (AOM). LS1 and LS2 are frequency-separated by $\Delta_{\mathrm{LS}} = 160\,\mathrm{MHz}$ and linearly polarized along orthogonal axes (horizontal and vertical, respectively). The quantization axis is chosen along the common LS propagation direction ($\hat{z}$). A weak green probe beam (555.8 nm) counter-propagates and its polarization is toggled between horizontal and vertical to project onto the dressed eigenstates associated with LS1 or LS2. Fluorescence is collected with a camera. This geometry allows us to test both the polarization selectivity of the light shift and the additivity of the contributions from two independent dressing beams.

Calibration of resonance with LS1 The seed laser wavelength was tuned such that LS1 became resonant with the ${}^3P_1 \rightarrow {}^3D_1$ transition (including its AOM shift). This reference condition defines the zero of the detuning axis.

Operating point for optically induced splitting From this resonance condition, the seed laser was further detuned by -76 MHz. In this configuration, LS1 and LS2 are both far detuned from the ${}^3P_1 \rightarrow {}^3D_1$ resonance, with opposite frequency offsets due to their ± 80 MHz AOM shifts. The total shift between two light shift beams is

160 MHz. Therefore, the detuning for both light shift beams LS1 and LS2 are fixed at $\Delta_{LS} = -76\,\text{MHz}$ and $\Delta_{LS} = 84\,\text{MHz}$ respectively. By varying the relative powers of LS1 and LS2, we generated light shifts of the $m = \pm 1$ sublevels of $^3P_1$.

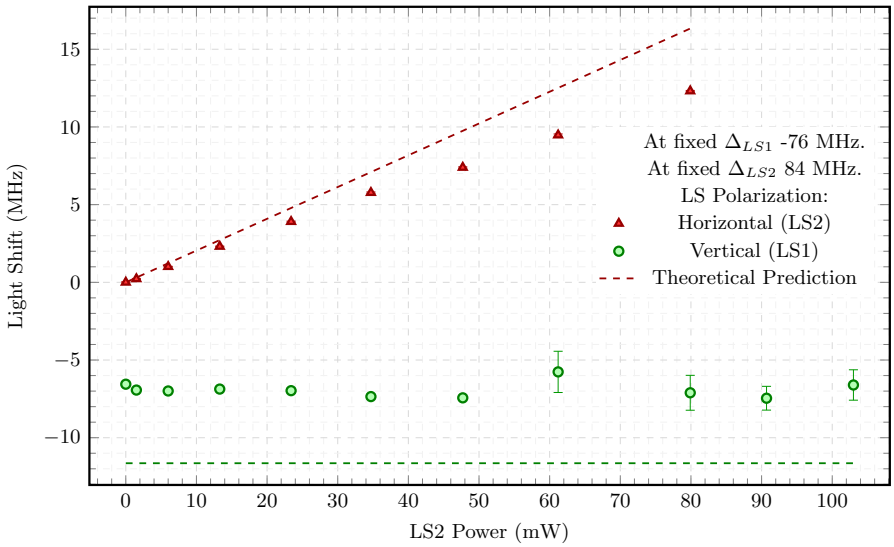

Figure 3.16: **Light shift vs. LS2 power at fixed LS1 power.** The detuning for both light shift beams LS1 and LS2 are fixed at $\Delta_{LS} = -76\,\text{MHz}$ and $\Delta_{LS} = 84\,\text{MHz}$ respectively. Red triangles: probe polarization parallel to LS2, the probe projects onto the eigenstate shifted by LS2, producing a strong linear light shift. Green circles: probe polarization orthogonal to LS2, the probe projects onto the dark eigenstate with negligible coupling, leaving only the constant light shift offset from LS1. This orthogonality demonstrates polarization selectivity; each probe polarization couples to only one dressed subspace. The linear slopes confirm that the total Stark shift is additive in the perturbative regime. Dashed line: linear prediction from the effective Hamiltonian, $\Delta' = -\frac{\hbar\Omega^2}{8\Delta_{LS}}$, with an offset equal to the contribution from the fixed LS1 beam. The contrasting slopes confirm that the probe selectively addresses the $|m = \pm 1\rangle$ channel and that Stark shifts from independent beams add linearly.

Conceptual Overview

The probe polarization acts as a projector onto a dressed eigenstate of the $J = 1 \to J' = 1$ manifold. The dressing beam induces the light shift; the probe polarization simply selects which shifted state is observed. The orthogonal dressing beam should contribute only a constant light shift offset.

Therefore, two key behaviors are expected:

1. **State selectivity:** The light-shift beam induces the level shifts, while the probe polarization determines which dressed eigenstate is addressed.

2. **Additivity:** In the perturbative regime, light shifts from independent beams add linearly, so the total shift is the sum of the individual contributions.

We then performed two complementary scans,

- Scan LS2 power while keeping LS1 power fixed at $P_1 = 51.5\,\text{mW}$.

- Scan LS1 power while keeping LS2 power fixed at $P_2 = 47.7\,\mathrm{mW}$.

For each scan, we recorded two spectra using the green probe with horizontal and vertical polarization, respectively. As in the single-beam case, the probe polarization projects onto a specific dressed eigenstate of the $J = 1 \rightarrow J' = 1$ manifold, one eigenstate is bright (shifted) for a given dressing polarization, while the orthogonal combination is dark (unshifted). Consequently, the measured line center should respond linearly to the power of the dressing beam whose polarization matches the probed eigenstate, and remain nearly constant when the scanned dressing beam is orthogonal.

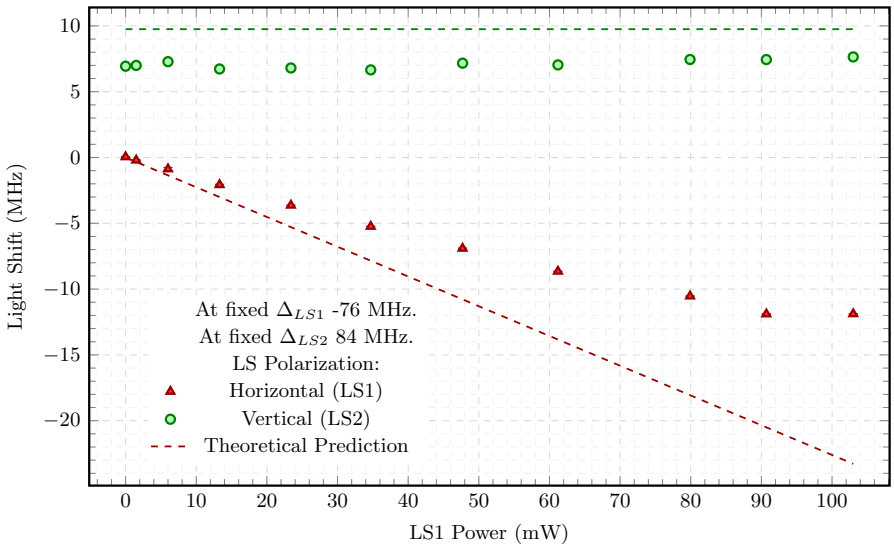

Figure 3.17: **Light shift vs. LS1 power at fixed LS2 power.** The detuning for both light shift beams LS1 and LS2 are fixed at $\Delta_{LS} = -76\,\mathrm{MHz}$ and $\Delta_{LS} = 84\,\mathrm{MHz}$ respectively. Red triangles: probe polarization parallel to LS1 (horizontal), the probe projects onto the eigenstate shifted by LS1, producing a strong linear light shift. Green circles: probe polarization orthogonal to LS1 (vertical), the probe projects onto the dark eigenstate with negligible coupling, leaving only the constant light shift offset from LS2. Dashed line: linear prediction from the effective Hamiltonian, $\Delta' = -\frac{\hbar\Omega^2}{8\Delta_{LS}}$, offset by the LS2 background. The complementary behavior to Fig. 3.16 confirms that each probe polarization projects selectively onto the dressed subspace aligned with the corresponding LS beam.

3.5.1 Effective Hamiltonian

These observations can be understood from a simple effective Hamiltonian for the far-detuned LS coupling. The quantization axis is taken along the beam propagation direction ($\hat{z}$). In the $\{|m_j = -1\rangle, |m_j = 0\rangle, |m_j = +1\rangle\}$ Zeeman basis, an x-polarized LS beam produces

$$H_{\mathrm{shift}}^{(x)} = \frac{\hbar\,\Omega_x^2}{16\Delta_{LS}} \begin{pmatrix} 1 & 0 & 1 \\ 0 & 2 & 0 \\ 1 & 0 & 1 \end{pmatrix}, \tag{3.66}$$

while a y-polarized beam produces

$$H_{\text{eff}}^{(y)} = \frac{\hbar\,\Omega_y^2}{16\Delta}\begin{pmatrix} 1 & 0 & -1 \\ 0 & 2 & 0 \\ -1 & 0 & 1 \end{pmatrix}. \tag{3.67}$$

The total effective Hamiltonian is simply

$$H_{\text{eff}}^{\text{tot}} = H_{\text{eff}}^{(x)} + H_{\text{eff}}^{(y)}.$$

For equal beam intensities ($\Omega_x^2 = \Omega_y^2 \equiv \Omega^2$), the off-diagonal terms cancel and the Hamiltonian becomes diagonal:

$$H_{\text{eff}}^{\text{tot}} = \frac{\hbar\,\Omega^2}{8\Delta_{LS}}\,\text{diag}(1,2,1). \tag{3.68}$$

Therefore, the $m = \pm 1$ states are shifted equally, while the $m = 0$ state shifts by twice as much. In our probe geometry (counter-propagating along $-\hat{z}$), only the $m = \pm 1$ channels are excited from the $J = 0$ ground state, so spectroscopy is sensitive only to this subspace, exactly as observed in Fig. 3.16 and Fig. 3.17.
Summary: The two-beam measurements establish that the light-shift mechanism is both polarization-selective and additive.

3.5.2 Full control of the $^3P_1$ Zeeman manifold

In the two-beam measurements described above, we demonstrated selective and additive control of the $m = \pm 1$ states of the $^3P_1$ manifold. This already highlights the ability of optical dressing to mimic the effect of a magnetic field along arbitrary transverse axes. More generally, however, optical dressing enables independent control of all three Zeeman sublevels.

Consider three far-detuned LS beams with orthogonal polarizations along x, y, and z, and with independently tunable intensities $I_{x,y,z}$ and detunings $\Delta_{x,y,z}$. The resulting light shifts of the three Zeeman sublevels are:

$$\Delta_{\text{LS},-} = \frac{\tilde{\Gamma}^2}{16\tilde{I}_{\text{sat}}}\left(\frac{I_x}{\Delta_x} + \frac{I_z}{\Delta_z}\right), \tag{3.69}$$

$$\Delta_{\text{LS},0} = \frac{\tilde{\Gamma}^2}{16 I_{\tilde{I}_{\text{sat}}}}\left(\frac{I_x}{\Delta_x} + \frac{I_y}{\Delta_y}\right), \tag{3.70}$$

$$\Delta_{\text{LS},+} = \frac{\tilde{\Gamma}^2}{16 I_{\tilde{I}_{\text{sat}}}}\left(\frac{I_y}{\Delta_y} + \frac{I_z}{\Delta_z}\right). \tag{3.71}$$

Because the detunings $\Delta_{x,y,z}$ can be chosen positive (blue) or negative (red), and the intensities $I_{x,y,z}$ are independently tunable, this system of equations is fully controllable. In other words, any desired set of shifts $\Delta_{\text{LS},-}, \Delta_{\text{LS},0}, \Delta_{\text{LS},+}$ can be realized with a suitable choice of laser parameters.

This means that, unlike a static magnetic field, which only generates a linear-in-m Zeeman splitting, the optical scheme allows the experimenter to engineer arbitrary energy landscapes within the $J = 1$ manifold. In principle, this provides access to synthetic Hamiltonians with tailored vector and tensor couplings, paving the way toward

atom-based implementations of designer spin models and quantum control protocols that are not achievable with magnetic fields alone.

This validates the effective Hamiltonian picture and provides a solid foundation for using LS beams as tunable, polarization-engineered tools in the Faraday-rotation experiments described in the next section.

3.6 Optically Induced Faraday Rotation

The phenomenon of Faraday rotation was first observed by Michael Faraday in 1845, who demonstrated that the plane of polarization of linearly polarized light is rotated when the light propagates through a medium placed in a longitudinal magnetic field [60]. This magneto-optical effect, now universally known as the Faraday effect, provided one of the earliest experimental links between optics and electromagnetism. Faraday himself interpreted the result as evidence for a deep connection between light and magnetic phenomena, more than a decade before Maxwell's field theory unified electricity, magnetism, and optics. Since then, Faraday rotation has become a central tool in atomic, molecular, and optical physics. In dilute atomic vapors, it serves as a sensitive probe of spin polarization and magnetization [61], underpinning techniques in precision magnetometry, quantum non-demolition (QND) measurements, and spin squeezing. In ultracold atomic gases, magnetically induced Faraday rotation has been widely exploited as a nondestructive probe to monitor spin dynamics in real time [62, 63, 64].

In the present work, we demonstrate an optical analogue of the traditional Faraday effect. Instead of using an external magnetic field to Zeeman split atomic levels, we employ an off-resonant dressing laser to couple the $^3P_1$ state to the $^3D_1$ manifold. The resulting light shifts lift the degeneracy of the $m = \pm 1$ Zeeman sublevels of $^3P_1$, producing circular birefringence that is formally equivalent to the effect of a magnetic field. A weak, linearly polarized probe on the $^1S_0 \rightarrow {}^3P_1$ transition thus experiences a polarization rotation as it traverses the cold atomic ensemble.

In ultracold atomic systems, generating and maintaining large magnetic fields can be technically challenging. This method replaces the static magnetic field with a dressing beam that produces the same kind of circular birefringence. The resulting optically induced Faraday effect has the same formal description as the magnetically induced version, but offers new advantages. This "all-optical" Faraday effect has the advantage of fast tunability, spatial selectivity, requiring no physical coils or static fields, and compatibility with ultracold atomic samples. This concept forms the basis of the present work, where the dressing beam plays the role of an effective magnetic field acting on the $^3P_1$ manifold.

These features make optically induced Faraday rotation an attractive tool not only for probing atomic ensembles but also for applications in quantum optics and metrology. In the following sections, we develop the theoretical description, describe the experimental implementation, and present measurements of this all-optical Faraday effect in a cold ensemble of ytterbium atoms.

3.6.1 Physical Mechanism

The Faraday effect originates from circular birefringence, a linearly polarized beam, which is a coherent superposition of left- and right-circular components that experience

different refractive indices, n_+ and n_-, in the presence of a magnetic field. Thus acquires a relative phase shift and emerges rotated with respect to its initial polarization.

A linearly polarized beam along x can be written as

$$\mathbf{E}_{\text{in}}(t) = E_0 e^{i(\omega t - kz)} \mathbf{u}_x = \frac{E_0}{\sqrt{2}} e^{i(\omega t - kz)} (\mathbf{e}_+ + \mathbf{e}_-), \tag{3.72}$$

where the circular polarization basis vectors are

$$\mathbf{e}_\pm = \frac{1}{\sqrt{2}} (\mathbf{u}_x \mp i \mathbf{u}_y). \tag{3.73}$$

As the components propagate through the medium, they acquire different phases,

$$\phi_\pm = k n_\pm L,$$

where $k = 2\pi/\lambda$ is the probe wavevector and L is the length of the medium.

So that the output field is given by,

$$\mathbf{E}_{\text{out}}(t) = \frac{E_0}{\sqrt{2}} e^{i(\omega t - kz)} \left(\mathbf{e}_+ e^{i\phi_+} + \mathbf{e}_- e^{i\phi_-} \right). \tag{3.74}$$

The output field in the x-y basis is therefore

$$\begin{aligned} \mathbf{E}_{\text{out}}(t) &= \frac{E_0}{\sqrt{2}} e^{i(\omega t - kz + \bar{\phi})} \sqrt{2} (\cos\theta \, \mathbf{u}_x + \sin\theta \, \mathbf{u}_y) \\ &= E_0 \, e^{i\left(\omega t - kz + \frac{kL}{2}(n_+ + n_-)\right)} \Big(\cos\theta \, \mathbf{u}_x + \sin\theta \, \mathbf{u}_y \Big), \end{aligned} \tag{3.75}$$

The resulting polarization rotation angle is

$$\theta = \frac{\phi_+ - \phi_-}{2} = \frac{kL}{2} (n_+ - n_-). \tag{3.76}$$

Thus, the effect provides a direct optical probe of the difference in dispersion for the two helicities of light. In a magnetized medium, this birefringence arises from the Zeeman splitting of atomic or molecular resonances.

In atomic media, magnetically induced Faraday rotation has long served as a powerful probe of spin polarization and as a diagnostic tool for magneto-optical phenomena in both hot vapors and cold atom ensembles. In this case, the magnetic field lifts the Zeeman degeneracy of the ground or excited states, leading to differential dispersion for the two circular components of a near-resonant probe.

Having established the polarization selectivity and linear additivity of the dressing-induced Stark shifts, we now turn to their direct manifestation as circular birefringence in the probe — the optically induced Faraday rotation.

3.7 Faraday Rotation in Atomic Media

The description of Faraday rotation in dilute atomic gases follows directly from the atomic polarizability.

At low density (no near-field, no multiple scattering), the refractive index of a dilute medium is related to the atomic polarizability $\alpha(\delta)$ by

$$n_\pm \simeq 1 + \frac{\rho}{2} \operatorname{Re}\Big[\alpha(\delta_\pm)\Big], \tag{3.77}$$

where ρ is the atomic density and $\delta_\pm$ are the effective detunings of the two circular components.

For a power-broadened two-level transition, the real part of the scalar polarizability can be written in a cross-section–normalized form as

$$\mathrm{Re}\,\alpha(\delta) \;=\; -\frac{6\pi}{k_{\mathrm{g}}^3}\,\frac{(2\delta/\Gamma_{\mathrm{g}})}{1+(2\delta/\Gamma_{\mathrm{g}})^2+s}, \tag{3.78}$$

where Γ_{g} is the natural linewidth of the probed transition, and $s = I/I_{\mathrm{sat,g}}$ is the on-resonance saturation parameter of the probe at intensity I (with $I_{\mathrm{sat,g}}$ the probe saturation intensity).

Although the excited $^3P_1$ state is three-fold degenerate, the absence of ground-state degeneracy ($J = 0$) ensures that the atom behaves effectively as a two-level system for the purposes of light scattering, absorption, and refractive index calculations. The only modification is that the saturation intensity $I_{\mathrm{sat},g}$ must be defined using the correct dipole strength for this $^1S_0 \rightarrow ^3P_1$ transition. With this substitution, the standard two-level atom formulas for polarizability, absorption cross-section, and Faraday rotation remain valid and quantitatively correct.

3.7.1 Zeeman Splitting and Magnetically Induced Faraday Effect

When a longitudinal magnetic field B is applied, the degeneracy of the excited $^3P_1$ manifold is lifted by the Zeeman effect as shown in Figure (3.18a). The magnetic moment of the state is $\boldsymbol{\mu} = -g_J\mu_B\mathbf{J}/\hbar$, where g_J is the Landé g–factor and μ_B the Bohr magneton. The corresponding Zeeman shift of a sublevel $|J = 1, m\rangle$ is

$$\Delta E_m = g_J\mu_B m B. \tag{3.79}$$

Thus the $m = \pm 1$ sublevels are shifted in opposite directions by $\pm\Delta_B$, where the total splitting is between them is $2\Delta_B$:

$$\Delta_B = g_J\mu_B B/\hbar. \tag{3.80}$$

The probe's two circular components couple selectively to these shifted transitions:

$$\sigma^+ : \quad \delta_+ = \delta - \Delta_B, \tag{3.81}$$
$$\sigma^- : \quad \delta_- = \delta + \Delta_B, \tag{3.82}$$

with δ the probe detuning in the absence of magnetic field.

Because the real part of the polarizability is dispersive,

$$n_\pm \;\simeq\; 1 + \frac{\rho}{2}\,\mathrm{Re}[\alpha(\delta_\pm)],$$

the opposite detunings $\delta_\pm$ translate into different refractive indices $n_+ \neq n_-$. The linearly polarized probe, being a superposition of $\sigma^\pm$, therefore acquires a relative phase shift and emerges rotated.

To first order in small Δ_B, the rotation angle is linear in the applied field:

$$\theta \;\propto\; \Delta_B \;\propto\; B. \tag{3.83}$$

and the refractive index difference becomes

$$n_- - n_+ = -\frac{6\pi\rho}{k^3}\left[\frac{(\delta+\Delta_B)/\Gamma}{1+(2(\delta+\Delta_B)/\Gamma)^2+s} - \frac{(\delta-\Delta_B)/\Gamma}{1+(2(\delta-\Delta_B)/\Gamma)^2+s}\right]. \tag{3.84}$$

For small Zeeman splittings compared to Γ, this reduces to a linear-in-B birefringence, yielding the familiar magneto-optical Faraday effect.

3.7.2 Optically induced Faraday rotation with a linearly polarized probe

In our case, no static magnetic field is applied. Instead, a far-detuned dressing laser couples the $^3P_1$ manifold to the $^3D_1$ state, inducing an light shift Δ_{LS} that plays the role of an effective Zeeman splitting as shown in Figure(3.18b).

A linearly polarized probe at wavelength λ_{g} (wave number $k_{\mathrm{g}} = 2\pi/\lambda_{\mathrm{g}}$) can be decomposed into equal $\sigma^{\pm}$ circular components. Equivalently, the $\sigma^{\pm}$ components experience equal and opposite detunings with respect to the nearest dressed resonance,

$$\delta_{\pm} \;=\; \mp\frac{\Delta'}{2}, \tag{3.85}$$

Replacing $\Delta_B \to \Delta'/2$ in the above expressions, we obtain

$$n_{\pm} = 1 \mp \frac{6\pi\rho}{k_g^3}\,\frac{(\Delta'/2\Gamma_g)}{1+(\Delta'/\Gamma_g)^2+I/I_{\mathrm{sat},g}}, \tag{3.86}$$

The phase accumulated by each circular mode after propagation through the cloud is $\phi_{\pm} = k_g \int n_{\pm}(z)\,dz$, hence the phase difference

$$\Delta\phi = \phi_+ - \phi_- = \sigma_0 \int \rho(z)\,dz\;\frac{\Delta'/\Gamma_g}{1+(\Delta'/\Gamma_g)^2+s}, \tag{3.87}$$

where $\sigma_0 = 6\pi/k_g^2 = 3\lambda_g^2/(2\pi)$. With $\mathrm{OD_g} = \sigma_0 \int \rho\,dz$, the final rotation angle (half the phase difference) is

$$\theta = \frac{1}{2}\Delta\phi = \frac{b_{0,g}}{2}\,\frac{\Delta'/\Gamma_g}{1+(\Delta'/\Gamma_g)^2+I/I_{\mathrm{sat},g}}. \tag{3.88}$$

Here $b_{0,g}$ is the on-resonance optical depth of the atomic cloud on the green $^1S_0 \to {}^3P_1$ probe transition, Γ_g its linewidth, and $I_{\mathrm{sat},g}$ the corresponding saturation intensity.

Equation (3.88) constitutes the central theoretical result for the optically induced Faraday rotation, the angle scales linearly with the effective light shift at small detunings, but saturates and eventually decreases for large shifts or strong probe intensities.

- **Saturation:** Increasing probe intensity reduces the rotation by the factor $1/(1+s)$, reflecting the reduced dispersive response at high s.
- **Sign:** The sign of θ follows the sign of Δ_{LS} (i.e. the sign of the circular birefringence induced by the dressing field).
- **No-absorption assumption:** Eq. (3.88) assumes a nearly constant probe intensity across the sample (weak absorption). If absorption is appreciable, one should propagate the coupled equations for the Stokes parameters (see below for discussion), in which case θ acquires an exponential weighting $\exp[-\mathrm{OD}(z)]$ along the path.

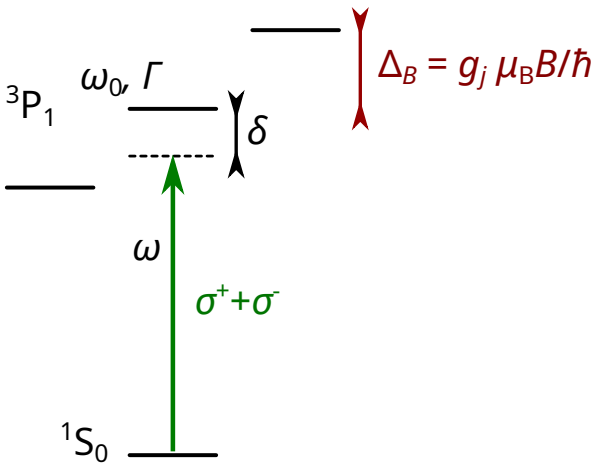

(a) Magnetically induced case: a longitudinal magnetic field lifts the degeneracy of the $m = \pm 1$ Zeeman sublevels of the $^3P_1$ state, shifting the $\sigma^\pm$ transition frequencies. The resulting Faraday rotation angle is given by $\theta = b_{0,g} \frac{\Delta_B/\Gamma_g}{1+(2\Delta_B/\Gamma_g)^2 + I/I_{\mathrm{sat},g}}$ with $\delta = 0$.

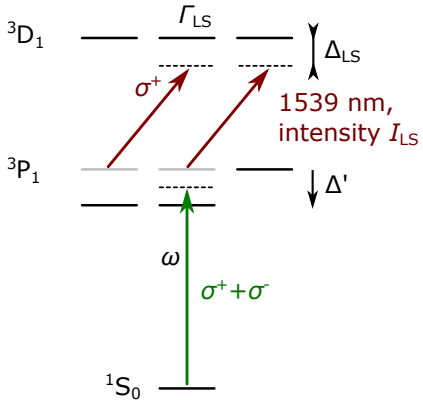

(b) Optically induced case: a far-detuned dressing beam couples $^3P_1$ to $^3D_1$, creating a light-shift splitting Δ_{LS} between the $m = \pm 1$ states. The resulting Faraday rotation angle is given by $\theta = b_{0,g} \frac{(\Delta'/2)\Gamma_g}{1+\left(2(\Delta'/2)/\Gamma_g\right)^2 + I/I_{\mathrm{sat},g}}$.

Figure 3.18: Energy-level schemes for Faraday rotation. (a) In the magnetically induced case, a longitudinal magnetic field creates a Zeeman splitting between $m = \pm 1$ sublevels, leading to circular birefringence and rotation of the probe polarization. (b) In the optically induced case, a circularly polarized dressing beam shifts the $m = -1$ sublevel relative to $m = +1$, producing an effective circular birefringence equivalent to a Zeeman splitting.

Equations (3.88) summarize the optically induced Faraday rotation for a cold, dilute gas in terms of directly measurable quantities: the LS-induced splitting Δ_{LS}, the probe parameters ($\Gamma_{\mathrm{g}}, I/I_{\mathrm{sat,g}}$), and the probe optical depth $\mathrm{OD_g}$.

In both the magnetically induced and optically induced cases, Faraday rotation arises from a differential phase shift between $\sigma^\pm$ probe components, generated by an effective splitting of the $m = \pm 1$ excited states. While a real magnetic field produces a Zeeman splitting $\Delta_B \propto B$, the light shit beam produces a light shift $\Delta'_{\mathrm{LS}} \propto I_{\mathrm{LS}}/\Delta_{\mathrm{LS}}$ that mimics the effect of a fictitious magnetic field. Thus, optically induced Faraday rotation is formally identical to the magnetically induced effect, but allows fast and spatially selective control of the polarization rotation.

3.8 Experimental Methodology: Stokes Parameter Measurement

3.8.1 Probe–Dressing Beam Geometry

To measure the optically induced Faraday rotation of the $^1S_0 \rightarrow ^3P_1$ probe transition, we employed a polarization-resolved detection scheme based on Stokes parameters. A linearly polarized probe beam at $\lambda_g = 556$ nm traverses the cold ensemble of ^{174}Yb atoms (waist ≈ 500 µm) in the MOT along the quantization axis (z). The probe waist

at the atoms is ~ 200 μm. A circularly polarized dressing beam at 1539 nm, waist ~ 1 mm, co-propagates with the probe and optically couples the $^3P_1 \rightarrow {}^3D_1$ transition. The dressing beam induces an AC Stark splitting Δ'_{LS} between the $m = \pm 1$ excited sublevels, giving rise to circular birefringence for the probe. The probe and dressing beams are overlapped on a dichroic mirror and co-aligned with the MOT center. The method to measure the light shift is already explained in an earlier section.

3.8.2 Waveplate Compensation and Polarimetry

Three waveplates are needed. The dichroic mirror used to combine the probe and dressing beams introduces a phase retardation between orthogonal probe polarizations. This artificial birefringence would mimic an S_3 signal (ellipticity) and corrupt the Faraday rotation measurement. To cancel it, we inserted a sequence of $\lambda/2$–$\lambda/4$–$\lambda/2$ waveplates before the detection system. By carefully adjusting their angles, the polarization state after the dichroic is restored to its state directly after the atoms, effectively "flattening" the mirror's Jones matrix. Because the phase retardance drifts slowly with laboratory temperature, this calibration had to be repeated three to four times per day to isolate the true atomic effect.

To characterize the probe polarization, we employed a full Stokes polarimetry analysis following the standard formalism of Ref. [65]. The transmitted probe field after the atomic cloud was reflected from the dichroic mirror (M1), analyzed using a rotatable "basis choice" stage (waveplates) to select the correct basis, followed by a polarizing beamsplitter (PBS) and a balanced photodiodes as shown in Fig. 3.19.

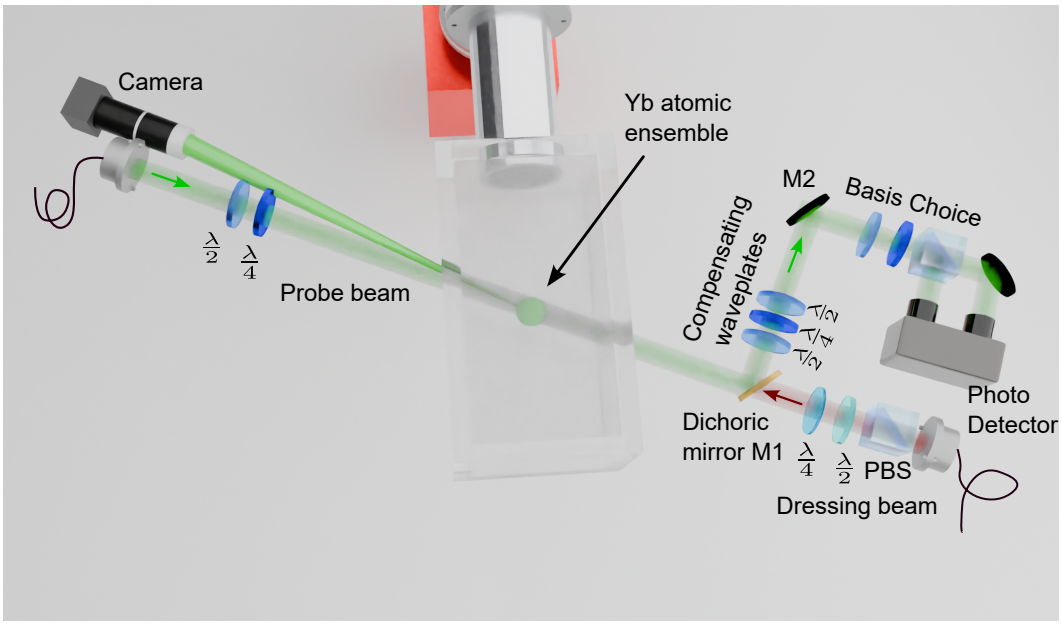

Figure 3.19: Experimental setup for Faraday rotation measurement. A linearly polarized probe beam ($\lambda_g = 556$ nm) passes through the Yb atomic ensemble overlapped with the 1539 nm dressing beam. The transmitted probe is analyzed by a sequence of waveplates and a polarizing beam splitter to reconstruct the Stokes parameters. The $\lambda/2$–$\lambda/4$–$\lambda/2$ combination compensates birefringence from the dichroic mirror.

3.8.3 Why Stokes Polarimetry is Essential

In many cold-atom Faraday rotation experiments, the angle θ is obtained from simple differential transmission through a PBS, i.e. from $I_{\parallel} - I_{\perp}$. In our experiment, this approach is insufficient for two key reasons:

1. The dichroic mirror adds uncontrolled phase retardance, which converts part of S_1 into S_3, faking ellipticity.

2. The dressing beam itself can induce genuine ellipticity ($S_3 \neq 0$) in addition to pure rotation.

Therefore a full Stokes vector reconstruction (S_0, S_1, S_2, S_3) is required to reliably distinguish:

- Pure Faraday rotation: real index difference $(n_+ \neq n_-) \Rightarrow$ change in (S_1, S_2).
- Induced ellipticity: imaginary index difference $\Rightarrow S_3$ component.

Only this complete polarimetric analysis allows an unambiguous measurement of the optically induced Faraday rotation angle.

3.8.4 Data Acquisition

For each dressing detuning Δ'_{LS}, the probe is detuned in the middle between bare and light-shifted transition, $\delta_g = \Delta'_{\mathrm{LS}}/2$, which maximizes the optically induced circular birefringence. The transmitted probe was analyzed sequentially in four complementary polarization bases,

- **Parallel/orthogonal linear:** $I_{\parallel}$ and $I_{\perp}$ are the probe intensities transmitted through the PBS in the horizontal and vertical bases, aligned parallel and perpendicular to the incident polarization.
- **Linear at** 45°**:** I_{45} is the intensity in the diagonal (45°) basis.
- **Circular:** I_{circ} corresponds to one of the two circular components.

An additional "background" channel (I_{bgd}) was recorded with the probe blocked to subtract detector offsets. For each setting, the probe signal was recorded on the balanced photodiodes for a 1 ms per experimental cycle. Each measurement was repeated ten times to allow averaging and to estimate statistical fluctuations. However, only the interval between $t = 70$ μs and $t = 270$ μs was retained for analysis. The first ~ 70 μs after switching on the probe contained transient electronic spikes and optical switching artifacts from the AOM drivers, which would otherwise contaminate the extracted Stokes parameters. Restricting the analysis to a 200 µs window ensured a flat, steady signal with sufficient signal-to-noise ratio while rejecting these transients. A CCD camera imaged the probe fluorescence for alignment diagnostics and to measure the light shift.

Before introducing atoms, the probe polarization was aligned vertically (along y) and measured after reflection from the mirror M2. The dichoric mirror introduces a relative phase shift between horizontal and vertical polarizations, to compensate this birefringence, a sequence of three waveplates ($\lambda/2 - \lambda/4 - \lambda/2$) was inserted. Their

angles were tuned until the transmitted probe was restored to a pure linear polarization state. Residual rotations introduced by the optics were calibrated by repeating the full Stokes analysis without atoms and subtracted from the atomic signal to suppress systematic offsets.

3.8.5 Data Treatment

The raw detector signals were first corrected by subtracting the background level I_{bgd}. The total probe intensity was then computed as

$$s_0 = I_{\parallel} + I_{\perp}, \tag{3.89}$$

and the normalized Stokes parameters [65] as

$$s_1 = \frac{I_{\parallel} - I_{\perp}}{s_0}, \tag{3.90}$$

$$s_2 = \frac{2I_{45}}{s_0} - 1, \tag{3.91}$$

$$s_3 = \frac{2I_{\mathrm{circ}}}{s_0} - 1. \tag{3.92}$$

This normalization by s_0 suppresses common-mode probe power fluctuations. From the normalized Stokes vector (s_1, s_2), one extracts the Faraday rotation angle θ (angle of the major axis of the polarization ellipse relative to the incident polarization) via

$$\tan 2\theta = \frac{s_2}{s_1}.$$

The error in the extracted rotation angle was determined by Gaussian error propagation,

$$\sigma_\theta^2 = \left(\frac{\partial\theta}{\partial s_1}\sigma_{s_1}\right)^2 + \left(\frac{\partial\theta}{\partial s_2}\sigma_{s_2}\right)^2, \tag{3.93}$$

where for $\theta = \frac{1}{2}\arctan(s_2/s_1)$,

$$\frac{\partial\theta}{\partial s_1} = -\frac{s_2}{2(s_1^2+s_2^2)}, \qquad \frac{\partial\theta}{\partial s_2} = \frac{s_1}{2(s_1^2+s_2^2)}.$$

with $\sigma_{s_1}, \sigma_{s_2}$ obtained from the standard deviation of repeated measurements. The angle was finally expressed in degrees, θ, with propagated uncertainties.

In addition to the rotation angle, the ellipticity of the transmitted polarization could be quantified from

$$\epsilon = \frac{1}{2}\arcsin\left(\frac{s_3}{P}\right), \quad P = \sqrt{s_1^2+s_2^2+s_3^2}, \tag{3.94}$$

providing a measure of any circular birefringence induced by the atomic medium.

Conversion of Optical Depth (OD) The optical depth in our setup is routinely measured on the strong blue ${}^1S_0 \to {}^1P_1$ transition. To obtain the OD relevant for the green probe, we rescale by a spectroscopic factor η accounting for oscillator strengths and detection geometry (explained in Chapter 2,2.31):

$$\mathrm{b}_{0,\mathrm{g}} = \eta\, \mathrm{b}_{0,\mathrm{blue}}, \quad \eta = 1.7. \tag{3.95}$$

Probe–Cloud Overlap Correction The probe beam (waist w) samples only part of the Gaussian atomic cloud (radius R). Because the detector integrates the transmitted power over the probe mode, the measured rotation is an intensity-weighted average of the local rotation across the beam. The effective optical depth is reduced by an overlap factor:

$$\mathrm{b}_{\mathrm{eff}} = \frac{R^2}{R^2 + w^2}\, \mathrm{b}_{0,\mathrm{g}}. \tag{3.96}$$

For our parameters ($w = 200\ \mu$m, $R = 250\ \mu$m), $\eta \approx 0.6$, giving $\mathrm{b}_{\mathrm{eff}} \approx 0.6 \times \mathrm{b}_{0,\mathrm{g}}$.

The measured polarization rotation angle θ (extracted from the Stokes parameters as described above) is directly related to the dressing-induced splitting Δ'_{LS} via the dispersive response of the probe transition. For a weak probe at frequency $\Delta'_{LS}/2$ (negligible absorption across the cloud), the accumulated Faraday rotation angle θ for a probe traversing the cloud is given by the theoretical relation derived in Sec. 3.7.2 is

$$\boxed{\theta(I, \Delta'_{LS}) \;=\; \frac{\eta \mathrm{b}_{0,\mathrm{g}}}{2}\, \frac{\Delta'_{LS}/\Gamma_g}{1 + \left(\frac{\Delta'_{LS}}{\Gamma_g}\right)^2 + I/I_{\mathrm{sat},g}},} \tag{3.97}$$

where OD_g is the probe optical depth, Γ_g the probe natural linewidth, and $s = I/I_{\mathrm{sat},g}$ the probe saturation parameter (all quantities evaluated for the probe wavelength).

Summary. Using this procedure, we extract the rotation angle θ of the probe polarization after propagation through the optically dressed cold atomic cloud. This rotation is directly related to the differential light shift Δ_{LS} between the Zeeman sublevels, providing a quantitative comparison between the theoretical model and experimental measurements.

3.9 Results and Discussion

When the dressing beam induces differential light shifts of the m_J sublevels of the $^3P_1$ state, the atomic medium becomes circularly birefringent for the near-resonant green probe. High probe power was required to achieve sufficient signal-to-noise on the balanced photodiodes, but this comes at the expense of reducing the dispersive response.

Rotation θ vs. probe intensity: We investigated the role of probe saturation. The figure 3.20 shows the measured angle θ as a function of normalized probe intensity $I/I_{\mathrm{sat,g}}$ for fixed OD and LS detuning (points with error bars) together with the theoretical curve obtained using the independently measured parameters $\Delta_{\mathrm{LS}} = 4.8$ MHz, $\Gamma_g = 184$ kHz and $\mathrm{OD}_{\mathrm{eff}}$ from Eq. (3.96). The low-intensity plateau gives the asymptotic rotation, while at large I/I_{sat} the rotation is suppressed as the denominator grows. At fixed dressing-induced splitting Δ_{LS} and fixed OD, Eq. (3.97) predicts the characteristic saturation behavior.

The measured saturation behaviour is in good agreement with the dispersive model. Small residual discrepancies can be attributed to (i) imperfect knowledge of the exact probe waist at the atom position, (ii) small intensity inhomogeneities of the dressing beam across the probe, and (iii) weak absorption of the probe (which slightly modifies the spatial dependence of I/I_{sat}).

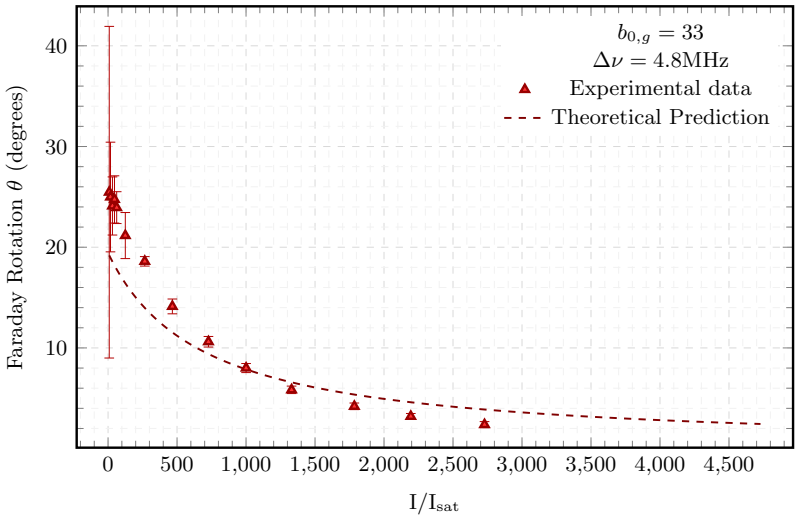

Figure 3.20: Faraday rotation angle θ vs. probe intensity $I/I_{\mathrm{sat},g}$. Red points: experimental data (error bars: propagated statistical uncertainty). Dashed line: theoretical prediction from Eq. (3.97) using $\Delta_{\mathrm{LS}} = 4.8\,\mathrm{MHz}$ and the overlap-corrected $\mathrm{OD}_{\mathrm{eff}}$. The rotation angle θ decreases with probe intensity as predicted by Eq. (3.97), which contains a suppression factor $1/(1+s)$ with $s = I/I_{\mathrm{sat,g}}$. The line is the theoretical curve without free parameters.

Rotation θ vs. optical depth: Figure 3.21 shows the measured Faraday rotation angle as a function of the effective optical depth $\mathrm{OD}_{\mathrm{eff}}$ for three different light shifts Δ'. The probe intensity was fixed at $I/I_{\mathrm{sat}} = 30$. The experimental points (symbols) follow the linear scaling predicted by Eq. (3.97) at low OD, where absorption and multiple scattering are negligible. At higher OD, the measured rotation saturates, consistent with the effective-medium picture in which the probe samples only the central portion of the cloud. Theoretical curves (dashed lines) are obtained with no free parameters, using the overlap-corrected $\mathrm{OD}_{\mathrm{eff}}$ and the measured detunings Δ.

Dependence on light shift: Figures 3.22 and 3.23 show the Faraday rotation as a function of the light shift Δ'. In Fig. 3.22, the light shift is varied by changing the intensity of the dressing beam, whereas in Fig. 3.23 it is varied by changing the detuning Δ_{LS}. The sign reversal between red- and blue-detuned dressing reflects the opposite circular birefringence induced on the $m = \pm 1$ sublevels. The theoretical curves (solid lines) reproduce the expected dispersive behavior, while the measured rotation angles are systematically smaller in magnitude than the unscaled theory. Applying a global rescaling factor (dashed lines) brings the theory into quantitative agreement with the data in both panels without altering the underlying line shape.

3.9.1 Discussion of deviations

When varying the atom number (hence OD) at fixed LS beam power, the dispersive profile retains its shape but the amplitude scales with OD. Across all data sets, the overall trends agree with theory, but the absolute magnitude of θ is smaller than the simplest prediction. We attribute this to the finite absorption; at large OD, exponential attenuation reduces the effective interaction length. Dressing polarization purity: any

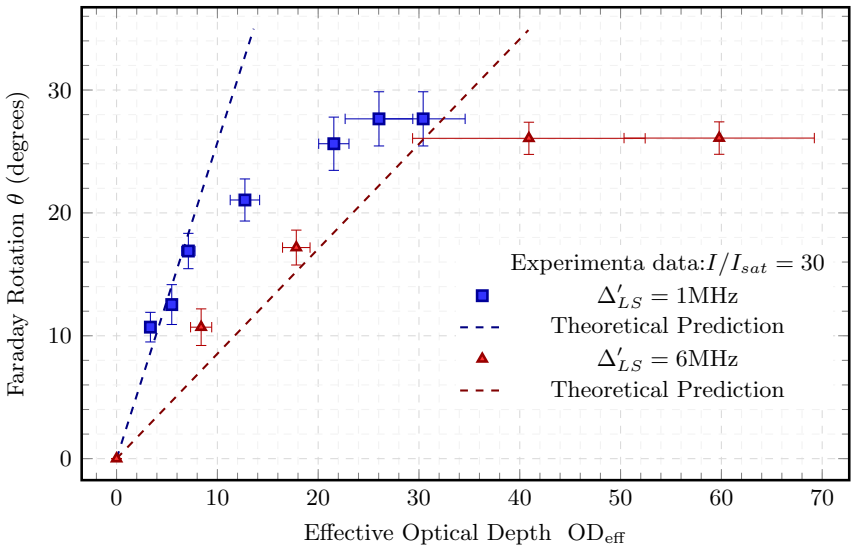

Figure 3.21: **Faraday rotation vs. optical depth.** Symbols: experimental data at $I/I_{\text{sat}} = 30$ for several light shifts. Dashed lines: theory from Eq. (3.97). The measured rotation angle θ increases linearly with effective optical depth OD_{eff} at small values, consistent with Eq. (3.97). Saturation and slight deviation from linearity appear at higher OD. Error bars reflect statistical scatter over repeated runs.

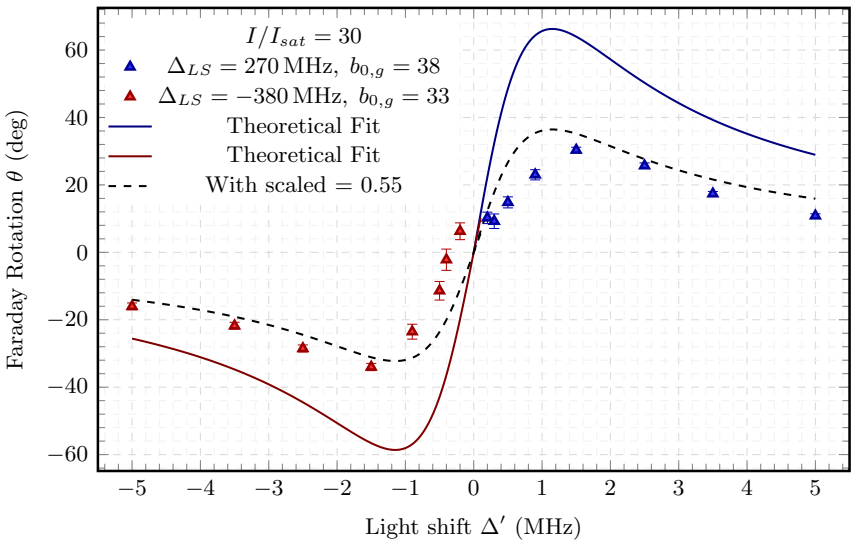

Figure 3.22: **Faraday rotation vs. light shift.** The rotation angle θ of the probe polarization is plotted as a function of Δ' for fixed $I/I_{\text{sat}} = 30$. Points: experimental data. Line: theoretical prediction from Eq. (3.97), rescaled by an overlap factor $\eta \simeq 0.4$ (see text). The dispersive lineshape, including the sign reversal of θ, is clearly observed.

residual ellipticity of the dressing beam modifies the balance of vector vs. tensor light shifts. Despite these limitations, the observed rotation systematically follows the predicted scalings, linear in OD, dispersive in Δ_{LS}, and suppressed at high probe intensity.

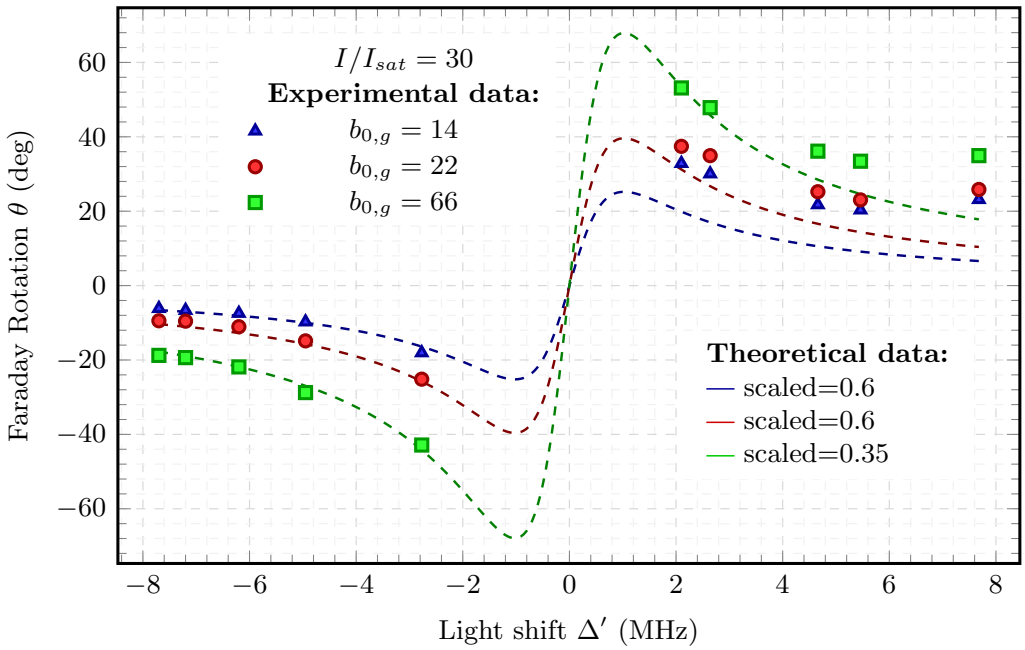

Figure 3.23: **Faraday rotation vs. light shift at different optical densities** The rotation angle θ of the probe polarization is plotted as a function of Δ' for fixed $I/I_{\text{sat}} = 30$ at different optical densities. Points: experimental data. Line: theoretical prediction from Eq. (3.97), rescaled by an overlap factor $\eta \simeq 0.35$ to 0.6 . The dispersive lineshape, including the sign reversal of θ, is clearly observed.

3.9.2 Summary

We have demonstrated optically induced Faraday rotation of a linearly polarized probe in a cold ^{174}Yb gas. A far-detuned dressing beam at 1539 nm induces light shifts of the $^3P_1$ Zeeman sublevels, producing circular birefringence equivalent to a Zeeman splitting. The results presented here establish a new regime of Faraday rotation, one driven not by Zeeman shifts from an external magnetic field, but instead by engineered light shifts produced by an off-resonant dressing beam. In this "all-optical" Faraday effect, the differential light shift of the $m = \pm 1$ sublevels of the $^3P_1$ manifold provides the necessary circular birefringence to rotate the probe polarization.

Compared to magnetically induced Faraday rotation, the all-optical approach offers several advantages, particularly for cold-atom experiments:

- **Fast tunability:** The effective Zeeman splitting is directly proportional to the dressing beam's intensity and detuning, allowing rapid control during experiments.
- **Spatial selectivity:** By shaping the dressing beam, birefringence can be engineered locally within the atomic sample.
- **Compatibility with ultracold systems:** The method avoids the need for large, homogeneous magnetic fields in ultrahigh-vacuum environments, thereby reducing magnetic noise and spatial inhomogeneities that can perturb delicate quantum states.

In summary, optically induced Faraday rotation not only reproduces the physics of the traditional magneto-optical effect but also introduces new flexibility that is uniquely

suited to precision experiments with ultracold atoms.

It is important to note that the Faraday effect is intrinsically non-reciprocal; the sense of rotation is determined by the direction of the effective field (magnetic or optical), but not by the propagation direction of the probe. Consequently, if a probe beam traverses the medium twice along the same axis, the rotation is not canceled but doubled. In the present optical case, the helicity of the dressing beam plays the role of the magnetic field direction, and thus, optically induced Faraday rotation inherits the same non-reciprocal character as the magnetically induced effect.

Chapter 4

Transport of Light in Optically Dense Atomic Ensemble

This chapter is based on the work presented in our publication [18].

4.1 Introduction and Motivation

The propagation of light through dense and disordered media is not only a central and active topic in both classical and quantum optics, but also a crucial and heavily studied topic in solid-state physics [66], atmospheric sensing [67], earth sciences, and LIDAR-based sensing [68]. Light propagation in an optically thick and disordered medium is notoriously difficult and no longer explained solely in terms of single-particle scattering. Instead, multiple light scattering events in an optically dense medium become dominant as the optical depth increases, distorting wavefronts and attenuating signals, making imaging and probing of the medium inherently difficult. These transport effects are important to modern studies of mesoscopic optics, wave physics, and quantum optics. The core difficulty lies in the fact that once light enters the diffusive regime, imaging inside the medium becomes extremely challenging. This problem is common across fields; for instance, medical imaging in biological tissues faces the same limitation. The scattering of light by cells and tissues severely limits penetration depth and blurs resolution [69, 70].

Optical imaging in scattering media is fundamentally constrained by the nature of light transport. In transparent samples or in the ballistic regime, conventional microscopy provides direct spatial resolution. Even in the single-scattering regime, where photons experience only one interaction, aberration-correction methods can often recover clear images by compensating for variations in refractive index [71]. But once light enters the multiple-scattering regime, the situation changes qualitatively; photons undergo many deflections before escaping, and there is no simple way to reconstruct the internal distribution of light. Several clever strategies have been developed, ranging from speckle correlations [69] to memory–effect–based imaging and computational wavefront shaping [72, 73]. Each has merit, but all face practical limits, whether in terms of depth penetration, spatial resolution, or the amount of prior information about the medium required. From a wave-physics point of view, two intertwined processes dominate. Attenuation, which reduces transmission as photons scatter or are absorbed, and wavefront distortion, which scrambles the phase due to spatial variations in optical paths. Together, these make it nearly impossible to form a clear image of the interior

once the medium becomes optically thick.

In dilute atomic gases, a probe undergoes a single-pass absorption/reemission process, and the exponential Beer-Lambert law applies. However, once the optical depth exceeds unity, scattered photons have a high probability of being rescattered before escaping the medium. The transport of light in this regime is best described in terms of random walks of photons through the disordered atomic ensemble. The cumulative effect of these random paths results in the diffusive propagation of light. Pioneering experiments with cold rubidium clouds have demonstrated several phenomena based on light scattering due to multiple scattering, such as coherent backscattering [74, 75, 76], where the constructive interference of reciprocal scattering paths leads to an enhanced reflection cone. Subsequent studies have revealed signatures of cooperative radiation, including subradiant and superradiant emission [77, 78, 19]. Additionally, the suppression of transport due to interference effects reminiscent of Anderson localization [8, 1, 13] can be expected.

This motivates a different approach; multiple scattering is an intrinsic property of an optically dense medium. One can embrace it to understand the propagation of light. That is, treat the scattered/diffuse light itself as the signal and extract transport properties directly from it [79]. The atomic cloud is excited/probed from the outside of the cloud, and the diffuse transmission is collected as a function of time. It decays exponentially with a time constant. One can extract the transport parameter from the time constant, which is a function of optical depth and diffusion coefficient. In another approach [45], the frequency response of various quantities (Diffuse transmission and reflection) linked to multiple scattering can be measured. The CBS enhancement factor is directly linked to the relative amount of single scattering versus the multiple scattering interference contrast.

4.1.1 Why Ultracold atomic ensembles are an ideal candidate for studying light propagation in disordered media

Historically, studies of light diffusion in atomic vapors provided insight into photon scattering, energy transport, and the transition from ballistic to diffusive regimes. Cold atoms provide a particularly clean platform for studying these complex physical phenomena. Unlike powders or colloids, the scatterers are identical and resonant, with a well-controlled and understood internal structure. This enables a quantitative comparison between theory and experiment, even in regimes where coherent interference and many-body correlations become significant. In the context of ultracold atoms, the ability to precisely control the atomic density, optical depth, temperature, and cloud geometry enables the exploration of both weak ($k\ell \gg 1$, where the transport mean ℓ free path is much larger than the wavelength), and strong $k\ell \sim 1$ scattering regimes in a single cold atomic ensemble setup, thereby opening new avenues for studying coherent transport phenomena.

The laser-cooled ytterbium (^{174}Yb) atomic ensemble has distinct advantages due to its clean atomic transition with different timescales. The broad $^1S_0 \rightarrow {}^1P_1$ transition with decay time of 5 ns and large saturation intensity $\mathrm{I_{sat}} \approx 60$ mW/cm^2 allows an accurate calibration of optical depth, while the narrow intercombination line $^1S_0 \rightarrow {}^3P_1$ with lifetime of 866 ns ($\mathrm{I_{sat}} \approx 0.14$ mW/cm^2) yields an optical depth roughly twice as large, which increases sensitivity to multiple-scattering and interference effects. Importantly, both transitions share the same ground state $^1S_0$, enabling consistent probing of

the same atomic sample across very different timescales. This dual accessibility makes ytterbium an excellent candidate for studying light propagation in dense and disordered media, and ultimately, the localization of light phenomena.

The motivation extends beyond imaging. Fundamentally, understanding photon transport in disordered, optically thick ensembles is a prerequisite for addressing Anderson localization of light, the complete suppression of transport due to interference between multiple scattering paths. Demonstrating localization requires, as a prerequisite, precise knowledge of the transport properties, such as the mean free path, diffusion coefficient, and photon dwell time, directly within the medium. Therefore, measuring light diffusion in a controlled and well-characterized atomic ensemble provides an essential bridge toward localization studies.

4.1.2 Challenges in In Situ Probing

To understand the propagation of light deep inside an atomic cloud is not straightforward. Two major challenges stem from the most conventional methods for probing light transport in dense ensembles. First, excitation is usually introduced through the boundaries of the cloud. This makes it difficult to excite only the center of the medium and to follow the excitation before it reaches the edges. There had been no way to address the selective part of the atomic cloud and follow the excitation spatially.

Second, detection is typically performed after photons escape the boundaries. Boundary observables, such as transmission or global fluorescence decay, provide only indirect access to the dynamics inside the medium. These far-field signals average over the entire cloud, limiting both spatial and temporal resolution. For example, fluorescence decay can estimate photon dwell times, but it does not reveal how photon density spreads spatially during diffusion. Moreover, the detected signal is dominated by surface emission, while contributions from the interior, where multiple scattering is strongest, remain hidden.

The major problem is not only the detection method but also creating the excitation deep inside the optically dense atomic cloud. To overcome these challenges, we introduced a new experimental approach to directly prepare optical excitation in the deep core of our optically thick atomic sample of Yb and to directly record the excitation spatial distribution, as well as to follow it temporally by monitoring the internal state population. We extracted the diffusion parameters without relying on boundary effects, providing a more complete picture of light transport in dense, optically thick ensembles. The results not only validate theoretical models but also pave the way for precise control of light-matter interactions in complex quantum systems.

4.2 Theoretical Background

The propagation of light in an optically dense medium can be described with radiative transport theory. Under this theory, as photons travel through the medium, they undergo a series of random scattering events and eventually perform a random walk before leaving the medium. The cumulative effect of these random paths leads to diffusive propagation of light, characterized by the scattering mean free path (ℓ_s) is the average distance between two successive scattering events, transport mean free path (ℓ) is the average distance traveled by the wave before its direction of propagation is randomized, diffusion coefficient (D) which characterizes how quickly light spreads out

over time, and transport time (τ_{tr}). The opacity of the optically dense medium can be characterized by the resonant optical depth (b_0), defined as the ratio of the atomic ensemble size L to the mean free path ℓ_s, $b_0 \sim L/\ell_s$.

For a dilute medium ($b_0 \ll 1$), identified as the ballistic regime and illustrated in Fig. 4.1a, light propagation is well described by the Beer–Lambert law, with photons undergoing mostly single-pass absorption and re-emission. When the optical depth increases ($b_0 \gtrsim 1$), Beer–Lambert's exponential attenuation still holds in the forward direction, but the transmitted intensity becomes exponentially small. In this regime, multiple scattering dominates, and transport inside the medium must be described in terms of diffusion, as shown in Fig. 4.1b.

The transport is described by a diffusion equation[1]for the photon energy density $n(\mathbf{r}, t)$ with diffusion constant D [80, 81],

$$\frac{\partial n(\mathbf{r}, t)}{\partial t} = D\nabla^2 n(\mathbf{r}, t), \tag{4.1}$$

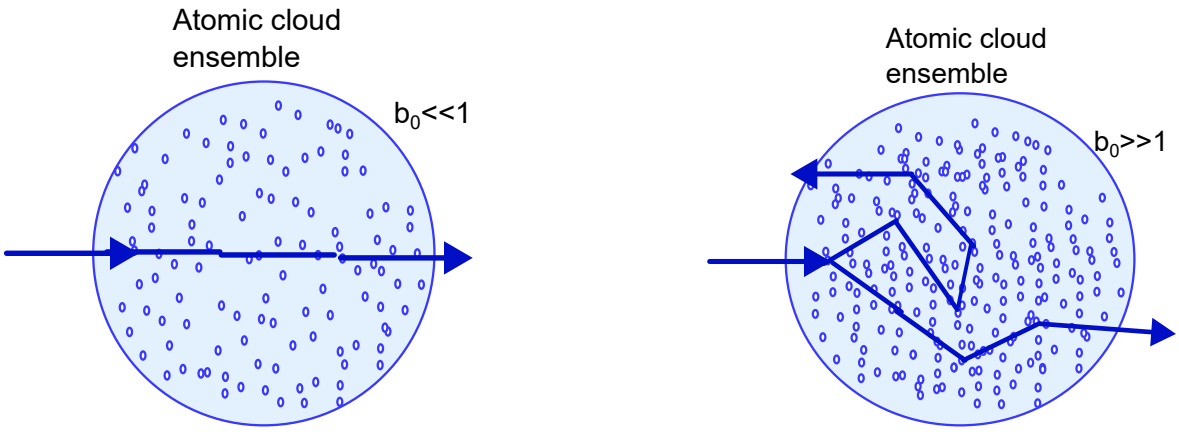

(a) Ballistic regime when mean free path length ℓ_s is larger than the size of the atomic ensemble r_0

(b) Multiple scattering regime when mean free path ℓ_s is smaller than the length of the atomic ensemble r_0

Figure 4.1: The transport regime is determined by the relation between the scattering mean free path ℓ_s and the atomic cloud size r_0.

4.2.1 Random walk model

The transport of photons in a strongly scattering medium can be modeled as a random walk, where each scattering event corresponds to a step of length ℓ_s. After many steps, the propagation converges to a diffusive regime described by Fick's law [82, 81]. The transport time can be defined as the propagation time between two subsequent scattering events and a waiting stage in which the electromagnetic energy resides in the scatterer (excited dipole) before being re-radiated.

[1]Following [81], absorption can be included in the diffusion equation via an additional decay term $-n/\tau_a$ where τ_a denotes the absorption time (i.e., the average time before absorption). For the ^{174}Yb $^1S_0 \rightarrow ^3P_1$ transition studied here is nearly closed, and absorption is negligible; we therefore focus on the lossless limit.

The total transport time per step can be written as follows,

$$\tau_{\mathrm{tr}} = \underbrace{\tau_w}_{\text{microscopic delay at the atom}} + \underbrace{\frac{\ell_s}{v_g}}_{\text{time between two scattering events}}. \tag{4.2}$$

Here, the microscopic waiting time is the Wigner time delay τ_w[83], associated with a single resonant scatterer, defined by the frequency derivative of the scattering phase shift, and ℓ_s/v_g is just the time it takes to cross one mean free path at the group velocity v_g. The flight time between scatterers is defined as,

$$\tau_{\text{flight}} = \frac{\ell_s}{v_g} = \frac{\ell_s n_g(\omega)}{c}, \tag{4.3}$$

The scattering phase shift is defined as the argument of the complex Lorentzian response $1/(\delta + i\Gamma/2)$, yielding the scattering phase shift is

$$\phi(\omega) = -\arctan\left(\frac{\Gamma/2}{\delta}\right), \tag{4.4}$$

with

$$\delta = \omega - \omega_0. \tag{4.5}$$

where ω is the angular frequency of the incident light and ω_0 is the atomic resonance frequency.

so the Wigner delay is given by

$$\tau_w(\delta) = \frac{d\phi}{d\omega} = \frac{\Gamma/2}{\delta^2 + (\Gamma/2)^2} = \frac{2/\Gamma}{1 + 4\delta^2/\Gamma^2}. \tag{4.6}$$

For an atomic gas of identical and independent scatterers of density ρ with scattering cross section $\sigma_s(\delta)$, the scattering mean free path is as follows,

$$\ell_s = \frac{1}{\rho\sigma_s}. \tag{4.7}$$

The transport mean free path [82, 81](including angular redistribution with θ defined as the scattering angle for a single scattering event) is

$$\ell_{tr} = \frac{\ell_s}{1 - \langle\cos\theta\rangle}, \tag{4.8}$$

and for the $J = 0 \to J' = 1$ dipole pattern probed on the intercombination line $^3P_1$, $\langle\cos\theta\rangle = 0$ shows isotropic transport, so $\ell_{tr} \approx \ell_s$. The scattering cross section of a two-level atom as a function of detuning is given by

$$\sigma_s(\delta) = \frac{\sigma_0}{1 + 4\delta^2/\Gamma^2}, \qquad \sigma_0 = \frac{3\lambda^2}{2\pi}. \tag{4.9}$$

Between scattering events, the probe propagates coherently in an effective medium described by the refractive index $n(\omega)$. The group velocity is

$$v_g(\omega) = \frac{c}{n(\omega) + \omega\,\frac{dn}{d\omega}} \equiv \frac{c}{n_g(\omega)}. \tag{4.10}$$

In a dilute, cold gas, the index is linked to the scalar susceptibility $\chi(\omega)$ [38] by

$$n(\omega) \simeq 1 + \frac{\chi(\omega)}{2}, \qquad \chi(\omega) = \frac{\rho\,\alpha(\omega)}{\epsilon_0}. \tag{4.11}$$

In the linear (weak-probe) regime of a two-level atom, the dispersion is determined by the real part of the polarizability, given by

$$\alpha(\delta) = -\frac{6\pi}{k^3}\frac{2\delta/\Gamma}{1+(2\delta/\Gamma)^2}. \tag{4.12}$$

Therefore,

$$n(\omega) \simeq 1 + \frac{\rho}{2\epsilon_0}\alpha(\delta). \tag{4.13}$$

So the group index becomes [38],

$$n_g(\omega) \simeq 1 + \frac{\rho}{2\epsilon_0}\left[\alpha(\omega) + \omega\frac{d}{d\omega}\alpha\right]. \tag{4.14}$$

Near resonance,the derivative $\omega\,\frac{d\alpha}{d\omega}$ is large and positive, so $n_g \gg 1$ and $v_g = c/n_g$ is strongly reduced. Off resonance $|\delta| \gg \Gamma$, both α and its slope vanish, so $v_g \to c$.

hence the total transport time per step is

$$\tau_{\rm tr}(\delta) = \frac{2/\Gamma}{1+4\delta^2/\Gamma^2} + \frac{\ell_s(\delta)}{v_g(\delta)}, \tag{4.15}$$

with

$$\ell_s(\delta) \approx \frac{1}{\rho\,\sigma_s(\delta)}. \tag{4.16}$$

Define the energy transport velocity v_E by the distance traversed per transport time:

$$v_E(\delta) = \frac{\ell_s(\delta)}{\tau_{tr}(\delta)}\,. \tag{4.17}$$

For isotropic transport $\ell_{tr} \simeq \ell_s$ and the diffusion constant is

$$D(\delta) = \frac{1}{3}v_E(\delta)\,\ell_{tr}(\delta) \simeq \frac{1}{3}\frac{\ell_s^2(\delta)}{\tau_{tr}(\delta)}\,. \tag{4.18}$$

Far from resonance when $|\delta| \gg \Gamma$ then $\tau_w \to 0$, $v_g \to c$, therefore, $\tau_{\rm tr} \approx \ell/c$. Near resonance ($|\delta| \lesssim \Gamma$), $\tau_w \approx 2/\Gamma$ dominates, $n_g \gg 1$ further slows flight, and $\tau_{\rm tr}$ is set by the atomic lifetime $\frac{1}{\Gamma}$. In other words, at resonance, most of the transport time is spent with the photon energy stored inside the atoms.

Beyond independent scattering: The situation becomes more subtle when the spatial density is large enough that the mean interatomic distance is comparable to the optical wavelength, resulting in resonant dipole–dipole interactions. These near-field couplings go beyond the independent-scatterer approximation of radiative transport theory and can modify the effective scattering cross-section and transport parameters [77].

In addition, at the mesoscopic level, interference between different scattered photon paths further enriches this picture. Reciprocal photon paths can interfere constructively,

resulting in coherent backscattering [74], which is visible as a cone of enhanced reflection. Subradiance and super-radiance appear in the temporal domain, as modifications of emission lifetimes, and also arise, even at relatively low densities [19]. At very high densities, interference may even halt transport altogether, the regime known as Anderson localization.

Altogether, the optical depth, detuning, and atomic density not only determine the scattering rate but also the extent to which collective and interference effects emerge. A complete understanding of light transport in cold atomic ensembles, therefore, requires both radiative transport theory and an account of collective dipole interactions. However, in our experiment, with spatial density $10^{12}\,\mathrm{cm}^{-3}$ (so $\rho\lambda^3 \simeq 0.17$, transport is governed by multiple scattering with a mean free path of order 7 μm ($k\ell \approx 77$). This places the system firmly in the diffusive regime, where collective dipole effects provide only minor corrections to photon transport. Our focus is therefore on measuring and modeling the diffusion process.

4.3 From Initial Idea to Method Development

The starting point for this work was a simple yet important observation about ytterbium's two primary optical transitions. The broad blue line

$$^1S_0 \rightarrow {}^1P_1, \qquad \Gamma_b \simeq 2\pi \times 29\ \mathrm{MHz}, \quad \text{lifetime} \sim 5.5\ \mathrm{ns}, \tag{4.19}$$

and the narrow green intercombination line

$$^1S_0 \rightarrow {}^3P_1, \qquad \Gamma_g \simeq 2\pi \times 184\ \mathrm{kHz}, \quad \text{lifetime} \sim 866\ \mathrm{ns}, \tag{4.20}$$

differ by nearly 160 orders of magnitude in lifetime. As a result, atoms excited to the green state remain in the $^3P_1$ level for almost a microsecond, during which they cannot participate in absorption on the blue transition. In other words, a population shelved in $^3P_1$ renders the medium effectively transparent to light resonant with the $^1S_0 \rightarrow^1 P_1$ line.

The underlying idea was to optically shift the $^3P_1$ transition using a dressing beam coupling $^3P_1 \rightarrow^3 D_1$ (as discussed in Chapter 3), while using an excitation beam on the $^1S_0 \rightarrow^3 P_1$ transition to create a localized excitation, and then detecting it through changes in absorption on the blue line. To test this approach, we first characterized the green MOT fluorescence and aligned a tightly focused excitation beam through the center of the MOT, with a beam waist smaller than the size of the MOT. In this initial test, no dressing beam was applied. We then took absorption images on the blue transition with an excitation (green) beam switched on and off (Figures 4.2a, 4.2b), loading a different MOT each time at $b_{0,g} = 5$. When computing the ratio of the two absorption pictures (Figures 4.2a/4.2b). The difference clearly reveals a localized reduction of absorption, corresponding to atoms transferred into the $^3P_1$ state (Figure. 4.2c). Each signal was averaged over 20 absorption images to improve the signal-to-noise ratio. For each absorption image, a fresh MOT was loaded. The spatial scale of the images is such that one CCD pixel corresponds to roughly 20 μm, while the FWHM of the MOT is on the order of 1 mm.

To verify that the excitation signal truly corresponds to the probe position, we deliberately displaced the tightly focused green excitation beam downward. Figure 4.3(a) shows the MOT fluorescence with a bright spot marking the excitation beam. Figure

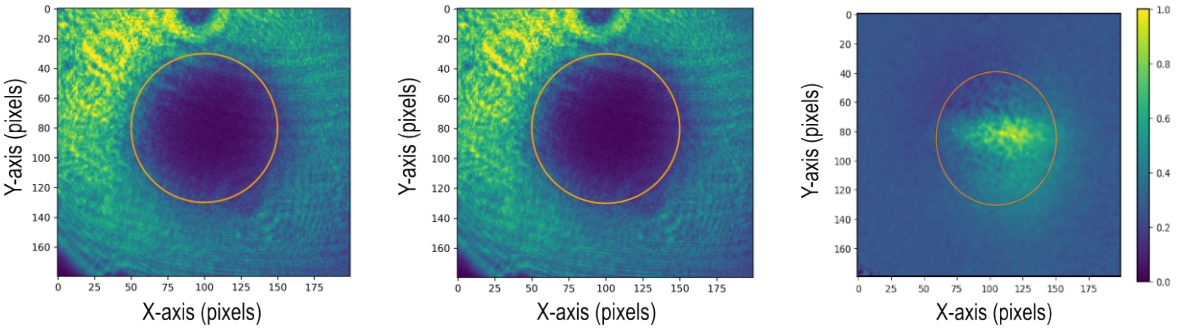

(a) Absorption image of the MOT on the strong ${}^1S_0 \rightarrow {}^1P_1$ transition with the green probe switched on.

(b) Reference absorption image under identical conditions but without the probe.

(c) The ratio of the two absorption images of (a) and (b), creating a visible localized excitation signal corresponding to atoms shelved in ${}^3P_1$ state.

Figure 4.2: (a) The absorption image on the ${}^1S_0 \rightarrow {}^1P_1$ transition with excitation beam applied, having depletion of atoms in the center due to missing ${}^3P_1$ population (this depletion is too small to be seen by eye). (b) Reference absorption image without excitation beam. (c) Atoms pumped into the metastable ${}^3P_1$ state become transparent to blue light in figure (a). Ratio of two absorption images with and without excitation beam showing the excited population in ${}^3P_1$ state (red circle indicates effective MOT size). Each image is averaged over 20 realizations. The image scale is such that one CCD pixel corresponds to approximately 20 μm, and the FWHM of the MOT is about 1 mm.

4.3(b) is the ratio of two absorption images on the ${}^1P_1$ (blue) transition, recorded with and without the excitation beam, which reveals a corresponding shift of the excitation spot, confirming that our method reliably tracks the probe position. To exclude possible artifacts, we repeated the measurement in the absence of the excitation probe beam and confirmed that no reduction in optical density was observed as shown in Figure. 4.3(c). Since each absorption image requires a fresh MOT loading cycle, shot-to-shot fluctuations in the atom number are unavoidable.

These early experiments laid the foundation for the in-situ method, which exploits the narrow green line to prepare localized excitations and probe their evolution indirectly through the strong blue transition. However, when the green probe is tuned to the free-space resonance of the ${}^1S_0 \rightarrow {}^3P_1$ transition, the excitation beam necessarily traverses the sample boundary and generates an extended excitation region. In this case, the excitation is not confined to the dense core of the MOT, and its spatial extent is too large to serve as a well-localized source.

To overcome this limitation, we employ off-resonant infrared dressing beams to optically shift the ${}^3P_1$ sublevels at the center of the cloud. By tuning the excitation beam frequency to the light-shifted resonance of the ${}^3P_1$ level, we can selectively address atoms deep inside the ensemble, thereby creating a compact and well-defined photon source within the medium.

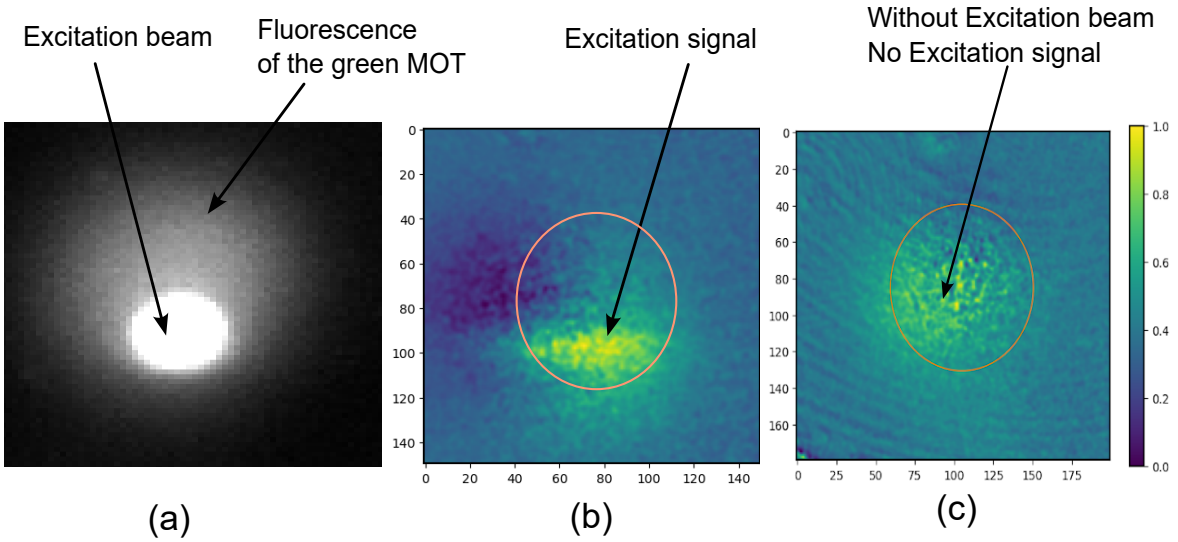

Figure 4.3: (a) Fluorescence image of the green MOT with the tightly focused green (or excitation) probe beam intentionally displaced downward. (b) Corresponding absorption image ratio ("with/without excitation probe"), showing the excitation signal shifted downward compared to the figure 4.2c. (c) The ratio of the two absorption images with the excitation beam blocked, showing no excitation signal. Each absorption image corresponds to a separate MOT loading cycle.

4.4 Light-Shift Calibration and Spatial Excitation Profiles

The relevant atomic transitions of ytterbium are shown in Figure 4.4. The excitation (green) beam addresses the ${}^1S_0 \rightarrow {}^3P_1$ intercombination line at $\lambda_g = 556\,\text{nm}$. The dressing beams couple ${}^3P_1 \rightarrow {}^3D_1$ at $\lambda_{\text{LS}} = 1539\,\text{nm}$. Far-detuned operation of these beams produces differential AC Stark shifts of the $m = \pm 1$ sublevels, which appear as shifted resonances in the probe spectrum. For calibration of the optical depth, the blue transition ${}^1S_0 \rightarrow {}^1P_1$ at ($\lambda_b = 399\,\text{nm}$) is used.

The experimental setup used to generate *in-situ* excitations deep inside the Yb atomic ensemble is illustrated in Fig. 4.5. The atoms are initially prepared in the ground state ${}^1S_0$. The ensemble is spatially dressed by two tightly focused infrared beams at 1539 nm (waist $\approx 300\ \mu$m), intersecting orthogonally at the MOT center with mutually orthogonal polarizations. An excitation beam at 556 nm, large enough to be approximated as a plane wave, then drives the ${}^1S_0 \rightarrow {}^3P_1$ transition shifted by the dressing fields. The resulting fluorescence is recorded on a CCD camera.

Both dressing beams are derived from the same seed laser, passing through the AOM operated at 80 MHz. While this introduces a frequency shift of 80 MHz to the diffracted light, the shift is irrelevant for our purposes; the AOMs are used solely as fast optical switches. Their extinction ratio, measured in our lab with a power meter, is better than 10^{-4}, ensuring negligible residual light between cycles. After passing through the AOM, the dressing beams are coupled to the polarization-maintaining fiber splitter (Thorlabs fiber splitter: TW1550R5A1) and delivered to the cell. This ensures identical frequency and power at the atomic sample. It simplifies the beam alignment. The excitation beam is also gated with an AOM, which provides a fall time of about 40 ns, fast enough for accurate synchronization with the dressing pulses.

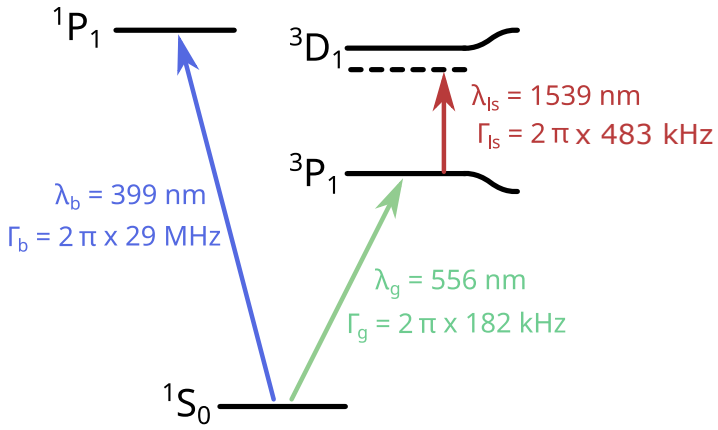

Figure 4.4: Energy-level scheme of ^{174} Yb relevant for creating localized excitations in a dense atomic ensemble.Off-resonant infrared dressing beams at 1539 nm couple the $^3P_1$ and $^3D_1$ states, inducing light shifts of the $^3P_1$ manifold. The narrow green inter-combination line ($^1S_0 \rightarrow {}^3P_1$, 556 nm) is then used to generate a localized excitation within the cloud, while the broad blue transition ($^1S_0 \rightarrow {}^1P_1$, 399 nm) is employed for absorption imaging to detect the presence and evolution of the excitation.

A crucial step is the alignment of the two infrared dressing beams passing through the dense atomic ensemble, which is arranged and focused in a crossed configuration, as illustrated in Fig. (4.5). The overlap region is chosen to coincide with the center of the atomic cloud, ensuring that excitations are generated where multiple scattering is strongest. Careful alignment is therefore essential to ensure that the fluorescence observed on the CCD originates from the dense central region of the ensemble rather than from the dilute wings.

To achieve this alignment, each dressing beam was first applied to the continuously loaded blue/green MOT while tuned on resonance with the $^3P_1 \rightarrow {}^3D_1$ transition. The resulting light shift moved the dressed atoms out of resonance with the MOT beams, producing a visible dark spot in the green MOT. This effect provided a rough reference for the initial beam positioning.

For fine alignment, we then applied the dressing beams simultaneously with the green excitation beam, tuned to the light-shifted resonance of the $^1S_0 \rightarrow {}^3P_1$ transition. In this case, only the atoms inside the overlap region scatter the probe, creating a localized fluorescence spot that allowed us to precisely steer the two beams into coincidence. Two CCD cameras placed at different angles were used to monitor this alignment; one is shown in Fig. (4.6), while the second, positioned orthogonally, is not depicted in the schematic.

The two dressing beams were applied simultaneously with equal frequency and power, thereby locally shifting the $^3P_1$ level. When the weak excitation beam was tuned to the light-shifted resonance, the CCD detected fluorescence only from atoms whose transitions were shifted into resonance by the presence of the two light beams. The apparent difference in their shapes arises solely from the camera's line of sight: dressing beam 2 is aligned along the imaging axis and therefore projects as a circular bright spot (or a thin ring if slightly detuned), while the transverse dressing beam 1 is seen in projection as a horizontal stripe [Fig. 4.6(a)]. When both beams are spatially overlapped inside the atomic cloud, their fluorescence signals merge into a single bright spot at the center of the elongated spot as shown in [Fig. 4.6(b)], confirming correct

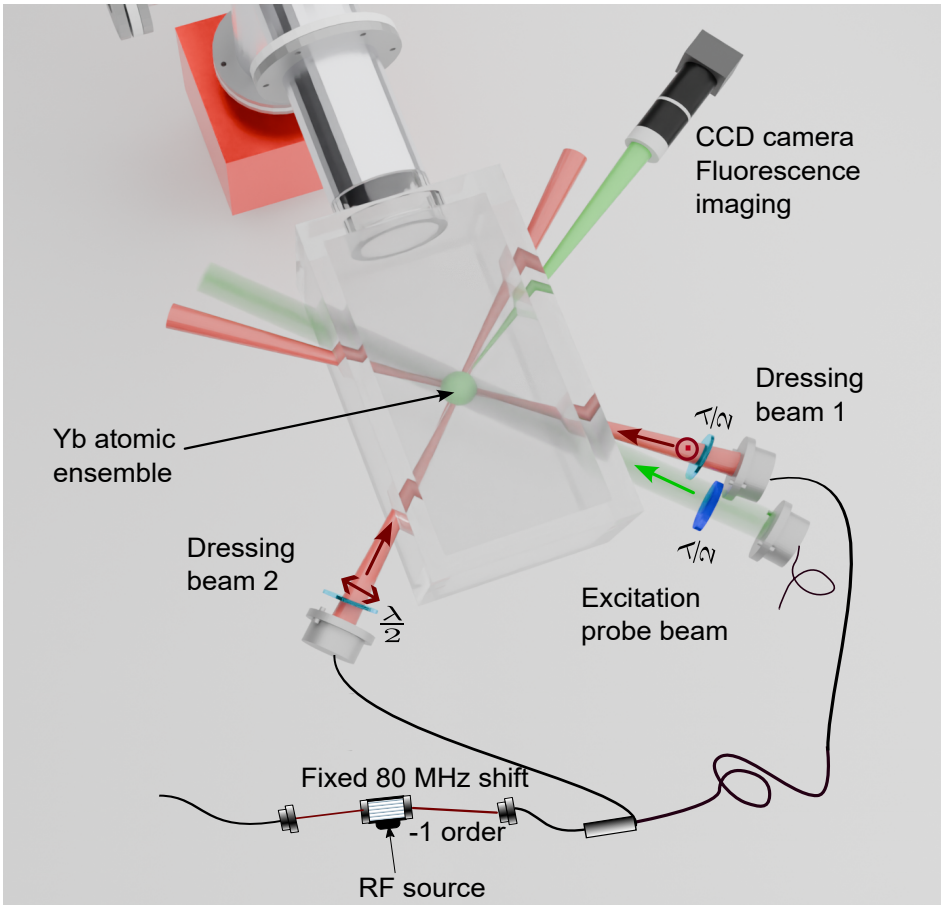

Figure 4.5: Two infrared dressing beams are focused and crossed at the center of the cold ytterbium ensemble, with typical waists of about 300 μm. A weak green excitation probe, resonant with the ${}^1S_0 \rightarrow {}^3P_1$ transition, overlaps the same region to create localized excitations. The resulting fluorescence is collected with a CCD camera, providing both alignment feedback and a direct measure of the induced light shift. The crossed geometry of the dressing beams ensures a selective addressing deep inside the dense atomic Yb ensemble.

alignment.

Strictly speaking, the probe frequency corresponding to the light-shifted resonance differs between panels (a) and (b), since the combined shift in (b) is approximately twice that in (a). In practice, however, we used the same probe detuning as in panel (b). This choice implies that the excitation in panel (a) is not exactly resonant, but the residual fluorescence remains sufficient to reveal the position of the dressed region for alignment purposes. By scanning the excitation frequency, we selectively address atoms in this overlapped region, where the light shift results from the combined contribution of both dressing beams.

In terms of the level scheme, the observed fluorescence originates only from atoms whose ${}^3P_1$ sublevels are shifted into resonance by both dressing beams, providing a direct, visual confirmation that the optical fields are properly overlapped and interacting with the relevant atomic states. This overlap is crucial to ensure that the two dressing fields produce a well-defined, localized excitation volume at the trap center, which forms the starting point for the diffusion measurements.

The overlap of the two dressing beams was verified from CCD fluorescence images.

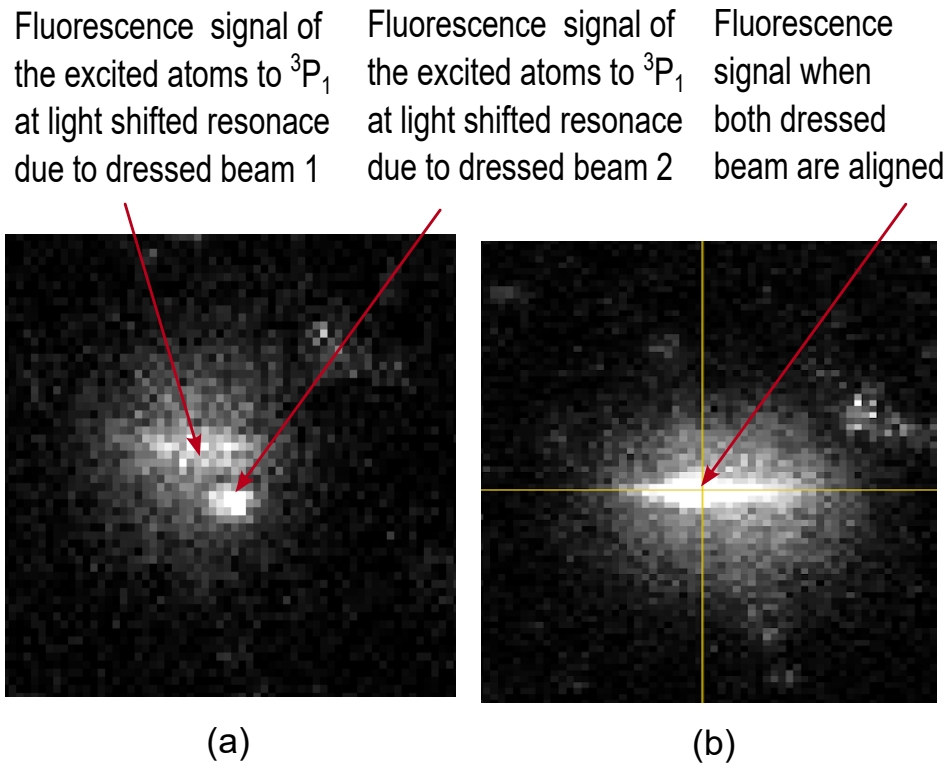

Figure 4.6: Fluorescence-based alignment of the two dressing beams. (a) Fluorescence image of the cloud when the probe is tuned to the light-shifted resonance created by both dressing beams. Because the CCD camera is positioned along the axis of dressing beam 2, that beam appears as a nearly circular spot at the cloud center, while dressing beam 1 traverses horizontally across the ensemble. (b) Same configuration after fine steering to overlap the two dressing beams. The merged fluorescence now forms a single elongated spot at the cloud center, confirming that both beams intersect inside the atomic ensemble. Yellow crosshairs mark the MOT center used as the alignment reference.

With a pixel size of ($20\,\mu$m), we compared horizontal and vertical line profiles from the single beam images. Co-alignment was achieved when the centroids agreed within 1-2 pixels ($\lesssim$ 20-40 μm) and the spot is symmetric. We scan the frequency of the excitation beam across the light-shifted resonance in the presence of both dressing beams to find the required waist of the excitation spot (r_{exc}).

The two benefits of the crossed-beam configuration of the dressing beam are as follows,

1. It ensures that the initial excitation is created in the deep core of the atomic ensemble, where multiple scattering is strongest, and avoids the issues encountered due to boundary effects

2. It creates a compact and nearly symmetric photon source (excitation radius $\sim$ 50–70 μm, see Sec. 4.6). When the optical depth is varied—either by reducing the number of loaded atoms or by allowing a longer time of flight- the cloud position and size change. In this case, the fluorescence signal provides direct feedback for realigning the dressing beams onto the atomic cloud.

4.4.1 Light shift calibration

To quantify the light shift of the $^3P_1$ manifold state induced by two infrared dressing beams in a crossed configuration (as discussed in the previous section), we use beams with a waist of about 300 μm on the atomic cloud. This choice represents a compromise; the beams are tightly focused enough to produce a position-dependent light shift and a localized excitation on the micrometer scale, while still being technically achievable with standard laboratory optics at moderate laser powers of ~ 60 mW. The same CCD camera can be used to record fluorescence spectra with the dressing beam at fixed power and detuning, scanning the frequency of the excitation beam across the light-shifted resonance.

In the previous chapter 3, the dressing beam had a waist of approximately 1 mm, which was larger than the MOT size. Although the shift was nearly uniform, the residual Gaussian intensity profile still introduced inhomogeneous broadening. To minimize its effect, we restricted our analysis to a small central region of interest. In the present configuration, the dressing beams are tightly focused with a waist smaller than the MOT ($\sigma \approx 600$ μm). In this case, only the central atoms are dressed, while the wings remain unshifted; therefore, we analyze the relative fluorescence from this central region, where the dressing effect is strongest.

We computed the normalized signal for each recorded image on the CCD camera as

$$S(\delta) = \frac{\sum_{\text{signal ROI}} I(x, y; \delta)}{\sum_{\text{MOT region}} I(x, y; \delta)}, \tag{4.21}$$

where $I(x, y; \delta)$ is the fluorescence intensity at a particular frequency of the excitation beam δ. The "signal ROI" and "MOT region"is defined as $100 \times 100\,\mu\text{m}^2$ and $2000 \times 2000\,\mu\text{m}^2$ respectively. The "signal ROI" is centered on the dressed excitation spot. In other words, the fluorescence signal of the ROI was normalized to the total cloud fluorescence. This ratio suppresses shot-to-shot fluctuations in the number of atoms. We first analyzed the light shift of the $^3P_1$ manifold as a result of one dressing beam ON. We first determined the light shift $^3P_1$ as a function of the dressing beam power. We recorded the fluorescence of the atomic ensemble by scanning the frequency of the excitation beam across the free-space resonance while keeping the dressing beam ON at fixed detuning and power. This measurement has been repeated and recorded for several dressing powers. For each set of data, the recorded image was analyzed by integrating the fluorescence within a small region of interest (ROI) centered on the dressed excitation spot, and normalizing this signal to the total MOT fluorescence recorded in the same frame.

We scan the frequency of the excitation beam at different dressing beam power, the resulting spectra for dressing powers from 65 to 147 mW are illustrated in Figure 4.7a. Each spectrum corresponds to the normalized fluorescence signal of the center region of interest to the total fluorescence of the MOT as a function of excitation beam detuning. The resonance peaks are shifted towards the negative (red) detuning, as expected from the light shift derived in the previous chapter 3, given by $\Delta' \propto -\frac{I}{\Delta_{\text{LS}}}$ where I is the dressing beam intensity and Δ_{LS} is its detuning from the $^3P_1 \rightarrow {}^3D_1$ transition.

From each spectrum, we extracted the light shift (represented by the resonance peak). The extracted light shift from the spectra shown in Figure (4.7a) is plotted against the dressing beam power in Figure (4.7b). The dashed line is a linear fit. The light shift increases in magnitude approximately linearly with dressing beam power with a slope of about -0.023 MHz/mW at specific detuning.

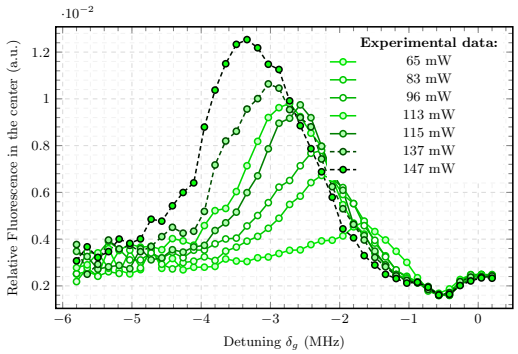

(a) Normalized fluorescence spectra recorded as a function of excitation beam detuning for different dressing beam powers. Each spectrum is obtained by dividing the fluorescence collected in a small ROI at the center of the cloud by the total MOT fluorescence in the same shot.

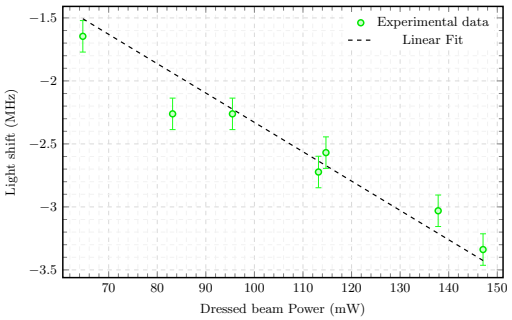

(b) Extracted resonance centers plotted versus dressing beam power. A linear fit (dashed line) confirms the expected proportionality of the light shift to the dressing power.

Figure 4.7: Calibration of the light shift induced by the dressing beam. As the dressing power increases, the radius of the shifted region decreases, leading to a more localized excitation and thus an enhanced relative amplitude of the central signal.

Spatial profile of the excited atoms in the light shifted $^3P_1$ state When the size of the dressing beam is smaller than the size of the MOT. The dressing beam intensity is not uniform throughout the atomic cloud. Then, the dressing beams from $^1S_0 \rightarrow {}^3P_1$ transition shift the $^3P_1$ state locally inside the atomic cloud. Consequently, the $^3P_1$ state is shifted by an amount $U(r) \propto \frac{I_{\mathrm{LS}}(r)}{\Delta_{\mathrm{LS}}}$ at the trap center ($r = 0$), depends on both the local intensity $I_{\mathrm{LS}}(r)$ of the dressing beams and their detuning Δ_{LS}. It should create a spatially varying potential across the MOT center. When the excitation beam frequency is scanned, atoms are optically excited only in the region where the shifted atomic transition matches the probe frequency. That means if we tune the excitation beam to the unshifted free-space resonance, we should be able to address the whole cloud except the very center of the cloud, where the dressing beam is focused. If we tune the excitation beam to the shifted resonance, we should be able to selectively excite only the atoms at the center of size given by $r_{\mathrm{exc}} \sim w_{\mathrm{LS}}\sqrt{\frac{\hbar\Gamma_g}{2|U|}}$[2]. The excitation size can be made much smaller than the size of the atomic cloud by varying the waist of the dressing beam (w_{LS}) or by increasing $|U|$. We choose the dressing beam waist in such a way that $r_0/r_{\mathrm{exc}} \sim 10$ where r_0 is the rms size of the atomic cloud. This ensures sufficient scattering events and collects an adequate excitation signal. The mechanism is visualized experimentally and discussed in the four characteristic cases of the fluorescence single shot as illustrated in Figure 4.8(b). It experimentally demonstrates how the light shifts induced by the focused dressing beams defined the spatial excitation landscape within the atomic cloud.

The linewidth of the $^3D_1$ state is $\Gamma_{\mathrm{LS}} = 2\pi \times 483$ kHz. The infrared dressing beams are detuned by $\Delta_{\mathrm{LS}} \sim -6$ GHz from the $^3P_1 \rightarrow {}^3D_1$ transition, such that $|\Delta_{\mathrm{LS}}| \gg \Gamma_{\mathrm{LS}}$.

[2]See Appendix B for derivation.

In this far-detuned regime, the off-resonant scattering rate $\Gamma_{\rm sc} \approx \left(\frac{\Omega^2}{8\Delta_{\rm LS}^2}\right)\Gamma_{\rm LS}$ of $\sim 50\ {\rm s}^{-1}$, each atom scatters < 0.05 photons during a 1 ms dressing window, rendering dressing-induced scattering negligible for our measurements, and the dominant effect of the dressing beams is the light shift. At the trap center, the induced shift is experimentally estimated to be $|U(r=0)| \sim 15\,\hbar\Gamma_g$, obtained with a dressing beam power of ~ 60 mW. To provide a qualitative demonstration of this technique, we directly map the light-shift potential $U(r)$. For this, we image the fluorescence emitted at 556 nm after applying a short excitation pulse of duration $t_{\rm fluo} = 1$ ms, while scanning the excitation frequency ω. The spatial dependence of the resonance across the cloud reveals the local Stark shift, which provides a direct mapping of the optical potential induced by the dressing beams, as illustrated in Fig. 4.8(b). The observed potential profile closely follows the Gaussian intensity distribution of the crossed infrared beams.

In the figure 4.8(a), a schematic illustration is shown. The frequency of the $^3P_1$ state is locally shifted downwards by an amount $U/\hbar$ at the trap center in the presence of the dressing beams.

In panel 4.8(b), four characteristic cases are experimentally illustrated depending on the excitation probe frequency ω. The images are shown in false color, normalized to their own maximum intensity, so that only the spatial distribution is highlighted rather than the absolute signal level. 1) When the probe is tuned far from resonance ($\omega = \omega_1$) where $\omega_1 \sim \omega_g - \frac{|U|}{\hbar} - 10\Gamma_g$ and $\omega_g = \frac{2\pi c}{\lambda_g}$, excitation is strongly suppressed across the cloud. Only atoms located at the very center, where the light shift is largest, remain slightly closer to resonance and thus contribute a weak residual fluorescence. 2) At the shifted resonance ($\omega = \omega_g - U$), a compact and well-defined spot of radius $r_{\rm exc} \sim 60\ \mu$m appears in the MOT center. This is a direct demonstration of a non-invasive optical method, where atoms are selectively excited deep within the very center of an optically thick medium, without addressing the outer regions of the cloud. 3) For intermediate detunings ($\omega = \omega_3$) with $\omega_3 = \omega_g - \frac{|U|}{\hbar} + 6\Gamma_g$, excitation occurs in a ring-shaped shell, reflecting the radial dependence of the light shift. 4) Finally, at the bare resonance ($\omega \approx \omega_g$), the excitation extends across the entire cloud, with a characteristic size $r_0 \sim 600\ \mu$m matching the MOT radius, giving rise to a broad halo with radius r_0. The corresponding spatial fluorescence profiles along a horizontal cut for the four excitation frequencies from the panel 4.8(b) are shown in Fig. 4.8(c), highlighting the progressive change of the optically excited atoms evolves from localized to extended region as the probe frequency is varied. 4.8(d) plots the relative fluorescence in the central ROI as a function of probe detuning, revealing a clear maximum at $\omega_g - U$, which we identify as the light-shifted resonance.

This highlights how the careful use of different atomic levels, combined with already well-understood physics, can be leveraged to create a powerful tool for engineering a truly non-invasive method that spatially addresses atoms deep inside an optically thick cloud, thereby avoiding boundary effects.

Mapping of the light-shifted potential landscape inside the dense atomic ensemble: This approach not only provides a source of photons deep inside the atomic cloud but also offers a direct way to map the spatial structure of the optically induced potential. By scanning the excitation probe frequency, we select different iso-potential contours of constant light shift, and atoms fluoresce only where their local Stark shift matches the probe frequency. By recording fluorescence images over a range

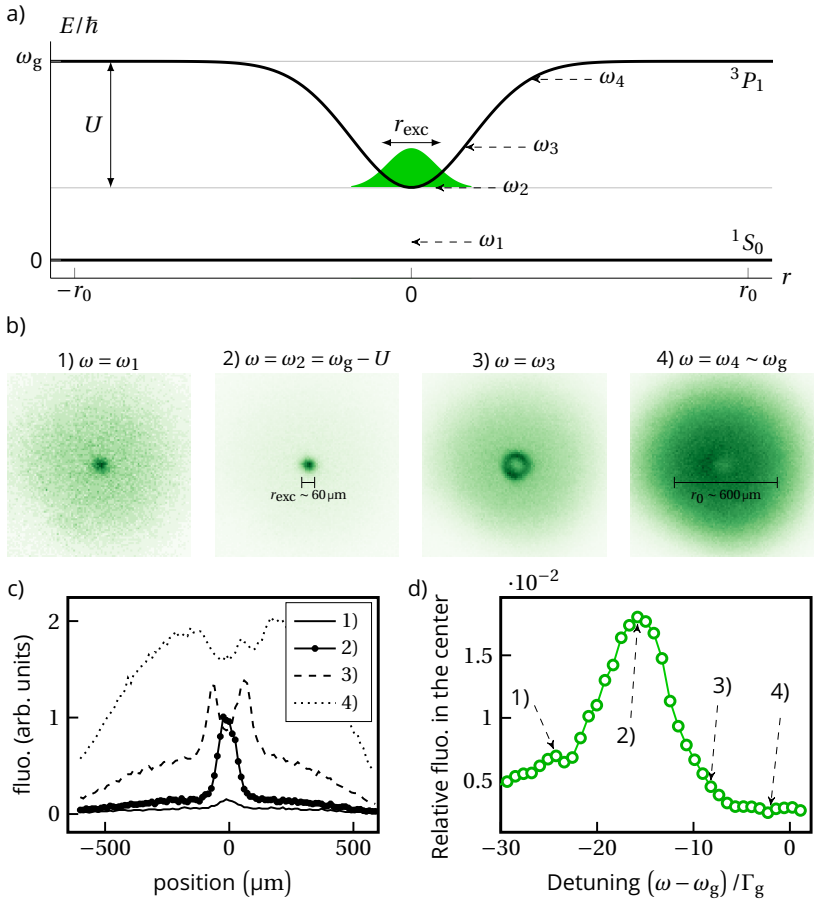

Figure 4.8: Spatially resolved excitation profiles of the light-shifted $^3P_1$ state. (a) Effective level diagram: the excitation beam detuning selects different spatial regions of the light-shifted potential of the $^3P_1$ state. (b) Single-shot fluorescence images (normalized, false color) recorded at four excitation beam frequencies illustrated: (1) weak off-resonant excitation $\omega_1 \sim \omega_g - \frac{|U|}{\hbar} - 10\Gamma_g$, (2) compact central excitation spot ($r_{\mathrm{exc}} \sim 60\,\mu$m) at $\omega_2 = \omega_g - \frac{|U|}{\hbar}$, (3) ring-shaped excitation at $\omega_3 = \omega_g - \frac{|U|}{\hbar} + 6\Gamma_g$, and (4) nearly uniform MOT excitation ($r_0 \sim 600\,\mu$m) except the central spot of size ($r_{\mathrm{exc}} \sim 60\,\mu$m) at $\omega_4 \sim \omega_g$. The peak optical density $b_{0,g}$ is 20. (c) Vertical fluorescence cuts of images of panel (b) illustrating the profile evolution. (d) Normalized fluorescence spectra versus excitation beam detuning, highlighting the resonance condition for compact localized excitation of size ($r_{\mathrm{exc}} \sim 60\,\mu$m) at $\omega_2 = \omega_g - \frac{|U|}{\hbar}$.

of detunings, one reconstructs the geometry of the potential well carved by the dressing beams.

1) This feature is especially useful in dense samples, where direct beam profiling inside the cloud is otherwise impossible.

2) The fluorescence images in Fig. 4.8(b) provide a tomographic picture of the light-shifted potential landscape generated by the crossed dressing beams. By calibrating the excitation detuning to the local Stark shift, these images could in principle be converted into a quantitative map of the potential (in MHz). Here, however, we restrict ourselves to presenting the qualitative profiles.

3) This gives a tomographic view of where atoms are brought into resonance, which is quite powerful.

4.5 Excitation detection spatially and temporally

We demonstrated a way to create and visualize the excitation inside the dense cold atomic cloud using the fluorescence imaging on the narrow $^3P_1$ transition. This method is useful to create an excitation but not sufficient to follow it temporally because the fluorescence detection window $t_{\text{fluo}} = 1$ ms is much longer (to collect sufficient signal, the geometric collection efficiency of the system is determined by the 1-inch diameter aperture placed at a distance of 35 cm from the atomic cloud is given by of 0.02 %, the quantum efficiency of CCD camera (BFS-U3-50S5M-C) [84] is 62% @532 nm) than the natural evolution time of the excited state, $\tau_g = 1/\Gamma_g \approx 866$ ns, this approach cannot resolve the fast temporal dynamics of the system. Instead, it provides a time-averaged/ static picture of the spatial distribution of the excitation but lacks temporal resolution. To understand the propagation of photons inside the atomic ensemble, it is

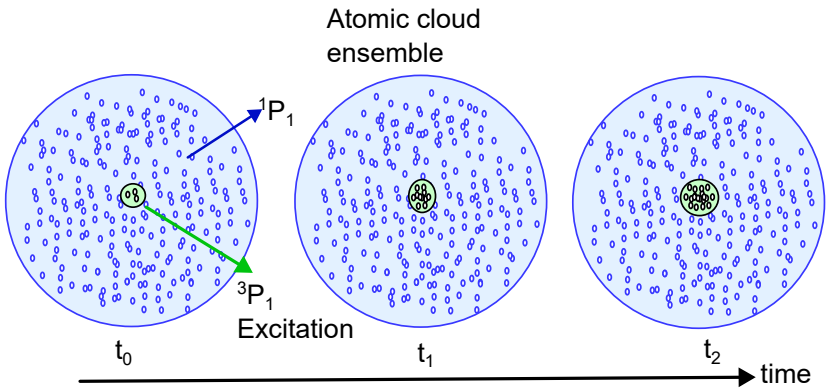

Figure 4.9: Schematic of the excitation and in-situ imaging sequence. A narrow-line excitation pulse transfers a fraction of atoms from the ground $^1S_0$ state into the excited $^3P_1$ state. After the excitation pulse ends, photons created inside the cloud undergo multiple scattering and spread outward. Short absorption images on the broad $^1S_0 \rightarrow {}^1P_1$ line (blue pulses) are taken at a sequence of delays t_0, t_1, t_2 to stroboscopically sample the spatial profile of the excited-atom density $\rho_e(x, y, t)$. Comparison of images with and without the excitation yields the evolution of the excitation (see text).

crucial to follow how the initial excitation evolves in space with time. We particularly want to distinguish between ballistic propagation and diffusive transport (multiple scattering events). This necessitates resolving both the mean-squared displacement (MSD) of the excitation and the decay of the excited population with ~ 100 ns precision. The approach to detect photons outside the atomic cloud washes out these dynamics. Therefore, we choose an alternative approach, rather than detecting the emitted photon outside the cloud. We can directly probe the depletion of the ground-state population caused by excitation to the $^3P_1$ transition through absorption imaging on the broad transition ($^1S_0 \rightarrow {}^1P_1$) with high temporal resolution. It can provide indirect access to the atomic density excited to the narrow transition without actually probing this transition. The broad transition is well suited for this purpose with a natural lifetime of ~ 5 ns . The time scale of diffusion is much longer than the time resolution, which is $\tau_g/150$. Therefore, it is possible to resolve the photon dynamics on the intercombination line with sufficient temporal precision and to record snapshots of the excitation evolution, as illustrated in Fig.(4.9).

It summarizes the measurement principle used to follow photon propagation *in*

situ. We create a small source of $^3P_1$ excitations at the trap center using the method explained in the last subsection. After the excitation pulse, the sample is interrogated at chosen delays using short (150 ns) absorption pulses on the broad 399 nm transition. By comparing images recorded with and without the excitation, we extract the density of excited atoms integrated along the imaging direction. Repeating these measurements for increasing delay times after the excitation pulse can map the spatial and temporal evolution of the excitation, thus providing a direct probe of photon diffusion within the dense ensemble. We moved from time-averaged fluorescence detection to time-resolved absorption imaging. It forms the basis of the results presented in the next subsection, where we extract transport parameters such as the diffusion coefficient and transport velocity directly from the measured dynamics.

4.5.1 Experimental setup and Timing sequence

The experimental setup for probing light diffusion in the ytterbium atomic ensemble is illustrated in Fig. (4.10).

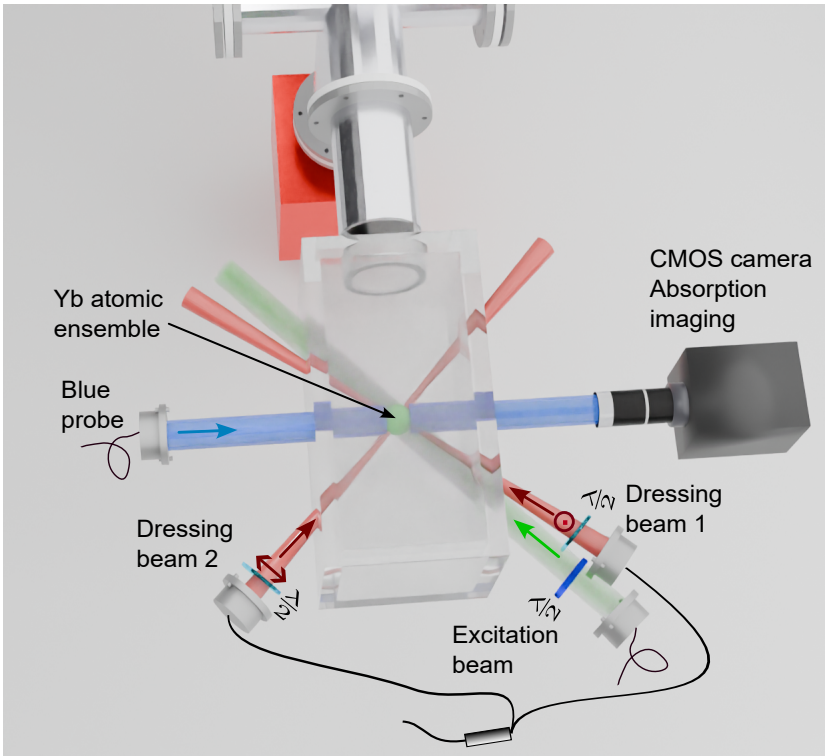

Figure 4.10: **Experimental setup for in-situ probing of light diffusion.** A cold atomic ensemble of ^{174}Yb is prepared in the center of the vacuum glass cell. Two crossed dressing beams (red) with orthogonal polarization shift the $^3P_1$ levels at the trap center. An excitation pulse of duration 10 µs on the $^1S_0 \rightarrow {}^3P_1$ (green) transition locally creates excitation inside the cloud. A short blue probe pulse (blue) of duration 150 ns is used for absorption imaging on a CMOS camera [85], providing time-resolved maps of the excited population. The excitation beam is roughly perpendicular to the absorption imaging beam. A Digital Delay Generator (SRS) controls the timing of all optical pulses, with its outputs connected to the AOMs that gate each beam, ensuring precise synchronization and high extinction.

The cold atomic ensemble of Yb is prepared and cooled down to about 15 μK

temperature in the center of the vacuum glass cell with spatial density $\sim 10^{12}\text{cm}^{-3}$. An excitation beam (556 nm, green) is used to create optically excited atoms localized in the center of the MOT, whose resonance is shifted in the trap center by two orthogonally crossed dressing beams at (1539 nm, red). Both the dressing beams are derived from the same seed laser and are fiber-delivered using a polarization-maintaining fiber splitter with orthogonally polarized fibers. The evolution of the excited population is monitored by absorption imaging on the broad transition at $\lambda = 399$ nm. Owing to its short natural lifetime ($\tau \sim 5$ ns) and correspondingly high scattering rate. This enables the use of very short probe pulses (blue) of up to 150 ns without compromising the recorded absorption signal on a high-speed CMOS camera positioned along the axis of the probe beam.

To monitor the diffusive transport of photons inside the dense medium, we implemented the timing sequence illustrated in Fig. (4.11). Each cycle began with the loading of a magneto-optical trap of a cold Yb ensemble, as explained in Chapter 2, followed by a short time-of-flight duration, depending on the required optical depth.

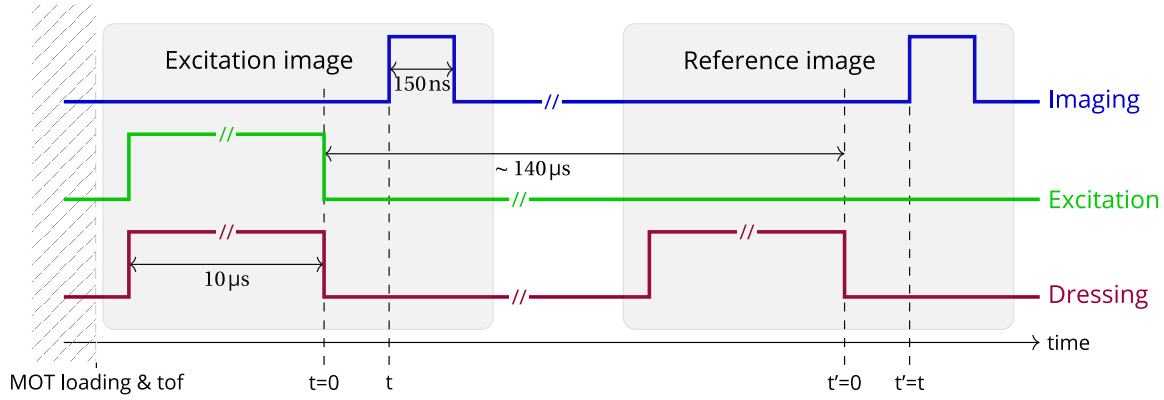

Figure 4.11: **Chronogram for diffusion measurements.** After MOT loading and time-of-flight expansion. For the excitation ("exc") absorption image, the excitation beam together with dressing beams is applied for typically ~ 10 μs to reach a steady state. At a chosen time t, the evolution of the excitation is probed by a short 150 ns absorption-imaging pulse on the strong transition ${}^1S_0 \rightarrow {}^1P_1$ (blue). A reference image ("ref") is acquired under identical conditions but without excitation. A "dark" image without light is also taken, allowing background subtraction. An experimental image is the ratio of the two absorption images, one with excitation and the other without excitation. Repeating this sequence for different delays builds a time-resolved picture of light diffusion inside the atomic cloud.

The two dressing beams (red) are applied for a duration of 10 μs. During this interval, an excitation beam pulse (556 nm) excites atoms into the light-shifted ${}^3P_1$ state, generating a localized excitation of size 60µm in the cloud center. The green excitation pulse is typically 10 μs long, ensuring that a steady-state population is established before probing.

At a variable delay time t after the end of the excitation beam, a short blue probe pulse of duration 150 ns is sent through the cloud. This duration is much shorter than the natural lifetime of the ${}^3P_1$ state ($\tau_g \approx 866$ ns), effectively freezing the dynamics of the narrow transition and providing a snapshot of the excitation at time t. The transmitted blue light is recorded on the CMOS camera, yielding what we call the excitation image ("exc").

To suppress shot-to-shot fluctuations in atom number, each excitation image is paired with a reference image. Both images (excitation and reference images) are taken on the same atomic sample. The shortest delay achievable between the two exposures is set by the CMOS camera readout time (~ 100 μs). The "dark" image, taken without light, is also captured, allowing for background subtraction. The ratio of excitation to reference images directly isolates the spatial distribution of atoms in the excited $^3P_1$ state, resulting in a movie of the excitation dynamics inside the dense cloud, with spatial resolution set by the imaging optics.

The imaging system was calibrated for optical density and provides a spatial resolution of ~ 22 μm, which is well below the initial excitation radius ($r_{\mathrm{exc}} \approx 60$ μm). This resolution is therefore sufficient to resolve the diffusive broadening of the excitation profile while still maintaining enough signal per pixel. By repeating the sequence, we can follow the excitation up to about $3\tau_g$ after the end of the excitation pulse.

Choice of blue probe parameters The broad line has a large saturation intensity ($I_{\mathrm{sat},b} \approx 60$ mW/cm^2), so we can send several mW of probe power in a cm-scale beam without saturating the atoms, while still obtaining sufficient absorption signal on the camera. For very optically thick samples on the broad line ($b_{0,b} \gtrsim 11$), the transmitted intensity can approach the 16-bit noise floor. In that case, we detune the blue probe slightly to reduce $\sigma_{\mathrm{sc},b}$ while maintaining the same effective optical thickness on the narrow line.

4.5.2 Principle of the time-resolved absorption imaging

As discussed, the basic idea is probing the population of the ground-state atoms $^1S_0$ directly; all the atoms in the ground state will strongly scatter light on the broad transition, and any missing fraction of atoms will correspond to atoms optically pumped into the $^3P_1$ state. By comparing two absorption images, one with the excitation applied ("exc") and one without ("ref"), the missing fraction corresponds directly to excitation in $^3P_1$.

Let the blue probe with incident intensity I_0 is traversing through the cloud along the z-axis, the transmitted intensity at position (x, y) and time t is given by

$$I_{\mathrm{exc/ref}}(x, y, t) = I_0 \exp\Big[- b_{\mathrm{exc/ref}}(x, y, t)\Big], \tag{4.22}$$

where $b_{\mathrm{exc/ref}}(x, y, t)$ is the optical depth along z. Here, "exc" denotes the case where the excitation beam is applied, while "ref" corresponds to the reference image taken without excitation.

The optical depth can be written as the integral of the ground-state density,

$$b_{\mathrm{exc/ref}}(x, y, t) = \sigma_{\mathrm{sc},b} \int \rho_{\mathrm{exc/ref}}(x, y, z, t)\, dz, \tag{1}$$

with $\sigma_{\mathrm{sc},b}$ the resonant scattering cross section for the broad transition.

The difference between the two cases arises because a fraction of atoms is transferred into the $^3P_1$ state during excitation. These atoms are dark to the imaging beam and, therefore, reduce the apparent optical density on the broad transition. The excited-state density can be defined as follows

$$\rho_e(x, y, z, t) = \rho_{\mathrm{ref}} - \rho_{\mathrm{exc}}, \tag{2}$$

Equivalently, we can write

$$\rho_{\mathrm{exc}} = (1-\alpha)\,\rho_{\mathrm{ref}}, \quad 0<\alpha<1, \tag{4.23}$$

where $\alpha(t)$ is an excitation parameter describing the fraction of atoms pumped out of the ground state at time t.

We see that the excited population is directly encoded in the difference of optical depths. If the difference between the two optical depths is small ($b_{\mathrm{ref}} - b_{\mathrm{exc}} \ll 1$), then the ratio of transmitted intensities can be linearized:

$$\frac{I_{\mathrm{exc}}(x,y,t)}{I_{\mathrm{ref}}(x,y,t)} \approx 1 + \sigma_{\mathrm{sc},b} \int \rho_e(x,y,z,t)\,dz. \tag{3}$$

Thus, the simple ratio of two absorption images (with and without excitation) yields the column density of excited atoms integrated along the imaging axis.

To further simplify the analysis, we assume that the excited population can be factorized into transverse and longitudinal parts,

$$\rho_e(x,y,z,t) = \rho_{e,\perp}(x,y,t)\,\rho_{e,z}(z,t). \tag{4.24}$$

This approximation is justified by the nearly spherical symmetry of the cloud in 3D, which allows the transverse profile and the longitudinal evolution to be treated independently to first order. The integral along z can then be absorbed into a time-dependent prefactor,

$$K(t) = \int \rho_{e,z}(z,t)\,dz, \tag{4.25}$$

so that

$$\frac{I_{\mathrm{exc}}(x,y,t)}{I_{\mathrm{ref}}(x,y,t)} \approx 1 + \sigma_{\mathrm{sc},b}\,K(t)\,\rho_{e,\perp}(x,y,t). \tag{4}$$

This expression shows that the two-dimensional imaging signal directly maps the transverse distribution of the excited atoms, up to an overall scaling factor $K(t)$. By fitting the 2D profiles with Gaussian functions, we can extract both the width $r(t)$ and amplitude $A(t)$ of the excitation cloud. Their time evolution encodes the underlying photon transport dynamics, broadening corresponds to diffusion, while the decay of the amplitude reflects the finite excited-state lifetime and the escape of photons from the medium.

In a more intuitive picture, the ratio of transmitted intensities becomes

$$\frac{I_{\mathrm{exc}}(x,y,t)}{I_{\mathrm{ref}}(x,y,t)} = 1 + \alpha(t)\,K_{x,y}, \tag{4.26}$$

a dimensionless form, where $\alpha(t)$ is an "excitation parameter" ($0<\alpha<1$) that captures the time-dependent fraction of atoms pumped into the $^3P_1$ state, while $K_{x,y}$ encodes the static geometry of the system. Since the excitation spot size r_{exc} is much smaller than the MOT radius r_0 ($r_{\mathrm{exc}} \ll r_0$), the surrounding atomic cloud acts as a large reservoir. Over the short timescales considered, the optical density of this reservoir remains essentially constant. Therefore, only the small central region where atoms are transferred to $^3P_1$ contributes to the observed change in OD, while the background OD can be treated as static.

4.6 Experimental Data

4.6.1 Method of data acquisition and processing

Our observable ρ_e is the small fraction of atoms optically excited to the $^3P_1$ state by the green excitation pulse. These optically excited atoms no longer absorb on the strong $^1S_0 \rightarrow {}^1P_1$ transition used for absorption imaging, and therefore their presence is revealed indirectly: they appear as a reduction in the measured optical density on the broad line. To reliably extract this small signal with a high signal-to-noise ratio, we record three raw absorption images for each delay t: the excitation image ("exc"), the reference image ("ref"), and the background ("dark"), as previously discussed. To minimize shot-to-shot fluctuations in atom number that arise from reloading different atomic ensembles, all three images, "exc", "ref", and "dark") are acquired from the same MOT realization. This ensures that the subtraction procedure reflects only the presence or absence of the excitation, rather than variations in the initial cloud. The raw absorption images with and without excitation are shown in Fig. 4.13(a,b), respectively.

The images are taken with an Andor Zyla 505 CMOS [85] camera operated in high-speed, global-shutter mode. We restrict the field of view to $\sim 200 \times 100$ pixels (about 4.4×2.2 mm), which allows two exposures separated by $\approx 100\,\mu$s. In practice, the camera exposure is fixed ($\approx 250\,\mu$s), with a minimum separation of approximately 100 µs between consecutive frames. To utilize this constraint, the optical sequence was adjusted so that the excitation pulse occurs at the end of the first exposure, while the reference pulse falls at the beginning of the second exposure, as shown in Figure 4.12. This configuration minimizes the effective delay while keeping both images within the same MOT cycle. The delay between the two absorption probes is chosen 140 μs. Precise synchronization of the camera exposures with the optical pulses is ensured using a digital delay generator.

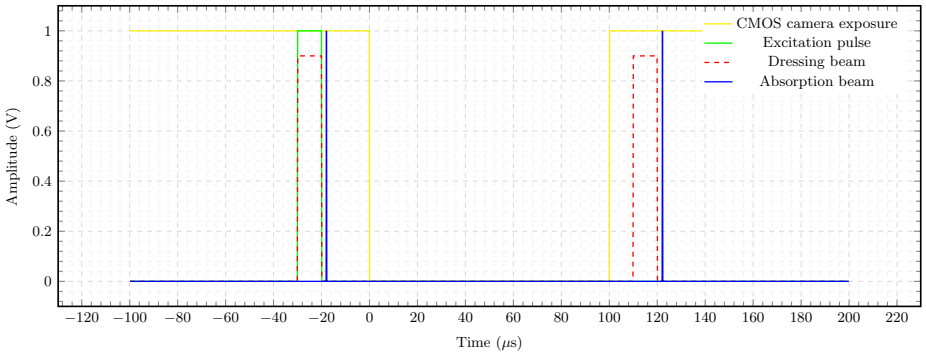

Figure 4.12: Timing sequence of the experiment. The CMOS camera (yellow) acquires two absorption images per cycle of MOT loading, separated by approximately 100 μs. A short green excitation pulse (green) promotes atoms from the ground state to $^3P_1$, while the dressing beams (red, dashed) are applied in synchrony. The absorption probe (blue) is triggered after the green pulse to measure the reduction in optical density caused by the excited population. The delay between the two absorption probes is chosen 140 μs to (i) avoid electronic jitter of the camera trigger and (ii) ensure enough time after the green pulse to follow excitation. (iii) ensure that the "ref" absorption image during the second exposure under an identical situation with the dressing beams present but without the excitation pulse.

After subtracting the dark frame from both images 4.13(a) and 4.13(b) and dividing by a background image (no atoms), The raw ratio and two orthogonal line cuts are shown in figure 4.13(c,d), given by the intensity ratio as follows:

$$R(x, y, t) = \frac{I_{\text{exc}}(x, y, t) - I_d(x, y)}{I_{\text{ref}}(x, y, t + 140\ \mu\text{s}) - I_d(x, y)}. \tag{4.27}$$

This ratio cancels out global fluctuations such as atom number drifts and probe intensity variations while highlighting the local effect of the excitation. However, the excitation appears as a small feature on top of a large-scale background gradient. The reason for the background vertical gradient is the 140 μs delay between the two frames, during which the cloud falls. After a 15-25 ms time of flight, this produces a center-of-mass shift of ~ 30–$40\,\mu$m, which shows up as a vertical gradient in R (a "moving baseline") as illustrated in image 4.13(d) (orange cut).

To remove it, we record, for each set of parameters, a calibration ratio with the excitation off in both frames. This ratio image [18] contains only the slow density change due to free fall and is subtracted from the ratio image 4.13(c):

$$R_{\text{excitaion}}(x, y, t) = \left.\frac{I_{\text{exc}}}{I_{\text{ref}}}\right|_{\text{exc on}} - \left.\frac{I_{\text{exc}}}{I_{\text{ref}}}\right|_{\text{exc off}}.$$

After subtraction, the excitation spot, as shown in Figure 4.13(e), becomes clearly visible with a well-defined peak and can be quantitatively analyzed. For display only, we apply a 1-pixel Gaussian smoothing; all fits are performed on unsmoothed data. Each frame shown is the average of at least 50 experimental runs to improve the signal-to-noise ratio.

To characterize the excitation, we extract horizontal (blue) and vertical (orange) cuts through the center of the excitation spot and fit them with Gaussian profiles (dashed line) as illustrated in Figure4.13(e). We also analyzed the data using a 2D Gaussian fit, giving similar results. The fitted peak amplitude gives the excitation density contrast, while the fitted width defines the transverse size of the excitation.

A 2D Gaussian fit is then used to extract the peak amplitude and spatial width, together with a residual constant offset. In most cases, the fit converges reliably and the residuals are structureless at the noise level 4.14a, confirming that the excitation can be well described by a Gaussian distribution. However, in a minority of cases, uncontrolled technical fluctuations (e.g., probe intensity noise, stray scattered light, or imperfect background subtraction) introduce large-scale structures that the Gaussian fit cannot capture. In such cases, the residual image retains significant spatial correlations 4.14b, making the extracted parameters unreliable. To ensure the robustness of our analysis, we systematically excluded such anomalous datasets from further averaging

To extract the diffusion coefficient, we fit the spatial profiles with a 2D Gaussian and obtain the time-dependent widths $\sigma_x(t)$ and $\sigma_y(t)$. From these, we define the effective squared width

$$\sigma^2(t) = \sigma_x(t)\,\sigma_y(t), \tag{4.28}$$

which captures the expansion of the excitation in two dimensions. We observe that σ_y is consistently 20-40% narrower than σ_x, indicating that the dynamics are elliptical rather than isotropic.

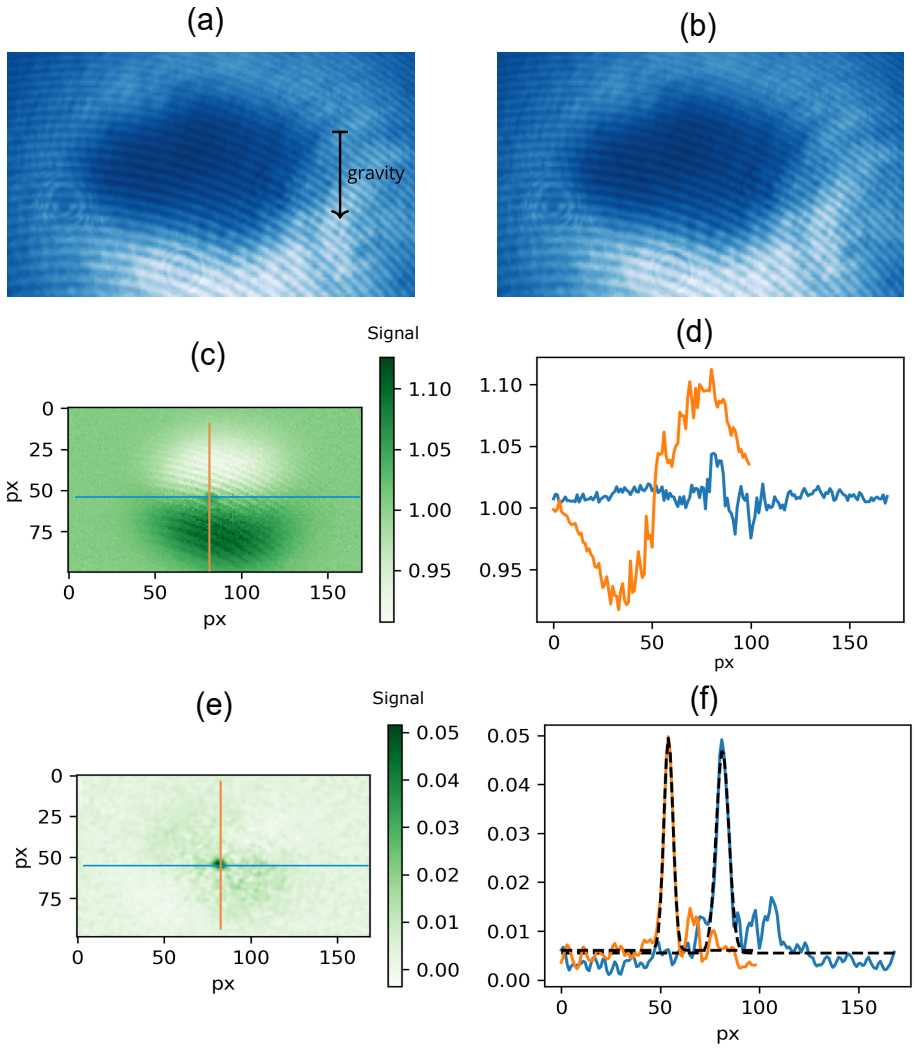

Figure 4.13: **Raw data processing of excitation images (1px= 22 μm). a)** Absorption image on the broad transition with the excitation I_{exc}. **b)** Absorption image on the broad transition under the same conditions as image (a) but without the excitation I_{ref}. **c)** Ratio of two absorption images (a) and (b) $I_{\mathrm{exc}}/I_{\mathrm{ref}}$ at a delay $t = 0$ after the end of the excitation pulse. The compact excitation spot is visible but superimposed on a large-scale vertical background gradient due to residual free fall during the 140 μs delay between two absorption images. **d)** A horizontal (blue) and vertical (orange) line cuts through the excitation center of image (c), clearly showing a slow vertical gradient. **e)** Background-subtracted image (c), the localized excitation is clearly isolated. **f)** A horizontal (blue) and vertical (orange) cuts through the excitation center of image (e), fitted with Gaussian profiles (dashed lines). The fitted peak and width are used to characterize the excitation density and spatial size.

On scales large compared to the transport mean free path ℓ, transport of resonant photons can be described by a diffusion equation for the photon energy density $n(\mathbf{r}, t)$,

$$\frac{\partial n(\mathbf{r}, t)}{\partial t} = D\,\nabla^2 n(\mathbf{r}, t) - \frac{n(\mathbf{r}, t)}{\tau_{\mathrm{a}}},$$

where D is the diffusion coefficient and τ_{a} parametrizes losses (escape through the finite

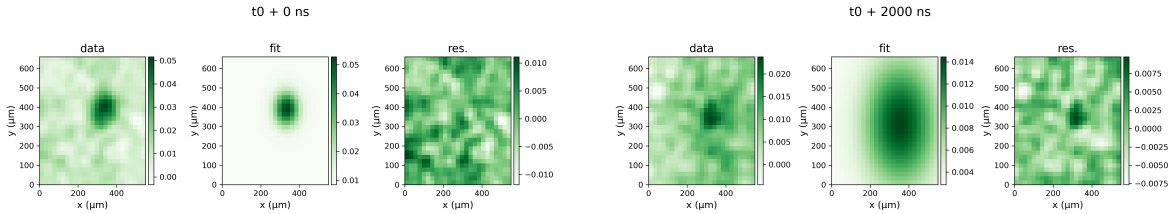

(a) Example of a "good" dataset at t=0, where the raw excitation image (left) is well captured by a 2D Gaussian fit (center), and the residuals (right) show only noise without correlated structure.

(b) Example of an "excluded" dataset at t=2 μs, where uncontrolled fluctuations produce structured residuals, indicating that the Gaussian fit does not provide a reliable description. Such data are discarded from the analysis to avoid systematic bias in the extracted diffusion parameters.

Figure 4.14: Data quality assessment through Gaussian fitting.

boundaries or absorption). For an initially Gaussian transverse profile

$$n(\mathbf{r}, t = 0) \propto \exp\Big[- (x^2 + y^2)/(2\sigma_0^2)\Big],$$

The solution remains Gaussian, and the variance per Cartesian axis evolves as

$$\sigma^2(t) = \sigma_0^2 + 3Dt,$$

so that the diffusion coefficient can be obtained from the slope of $\sigma^2(t)$:

$$D \;=\; \tfrac{1}{3}\,\frac{d}{dt}\sigma^2(t).$$

Figure (4.15) illustrates the process of extracting the diffusion coefficient. Each point corresponds to the width extracted from a 2D Gaussian fit of a background-corrected excitation image at a given time delay. The linear growth of $\sigma^2(t)$ with time confirms the diffusive nature of photon transport in the optically dense ytterbium ensemble. The solid line represents a linear fit used to determine D, while the dashed lines indicate the uncertainty associated with the fit.

The analysis shown in Figure 4.15 was used to extract the diffusion coefficient D at various optical depths, which characterizes the rate at which resonant photons spread through the dense ytterbium cloud. To connect this coefficient to microscopic scattering parameters, we compute the transport mean free path,

$$\ell_{tr} = \frac{\sqrt{2\pi} r_0}{b_{0,g}}, \tag{4.29}$$

using the measured cloud size r_0 and optical depth $b_{0,g}$.

In the diffusive regime, photon transport is expected to obey

$$D = \frac{\ell_{tr}^2}{3\tau_g}, \tag{4.30}$$

where $\tau_g = 1/\Gamma_g \approx 866$ ns is the lifetime of the narrow intercombination line.

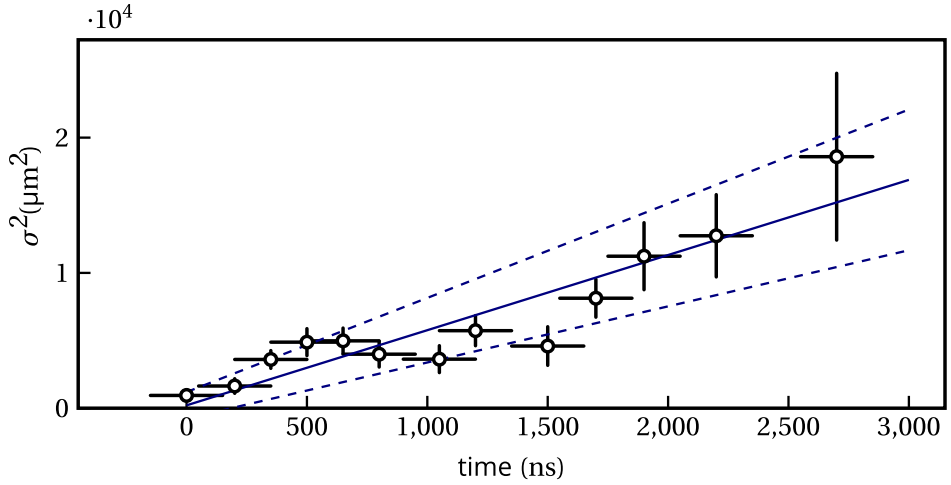

Figure 4.15: The squared width $\sigma^2(t)$ extracted from 2D Gaussian fits is plotted as a function of time delay after the excitation pulse. The linear growth is the hallmark of diffusive transport. The slope yields the diffusion coefficient D, while the intercept corresponds to the initial excitation size. Dashed lines represent the statistical uncertainty of the fit.

This allows us to directly compare the experimentally extracted diffusion coefficient with theoretical predictions of multiple scattering theory in the narrow-line regime, as illustrated in Figure 4.16.

The photons transport inside the dense atomic cloud can be well described by a random walk with step size equal to the transport mean free path ℓ_{tr}. After N steps, the rms displacement is $\sqrt{N_{\mathrm{scatt},g}}\,\ell_{tr}$ [86]. To traverse a distance comparable to the cloud size r_0 (the Gaussian $1/e^2$ radius), one therefore needs

$$\sqrt{N_{\mathrm{scatt},g}}\,\ell_{tr} \sim r_0 \quad \Rightarrow \quad N_{\mathrm{scatt},g} \sim \left(\frac{r_0}{\ell_{tr}}\right)^2 . \tag{4.31}$$

Substituting Eq. (4.29) into Eq. (4.31) eliminates ℓ_{tr} and yields the useful mapping

$$N_{\mathrm{scatt},g} \simeq \frac{b_{0,g}^2}{2\pi} \quad \Longleftrightarrow \quad b_{0,g} \propto \sqrt{N_{\mathrm{scatt},g}}\,. \tag{4.32}$$

This provides an intuitive reading of the color map in our measurement 4.16. Points with larger central $b_{0,g}$ correspond to excitations that, on average, undergo many more scattering events before escaping. In the limit $N_{\mathrm{scatt},g} \gg 1$ (equivalently $b_{0,g} \gg 1$), a diffusive regime is expected and indeed observed in our data. Conversely, when $N_{\mathrm{scatt},g} \sim 1$ (small $b_{0,g}$), photons exit the sample after only a few events and the dynamics approach the ballistic regime.

Our measurements show good agreement with this scaling when the optical depth is sufficiently large ($b_{0,g} \gtrsim 8$), corresponding to a mean free path $\ell \lesssim 100$ μm. For lower optical depths, deviations appear as photons leave the cloud before undergoing enough scattering events, marking a crossover to the ballistic regime.

The rhombus marker in Fig. 4.16, which corresponds to the control configuration discussed in Sec. (4.6.2) [case (b)]. In this situation, the dressing beam remains on after the initial preparation, and the emitted photons are shifted by $-15\Gamma_g$ away from resonance. Because the rest of the cloud is transparent at this detuning, the photons

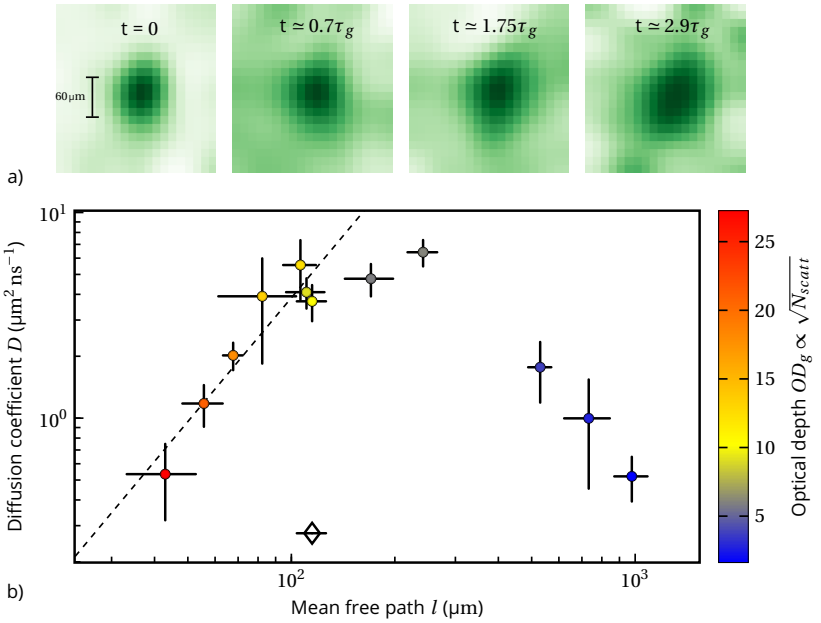

Figure 4.16: (a) Excitation evolution for four different times between 0 and $\sim 3\tau_g$, normalized and smoothed for display. The profile broadens with time, illustrating diffusive propagation. (b) Diffusion coefficient D as a function of transport mean free path ℓ_{tr}. The dashed line is the theoretical prediction $D = \ell^2/(3\tau_g)$ with no free parameters. The color scale indicates the optical depth.

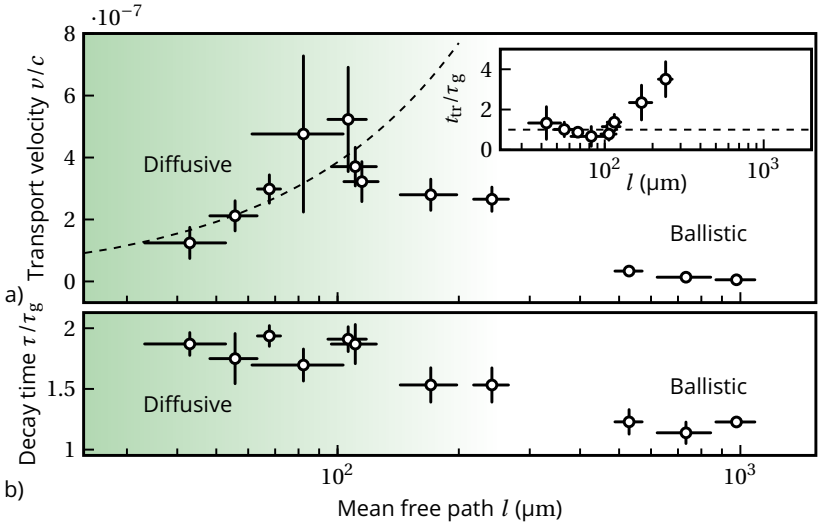

Figure 4.17: (a) Extracted transport velocity v and transport time t_{tr}, confirming the narrow-line scaling $t_{\mathrm{tr}} \approx \tau_g$.
(b) Effective excitation lifetime τ versus optical depth, showing the crossover from ballistic to diffusive transport.

propagate ballistically, and no diffusion occurs. Consistently, the extracted diffusion coefficient is essentially zero, as indicated by the isolated rhombus point.

From the same data, we extract the transport velocity [80],

$$v = \frac{3D}{\ell_{\mathrm{tr}}}, \tag{4.33}$$

and the transport time,

$$t_{\mathrm{tr}} = \frac{\ell_{\mathrm{tr}}^2}{3D}. \tag{4.34}$$

Remarkably, we find that $t_{\mathrm{tr}} \approx \tau_g$, confirming the prediction that photon transport in the multiple-scattering regime is set by the natural lifetime of the excited state. The extracted transport velocity is nearly seven orders of magnitude smaller than the speed of light in vacuum, and two orders of magnitude slower than values previously obtained with alkali atoms [79], highlighting the dramatic role of the narrow linewidth in ytterbium.

Finally, by monitoring the temporal decay of the excitation amplitude $A(t)$ as illustrated in Figure 4.17, we extract an effective excitation lifetime τ. In the ballistic regime, $\tau \approx \tau_g$, while in the diffusive regime the lifetime increases up to about $2\tau_g$, reflecting the enhanced trapping of photons inside the dense medium. However, these decay times are significantly shorter than those measured via transmitted diffuse light in radiation-trapping experiments [79, 87]. We attribute this discrepancy to the fact that our method captures only the early part of the decay and thus does not resolve the slowest Holstein mode[3], which scales as $b_{0,g}^2\tau_g$ [79]. This long-lived mode is not accessible here because the signal-to-noise ratio becomes too low after a few τ_g.

This measurement thus provides a complementary probe of the transport regime and confirms the diffusive nature of photon propagation in the optically thick ytterbium ensemble.

4.6.2 Control of Photon Frequency Launched into the Dense Ensemble

The key question is whether the initial excitation emits photons resonant with the bare transition, or photons shifted by the dressing beams ($\approx 15\Gamma_g$). To answer this, we compare photon propagation with the dressing beams switched off or kept on after excitation.

In the first configuration illustrated in the Figure (4.18)(a), the excitation pulse is applied simultaneously with the dressing beams during the preparation stage. This is the standard sequence used throughout this chapter. Once the initial excitation is created, the dressing beams are switched off before the probing window. The atoms then return to their unperturbed ground state, and the photons subsequently emitted are resonant at the bare transition frequency, $\omega_{0,g}$. As discussed above, this situation results in multiple scattering, and we observe clear diffusive spreading, with a diffusion constant consistent with the measured on-resonance mean free path.

By contrast, in the second configuration Figure (4.18)(b), the dressing beams remain on after the preparation stage. The emitted photons are then shifted to $\omega = \omega_{0,g} - 15\Gamma_g$,

[3]For comparison, in our experimental conditions with $b_{0,g} \sim 20$, the lowest Holstein mode [88] would correspond to decay times on the order of $b_{0,g}^2\tau_g \sim 320$ μs, i.e., more than an order of magnitude longer than the $\sim 2\tau_g$ lifetimes accessible in our measurement.

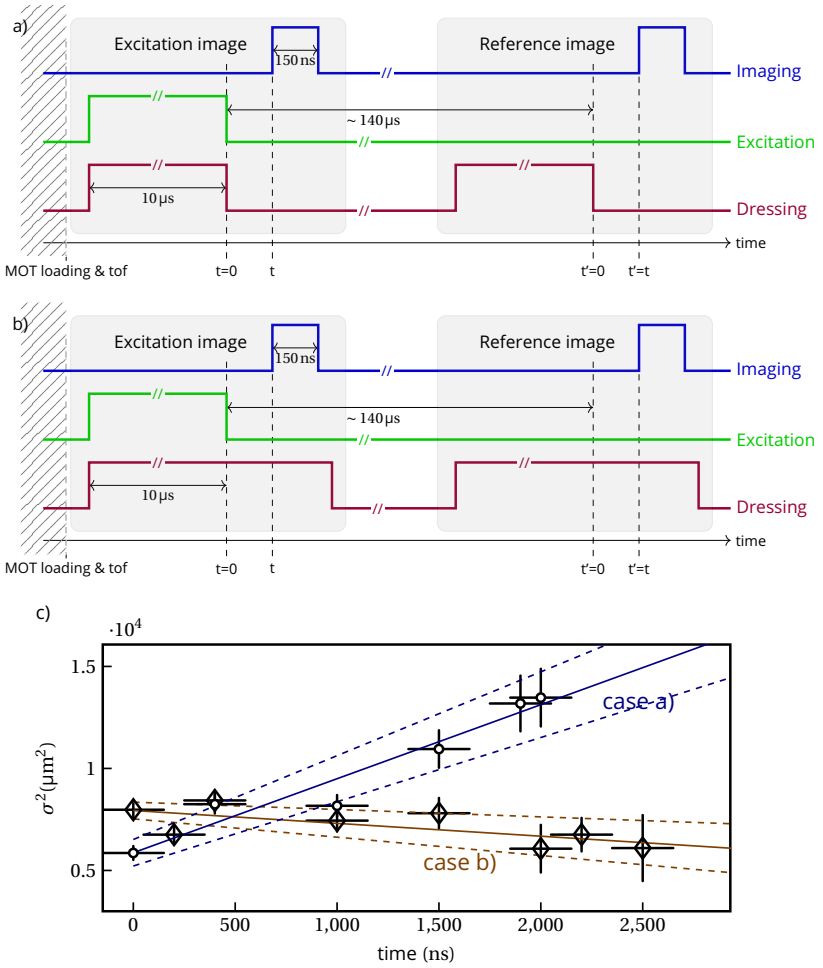

Figure 4.18: Control test of excitation propagation during preparation. **(a)** Timing sequence where the excitation pulse is applied simultaneously with the dressing beams during the preparation stage. The excitation pulse is off during probing on a broad transition. **(b)** Timing sequence where the dressing beams remain on even after the preparation stage. In this case, the spot size remains constant, showing that no significant propagation occurs during preparation. **(c)** Extracted mean-square radius $\sigma^2(t)$. Case (a) (blue) shows linear growth in time, characteristic of diffusion, while case (b) (brown) remains flat, confirming that the initial preparation does not contribute to transport.

i.e., far off-resonance for the surrounding atoms. These photons propagate essentially ballistically, without multiple scattering, corresponding to the limit where the diffusion constant vanishes ($D \to 0$) and the mean free path diverges. This behavior is visible in the data, marked by the diamond point in Fig. 4.16.

Figure (4.18)(c) compares the temporal evolution of the mean-square radius $\sigma^2(t)$ for the two cases. With the dressing switched off (case a), the squared width increases linearly in time, consistent with diffusion. With the dressing kept on (case b), the width remains essentially unchanged over the full delay range, confirming that no spreading occurs. This control sequence thus validates our interpretation; the observed propagation indeed reflects photon diffusion during the probing interval, not an artifact of the initial preparation process. This novel method enables control over the photon frequency launched into the dense and disordered atomic ensemble.

Doppler-Induced Frequency Redistribution in Our System A final point concerns the role of Doppler broadening in multiple scattering. At our cloud temperature of $T \approx 15\,\mu$K, the rms atomic velocity is on the order of $v_{\mathrm{rms}} \sim 4$–$5\,$cm/s, giving a Doppler width $kv_{\mathrm{rms}} \approx 90\,$kHz. This is smaller than the natural linewidth of the intercombination transition ($\Gamma = 184\,$kHz), So, single-scattering processes are essentially lifetime-limited, and Doppler effects can be neglected at the first step.

However, in the multiple scattering regime, each scattering event introduces a small frequency shift, and over many events, the photon frequency undergoes a random walk. The variance of this redistribution grows as discussed in Ref. [79].

$$\langle \delta\omega^2 \rangle \sim \frac{2}{3} N (k v_{\mathrm{rms}})^2, \tag{4.35}$$

So after a characteristic number of scatterings ($N \sim 6$), the initially narrow photon distribution broadens substantially. This broadening effectively shifts a fraction of the photon population out of resonance, reducing the scattering cross section and thereby increasing the effective transport speed compared to the purely elastic diffusion picture.

4.7 Conclusion

In this chapter, we presented *in situ* measurements of light diffusion in an optically dense and disordered ytterbium ensemble. By creating a localized excitation deep within the cloud and monitoring its time evolution, we extracted the photon diffusion coefficient across a wide range of optical depths. Our results confirm that the propagation of light in this system is well described by a diffusive model, and the extracted parameters are in good agreement with theoretical expectations. These results establish ultracold atoms as a clean platform to study light propagation in strongly scattering media. The main findings of this work have been published in our paper [18].

We demonstrate that we can monitor the propagation of a small excitation with a good spatial and temporal resolution, which can be useful to characterize a localized state. A precise characterization of diffusion is a necessary prerequisite for identifying and interpreting possible localization signatures, hereby providing the essential bridge between multiple scattering and interference-driven localization physics.

Looking forward, the methods developed here pave the way for quantitative studies of cooperative effects and, ultimately, for the exploration of disorder-induced localization in cold atomic ensembles.

Chapter 5

Conclusion

The long-term objective of our project is to demonstrate a clear experimental signature of Anderson localization of light in a 3D cloud of ^{174}Yb. We have three different approaches to pursue localization as discussed in the Introduction chapter, but we did not had the proper experimental technique to observe the signature of localization. Moreover, understanding photon transport in disordered, optically thick ensembles is a prerequisite for addressing Anderson localization of light. Therefore, measuring light diffusion in a controlled and well-characterized atomic ensemble is also crucial and a primary objective of the thesis.

In the framework of this thesis, we have optimized and characterized the magneto-optical trap of ^{174} Yb to enhance the experiment's stability and achieve ultracold temperatures of 14 μK with atom numbers on the order of $5 * 10^8$. The peak optical density on the $^3P_1$ transition reaches values up to 100 on a narrow-linewidth transition $^1S_0 \rightarrow {}^3P_1$, optically dense enough to be in the multiple-scattering regime.

The main challenge is not only to develop the detection technique but also to create a well-controlled and compact source of photons deep inside the optically dense atomic cloud so that its propagation can be studied before it reaches the cloud boundary to identify the diffusive/localized regime. To pursue this, tunable optical shifts are implemented as a tool to engineer internal state structure and successfully demonstrate the independent control of the magnetic sublevels $m = \pm 1, 0$ of the $^3P_1$ state without the need for an external magnetic shift. Overall, the measured light shifts are in good qualitative agreement with theoretical predictions. This qualitative study of the light shift is important for the two approaches toward localization, "Optically Induced Zeeman Splitting via Light Shifts" and "Diagonal Disorder via Random Light Shifts," discussed in the Introduction chapter. Building on this mechanism, we demonstrate an all-optical analogue of the Faraday effect. Our observations confirm the emergence of birefringence and polarization rotation of a probe as a result of differential optical dressing, opening new possibilities.

At last, we demonstrated a new experimental method to directly launch an *in-situ* optical excitation with a desired frequency in the deep core of our optically thick cloud. We further introduced a method to follow the propagation of the launched excitation spatially and temporally by monitoring the internal state population. The observed propagation dynamics of the launched photons agree with theoretical diffusion models, validating our approach and establishing a platform that brings us closer to exploring strong localization phenomena.

Our theoretical and experimental results on $^3P_1$ light shifts will provide a useful

foundation for introducing optical speckle fields to generate a controlled disordered environment in future studies. Overall, this thesis combines precise atomic-state control with real-time observation of photon transport, providing the essential step toward realizing Anderson localization of light in three-dimensional disordered atomic media.

5.1 Outlook

An interesting feature of probing ground-state depletion or excited-state populations is that it also provides local spatial information. The population-probing technique developed in this work has proven to be a robust method for exploring cooperative phenomena and can also be applied to investigate various forms of light–atom coherent evolution. A direct extension of this approach is the study of subradiant dynamics in a cold atomic cloud of ^{174}Yb, as demonstrated in our recent work [19]. Using the same *in situ* probing method allows time- and space-resolved measurements of subradiant excited-state population and enables characterization of the decay dynamics of the subradiant modes. These measurements are particularly useful for comparing how the population-based and intensity-based observations provide complementary information about the system.

Another application of the ground state population-probing approach could also be applied to the precise measurement of driven dynamics. Some preliminary data have been acquired. No detailed analysis was performed on these data (see C). But it would be interesting to compare Rabi frequency measurements obtained via population dynamics and fluorescence detection. While both probe the same atom–field coupling, differences may arise in optically thick media due to reabsorption, spatial variations of the driving field, and collective effects. Such comparisons would provide valuable insight into how coherent driving and light propagation interplay in dense atomic ensembles.

Apart from that, we have demonstrated all-optical Faraday effect, which opens new opportunities for atomic physics and quantum optics. It provides a new, tunable approach to controlling atomic birefringence without magnetic fields, tunable optical elements in situ, enabling noise-free probing for field-sensitive systems and spatially structured light-atom coupling. In short, optically induced Faraday rotation is not only a replacement for magnetic fields but also represents a qualitatively new approach to controlling atomic birefringence with speed, flexibility, and spatial selectivity inaccessible to conventional magneto-optics.

Appendix A

Laboratory relocation and issues encountered

In March 2023, the laboratory was moved from Sophia Antipolis to Nice. The transfer of equipment proceeded smoothly, and all optical systems were successfully reinstalled. However, shortly after the move, a water leakage occurred from the air-conditioning system, resulting in water leakage on the optical table and condensation on several components, most notably the Verdi pump used for the blue laser system.

Figure A.2 shows the water leakage on the optical table and on various optical elements and the resulting condensation observed on the Coherent pump. These images illustrate the impact of lab temperature instability on sensitive optical elements.



Figure A.1: Photographs taken during the optical table relocation from Sophia Antipolis to Nice.

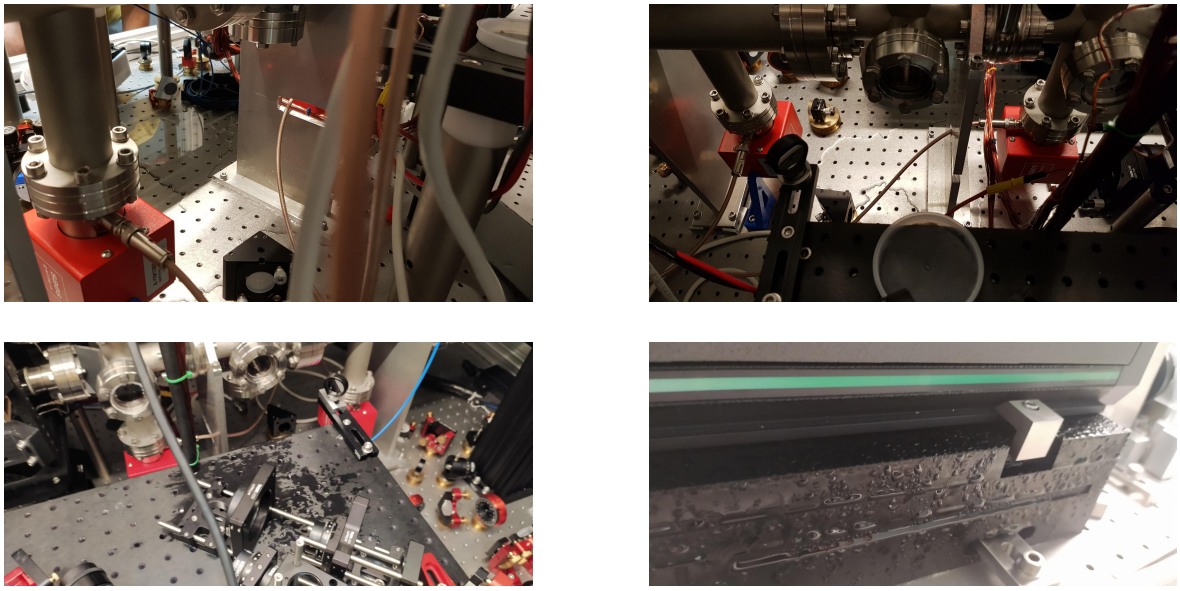

Figure A.2: Laboratory relocation and resulting issues: Photographs taken after the laboratory relocation to Nice: (left) water leakage on the optical table, (right) condensation on the Verdi pump of the blue laser system.

Appendix B

Derivation of the Excitation Radius

The dressing beam of waist w_{LS} has a Gaussian intensity profile

$$I(r) = I_0 e^{-2r^2/w_{\mathrm{LS}}^2}. \tag{B.1}$$

In the far-detuned regime, the AC Stark shift is proportional to intensity:

$$U(r) = U_0 e^{-2r^2/w_{\mathrm{LS}}^2}, \tag{B.2}$$

where U_0 is the shift at the beam center.

We tune the probe frequency such that atoms at the center are resonant:

$$\omega_p = \omega_{0,g} - \frac{U_0}{\hbar}. \tag{B.3}$$

At position r, the local detuning is

$$\Delta(r) = \omega_p - \left(\omega_{0,g} + \frac{U(r)}{\hbar}\right) = -\frac{(U_0 + U(r))}{\hbar}. \tag{B.4}$$

The excitation radius r_{exc} is defined by the condition

$$\Delta(r_{\mathrm{exc}}) = \Gamma_g. \tag{B.5}$$

At this point, the scattering cross section has decreased by a factor of five compared to resonance, so atoms outside this region contribute negligibly to the excitation. This yields

$$1 - e^{-2r_{\mathrm{exc}}^2/w_{\mathrm{LS}}^2} = \frac{\hbar\Gamma_g}{U_0}. \tag{B.6}$$

For $U_0 \gg \hbar\Gamma_g$, the right-hand side is small, and we expand $\ln(1-\varepsilon) \approx -\varepsilon$. Solving gives

$$r_{\mathrm{exc}} \approx w_{\mathrm{LS}}\sqrt{\frac{\hbar\Gamma_g}{2|U_0|}}. \tag{B.7}$$

Appendix C

Preliminary measurement of excited-state population during driven dynamics (Rabi oscillations)

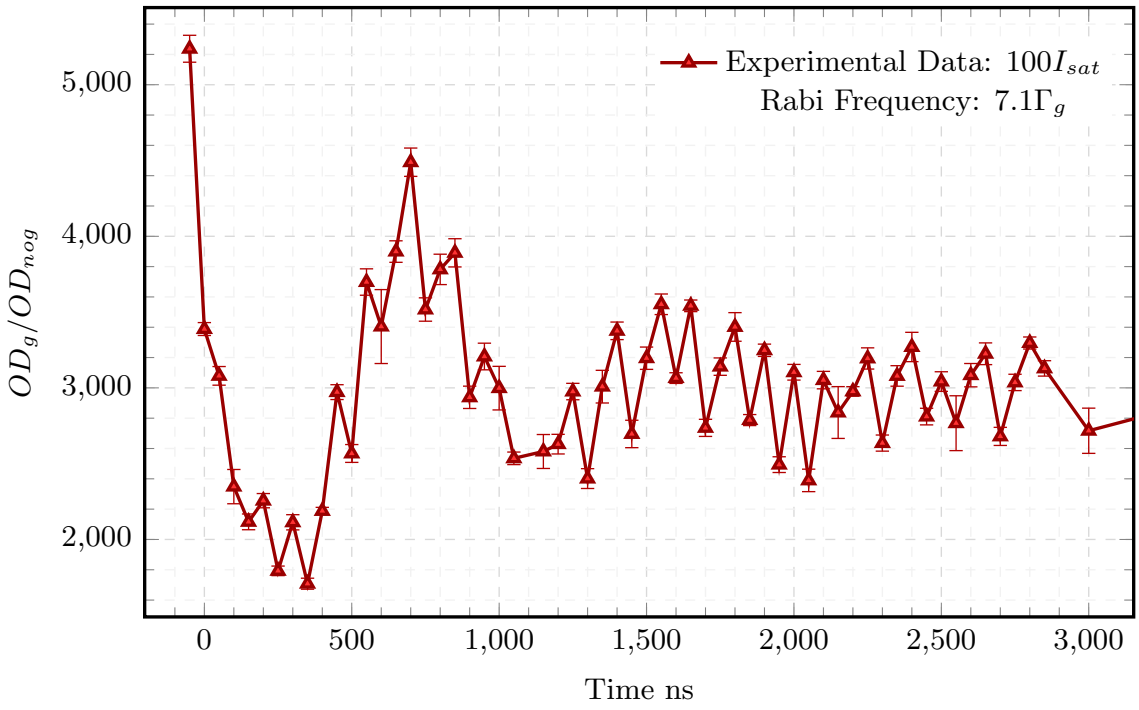

Figure C.1: Observation of Rabi oscillations in ^{174}Yb on the $^1S_0 \rightarrow {}^3P_1$ (556 nm) transition, recorded using the *in-situ* light diffusion technique. The plotted ratio $\mathrm{OD}_g/\mathrm{OD}_{nog}$ reflects changes in the ground-state population as a function of the blue pulse timing after the start of the excitation pulse at $100\,I_{\mathrm{sat}}$. The oscillation appears inverted relative to the typical excited-state population dynamics, since it represents the damped oscillation of the ground-state population. These preliminary data illustrate an additional application of the population-based measurement method, but were not further analyzed.

In situ measurement of Rabi oscillations on the $^1S_0 \rightarrow {}^3P_1$ (556 nm) transition in ^{174}Yb using the *in-situ* light diffusion technique [18]. After loading a magneto-optical trap

(MOT) with initial optical density $b_{0,g} \approx 10$, the atoms were released and driven by a 2 ms green pulse at 100 I_{sat}. A 150 ns blue pulse was used for absorption imaging at variable delays relative to the start of the green pulse. For each delay, a new MOT cycle was prepared, alternating between measurements with and without the green excitation pulse to obtain the ratio $\mathrm{OD}_g/\mathrm{OD}_{\mathrm{no,g}}$. The horizontal axis shows the blue pulse timing (in ns) relative to the beginning of the green pulse. These preliminary data illustrate coherent Rabi oscillations as shown in Figure (C.1), which are damped in about $\frac{1}{2\pi\Gamma_g} \approx 1$ μs but were not analyzed further.

Bibliography

[1] P. W. Anderson. "Absence of Diffusion in Certain Random Lattices". In: *Physical Review* 109.5 (1958), pp. 1492–1505. ISSN: 0031-899X. DOI: 10.1103/physrev.109.1492.

[2] Ad Lagendijk, Bart van Tiggelen, and Diederik S. Wiersma. "Fifty years of Anderson localization". In: *Physics Today* 62.8 (Jan. 2009), p. 24. DOI: 10.1063/1.3206091.

[3] P. Sheng. *Introduction to Wave Scattering, Localization, and Mesoscopic Phenomena*. 2nd. Springer, 2006.

[4] E. Abrahams et al. "Scaling Theory of Localization: Absence of Quantum Diffusion in Two Dimensions". In: *Phys. Rev. Lett.* 42 (10 Mar. 1979), pp. 673–676. DOI: 10.1103/PhysRevLett.42.673. URL: https://link.aps.org/doi/10.1103/PhysRevLett.42.673.

[5] Ferdinand Evers and Alexander D. Mirlin. "Anderson transitions". In: *Rev. Mod. Phys.* 80 (4 Oct. 2008), pp. 1355–1417. DOI: 10.1103/RevModPhys.80.1355. URL: https://link.aps.org/doi/10.1103/RevModPhys.80.1355.

[6] AF Ioffe and AR Regel. "Non-crystalline, amorphous, and liquid electronic semiconductors". In: *Progress in semiconductors*. 1960, pp. 237–291.

[7] S. E. Skipetrov and I. M. Sokolov. "Ioffe-Regel criterion for Anderson localization in the model of resonant point scatterers". In: *Phys. Rev. B* 98 (6 Aug. 2018), p. 064207. DOI: 10.1103/PhysRevB.98.064207. URL: https://link.aps.org/doi/10.1103/PhysRevB.98.064207.

[8] Diederik S. Wiersma et al. "Localization of light in a disordered medium". In: *Nature* 390.6661 (Dec. 1997), pp. 671–673. ISSN: 1476-4687. DOI: 10.1038/37757. URL: https://doi.org/10.1038/37757.

[9] A. A. Chabanov, M. Stoytchev, and A. Z. Genack. "Statistical signatures of photon localization". In: *Nature* 404.6780 (Apr. 2000), pp. 850–853. ISSN: 1476-4687. DOI: 10.1038/35009055. URL: https://doi.org/10.1038/35009055.

[10] C. M. Aegerter, M. Störzer, and G. Maret. "Experimental determination of critical exponents in Anderson localisation of light". In: *Europhysics Letters* 75.4 (July 2006), p. 562. ISSN: 0295-5075. DOI: 10.1209/epl/i2006-10144-3. URL: https://doi.org/10.1209/epl/i2006-10144-3.

[11] Frank Scheffold et al. "Localization or classical diffusion of light?" In: *Nature* 398.6724 (Mar. 1999), pp. 206–207. DOI: 10.1038/18347. URL: https://doi.org/10.1038/18347.

[12] T. Sperling et al. “Can 3D light localization be reached in ‘white paint’?” In: *New Journal of Physics* 18.1 (Jan. 2016), p. 013039. ISSN: 1367-2630. DOI: 10.1088/1367-2630/18/1/013039. URL: https://doi.org/10.1088/1367-2630/18/1/013039.

[13] S E Skipetrov and J H Page. “Red light for Anderson localization”. In: *New Journal of Physics* 18.2 (Jan. 2016), p. 021001. DOI: 10.1088/1367-2630/18/2/021001. URL: https://doi.org/10.1088/1367-2630/18/2/021001.

[14] S. E. Skipetrov and I. M. Sokolov. “Magnetic-Field-Driven Localization of Light in a Cold-Atom Gas”. In: *Physical Review Letters* 114 (5 Feb. 2015), p. 053902. DOI: 10.1103/PhysRevLett.114.053902. URL: https://link.aps.org/doi/10.1103/PhysRevLett.114.053902.

[15] Luca Giuseppe Celardo et al. “Localization of light in three dimensions: A mobility edge in the imaginary axis in non-Hermitian Hamiltonians”. In: *Europhysics Letters* 145.3 (Feb. 2024), p. 35002. ISSN: 0295-5075. DOI: 10.1209/0295-5075/ad222c. URL: https://doi.org/10.1209/0295-5075/ad222c.

[16] S. E. Skipetrov and I. M. Sokolov. “Absence of Anderson Localization of Light in a Random Ensemble of Point Scatterers”. In: *Physical Review Letters* 112 (2 Jan. 2014), p. 023905. DOI: 10.1103/PhysRevLett.112.023905. URL: https://link.aps.org/doi/10.1103/PhysRevLett.112.023905.

[17] Álvaro M. G. de Melo et al. “Laser frequency stabilization by modulation transfer spectroscopy and balanced detection of molecular iodine for laser cooling of 174Yb”. In: *Optics Express* 32.4 (Feb. 2024), pp. 6204–6214. DOI: 10.1364/OE.512281. URL: https://doi.org/10.1364/OE.512281.

[18] Antoine Glicenstein et al. “In Situ Measurements of Light Diffusion in an Optically Dense Atomic Ensemble”. In: *Physical Review Letters* 133 (23 Dec. 2024), p. 233401. DOI: 10.1103/PhysRevLett.133.233401. URL: https://link.aps.org/doi/10.1103/PhysRevLett.133.233401.

[19] Antoine Glicenstein et al. *Probing subradiant dynamics in cold atomic ensembles via population and emitted light measurements*. 2025. arXiv: 2507.16549 [physics.atom-ph]. URL: https://arxiv.org/abs/2507.16549.

[20] M. H. Anderson et al. “Observation of Bose-Einstein Condensation in a Dilute Atomic Vapor”. In: *Science* 269.5221 (1995), pp. 198–201. DOI: 10.1126/science.269.5221.198. eprint: https://www.science.org/doi/pdf/10.1126/science.269.5221.198. URL: https://www.science.org/doi/abs/10.1126/science.269.5221.198.

[21] J. Pellegrino et al. “Observation of Suppression of Light Scattering Induced by Dipole-Dipole Interactions in a Cold-Atom Ensemble”. In: *Phys. Rev. Lett.* 113 (13 Sept. 2014), p. 133602. DOI: 10.1103/PhysRevLett.113.133602. URL: https://link.aps.org/doi/10.1103/PhysRevLett.113.133602.

[22] Stephan Jennewein et al. “Coherent scattering of near-resonant light by a dense, microscopic cloud of cold two-level atoms: Experiment versus theory”. In: *Phys. Rev. A* 97 (5 May 2018), p. 053816. DOI: 10.1103/PhysRevA.97.053816. URL: https://link.aps.org/doi/10.1103/PhysRevA.97.053816.

[23] Robin Kaiser. "Quantum multiple scattering". In: *Journal of Modern Optics* 56.18-19 (2009), pp. 2082–2088. DOI: 10.1080/09500340903082663. eprint: https://doi.org/10.1080/09500340903082663. URL: https://doi.org/10.1080/09500340903082663.

[24] Yosuke Takasu et al. "Spin-Singlet Bose-Einstein Condensation of Two-Electron Atoms". In: *Phys. Rev. Lett.* 91 (4 July 2003), p. 040404. DOI: 10.1103/PhysRevLett.91.040404. URL: https://link.aps.org/doi/10.1103/PhysRevLett.91.040404.

[25] T. Kuwamoto et al. "Magneto-optical trapping of Yb atoms using an intercombination transition". In: *Phys. Rev. A* 60 (2 Aug. 1999), R745–R748. DOI: 10.1103/PhysRevA.60.R745. URL: https://link.aps.org/doi/10.1103/PhysRevA.60.R745.

[26] Benjamin Plotkin-Swing et al. "Crossed-beam slowing to enhance narrow-line ytterbium magneto-optic traps". In: *Review of Scientific Instruments* 91.9 (Sept. 2020), p. 093201. ISSN: 0034-6748. DOI: 10.1063/5.0011361. eprint: https://pubs.aip.org/aip/rsi/article-pdf/doi/10.1063/5.0011361/14798714/093201_1_online.pdf. URL: https://doi.org/10.1063/5.0011361.

[27] Xiao Li et al. "Two-color magneto-optical trapping of ytterbium atoms". In: *Phys. Rev. Appl.* 24 (4 Oct. 2025), p. 044039. DOI: 10.1103/541j-2sj9. URL: https://link.aps.org/doi/10.1103/541j-2sj9.

[28] Jeongwon Lee et al. "Core-shell magneto-optical trap for alkaline-earth-metal-like atoms". In: *Phys. Rev. A* 91 (5 May 2015), p. 053405. DOI: 10.1103/PhysRevA.91.053405. URL: https://link.aps.org/doi/10.1103/PhysRevA.91.053405.

[29] Hector Letellier et al. "Loading of a large Yb MOT on the $^1S_0 \rightarrow {}^1P_1$ transition". In: *Review of Scientific Instruments* 94.12 (2023), p. 123203. ISSN: 0034-6748. DOI: 10.1063/5.0169772.

[30] Sören Erik Dörscher. "Creation of ytterbium quantum gases with a compact 2D-/3D-MOT setup". Dissertation zur Erlangung des Doktorgrades des Department Physik. Dissertation. Hamburg, Germany: Universität Hamburg, 2013.

[31] Jun Woo Cho et al. "Optical repumping of triplet-P states enhances magneto-optical trapping of ytterbium atoms". In: *Phys. Rev. A* 85 (3 Mar. 2012), p. 035401. DOI: 10.1103/PhysRevA.85.035401. URL: https://link.aps.org/doi/10.1103/PhysRevA.85.035401.

[32] W. C. Martin and R. Zalubas. *Energy Levels of Neutral Ytterbium (Yb I)*. NIST Atomic Spectra Database. 1978. URL: https://physics.nist.gov/PhysRefData/Handbook/Tables/ytterbiumtable5.htm.

[33] K. Beloy et al. "Determination of the $5d6s\ {}^3D_1$ state lifetime and blackbody-radiation clock shift in Yb". In: *Phys. Rev. A* 86 (5 Nov. 2012), p. 051404. DOI: 10.1103/PhysRevA.86.051404. URL: https://link.aps.org/doi/10.1103/PhysRevA.86.051404.

[34] Y. Takasu et al. "Photoassociation Spectroscopy of Laser-Cooled Ytterbium Atoms". In: *Phys. Rev. Lett.* 93 (12 Sept. 2004), p. 123202. DOI: 10.1103/PhysRevLett.93.123202. URL: https://link.aps.org/doi/10.1103/PhysRevLett.93.123202.

[35] K.B. Blagoev and V.A. Komarovskii. “Lifetimes of Levels of Neutral and Singly Ionized Lanthanide Atoms”. In: *Atomic Data and Nuclear Data Tables* 56.1 (1994), pp. 1–40. ISSN: 0092-640X. DOI: https://doi.org/10.1006/adnd.1994.1001. URL: https://www.sciencedirect.com/science/article/pii/S0092640X84710011.

[36] P. D. Lett et al. “Optical molasses”. In: *J. Opt. Soc. Am. B* 6.11 (Nov. 1989), pp. 2084–2107. DOI: 10.1364/JOSAB.6.002084. URL: https://opg.optica.org/josab/abstract.cfm?URI=josab-6-11-2084.

[37] T.W. Hänsch and A.L. Schawlow. “Cooling of gases by laser radiation”. In: *Optics Communications* 13.1 (1975), pp. 68–69. ISSN: 0030-4018. DOI: https://doi.org/10.1016/0030-4018(75)90159-5. URL: https://www.sciencedirect.com/science/article/pii/0030401875901595.

[38] H.J. Metcalf and P. Van der Straten. *Laser Cooling and Trapping*. Graduate texts in contemporary physics. Springer, 1999. ISBN: 9780387987477. URL: https://books.google.fr/books?id=i-40VaXqrj0C.

[39] E. L. Raab et al. “Trapping of Neutral Sodium Atoms with Radiation Pressure”. In: *Phys. Rev. Lett.* 59 (23 Dec. 1987), pp. 2631–2634. DOI: 10.1103/PhysRevLett.59.2631. URL: https://link.aps.org/doi/10.1103/PhysRevLett.59.2631.

[40] TOPTICA Photonics AG. *DL pro / TA-SHG pro User Manual*. Accessed via internal documentation. TOPTICA Photonics AG. 2021.

[41] Hector Letellier. “Piégeage magnéto-optique de l’ytterbium sur la transition ^{1}S $\rightarrow$ ^{1}P”. French. NNT : 2024COAZ5030. Thèse de doctorat. Université Côte d’Azur, 2024. URL: https://theses.hal.science/tel-04745952v1.

[42] C.J. Foot. *Atomic Physics*. Oxford Master Series in Physics. OUP Oxford, 2004. ISBN: 9780191037078. URL: https://books.google.fr/books?id=yf6BAwAAQBAJ.

[43] Fachao Hu et al. “Observation of photon recoil effects in single-beam absorption spectroscopy with an ultracold strontium gas”. In: *Chinese Physics B* 31.1 (2022), p. 016702. ISSN: 1674-1056. DOI: 10.1088/1674-1056/ac2486. eprint: 2101.11176.

[44] V. Natarajan. *Modern Atomic Physics*. CRC Press, 2015. ISBN: 9781482242041. URL: https://books.google.fr/books?id=b5K9BwAAQBAJ.

[45] G. Labeyrie et al. “Multiple scattering of light in a resonant medium”. In: *Optics Communications* 243.1 (2004). Ultra Cold Atoms and Degenerate Quantum Gases, pp. 157–164. ISSN: 0030-4018. DOI: https://doi.org/10.1016/j.optcom.2004.10.037. URL: https://www.sciencedirect.com/science/article/pii/S0030401804010612.

[46] Steven Chu et al. “Experimental Observation of Optically Trapped Atoms”. In: *Phys. Rev. Lett.* 57 (3 July 1986), pp. 314–317. DOI: 10.1103/PhysRevLett.57.314. URL: https://link.aps.org/doi/10.1103/PhysRevLett.57.314.

[47] Rudolf Grimm, Matthias Weidemüller, and Yurii B. Ovchinnikov. "Optical Dipole Traps for Neutral Atoms". In: ed. by Benjamin Bederson and Herbert Walther. Vol. 42. Advances In Atomic, Molecular, and Optical Physics. Academic Press, 2000, pp. 95–170. DOI: https://doi.org/10.1016/S1049-250X(08)60186-X. URL: https://www.sciencedirect.com/science/article/pii/S1049250X0860186X.

[48] Tim O. Höhn et al. "State-dependent potentials for the $^1S_0$ and $^3P_0$ clock states of neutral ytterbium atoms". In: *Phys. Rev. A* 108 (5 Nov. 2023), p. 053325. DOI: 10.1103/PhysRevA.108.053325. URL: https://link.aps.org/doi/10.1103/PhysRevA.108.053325.

[49] Andrew D. Ludlow et al. "Optical atomic clocks". In: *Rev. Mod. Phys.* 87 (2 June 2015), pp. 637–701. DOI: 10.1103/RevModPhys.87.637. URL: https://link.aps.org/doi/10.1103/RevModPhys.87.637.

[50] M. S. Safronova et al. "Blackbody-radiation shift in the Sr optical atomic clock". In: *Phys. Rev. A* 87 (1 Jan. 2013), p. 012509. DOI: 10.1103/PhysRevA.87.012509. URL: https://link.aps.org/doi/10.1103/PhysRevA.87.012509.

[51] Z. W. Barber et al. "Optical Lattice Induced Light Shifts in an Yb Atomic Clock". In: *Phys. Rev. Lett.* 100 (10 Mar. 2008), p. 103002. DOI: 10.1103/PhysRevLett.100.103002. URL: https://link.aps.org/doi/10.1103/PhysRevLett.100.103002.

[52] Yukun Guo. "3D Anderson transition of ultracold atoms in disordered potentials: observation of the mobility edge". PhD thesis. Université Paris-Saclay, 2023. URL: https://pastel.hal.science/tel-04059506v1/file/120670_GUO_2023_archivage.pdf.

[53] T. A. Zheng et al. "Magic wavelengths of the Yb ($6s^2\ ^1S_0 - -6s6p\ ^3P_1$) intercombination transition". In: *Phys. Rev. A* 102 (6 Dec. 2020), p. 062805. DOI: 10.1103/PhysRevA.102.062805. URL: https://link.aps.org/doi/10.1103/PhysRevA.102.062805.

[54] Yong-Hui Zhang, Li-Yan Tang, and Ting-Yun Shi. "Proposal for suppressing the ac Stark shift in the He($2\ ^3S_1 \rightarrow 3\ ^3S_1$) two-photon transition using magic wavelengths". In: *Phys. Rev. A* 104 (4 Oct. 2021), p. 042817. DOI: 10.1103/PhysRevA.104.042817. URL: https://link.aps.org/doi/10.1103/PhysRevA.104.042817.

[55] S. H. Autler and C. H. Townes. "Stark Effect in Rapidly Varying Fields". In: *Phys. Rev.* 100 (2 Oct. 1955), pp. 703–722. DOI: 10.1103/PhysRev.100.703. URL: https://link.aps.org/doi/10.1103/PhysRev.100.703.

[56] C. Cohen-Tannoudji, J. Dupont-Roc, and G. Grynberg. *Atom-Photon Interactions: Basic Processes and Applications*. Wiley, 1998. ISBN: 9780471293361. URL: https://books.google.fr/books?id=hNWbEAAAQBAJ.

[57] B. Efron and R.J. Tibshirani. *An Introduction to the Bootstrap*. Chapman & Hall/CRC Monographs on Statistics and Applied Probability. CRC Press, 1994. ISBN: 9781000064988. URL: https://books.google.fr/books?id=MWC1DwAAQBAJ.

[58] Bradley Efron and Robert J. Tibshirani. *An Introduction to the Bootstrap*. https://www.stat.cmu.edu/~larry/=sml/Boot.pdf. Lecture notes, Department of Statistics, Carnegie Mellon University. 1994.

[59] AbdulAzeez S. AlOmar. "Line width at half maximum of the Voigt profile in terms of Gaussian and Lorentzian widths: Normalization, asymptotic expansion, and chebyshev approximation". In: *Optik* 203 (2020), p. 163919. ISSN: 0030-4026. DOI: https://doi.org/10.1016/j.ijleo.2019.163919. URL: https://www.sciencedirect.com/science/article/pii/S0030402619318170.

[60] Michael Faraday. "On the Magnetization of Light and the Illumination of Magnetic Lines of Force". In: *Philosophical Transactions of the Royal Society of London* 136 (1846), pp. 1–20. DOI: 10.1098/rstl.1846.0002. URL: https://doi.org/10.1098/rstl.1846.0002.

[61] D. Budker et al. "Resonant nonlinear magneto-optical effects in atoms". In: *Rev. Mod. Phys.* 74 (4 Nov. 2002), pp. 1153–1201. DOI: 10.1103/RevModPhys.74.1153. URL: https://link.aps.org/doi/10.1103/RevModPhys.74.1153.

[62] J. M. Higbie et al. "Direct Nondestructive Imaging of Magnetization in a Spin-1 Bose-Einstein Gas". In: *Phys. Rev. Lett.* 95 (5 July 2005), p. 050401. DOI: 10.1103/PhysRevLett.95.050401. URL: https://link.aps.org/doi/10.1103/PhysRevLett.95.050401.

[63] M. Vengalattore et al. "High-Resolution Magnetometry with a Spinor Bose-Einstein Condensate". In: *Phys. Rev. Lett.* 98 (20 May 2007), p. 200801. DOI: 10.1103/PhysRevLett.98.200801. URL: https://link.aps.org/doi/10.1103/PhysRevLett.98.200801.

[64] K. Pandey et al. "Linear and nonlinear magneto-optical rotation on the narrow strontium intercombination line". In: *Phys. Rev. A* 93 (5 May 2016), p. 053428. DOI: 10.1103/PhysRevA.93.053428. URL: https://link.aps.org/doi/10.1103/PhysRevA.93.053428.

[65] G. Labeyrie, C. Miniatura, and R. Kaiser. "Large Faraday rotation of resonant light in a cold atomic cloud". In: *Phys. Rev. A* 64 (3 Aug. 2001), p. 033402. DOI: 10.1103/PhysRevA.64.033402. URL: https://link.aps.org/doi/10.1103/PhysRevA.64.033402.

[66] Antonios Gonis and William H Butler. *Multiple scattering in solids*. Springer Science & Business Media, 1999.

[67] Howard B. Bluestein, Frederick H. Carr, and Steven J. Goodman. *Atmospheric Observations of Weather and Climate*. 2022. URL: https://repository.library.noaa.gov/view//59391.

[68] Zhen Wang, Jingxin Zhang, and Haiyang Gao. "Impacts of laser beam divergence on lidar multiple scattering polarization returns from water clouds". In: *Journal of Quantitative Spectroscopy and Radiative Transfer* 268 (2021), p. 107618. DOI: https://doi.org/10.1016/j.jqsrt.2021.107618.

[69] M. A. Davis, S. S. Kazmi, and A. K. Dunn. "Imaging depth and multiple scattering in laser speckle contrast imaging". In: *Journal of Biomedical Optics* 19.8 (2014), p. 086001. DOI: 10.1117/1.JBO.19.8.086001.

[70] C. M. Tempany and B. J. McNeil. "Advances in biomedical imaging". In: *JAMA* 285 (2001), pp. 562–567. DOI: 10.1001/jama.285.5.562.

[71] Daniël W. S. Cox, Tom Knop, and Ivo M. Vellekoop. "Model-based aberration corrected microscopy inside a glass tube". In: *Journal of Microscopy* 298.3 (2025), pp. 316–323. DOI: 10.1111/jmi.13402.

[72] Seokchan Yoon et al. "Deep optical imaging within complex scattering media". In: *Nature Reviews Physics* 2.3 (2020), pp. 141–158. DOI: 10.1038/s42254-019-0143-2.

[73] Stefan Rotter and Sylvain Gigan. "Light fields in complex media: Mesoscopic scattering meets wave control". In: *Rev. Mod. Phys.* 89 (1 Mar. 2017), p. 015005. DOI: 10.1103/RevModPhys.89.015005. URL: https://link.aps.org/doi/10.1103/RevModPhys.89.015005.

[74] G. Labeyrie et al. "Observation of coherent backscattering of light by cold atoms". In: *Journal of Optics B: Quantum and Semiclassical Optics* 2.5 (Oct. 2000), p. 672. ISSN: 1464-4266. DOI: 10.1088/1464-4266/2/5/316. URL: https://doi.org/10.1088/1464-4266/2/5/316.

[75] David Wilkowski et al. "Coherent backscattering of light by resonant atomic dipole transitions". In: *J. Opt. Soc. Am. B* 21.1 (Jan. 2004), pp. 183–190. DOI: 10.1364/JOSAB.21.000183. URL: https://opg.optica.org/josab/abstract.cfm?URI=josab-21-1-183.

[76] S. Jennewein et al. "Coherent Scattering of Near-Resonant Light by a Dense Microscopic Cold Atomic Cloud". In: *Phys. Rev. Lett.* 116 (23 June 2016), p. 233601. DOI: 10.1103/PhysRevLett.116.233601. URL: https://link.aps.org/doi/10.1103/PhysRevLett.116.233601.

[77] W. Guerin, M. T. Rouabah, and R. Kaiser. "Light interacting with atomic ensembles: collective, cooperative and mesoscopic effects". In: *Journal of Modern Optics* 64.9 (May 2017), pp. 895–907. ISSN: 0950-0340. DOI: 10.1080/09500340.2016.1215564. URL: https://doi.org/10.1080/09500340.2016.1215564.

[78] William Guerin. "Chapter Four - Super- and subradiance in dilute disordered cold atomic samples: observations and interpretations". In: *Advances in Atomic, Molecular, and Optical Physics*. Ed. by Louis F. DiMauro, Hélène Perrin, and Susanne F. Yelin. Vol. 72. Advances In Atomic, Molecular, and Optical Physics. Academic Press, 2023, pp. 253–296. DOI: https://doi.org/10.1016/bs.aamop.2023.04.002. URL: https://www.sciencedirect.com/science/article/pii/S1049250X23000022.

[79] G. Labeyrie et al. "Slow Diffusion of Light in a Cold Atomic Cloud". In: *Phys. Rev. Lett.* 91 (22 Nov. 2003), p. 223904. DOI: 10.1103/PhysRevLett.91.223904. URL: https://link.aps.org/doi/10.1103/PhysRevLett.91.223904.

[80] Ad Lagendijk and Bart A. van Tiggelen. "Resonant multiple scattering of light". In: *Physics Reports* 270.3 (1996), pp. 143–215. ISSN: 0370-1573. DOI: https://doi.org/10.1016/0370-1573(95)00065-8. URL: https://www.sciencedirect.com/science/article/pii/0370157395000658.

[81] M. C. W. van Rossum and Th. M. Nieuwenhuizen. "Multiple scattering of classical waves: microscopy, mesoscopy, and diffusion". In: *Rev. Mod. Phys.* 71 (1 Jan. 1999), pp. 313–371. DOI: 10.1103/RevModPhys.71.313. URL: https://link.aps.org/doi/10.1103/RevModPhys.71.313.

[82] P. Sheng. *Introduction to Wave Scattering, Localization, and Mesoscopic Phenomena*. Elsevier Science, 1995. ISBN: 9780126398458. URL: https://books.google.fr/books?id=KLDvAAAAMAAJ.

[83] Eugene P. Wigner. "Lower Limit for the Energy Derivative of the Scattering Phase Shift". In: *Phys. Rev.* 98 (1 Apr. 1955), pp. 145–147. DOI: 10.1103/PhysRev.98.145. URL: https://link.aps.org/doi/10.1103/PhysRev.98.145.

[84] Teledyne FLIR. *FLIR Blackfly S USB3: 5 MP Monochrome Camera, BFS-U3-50S5M-C*. https://www.teledynevisionsolutions.com/products/blackfly-s-usb3/?model=BFS-U3-50S5M-C.

[85] Andor Technology Ltd. *Zyla 5.5 Scientific CMOS Camera*. https://andor.oxinst.com/products/scmos-camera-series/zyla-5-5-scmos. Accessed: 2025-09-25. Belfast, UK, 2025.

[86] C. Kittel. *Thermal Physics*. Wiley, 1969. ISBN: 9780471490302. URL: https://books.google.fr/books?id=iCA-AAAAIAAJ.

[87] Guillaume Labeyrie. "Coherent transport of light in cold atoms". In: *Modern Physics Letters B* 22.02 (2008), pp. 73–99. ISSN: 0217-9849. DOI: 10.1142/s0217984908014699.

[88] T. Holstein. "Imprisonment of Resonance Radiation in Gases". In: *Phys. Rev.* 72 (12 Dec. 1947), pp. 1212–1233. DOI: 10.1103/PhysRev.72.1212. URL: https://link.aps.org/doi/10.1103/PhysRev.72.1212.